



University of
Nottingham

UK | CHINA | MALAYSIA

**Investigating the Size Dependent Toxicological
Effects of Zinc Oxide Nanoparticles on
Caenorhabditis elegans and the Inhibitory
Potential on Cytochrome P450 Isozymes**

Master of Philosophy in Biomedical Sciences
Lamia Noushin Sadeque Chowdhury

Supervisor: Dr Pan Yan

University of Nottingham, School of Pharmacy, Division of
Biomedical Science

I: Abstract	V
II: Conference Abstracts	VII
Pharm/Biomed 6 th Annual Postgraduate Research Symposium – Poster Presentation	VII
35 th Annual Scientific Meeting For Malaysian Society of Pharmacology and Physiology - Oral Presentation	VIII
III: Acknowledgements	IX
IV: List of Abbreviations	X
V: List of Figures	XII
VI: List of Tables	XIV
Chapter 1: Introduction and Literature Review	1
1.1 Zinc Oxide Nanoparticles	1
1.1.1 Applications of ZnONPs	1
1.1.2 Toxicity of ZnONPs	3
1.1.2.1 Exposure Routes of ZnONPs	3
1.1.2.2 Reproductive Toxicity	4
1.1.2.3 Developmental Toxicity	5
1.1.2.4 Hepatotoxicity	5
1.1.2.5 Neurotoxicity	6
1.2 The Role of <i>Caenorhabditis elegans</i> as a Pre-clinical Model	7
1.2.1 Anatomy of <i>C. elegans</i>	7
1.2.2 Reproduction in <i>C. elegans</i>	8
1.2.3 Life Cycle of <i>C. elegans</i>	9
1.2.4 Feeding Mechanism of <i>C. elegans</i>	12
1.2.5 <i>C. elegans</i> ' Genome	13
1.2.5.1 External Influences on Gene Expression of <i>C. elegans</i>	13
1.2.5.2 Genes of Interest	14
1.2.6 Advantages of Using <i>C. elegans</i> as a Toxicological Model	15
1.2.7 Investigation of Toxicological Effects of NPs by Employing <i>C. elegans</i>	16
1.3 Introduction to Cytochrome P450	17
1.3.1 CYP and its Role in Drug Metabolism	18
1.3.2. Drug Metabolising CYP Isozymes	19
1.3.3 Inhibition of CYP Isozymes	20
1.3.3.1 Reversible Inhibition	21
1.3.3.2 Irreversible Inhibition	23
1.3.4 Investigation of Inhibitory Effects of NPs on CYP Isozymes	23
1.4 Problem Statement and Research Gap	24
1.5 Scope of Research Project	24
1.6 Objectives of Research Project	25
1.7 Hypothesis of Research Project	25
Chapter 2: Characterisation of ZnO Particles	26
2.1 Background	26
2.2 Methodology	28
2.2.1 Materials and Reagents	28
2.2.2 ZnO Particles' Characterization	28

2.3 Results and Discussion	29
2.4 Conclusion	33
Chapter 3: Toxicological Effects of Various Sized Zinc Oxide Particles on <i>Caenorhabditis elegans</i>	34
3.1 Background	34
3.2 Methodology	36
3.2.1 Materials and Reagents	36
3.2.2 Preparation of ZnO Particles	36
3.2.3 Solution Preparation	37
3.2.4 Selection of Optimal FUDR Concentration	38
3.2.5 Agar Preparation	38
3.2.5.1 Nematode Growth Medium (NGM) Agar	38
3.2.5.2 Lysogeny Broth (LB) Agar	38
3.2.6 Bacterial Food Source Preparation	38
3.2.7 Age Synchronisation Procedure	39
3.2.8 Cryopreservation	39
3.2.8.1 <i>E. coli</i> OP50	39
3.2.8.2 N2	39
3.2.9 Reproductive Capacity Assay	39
3.2.10 Pharyngeal Pumping Rate Assay	40
3.2.11 Lifespan Assay	40
3.2.12 Sample Preparation for Gene Expression Study	41
3.2.13 Ribonucleic Acid (RNA) Extraction	41
3.2.14 Complementary Deoxyribonucleic Acid (cDNA) Synthesis	42
3.2.15 Primer Design and Polymerase Chain Reaction	42
3.2.16 Gel Electrophoresis, and Gel Imaging	43
3.2.17 Data Analysis	43
3.2.17.1 Reproductive Capacity Assay and Pharyngeal Pumping Rate Assay	43
3.2.17.2 Lifespan Assay	43
3.2.17.3 Gene Expression Study	44
3.3 Results and Discussion	45
3.3.1 Selection of Optimal FUDR Concentration	45
3.3.2 Reproduction Capacity of <i>C. elegans</i> Treated with Zinc Oxide Particles	46
3.3.3 Pharyngeal Pumping Rate of <i>C. elegans</i> Treated with Zinc Oxide Particles	49
3.3.4 Lifespan of <i>C. elegans</i> Treated with Zinc Oxide Particles	51
3.3.5 Primer Design	53
3.3.6 Extracted Ribonucleic Acid (RNA)'s Concentration and Purity	53
3.3.7 Agarose Gel Analysis of N2 Genes	54
3.4 Conclusion	60
Chapter 4: Inhibitory Effects of Various Sized Zinc Oxide Particles on Human CYP isozymes	61
4.1 Background	61
4.2 Methodology	63
4.2.1 Materials and Reagents	65
4.2.2 Establishment of Standard Curves	65
4.2.3 Establishment of Time Curves	65
4.2.4 Inhibition of CYP Isozymes by Positive Inhibitors	66
4.2.5 Preparation of ZnO Particles	66
4.2.6 Determination of Half Maximal Inhibitory Concentration (IC ₅₀)	66
4.2.7 Time-Dependent Inhibition (TDI) Assay	67
4.2.8 Determination of K _i and Mode of Inhibition	67

4.2.9 Data Analysis	69
4.2.9.1 Determination of Half Maximal Inhibitory Concentration (IC_{50})	69
4.2.9.2 Determination of IC_{50} Shift	69
4.2.9.3 Determination of K_i and Mode of Inhibition	69
4.3 Results and Discussion	70
4.3.1 Establishment of Standard Curves	70
4.3.2 Establishment of Time Curves	70
4.3.3 Inhibition of CYP Isozymes by Positive Inhibitors	71
4.3.4 Determination of Half Maximal Inhibitory Concentration (IC_{50})	76
4.3.5 Determination of IC_{50} Shift and Time-Dependent Inhibition	87
4.3.6 Determination of K_i and Mode of Inhibition	93
4.4 Conclusion	113
References	114
Appendix	141

I: Abstract

Zinc oxide nanoparticles (ZnONPs) are used in several industries including the cosmetics, textiles, and therapeutics. Wild-type *Caenorhabditis elegans* (N2) is commonly used as an ecotoxicological model, and as an *in vivo* model to understand the toxicity of xenobiotics in humans. Cytochrome P540 (CYP) isozymes are responsible for drug metabolism in humans, and its inhibition may lead to adverse drug reactions due to the decreased metabolism and subsequent delayed clearance of co-administered drugs. However, the size-dependent toxicological potential of ZnO particles towards N2 and inhibitory potential towards CYP isozymes are not well known. Firstly, this project aimed to investigate the size-dependent toxicological potential of ZnONP50 (zinc oxide nanoparticles <50 nm), ZnONP100 (zinc oxide nanoparticles <100 nm), and ZnOBP (zinc oxide bulk particle) towards the reproductive capacity, pharyngeal pumping rate, and lifespan of N2. Additionally, gene expression studies were carried out to assess the variation of the nematode's *cep-1* and *pmk-1* genes. Secondly, this project aimed to elucidate the size-dependent *in vitro* inhibitory effect and mode of inhibition of the ZnO particles towards CYP1A2, CYP2A6, CYP2B6, CYP2C8, CYP2E1, CYP2J2, and CYP3A5.

Behavioural assays were conducted using N2 to investigate the size-dependent toxicological effect of ZnONP50, ZnONP100, and ZnOBP on the nematode's reproductive capacity, pharyngeal pumping rate, and lifespan. A gene expression study using conventional PCR was performed to assess the variation in the expression of the *cep-1* and *pmk-1* genes to elicit the plausible mechanism of ZnO particles' toxicity. Inhibitory potential of ZnONP50, ZnONP100, and ZnOBP on CYP isozymes was investigated using *in vitro* fluorescence enzymatic assays. Half maximal inhibitory concentration (IC₅₀), IC₅₀-shift, inhibitor constant (K_i), and the mode of inhibition were determined.

ZnONP50 exhibited the strongest toxicological effect in terms of N2's lifespan, while the nematode's reproduction capacity and pharyngeal pumping rate was negatively altered the most by ZnONP100. Based on the gene expression study, ZnONP50 upregulated the expression of *cep-1* and *pmk-1* when compared to ZnONP100 and ZnOBP. ZnO particles were able to inhibit the CYP isozymes with various potencies in various reversible inhibition modes. ZnONP50 was able to significantly inhibit CYP2B6 (K_i:20.33 µg/mL, mixed-mode), CYP2C8 (K_i:43.33 µg/mL, competitive-mode), CYP2E1 (K_i: 16.63 µg/mL, mixed-mode), CYP2J2 (K_i: 8.18 µg/mL, non-competitive-mode), and CYP3A5 (K_i: 2.54 µg/mL, non-competitive mode). ZnONP100 inhibited CYP2B6 (K_i: 6.67 µg/mL, mixed-mode), CYP2E1 (K_i: 40.1 µg/mL,

mixed-mode), CYP2J2 (K_i : 20.0 $\mu\text{g/mL}$, mixed/non-competitive-mode), and CYP3A5's (K_i : 0.5 $\mu\text{g/mL}$, non-competitive-mode) enzymatic activity. ZnOBP inhibited the enzymatic activity of CYP2E1 (K_i : 28.3 $\mu\text{g/mL}$, competitive-mode).

Size-dependent toxicity demonstrated by ZnO particles towards N2, and the targeted genes were investigated. Based on the gene expression study results, it is suggested that ZnONPs likely elicited its toxicological effects through the production of ROS and the subsequently generated oxidative stress. Size-dependent inhibition was exhibited towards CYP2B6, CYP2J2, and CYP2E1. Based on the results of this project, future studies are recommended to quantify the production of ROS and the subsequent oxidative stress production to improve the understanding of ZnONPs' toxicological impact in N2 and in humans. Additionally, *in silico* studies using CYP isozymes are required to improve the understanding of the mechanism of ZnONPs' inhibitory potential.

II: Conference Abstracts

Pharm/Biomed 6th Annual Postgraduate Research Symposium – Poster Presentation

Inhibitory Potential of Zinc Oxide Bulk Particles on Cytochrome P450 Isoforms *in vitro*

Lamia Noushin Sadeque Chowdhury¹, Pan Yan^{1*}

¹Division of Biomedical Science, School of Pharmacy, Faculty of Science and Engineering, University of Nottingham Malaysia Campus, Jalan Broga, 43500 Semenyih, Selangor Darul Ehsan, Malaysia

*Corresponding author: pan.yan@nottingham.edu.my

Introduction: Zinc oxide is a multifunctional material owing to its chemical stability, broad range of radiation absorption, and electrochemical coupling coefficient. Due to these characteristics, the material is used in several industries including cosmetics, textiles, and pharmaceuticals. Its good biocompatibility allows it to also be used in a therapeutic setting. While certain materials are known to hinder the activity of drug-metabolising cytochrome P450 (CYP) enzymes, the mechanism of inhibition by zinc oxide bulk particles (ZnOBP) is not well understood. As the probable inhibition of CYP isoforms may lead to adverse reactions due to delayed clearance of co-administered drugs, it is essential that the physiological effects are identified. This study is designed to investigate the *in vitro* inhibitory effects of ZnOBP on the following human drug metabolising isoforms: CYP1A2, CYP2A6, CYP2B6, CYP2C8, CYP2E1, CYP2J2, and CYP3A5.

Methodology: Inhibitory potential of ZnOBP on CYP isoforms was investigated through *in vitro* fluorescence-based high-throughput screening enzymatic assays in the presence of various ZnOBP concentrations, using Vivid® CYP450 Screening Kits. Inhibition ability (IC₅₀; half maximal inhibitory concentration) and mode of inhibition (TDI; time-dependent inhibition) were determined. The results were analysed using GraphPad Prism 9.2.0.

Results: At the highest concentration of ZnOBP, 100µg/ml, enzymatic activity remained at 145%, 98%, 94%, 105%, 91% and 120% for the following isoforms respectively: CYP1A2, CYP2A6, CYP2B6, CYP2C8, CYP3A5 and CYP2J2. 51.1% enzymatic activity was reduced for CYP2E1 upon exposure to the highest concentration of ZnOBP. Additionally, the IC₅₀ value was determined to be 44.51µg/ml and IC₅₀ shift of 1.48 was derived for CYP2E1.

Discussion/Conclusion: It was concluded that ZnOBP demonstrated negligible inhibitory effect towards all isoforms, except CYP2E1. Concentration dependent inhibition of CYP2E1 was observed, and ZnOBP was classified as a weak inhibitor. Additionally, ZnOBP was categorised as a moderate time-dependent inhibitor of CYP2E1. Further *in vitro* studies will be conducted, as it is essential to better understand the effect of varying factors; namely different classes of shapes and sizes of zinc oxide nanoparticles. Additional *in vivo* and *in silico* studies are warranted to confirm potential adverse side effects and to understand the molecular interaction between the zinc oxide particles and CYP isoforms.

Keywords: bulk particles, nanoparticles, zinc oxide, cytochrome P450, *in vitro* inhibitory studies

35th Annual Scientific Meeting For Malaysian Society of Pharmacology and Physiology - Oral Presentation

Investigating Size-Dependent Inhibition of Cytochrome P450 Isozymes by Zinc Oxide Bulk particles and Nanoparticles

Lamia Noushin Sadeque Chowdhury¹, Pan Yan^{1*}

¹Division of Biomedical Science, School of Pharmacy, Faculty of Science and Engineering, University of Nottingham Malaysia Campus, Jalan Broga, 43500 Semenyih, Selangor Darul Ehsan, Malaysia

*Corresponding author: pan.yan@nottingham.edu.my

Introduction: Zinc oxide is a multifunctional material used in several industries including cosmetics, textiles, and therapeutic settings. The potential of inhibition of drug metabolizing cytochrome p450 (CYP) isozymes by zinc oxide bulk (ZnOBP) and nanoparticles (ZnONPs) is not well understood. Inhibition of CYP isozymes may lead to adverse drug reactions due to delayed clearance of co-administered drugs. Thus, this study was designed to investigate the in vitro inhibitory effect of ZnOBP and ZnONPs on CYP1A2, CYP2A6, CYP2B6, CYP2C8, CYP2E1, CYP2J2 and CYP3A5. Additionally, the investigation focused on potential size-dependent inhibitory effects.

Methodology: Inhibitory potential of ZnOBP and ZnONPs (<50 nm and <100 nm) on CYP isozymes were investigated using in vitro fluorescence enzymatic assays in the presence and absence of various ZnO compound concentrations. IC₅₀ and IC₅₀-shift values were determined.

Results: ZnOBP did not demonstrate significant reversible inhibition on any CYP isozyme, except for CYP2E1 with an IC₅₀ value 16.32 µg/ml. ZnONPs with size <100 nm demonstrated significant reversible inhibition of CYP2B6, CYP2E1, CYP2J2, and CYP3A5 except CYP1A2, CYP2A6, and CYP2C8 with IC₅₀ values of 8.43, 36.10, 23.25, and 7.93 µg/ml. Irreversible inhibition of the CYP isozymes by <100 nm ZnONPs was not discovered. ZnONPs with size <50 nm demonstrated significant reversible inhibition on CYP2B6, CYP2C8, CYP2E1, CYP2J2, and CYP3A5 except CYP1A2 and CYP2A6 with IC₅₀ values of 13.22, 10.15, 4.85, and 10.15 µg/ml. Irreversible inhibition of the CYP isozymes by 50 nm ZnONPs was evident for CYP2B6, CYP2C8 and CYP2J2.

Discussion/Conclusion: CYP metabolism mediated ZnO-drug interactions are possible post co-bioavailability of zinc oxide bulk particles and zinc oxide nanoparticles with drugs metabolized by CYP2B6, CYP2C8, CYP2E1, CYP2J2 and CYP3A5. Smaller sized ZnONPs were able to elicit stronger inhibition in all isozymes, except for CYP2J2, indicating size-dependent inhibitory effects. Future in vitro studies will allow confirmation modes of inhibition. Further in vivo and in silico studies involving zinc oxide bulk particles and nanoparticles and these CYP isozymes are required to confirm the potential of adverse drug reaction and to understand the molecular interaction between these compounds and CYP isozymes.

Keywords: zinc-oxide, bulk particles, nanoparticles, cytochrome P450, nanoparticle-drug interaction

III: Acknowledgements

I would like to express my sincere gratitude to my supervisor, Dr. Pan Yan, for her valuable guidance, support, and encouragement throughout my research work. Her feedback allowed me to deepen and refine my research, and the results presented in this thesis would not have been possible without her supervision. I am also thankful to my colleagues, friends, and the support staff for their assistance, feedback and motivation. I would like to acknowledge the help of my family members, who have been a constant source of support and inspiration. Finally, I would like to thank the Fundamental Research Grant Scheme for providing financial assistance for this research work.

IV: List of Abbreviations

Abbreviation	Definition
$\cdot\text{O}_2^-$	Superoxide anion radical
AgNPs	Silver nanoparticles
ALP	Alkaline phosphatase
ALT	Alanine aminotransferase
AST	Aspartate aminotransferase
AuNPs	Gold nanoparticles
<i>B. subtilis</i>	<i>Bacillus subtilis</i>
BBB	Blood-brain-barrier
BP	Bulk particle
<i>C. elegans</i>	<i>Caenorhabditis elegans</i>
CaCl ₂	Calcium chloride
cDNA	Complementary deoxyribonucleic acid
CEMs	Cephalic companion neurons
<i>cep</i>	<i>C. elegans</i> P53-like protein
CNS	Central nervous system
CuONPs	Copper oxide nanoparticles
CYP	Cytochrome P450
CYP1A2	Cytochrome P450 1A2
CYP1A2	Cytochrome p450 1A2
CYP2A6	Cytochrome P450 2A6
CYP2B6	Cytochrome P450 2B6
CYP2C11	Cytochrome P450 2C11
CYP2C8	Cytochrome P450 2C8
CYP2E1	Cytochrome P450 2E1
CYP2J2	Cytochrome P450 2J2
CYP3A2	Cytochrome P450 3A2
CYP3A5	Cytochrome P450 3A5
DMSO	Dimethyl sulfoxide
DNA	Deoxyribonucleic acid
DTC	Distal tip cells
<i>E. coli</i> OP50	<i>Escherichia coli</i> strain OP50
EDX	Energy dispersive X-ray elemental analysis
FESEM	Field emission scanning electron microscopy
FRU	Fluorescent reading
FSH	Follicle stimulating hormones
FUDR	5-fluorodeoxyuridine
GFAP	Glial fibrillary acidic protein
GGT	Gamma-glutamyl transferase
H ₂ O	Water
H ₂ O ₂	Hydrogen peroxide
HIV	Human immunodeficiency virus
HPLC	High performance liquid chromatography
IC ₅₀	Half maximal inhibitory concentration
IL-8	Interleukin 8
IPTG	Isopropyl β -d-1-thiogalactopyranoside
K ₂ HPO ₄	Di-potassium hydrogen phosphate
KH ₂ PO ₄	Potassium dihydrogen phosphate

K_i	Inhibition constant
K_m	Michaelis constant
L1	First-larval stage
L2	Second-larval stage
L2D	L2-dauer larva stage
L3	Third-larval stage
L4	Fourth-larval stage
LB	Lysogeny broth
LH	Luteinizing hormone
M	Motor
MAPK	Mitogen-activated protein kinases
$MgSO_4$	Magnesium sulfate
NaCl	Sodium chloride
$NADP^+$	Nicotinamide adenine dinucleotide phosphate
NADPH	Nicotinamide adenine dinucleotide phosphate
NaOH	sodium hydroxide
NDI	Nanoparticle-drug interactions
NGM	Nematode growth medium
NPs	Nanoparticles
OH^{\bullet}	Hydroxyl radical
P_4	Germline blastomere
<i>p53</i>	Tumour protein p53
PAMPA	Parallel artificial membrane permeability assays
PCLS	Precision-cut liver slices
PCR	Polymerase chain reaction
<i>pmk</i>	P38 MAP Kinase
PMMA-AA-ZnONPs	Conjugated ZnONPs and polymer PMMA-AA
PTFE	Polytetrafluoroethylene
RNA	Ribonucleic acid
SNPs	Silica nanoparticles
TAE	Tris-acetate-EDTA
<i>tba</i>	TuBulin Alpha
TDI	Time-dependent inhibition
TiO_2 NPs	Titanium dioxide nanoparticles
two-way ANOVA	Two-way analysis of variance
UV	Ultraviolet
V_{max}	Maximum velocity
N2	Bristol strain N2
ZnO	Zinc oxide
ZnO-Fe ₃ O ₄ NPs	Zinc oxide and black iron oxide conjugated nanoparticles
ZnOBP	Zinc oxide bulk particles
ZnONP100	Zinc oxide nanoparticles <100 nm
ZnONP50	Zinc oxide nanoparticles <50 nm
ZnONPs	Zinc oxide nanoparticles

V: List of Figures

Figure Number	Title	Page Number
1.1	Diagram illustrating the life cycle of <i>C. elegans</i> .	9
1.2	Percentage of clinical drugs metabolised by Cytochrome P450 isozymes.	19
1.3	Lineweaver-Burk plots of different types of reversible inhibition: competitive, uncompetitive, and noncompetitive	21
2.1	Characterisation and analysis of ZnOBPs	29
2.2	Characterisation and analysis of ZnONP100	30
2.3	Characterisation and analysis of ZnONP50	31
3.1	Reproductive capacity of L4 N2 post-exposure to ZnO particles	46
3.2	Pharyngeal pumping rate of L4 N2 post-exposure to ZnO particles	49
3.3	Lifespan of L4 N2 post-exposure to ZnO particles	51
3.4	Agarose gel electrophoresis (2% agarose) of PCR amplified DNA samples (<i>cep-1</i> , <i>tba-1</i> , <i>pmk-1</i>) of L4 N2 post-exposure to ZnO particles (100 µg/mL) for 72 hours	54
3.5	Relative fold change of ZnO particle-treated <i>cep-1</i> and <i>pmk-1</i> DNA bands of L4 N2 in comparison to their respective untreated-control DNA bands	55
4.1	Schematic representation of the metabolism of Vivid® Substrates into fluorescent metabolites by CYP450 BALCUSOMES® Plus Reagents	61
4.2	Schematic representation of the six steps of a Vivid®CYP450 assay conducted in the end-point mode	63
4.3	Time curves of CYP isozymes	70
4.4	Inhibition analysis of CYP isozymes by their positive inhibitors	72
4.5	Inhibitory effects of ZnO particles on CYP1A2	76
4.6	Inhibitory effects of ZnO particles on CYP2A6	77
4.7	Inhibitory effects of ZnO particles on CYP2B6	78
4.8	Inhibitory effects of ZnO particles on CYP2C8	79
4.9	Inhibitory effects of ZnO particles on CYP2E1	80
4.10	Inhibitory effects of ZnO particles on CYP2J2	81

4.11	Inhibitory effects of ZnO particles on CYP3A5	82
4.12	Evaluation of the size-dependent inhibition of CYP isozymes by ZnO particles	86
4.13	Time dependent inhibition of CYP2B6 by ZnO particles	88
4.14	Time dependent inhibition of CYP2C8 by ZnO particles	89
4.15	Time dependent inhibition of CYP2E1 by ZnO particles	89
4.16	Time dependent inhibition of CYP2J2 by ZnO particles	91
4.17	Time dependent inhibition of CYP3A5 by ZnO particles	92
4.18	Lineweaver-Burk plot of inhibition and secondary plot of CYP2B6 by ZnONP50	94
4.19	Lineweaver-Burk plot of inhibition and secondary plot of CYP2B6 by ZnONP100	95
4.20	Lineweaver-Burk plot of inhibition and secondary plot of CYP2C8 by ZnONP50	96
4.21	Lineweaver-Burk plot of inhibition and secondary plot of CYP2E1 by ZnONP50	97
4.22	Lineweaver-Burk plot of inhibition and secondary plot of CYP2E1 by ZnONP100	98
4.23	Lineweaver-Burk plot of inhibition and secondary plot of CYP2E1 by ZnOBP	99
4.24	Lineweaver-Burk plot of inhibition and secondary plot of CYP2J2 by ZnONP50	100
4.25	Lineweaver-Burk plot of inhibition and secondary plot of CYP2J2 by ZnONP100	101
4.26	Lineweaver-Burk plot of inhibition and secondary plot of CYP3A5 by ZnONP50	102
4.27	Lineweaver-Burk plot of inhibition and secondary plot of CYP3A5 by ZnONP100	103

VI: List of Tables

Table Number	Title	Page Number
3.1	Concentration and sonication specifications for ZnO particle	37
3.2	Summary of FUDR Concentrations 30-Day Trial (n=3)	45
3.3	Product size, NCBI reference sequence, primer sequence, annealing temperature, guanine-cytosine percentage, self-complementary score, and self-3' complementary score of the chosen primer pairs for the target genes' (<i>cep-1</i> and <i>pmk-1</i>) and the reference gene's (<i>tba-1</i>) amplification by PCR	53
3.4	Concentration and purity results of extracted RNA from N2	53
4.1	Vivid® Substrates and their corresponding metabolites	62
4.2	Varioskan Flash Plate Reader's settings based on each CYP isozymes and their respective Vivid® Fluorescent Standards	64
4.3	Final concentration of reagents for each CYP isozyme reaction	64
4.4	Concentration range of each CYP isozyme's positive inhibitor	66
4.5	Concentration range of each CYP isozyme's ZnO particle and Vivid® Substrate's concentration for their respective K_i assays	68
4.6	Summary of derived IC_{50} values and the remaining enzymatic activity of CYP isozymes post-exposure to the highest concentration of their respective positive inhibitors	71
4.7	Retrieved and reported IC_{50} values of CYP isozymes under the presence of their respective positive inhibitors	75
4.8	Summary of IC_{50} assay' results for each CYP isozyme	85
4.9	Summary of IC_{50} -shift ratios for all CYP isozymes tested for mechanism-based inhibition by their respective ZnO particle	93
4.10	Summary of the modes of inhibition and K_i for all CYP isozymes under the presence of the respective ZnO particle	105

Chapter 1: Introduction and Literature Review

1.1 Zinc Oxide Nanoparticles

Nanotechnology, comprising of nanoparticles (NPs) and nanostructured materials, is an active research focus in the fields of science and technology. NPs acquired popularity in several industries owing to their physicochemical characteristics including electrical and thermal conductivity, melting point, wettability, light absorption, and catalytic activity. NPs are particles of a diameter between 1 to 100 nm. Within the scope of NPs, metal oxide NPs are a type of inorganic material which are synthesized via several techniques including the sol-gel method and the chemical precipitation method. Zinc oxide nanoparticles (ZnONPs) are a type of metal oxide NPs which have gained significant attention due to its wide range of applications (Altammar, 2023; Gupta & Xie, 2018; Jeevanandam et al., 2018).

1.1.1 Applications of ZnONPs

ZnONPs' physicochemical characteristics allow them to be used in various biomedical applications including its anti-ultraviolet radiation, antimicrobial, and anticancer properties.

A strong advantage of engineering ZnONPs is their anti-ultraviolet radiation property. Sunscreens are utilised to protect the skin against the detrimental effects of solar ultraviolet (UV) radiation (Smijs & Pavel, 2011). Minerals such as zinc oxide (ZnO) are commonly used as inorganic physical sun blockers, as they are inert, and are able to minimise dermal irritation, sensitization, and penetration (Antoniou et al., 2008). ZnO particles, which range between the 200 and 400 nm sizes, are naturally opaque due to their ability to absorb and scatter light. This results in a visible white cast when applied on the skin. However, ZnONPs between the sizes of 40 nm and 100 nm, are able to block UV efficiently and are also able to absorb the majority of visible wavelengths (Ginzburg et al., 2021). This property of ZnONPs eliminates the inherent opaqueness of ZnO particles, and makes sunscreens made of ZnONPs undetectable on the skin; ZnONPs based sunscreens are inclusive of all skin tones (Nohynek et al., 2008).

The anti-microbial property of ZnONPs allows it to be used in medical ointments and creams meant to accelerate wound healing, dental fillings, and as a component of the preservative coating in food packaging (Gudkov et al., 2021; Kolodziejczak-Radzimska & Jesionowski, 2014; Xie et al., 2011). In a study conducted to develop nanomedicine focusing on the effect of ZnONPs against *Vibrio cholera*, the bacterium responsible for causing cholera, concluded that ZnONPs have the ability to damage and increase the permeability of the bacterium's membrane, and significantly modify the bacterium's morphology (Sarwar et al., 2016). There are two primary mechanisms hypothesised for ZnONPs' antimicrobial activity.

The first mechanism is through photoactivation of ZnONPs, which results in a series of chemical reactions, and subsequently the formation of reactive oxygen species (ROS) in the intracellular and extracellular regions of the bacterium. ROS formed includes hydrogen peroxide (H_2O_2), hydroxyl radical (OH^\bullet), and superoxide anion radical ($^{\bullet}\text{O}_2^-$). Accumulation of ROS is able to damage cellular organelles of the bacterium, which results in necrosis (Sirelkhatim et al., 2015; Verbic et al., 2019). The second mechanism of ZnONPs' antimicrobial activity occurs in the absence of light, and it is associated with the dissolution of ZnONPs. This results in an increased concentration of Zn^{2+} ions within the cytoplasm of the bacterium, which leads to necrosis (Verbic et al., 2019; Xie et al., 2011). Under dark conditions, oxygen radicals and H_2O_2 are generated from ZnONPs through oxygen defect sites. Oxygen defect mediated ROS generation is considered as the primary reason for anti-bacterial properties in the absence of light. Transfection of ZnONPs have also been attributed as a mechanism for bacterial cell wall damage (Joe et al., 2017).

Cancer is a disease which develops from uncontrolled and abnormal proliferation of cells within the body (Anjum et al., 2021). Conventional therapy of cancer includes radiotherapy, chemotherapy, and surgery. While conventional therapy choices are effective, they are non-selective which leads to a multitude of adverse side effects (Shah & Rajput, 2019). To overcome the adverse side-effects, research focus has been placed on nanomedicine as they provide increased drug delivery capacity, specific targeting, surface functionalisation, and biocompatibility (Peer et al., 2007). As ZnONPs are highly biocompatible, they are considered viable candidates for potential cancer treatments (Zhang et al., 2013). As such, several *in vitro* studies have investigated the use of ZnONPs' anti-cancer property towards different cancer cell lines. In terms of breast cancer, ZnO and black iron oxide conjugated nanoparticles (ZnO- Fe_3O_4 NPs) demonstrated significant toxicity towards the epithelial human breast cancer line, MDA-MB-231 (Bisht et al., 2016). Additionally, ZnONPs exhibited significant induction of cytotoxicity, autophagy, and apoptosis towards the SKOV3 cell line via increasing the amount of oxidative stress and generation of ROS (Bai et al., 2017). In regards to cervical cancer, ZnONPs were able to induce apoptosis of the cervical carcinoma cells through increasing the levels of ROS intracellularly and upregulating the expression of the apoptotic genes tumour protein p53 (*p53*) and caspase-3 (Pandurangan et al., 2016). In reference to colon cancer, ZnONPs were able to decrease the viability of the Caco-2 cell line through increasing the levels of ROS and inducing the expression of interleukin 8 (IL-8) (De Angelis et al., 2013). Additionally, conjugated ZnONPs-peptides were able to induce anti-proliferation of the H2-29 colon cancer lines (Bai Aswathanarayan et al., 2018). Conjugated ZnONPs and polymer

PMMA-AA (PMMA-AA-ZnONPs) were able to encapsulate and transport significant amounts of curcumin, which is known to produce substantial anti-gastric cancer activity (Dhivya et al., 2018). In terms of lung cancer treatment, liposome-incorporated ZnONPs exhibited chemophotodynamic anticancer action, as they were able to perform pH-responsive release of the therapeutic, daunorubicin (Tripathy et al., 2015).

1.1.2 Toxicity of ZnONPs

Despite the several advantageous characteristics of ZnONPs, it is important to note that ZnONPs have demonstrated toxicological effects towards humans and several animal models (Chong et al., 2021). Several *in vivo* assessments have been conducted using various animal models to understand the toxicological effects of ZnONPs in various organs. Through the use of different animal models, greater insights of the potential impact on human health can be achieved.

1.1.2.1 Exposure Routes of ZnONPs

With the increasing use of ZnONPs in various industries, contact with it is inevitable for humans via three primary exposure routes: inhalation, dermal absorption, and ingestion.

The inhalation route of exposure to ZnONPs refers to the process by which the NPs are introduced into the body via the respiratory system; the ZnONPs are inhaled as small particles or as aerosols (Morimoto et al., 2016). Inhalation of ZnONPs occurs through various occupational settings including manufacturing and handling of ZnONPs and manufacturing of products consisting of ZnONPs. Additionally, ZnONPs are present in the general environment through air pollution and exposure to consumer products which contain ZnONPs (Greenberg & Vearrier, 2015). Once the NPs enter the lungs, they are deposited into the alveoli, bronchioles, and other components of the respiratory tract, and are able to interact with the surrounding tissue via physical deposition, phagocytosis, and translocation (Cho et al., 2011; Larsen et al., 2016).

The dermal absorption route of exposure to ZnONPs refers to the penetration of the NPs through the skin and subsequently into the bloodstream (Chen et al., 2022). Exposure to NPs may result from the use of sunscreen, cosmetics, textiles, and/or medical materials consisting of ZnONPs (Ruszkiewicz et al., 2017). Dermal exposure can occur through hair follicles, sweat glands, and the intercellular spaces (Osmond-Mcleod et al., 2014). Once ZnONPs are able to penetrate the skin, they are able to interact with the proteins, lipids, and deoxyribonucleic acid (DNA) components of the skin. Through these interactions, ZnONPs are

able to induce oxidative stress, inflammation, and DNA damage within several types of cells (Wang et al., 2022).

The ingestion route of exposure to ZnONPs refers to the intake of the NPs through various sources such as contaminated habitats, contaminated food and drinking water, food packaging, and drug delivery systems (Grasso et al., 2022). Once the NPs are ingested, ZnONPs are able to penetrate into the bloodstream via the gastrointestinal tract. Entering the circulatory system allows ZnONPs to be distributed to other organs including the liver, kidneys, and the spleen. Additionally, small sized ZnONPs are able to permeate across the blood-brain-barrier (BBB) and accumulate within the brain (Jo et al., 2013). Toxicity via the ingestion route results in inflammation, damage to the gastrointestinal lining, and the accumulation within the different organs, which results in oxidative stress and damage to these organs (Pei et al., 2022).

1.1.2.2 Reproductive Toxicity

ZnONPs have the ability to disperse and accumulate in the reproductive organs, including the ovaries and the testes, as the NPs are able to penetrate through the blood-testes-barrier and accumulate in the region. Abnormalities in spermatogenesis, and damage of the testicles was observed in three-week old Kumming mice (Kong et al., 2020). Histopathological changes within the testes were observed in two-month old male NMRI mice exposed to ZnONPs; shrinkage in the thickness and diameter of the seminiferous tubules, and germ cell loss were observed (Han et al., 2016; Mozaffari et al., 2015). Oral administration of ZnONPs to 6-week old male Kumming mice resulted in the sperm number reduction within the lumen and the segregation of the seminiferous tubules. These outcomes suggested that ZnONPs exposure resulted in testicular atrophy (Tang et al., 2019). In another study, it was reported that ZnONPs-based treatment in four to five months old Wistar male albino rats resulted in hormonal fluctuations: increment of thyroxin, tri-Iodothyronine, luteinizing hormone (LH), and follicle stimulating hormone (FSH), and decrement of testosterone and thyroid-stimulating hormone (Yousef et al., 2019). In two studies conducted on adult Wistar female rats and seven-week old female SD rats, physical alterations were evident post-ZnONPs treatment. The ovaries' and the uterus' weight increase were noted. Additionally, atrophied ovaries with hyperaemia, follicular cysts, fibrosis, and the increment of corpus luteum and inflammatory cells were noted as well. Hyperplasia of endometrial glands and epithelial deterioration within the uterus was evident (Hosseini et al., 2019; Jo et al., 2013). It was suggested that the increased circulation of the endogenous sex hormones, oestrogen and progesterone, influenced the morphological changes noted. The increased circulation of the abovementioned sex hormone

resulted in the induction of a negative feedback loop for the production and release of FSH and LH, which led to ovarian atrophy (da Silva Faria et al., 2010; Drummond & Findlay, 1999; Kumar et al., 1997).

1.1.2.3 Developmental Toxicity

Parental exposure to xenobiotics can lead to developmental toxicity, which refers to the adverse effect on the offspring's development which may present as embryotoxicity or teratogenicity (Cordier, 2008; Frontiers et al., 2000; Willhite & Mirkes, 2014). The placenta plays several crucial roles during pregnancy. One of these vital roles is to act as a barrier, which prevents the passing of harmful xenobiotics from the mother to the developing foetus (Kapila & Chaudhry, 2022). In a rodent-based study, it was found that repeated exposure of ZnONPs in pregnant mice led to a significant increase in Zn concentration and accumulation in various organs of the offspring. This suggested that there is a connection between maternal absorption and placental transfer of Zn during pregnancy (Chong et al., 2021). In a study conducted by Teng, it was revealed that the placental transfer of Zn is size-dependent. Seven-weeks old ICR mice dams were exposed to 13 nm and 54 nm ZnONPs, however, only 13 nm ZnONPs were observed in the accumulated regions of the offspring (Teng et al., 2019). Oral administration of ZnONPs to eight to ten-week old female Kunming mice exhibited structural damage of the placenta, impairment of placental function, and a reduction in the size of the spongiotrophoblast layer of the placenta. These observations subsequently led to growth restrictions of the foetus and decreased the number of viable offspring (Chen et al., 2020). Paternal exposure of ZnONPs have demonstrated the ability to induce DNA damage in the sperm cells of sea urchins (*P. lividus*). The DNA damage subsequently affected the development of respective offspring (Manzo et al., 2017). ZnONPs have demonstrated toxicity towards zebrafish embryos: structural alterations, impediment of hatching embryos, and deterioration of cardiovascular function. Additional morphological changes observed in zebrafish embryo due to ZnONPs exposure included bending of the notochord, oedemas on the pericardium, shortened body length, spinal curvature, and tail deformities (Choi et al., 2016; Zhao et al., 2013). Increased deformities, heart rate, delayed hatching, and mortality were observed of Medaka fish embryos upon exposure to ZnONPs (Cong et al., 2017).

1.1.2.4 Hepatotoxicity

Exposure of ZnONPs has demonstrated hepatotoxicity induction which impair the liver's function. Morphological alterations in male Wistar albino rats and tilapia include the overgrowth of Kupffer cells and the bile duct, increment of steatosis, induction of anisokaryosis

and karyolysis (Hegazy et al., 2018; Shahzad et al., 2019; Suganthi et al., 2015). Upregulation of alanine aminotransferase (ALT), aspartate aminotransferase (AST), gamma-glutamyl transferase (GGT), and alkaline phosphatase (ALP) were recorded post exposure to ZnONPs, which indicated hepatic injury in the animal models (Hegazy et al., 2018; Shahzad et al., 2019; Tang et al., 2016). Alterations in ALT and AST levels were noted at low concentrations (1 mg/kg) of ZnONPs treatment. Increased concentration of ALT in the serum is correlated with cholestatic injury of the liver, while increased concentration of AST is associated with hepatocyte damage (Musana et al., 2004). Upregulation of GGT, which is an enzyme with a vital role in the antioxidant system, is linked with oxidative stress. Increased levels of ALP indicated biliary injury (Goessling & Stainier, 2016). ZnONPs were administered orally to four-week old male Sprague Dawley rats, which elevated the levels of GGT and ALP of the liver's serum. Additionally, administration of ZnONPs increased the level of cytokines, which are associated with inflammatory stress (Tang et al., 2016). ZnONPs induced hepatotoxicity's mechanism is reportedly associated with the NPs' oxidative stress and the subsequent inflammation (Luster et al., 2001). Inflammation of the liver inhibits the expression and the enzymatic activity of the drug metabolizing enzyme, cytochrome P450 (CYP) (de Jong et al., 2020). Exposure to ZnONPs has demonstrated downregulated expression and activity of cytochrome P450 1A2 (CYP1A2), cytochrome P450 2C11 (CYP2C11), and cytochrome P450 3A2 (CYP3A2), which may result from conformation alteration of the isozymes through ZnONPs-induced generation of ROS and inflammation (Tang et al., 2016).

1.1.2.5 Neurotoxicity

Findings have suggested that ZnONPs are able to penetrate the BBB and travel to the central nervous system (CNS) through the circulatory system. This results in an increment of Zn concentration within the brain tissue of rodents (de Souza et al., 2018). Translocation to the CNS has also been observed via the taste nerve translocation pathway and the olfactory pathway in four to six-weeks old male Wistar rats (Aijie et al., 2017; Liang et al., 2018). Induction of excessive production of oxidative stress, inflammatory response, and morphological changes results from the accumulation of ZnONPs in the brain. These alterations lead to subsequent functional impairment and neurodegeneration. The CNS is characterised by its high content of unsaturated lipids, minimal amount of antioxidant enzymes, high oxygen consumption, and constrained cellular regeneration of neuronal tissue; these characteristics make the CNS more vulnerable to ZnONPs' toxicological effects (Ortiz et al., 2017; Salim, 2017; Sayre et al., 2008). Administration of ZnONPs orally in rodents resulted in

the increased expression of oxidative and nitrosative stresses. These stresses are able to enhance inflammation within the CNS through the activation of astrocytes and microglial, and the release of pro-inflammatory markers (Attia et al., 2018; Liang et al., 2018). The expression of pro-inflammatory markers (TNF- α , IL-1 β , and NOS2) are known to increase post-exposure to ZnONPs in six-weeks old male Wistar rats (Liu et al., 2020). Appearance of acute neuronal lesions and neuronal apoptosis is associated with increased levels of IL-1 β (Fogal & Hewett, 2008). ZnONPs treated rats have showcased an upregulation in the glial fibrillary acidic protein (GFAP). The upregulation of GFAP is known to be associated with astrogliosis and astrocytosis (Giovannoni, 2014). The activation and accumulation of astrocytes within the CNS halts the growth and regeneration of axons, which subsequently leads to neurodegeneration within the treated model (Aijie et al., 2017; Gallo & Deneen, 2014). Inactivation of autophagy is another characteristic of ZnONPs exposure, which leads to the formation of tau aggregates within the brain (Llorens et al., 2018). Behavioural changes post-ZnONPs treatment has been noted as well. Deficit in regular motor functions were observed in ten to twelve-weeks old male Swiss mice treated with ZnONPs at concentrations ranging between 250 to 500 mg/kg (Yaqub et al., 2020). Oral administration of ZnONPs were noted to affect the neuromuscular coordination and impaired crawling abilities in *Drosophila melanogaster* (Sood et al., 2017).

1.2 The Role of *Caenorhabditis elegans* as a Pre-clinical Model

Caenorhabditis elegans (*C. elegans*) are free-living nematodes which reside in soil, compost, and decaying vegetation. The nematodes primarily feed on bacteria and microbes found within the soil and decomposing organic matter (Zečić et al., 2019). *C. elegans* display sexual dysmorphism, with males (XO) and hermaphrodites (XX) as the two sexes (Meneely et al., 2019). Hermaphrodite nematodes are able to self-fertilize and are able to produce approximately 300 offspring per reproductive cycle, which takes 3.5 days (Riddle et al., 1997). The self-fertilizing nematodes are able to propagate a genetically identical progeny. The nematode's life begins as a fertilized egg and its developmental sequence takes approximately three days (Muschiol et al., 2009; Scharf et al., 2021).

1.2.1 Anatomy of *C. elegans*

C. elegans have a cylindrical and seamless body shape, with a narrowed end. Its body plan consists of an external and an internal tube, which is partitioned by a pseudo-coelomic space. The body wall, also known as the external tube, comprises of the cuticle, excretory system, hypodermis, muscles, and neurons. The internal tube comprises of the adult-stage gonad, intestine, and pharynx. All components of the nematode's body are regulated via the

osmoregulatory system and are surrounded by internal hydrostatic pressure. Despite its simple anatomical makeup, *C. elegans* have extensive organ systems in place (Alberts et al., 2002; Corsi, 2006; Riddle et al., 1997).

1.2.2 Reproduction in *C. elegans*

The reproductive system of *C. elegans* is organised into two gonadal arms which are connected by a central uterus. The central uterus encompasses the nematode's germ line, the somatic gonad, and the egg-laying contraction (Athar & Templeman, 2022). The reproductive organs of *C. elegans* are able to generate mature gametes, fertilize oocytes, and lay eggs (Scharf et al., 2021).

The initiation of the reproductive system's development occurs during embryogenesis, during which the germline blastomere (P₄) is formed. P₄ serves as the founder cell, and it generates all subsequent germline cells. During embryogenesis, P₄ splits into two primordial germ cells, Z₂ and Z₃. Z₂ and Z₃ proliferate during the larval stages to form adult germ cells, and they are situated between Z₁ and Z₄, which are somatic gonad precursors (Hubbard & Greenstein, 2005). Distal tip cells (DTC) propagate from Z₁ and Z₄, and they form the ends of the gonad, and manage germ cell proliferation. As the germ cells develop, they translocate from the DTC to the neighbouring ends of the gonad, where they gather while awaiting fertilization (McCarter et al., 1999).

Hermaphrodites start production of sperm from the fourth-larval stage (L₄) until adulthood, and after which they solely produce oocytes (Hubbard & Greenstein, 2005). The produced sperm are stowed in the spermatheca at the proximal end of the gonad, where they are able to fertilize mature oocytes (L'Hernault, 2006; Singson, 2001). Embryogenesis occurs instantly post fertilization. Embryos are deposited in the uterus and expelled through the vulva (Hall & Herndon, 2017).

The production of fertilized eggs adheres to a timed schedule. Once the nematode reaches sexual maturity, the production of progeny increases. Peak production is reached on adult-day-2; adult-day-2 refers to the 48-hour period post expulsion of the nematode's first egg. During peak production, an oocyte is approximately ovulated every 23 minutes, which results in the production of around 150 progeny per day. Production of progeny starts declining post adult-day-2 and it ceases around adult-day-6 to adult-day-9 (McCarter et al., 1999; Scharf et al., 2021).

1.2.3 Life Cycle of *C. elegans*

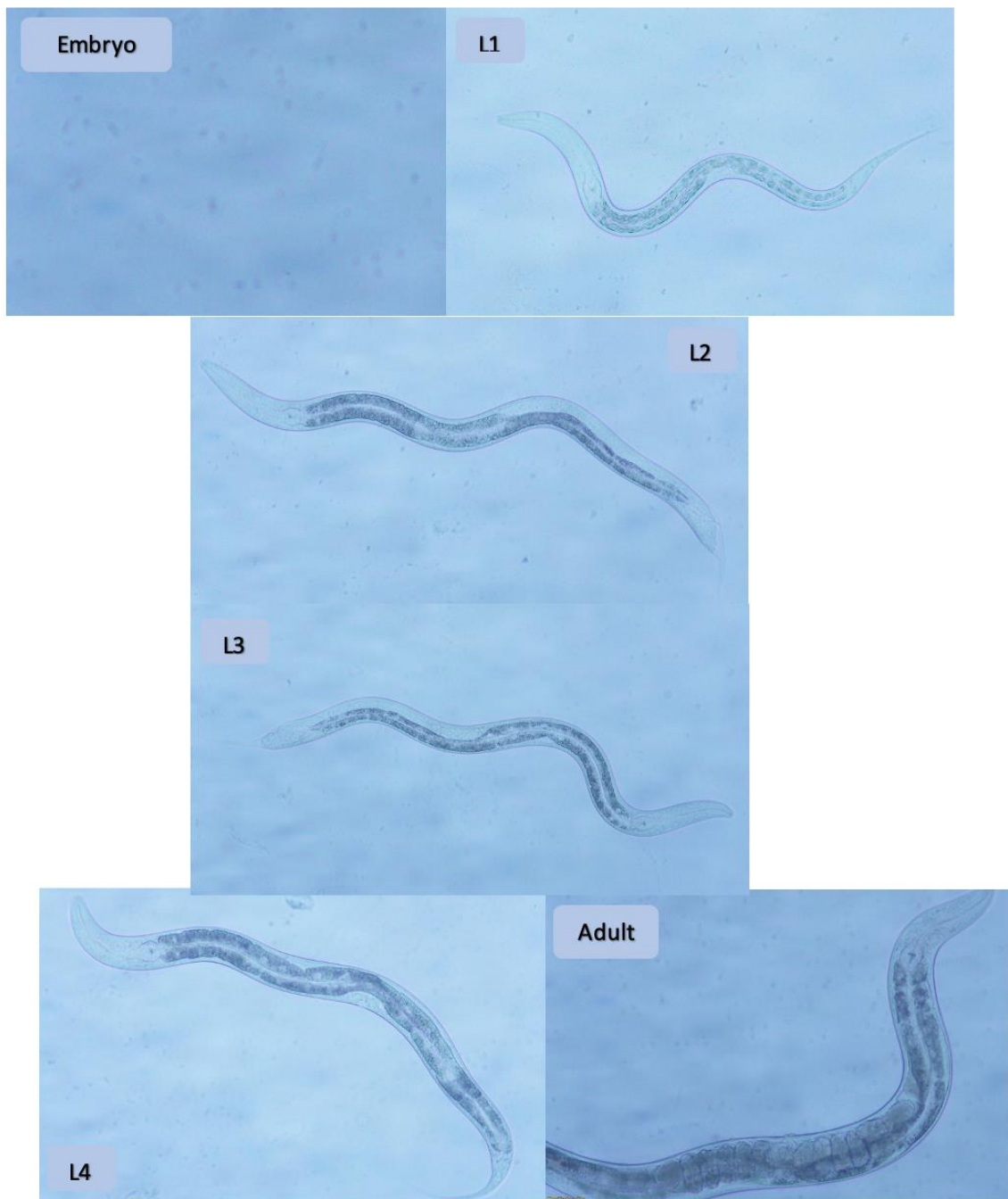


Figure 1.1. Diagram illustrating the life cycle of *C. elegans*. L1, L2, L3, and L4 denote the four respective larval stages. As the nematode grows into each stage, including the adult stage, the girth of the body increases. (Zeiss Axioscope 5, Magnification: 20X) (Photos taken by author).

The life cycle of *C. elegans*, depicted in Figure 1.1, comprises of embryonic stage, the four larval stages, and the adulthood stage. The ending of each larval stage is characterised by a molt which forms through three steps: detachment of the former cuticle from the hypodermis (apolysis), construction of the latter cuticle from the hypodermis, and the sloughing of the former cuticle (ecdysis) (Byerly et al., 1976; Muschiol et al., 2009).

The embryogenesis stage is subdivided into two distinct stages: proliferation and organogenesis. The proliferation stage initiates approximately 5-hours post fertilization, during which a single cell propagates 558 undifferentiated cells. The first phase of proliferation covers the zygote formation until the generation of the embryonic founder cells within the nematode's uterus. Once the embryo reaches the 30-cells stage, the embryo is expelled through the vulva (Gilbert, 2000). The second phase of proliferation encompasses the remaining cell division and gastrulation until organogenesis. The culmination of the proliferation stage is noted by the division of the embryo into three germ layers: ectoderm, mesoderm, and endoderm. The hypodermis and neurons develop from the ectoderm. The mesoderm develops into the pharynx and muscle. The endoderm develops into the germline and the intestine. During organogenesis, the terminal differentiation of cells initiates, the embryo elongates, and the tissues and organs completely differentiate (Pazdernik & Schedl, 2013). Sexual dimorphism is evident 8-hours post fertilisation; the cephalic companion neurons (CEMs) degenerate in hermaphrodites. Pharyngeal pumping begins at 12.6-hours post fertilisation, and the embryo hatches at 13.3-hours. At the end of the organogenesis stage, the full body plan is fixed (Riddle et al., 1997).

During the first-larval stage (L1), the nematode is approximately 250 μm long. The nervous and reproductive system develop during this stage. In terms of the nervous system, five of the eight classes of the ventral cord are formed and one class undergoes synaptic reorganisation. During the latter part of L1, a group of neurons alter their synaptic patterns, which turns their dorsal branches presynaptic and inhibitory to the dorsal body wall muscles, and turns their ventral branches postsynaptic and excitatory to the ventral body wall muscles (Zhang et al., 2020). Alterations in the reproductive system initiate during the latter part of L1. Z1 and Z4, the somatic gonad precursors, produce twelve cells within the hermaphrodite. Z2 and Z3, the germline precursors, start proliferating and continue throughout all larval stages until adulthood is reached (Nagy et al., 2013; Zhang et al., 2020).

After 12-hours, *C. elegans* transform into the second-larval stage (L2). During L2, the nematode is approximately 360-380 μm long. The nervous and reproductive system continues to develop during this stage for the hermaphrodite. In the nervous system, the postdeirid sensilla and two ventral ganglion neurons are generated. In terms of the reproductive system,

the germ cells originating from Z2 and Z3 continue proliferating, while the cells originating from Z1 and Z4 do not proliferate. The somatic and germ cells converge, and they rearrange to form the future gonad (Nagy et al., 2013; Zhang et al., 2020).

The dauer larva is an arrested state the nematode enters after L2, if the environmental conditions deem it necessary. Conditions which determine whether *C. elegans* enter the arrested state include population density, availability of food source, and ambient temperature; an environment with a high population density, absence of nutrients, and/or higher than optimal ambient temperature may trigger the morphological transformation of the nematode into the L2-dauer larva stage (L2D). If the unfavourable environmental condition persists for an hour or turns favourable within an hour, L2D is able to progress into a dauer or move onto the third-larval stage (L3) respectively. In terms of its morphology, dauer larva are thin and they have a thick cuticle; the pharyngeal and intestinal lumens shrink, the excretory glands exclude secretory granules, and the excretory pore remains open (Byerly et al., 1976; Riddle et al., 1997).

During L3, the nematode is approximately 490-510 μm long. The reproductive system continues developing within the hermaphrodite. The somatic gonad precursors generate 143 cells to assemble the posterior and anterior gonadal sheaths, uterus, and the spermathecae. The gonad arms continue to extend towards their respective direction, and the vulva terminal is generated from the vulva precursors. Lastly, sex muscle cells are generated from myoblasts (Gilbert, 2000; McCarter et al., 1999).

The L4 nematode is approximately 620-650 μm . Gonadogenesis is completed during L4. The distal gonad arms continue extending and migrating along their path. The germline, within the proximal arm, undergoes meiosis. The germ cells undergo differentiation to produce sperm, which stops during the latter part of L4; remaining germ cells undergo meiosis to differentiate into oocytes. Tissue morphogenesis occurs once the generation of the vulva's cell line and the uterine terminal is concluded. The tissue, egg-laying neurons, and sex muscles give rise to the egg-laying apparatus (Muschiol et al., 2009; Nagy et al., 2013).

The final stage of *C. elegans* life cycle is the adult stage, which is reached within three days of egg-hatching at 25°C. The adult hermaphrodite is able to lay eggs, which indicates the completion of a three-day reproductive cycle. Throughout the entire life cycle, a total of 1090 somatic cells are generated while 131 of these cells undergo apoptosis. Thus by the time the nematode reaches the adult stage, 959 somatic cells remain (Zhang et al., 2020).

1.2.4 Feeding Mechanism of *C. elegans*

Feeding activity is fulfilled by the rhythmic contractions and relaxation of the pharynx. As a neuromuscular pump, it is able to ingest provisions in the surrounding environment and transport it through the mouth to the intestine (Avery & Shtonda, 2003). The pharyngeal muscle is constructed from three functional groups: corpus, isthmus, and the terminal bulb. The corpus is located in the anterior end of the pharynx, and it is able to draw in the bacterial food when the pharynx contracts. The terminal bulb is located in the posterior end of the pharynx, and it contains the grinder. The grinder is made up of three cuticular plates, which are able to grind the bacteria to allow absorption by the intestine. The corpus and the terminal bulb are connected by the isthmus (Albertson & Thomson, 1976).

The pharynx has its own nervous system known as the pharyngeal nervous system. It encompasses twenty neurons of fourteen distinct types. The pharyngeal neurons contain neuropeptides and neurotransmitters, and they are located under the basal lamina. Important small-molecule neurotransmitters include acetylcholine, glutamate, and serotonin (Trojanowski et al., 2016). Of the fourteen types of neurons, three types of motor (M) neurons (M3, M4, and MC) are involved in the feeding process. The M3 and MC neurons control the beginning and ending of a contraction respectively, while the M4 neuron is required for isthmus peristalsis and growth under certain conditions (Fang-Yen et al., 2009).

The two feeding motions carried out by *C. elegans* are isthmus peristalsis and pumping. The pumping motion is utilized to draw in the bacteria, and it starts with the concurrent contraction of the anterior isthmus, corpus, and the terminal bulb. The simultaneous contraction opens the lumen in a triangular cross-section (Marder & Calabrese, 1996). The opening allows the nematode to suck in the bacterial suspension. The contraction of the corpus, anterior isthmus, and the terminal bulb is simultaneous, and it is followed by simultaneous relaxation. The relaxation of the muscle expels the liquid, while the bacteria remain within the nematode. Isthmus peristalsis occurs after the pumping motion; however, it is only transpired one out of every four pumps (Trojanowski et al., 2016). Isthmus peristalsis is defined as the peristaltic traction of the posterior isthmus's muscles, which allows ingested bacteria to be transported to the terminal bulb (Marder & Calabrese, 1996).

Each pumping cycle corresponds to a singular action potential, which occurs within the pharyngeal muscle. It is regulated by duration and frequency (Fang-Yen et al., 2009; Marder & Calabrese, 1996). Each action potential is carried out by the sequential action of five distinguished ion channels. The first ion channel is a nicotinic acetylcholine receptor, which is activated by the MC neuron. The second ion channel is a voltage-gated calcium channel, which

has a low threshold. The third ion channel is a voltage-gated calcium channel as well; however, it has a higher threshold. The fourth ion channel is a glutamate-gated chloride channel, which is activated by the M3 neuron. The fifth ion channel is a voltage-gated potassium channel (Avery & Horvitz, 1987; Selverston, 2010; Trojanowski et al., 2016).

1.2.5 *C. elegans*' Genome

The first multicellular organism to have its complete genome sequenced was *C. elegans* in 1998, which comprises of approximately 100 million base pairs encoding 20,470 protein coding genes. Hermaphrodites have 5 pairs of autosomes and 1 pair of sex chromosomes. The nematodes' genome is structured in a simple and an organized manner, as the gene density is similar across all the chromosomes; the gene density is approximately one gene per five kilobase pairs. *C. elegans*' genes contain 131,083 exons which account for 26% of the genome, and 108,151 introns within the coding sequences of the genome (Cutter et al., 2009; Spieth et al., 2014; Waterston & Sulston, 1995).

1.2.5.1 External Influences on Gene Expression of *C. elegans*

Gene expression can be defined as the synthesis of a functional gene product from the information provided by DNA, and it is dependent on both environmental and genetic factors (Liu et al., 2022; Singh et al., 2018).

Temperature fluctuations and dietary alterations are common parameters known to alter the physiology and expression of genes in *C. elegans*. In laboratory settings, *C. elegans* are able to complete their life cycle in 2.5 days at 25°C, while their life cycle is extended to 5 days at 15°C (Klass, 1977). *Escherichia coli* strain OP50 (*E. coli* OP50) is the standard diet provided for the nematode in the laboratory setting (Montalvo-Katz et al., 2013). However, *Bacillus subtilis* (*B. subtilis*) has also been utilised as an alternate diet in several projects (Cabreiro & Gems, 2013; Lezzerini et al., 2015; Sánchez-Blanco et al., 2016). The average lifespan of *E. coli* OP50 fed nematodes maintained at 20°C is approximately 17 days, while *B. subtilis* fed nematodes maintained at the same temperature had lifespans of around 27 days (Sánchez-Blanco et al., 2016). An *in vivo* study has demonstrated gene expression fluctuations when the nematodes were exposed to pre-determined diet and ambient temperature combinations. With the *E. coli* OP50 diet, an ambient temperature of 25°C resulted in an increased expression of 571 genes when compared to nematodes maintained at 15°C. Of the 571 genes, 184 genes also increased in expression under 25°C when compared to maintenance under 20°C. 183 of the 184 genes retained the same expression level at both 15°C and 20°C. With the *B. subtilis* diet, an ambient temperature of 25°C resulted in increased expression of 919 genes when compared

to nematodes maintained at 15°C. Of the 919 genes, 161 genes also increased in expression under 25°C when compared to maintenance under 20°C. 147 of the 184 genes retained unchanged expression level at both 15°C and 20°C. The upregulated genes belonged to the defense response pathways and the metabolism of amino acids, lipids, and organic acids for nematodes under *E. coli* OP50 diet and *B. subtilis* diet respectively. This demonstrated that the expression of a significant number of *C. elegans*' genes are influenced by their ambient temperature and type of bacterial diet present (Gómez-Orte et al., 2018).

Oxidative stress induced by the presence of xenobiotics and toxic compounds in the environment is a factor known to alter gene expression within *C. elegans*. Oxidative stress is defined as the imbalance between ROS and detoxification enzymes which leads to significant oxidative damage to macromolecules including DNA, protein, and lipids (Hu et al., 2018). In the nematode, air pollutants, NPs, and pesticides are known to induce oxidative stress (Haghani et al., 2019; Huang et al., 2019; Liu et al., 2023). The primary mechanism through which oxidative stress alters gene expression in *C. elegans* is through the activation of transcription factors including DAF-16 and SKN-1. DAF-16 and SKN-1 are activated and able to respond rapidly to oxidative stress as they are able to translocate from the cytoplasm to the nucleus, where they subsequently activate transcription. DAF-16 is activated through the inhibition of insulin/insulin-like growth factor signalling. It is able to regulate downstream target genes which influence dauer formation, lifespan, energy metabolism, and stress resistance in the nematode (Kondo et al., 2005). SKN-1 promotes gene expression involved in resistance towards oxidative stress, and alteration in the nematode's lifespan (Tullet et al., 2017).

1.2.5.2 Genes of Interest

DNA damage-induced apoptosis is associated with various human malignancies. The tumour suppression protein, p53, is a transcription factor which is involved in initiating cell cycle arrest, apoptosis, autophagy, and DNA repair (Riley et al., 2008). In human cells, wild-type p53 is stable and expressed at low levels. However, upon DNA damage and exposure to environmental stress, p53 expression increases which activates the down-stream target genes (Hoffman et al., 2014). In *C. elegans*, the p53 ortholog CEP-1 protein has the same function. CEP-1 is encoded by the gene *cep-1*, which belongs to the *C. elegans* P53-like protein (*cep*) gene class (Schumacher et al., 2005). It is activated by DNA damage and oxidative stress, and subsequently induces germline cell death by the upregulation of target genes: *egl-1* and *ced-13* (O'Donnell et al., 2017). Under normal conditions, approximately 50% of oocytes undergo predetermined apoptosis, and the dead oocytes function as cytoplasmic components for the

remaining mature oocytes. However, the increased expression of the *cep-1* gene, as a result of internal and external stressors, results in reduced number of offspring (O'Donnell et al., 2017; Riley et al., 2007; Sang et al., 2022).

Stress-activated mitogen-activated protein kinases (MAPK) pathways are regulated by intra-cellular and extra-cellular stresses, which include environmental physical and/or chemical alterations. The pathways are able to phosphorylate substrates, which leads to a network response (Zarubin & Han, 2005). Within the MAPK pathways, p38 MAP kinase responds primarily to extracellular and intracellular stress; it responds to inflammation, changes in the physical and chemical environment, DNA damage, and oxidative stress (Soltanmohammadi et al., 2022). In *C. elegans*, p38 MAP kinase ortholog PMK-1 protein serves the same function. PMK-1 is encoded by the gene *pmk-1*, which belongs to the P38 MAP Kinase (*pmk*) gene class. PMK-1 is able to directly phosphorylate SKN-1, which translocates from the cytoplasm to the nucleus. A study conducted has suggested that oxidative stress activates the PMK-1 pathway, and induces the accumulation of SKN-1 in the intestine and the activation of stress-induced genes such as *gcs-1* (Inoue et al., 2005). Increased expression of the *pmk-1* gene is hypothesized to alter the lifespan and developmental processes in *C. elegans* (Hotamisligil & Davis, 2016).

C. elegans' *tba-1* gene belongs to the TuBulin Alpha (*tba*) gene class, and it is an ortholog to the human TUBAL3 protein. It is a reference gene commonly used in *C. elegans'* studies (Zhang et al., 2012). Tubulins are globular protein within the cytoplasm, which are components of microtubules; the *C. elegans* tubulin family comprises of α -tubulins, β -tubulins, and γ -tubulins (Lu & Zheng, 2022). The *tba-1* gene encodes for β -tubulins in eukaryotic cells. Microtubules are involved in cell division, cell shape maintenance, and intracellular transport. *tba-1* is ubiquitously present in all cells at all stages of the nematode's life cycle, which makes it a suitable housekeeping gene (Taki & Zhang, 2013). The TBA-1 protein is expressed within the germline, as it is involved in the meiotic and mitotic spindle assembly in early embryos (Hurd, 2018). It is also expressed in excitatory motor neurons, and serve as a component of the cytoskeleton and enables guanosine triphosphate binding activity (Lu & Zheng, 2022).

1.2.6 Advantages of Using *C. elegans* as a Toxicological Model

C. elegans are commonly utilised in toxicological studies owing to their multitude of advantages. Firstly, its short life cycle of 3.5 days and short life expectancy of 25-30 days allow it to be an efficient model to investigate the toxicological influence of xenobiotics on parameters such as alterations in the average lifespan and reproductive capacity (Johnson, 2003; Riddle et al., 1997). Secondly, as a single adult hermaphrodite *C. elegans* is able to give rise to

a substantial number of offspring, it results in an ample supply of nematodes for experimental purposes (Meneely et al., 2019). Thirdly, as the nematode's torso is transparent, it allows researchers to observe morphological changes. Additionally, the transparency allows researchers to monitor the pumping mechanism of the pharynx which allows the investigation of the toxicological influence of xenobiotics on parameters such as the pharyngeal pumping rate (Kerr, 2006; Raizen et al., 2012; Trojanowski et al., 2016). Fourthly, these nematodes are easy and in-expensive to maintain in the lab (Stiernagle, 2006). Lastly, the complete genome sequence of the nematode is a crucial advantage. It allows researchers to investigate alterations at the molecular level which may correlate to the physical alterations observed. Furthermore, 40-80% of the genes are orthologous to human genes, which may be beneficial to yield clinically applicable results (Culetto & Sattelle, 2000; Forslund et al., 2011).

1.2.7 Investigation of Toxicological Effects of NPs by Employing *C. elegans*

Due to its numerous advantages, a good number of toxicological studies have employed *C. elegans* to investigate the effect of NPs' exposure.

Bristol strain N2 (N2) nematodes were exposed to silver nanoparticles (AgNPs) at a concentration of 10^{10} /particle/mL at the L4 point in their life cycle. 48-hours of exposure resulted in shortened body length of the treatment group, and the number of NP-treated living nematodes reduced significantly at the 72-hours' time point. Based on the transcriptome analysis, exposure to AgNPs resulted in alterations of 43 genes' expression, with 34 overexpressed and 9 suppressed at the 72-hours' time point. These genes belonged to nine distinct pathways, and they represent 12% of the active genes within the respective pathways (Walczyńska et al., 2018).

Gold nanoparticles (AuNPs) were utilised to investigate their impact on the lifespan and reproductive capacity of *C. elegans*. 11 nm and 150 nm sized AuNPs were introduced to the nematodes at a concentration range of 0 to 100 μ g/mL. Upon exposure to 11 nm AuNPs at a concentration of 100 μ g/mL, statistically significant reduction in the lifespan compared to the control group was observed. Furthermore, reduction in reproduction capacity was observed as well. As for the 150 nm AuNPs, they were neither able to elicit significant alterations on the survival rate nor the reproduction capacity of the nematodes. Furthermore, *C. elegans* were able to ingest 500 times more of the 11 nm AuNPs compared to the 150 nm AuNPs. However, alterations in the markers of endocytosis and intestinal barrier integrity was not observed (Gonzalez-Moragas et al., 2017).

Toxicity of spherical 28.4 nm copper oxide nanoparticles (CuONPs) was investigated at a concentration range of 5 to 20 mg/L. When exposed to the highest concentration of CuONPs, statistically significant reduction in the nematode's body length was noted when compared to the control group. Additionally, the exposure to CuONPs significantly decreased the pharyngeal pumping rate of *C. elegans*. Degeneration of dopaminergic neurons was observed in 10% of the treatment group post-exposure to the NPs. However, CuONPs were not able to diminish the nematodes' reproduction capacity (Mashock et al., 2016).

Rod-shaped 108 nm and bipyramidal-shaped 38 nm titanium dioxide nanoparticles (TiO₂NPs) were employed to investigate their effect on *C. elegans*. Biodistribution and accumulation was neither dependent on the size nor the shape of TiO₂NPs; however, these factors influenced the elicited toxicity. Both 108 nm and 38 nm TiO₂NPs were ingested and were able to permeate the intestinal barrier to reach the reproductive system of the nematode efficiently. The 108 nm rod-shaped TiO₂NPs elicited a more significant impact on the pharyngeal pumping rate, reproduction capacity, and growth of the nematodes when compared to the 38 nm bipyramidal-shaped TiO₂NPs (Iannarelli et al., 2016).

1.3 Introduction to Cytochrome P450

CYP monooxygenases are membrane-bound haemoproteins which catalyse the oxidation and metabolism of several xenobiotics and endogenous compounds. They are ubiquitously present within the endoplasmic reticulum of cells in most body tissues; however, they are predominantly expressed in the liver, intestines, and the kidney. The highest expression level of CYPs is found within the liver (Gerth et al., 2019). As of present, 57 CYP isozymes have been identified and sequenced within the human genome. These isozymes are divided into 18 families and 43 subfamilies (Veith et al., 2009). The structure of CYPs is highly conserved amongst all the members of the family; the superfamily of CYP isozymes share 40% of sequence homology, and 55% of sequence homology is shared amongst subfamilies (Sirim et al., 2010). The CYP enzyme is composed of approximately 500 amino acids, and has an estimated molecular weight of 55,000Da (Akiyama et al., 2002; Sasaki et al., 2005). The enzyme is organised into two domains: N-terminal domain and C-terminal domain. The N-terminal domain contains the heme-binding and the substrate-binding sites. The C-terminal domain contains a hydrophobic core, and flexible loops which undergo conformation change upon substrate binding (Aslantas & Surmeli, 2019).

1.3.1 CYP and its Role in Drug Metabolism

CYP isozymes are responsible for the metabolism of the majority of clinically prescribed medication through Phase I metabolism (Zhao et al., 2021). Lipid-soluble drugs partition into the lipid bilayer of the endoplasmic reticulum and it is enzymatically metabolised into a hydrophilic metabolite (McDonnell & Dang, 2013). The hydrophilic metabolite is suitable for excretion, or it may require additional metabolism in the form of sequential Phase I or Phase II reactions (Susa et al., 2023).

CYP's catalysation occurs in the form of oxidation via multiple steps. CYP isozymes' active site is made up of a heme-iron center, where the iron compound is attached to the enzyme through a cysteine thiolate molecule (Barr et al., 2020). Conformation change of the active site is induced once the substrate binds to the active site within the heme group (Parisi et al., 2019). An electron is transferred from nicotinamide adenine dinucleotide phosphate (NADPH) through reductases. Post-reduction, an oxygen molecule binds to the ferrous-heme group. Reduction adds an additional electron, and the reaction yields a peroxide group, Fe-O₂ (Munro et al., 2018). Fe-O₂ exists briefly as it is protonated twice, and subsequently releases a water (H₂O) molecule and a P450 compound, FeO₃⁻; this step allows the further hydroxylation of the compound, which increases its ability to be excreted and makes it hydrophilic (Rodeiro et al., 2013).

CYP1, CYP2, and CYP3 gene families are essential for drug metabolism; of the 57 CYP isozymes identified, the following seven are responsible for metabolising 60% of CYP-metabolised drugs: cytochrome P450 1A2 (CYP1A2), cytochrome P450 2A6 (CYP2A6), cytochrome P450 2B6 (CYP2B6), cytochrome P450 2C8 (CYP2C8), cytochrome P450 2E1 (CYP2E1), cytochrome P450 2J2 (CYP2J2), and cytochrome P450 3A5 (CYP3A5). The percentage of clinical drugs metabolised by these CYP isozymes is presented in Figure 1.2 (Zanger & Schwab, 2013).

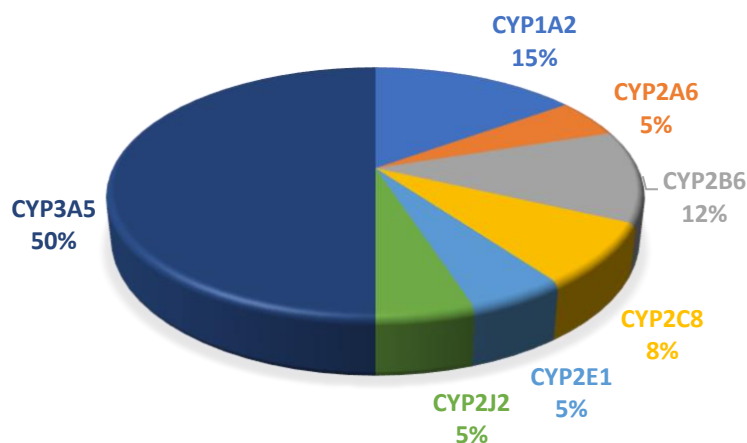


Figure 1.2. Percentage of clinical drugs metabolised by Cytochrome P450 isozymes (Zanger & Schwab, 2013).

1.3.2. Drug Metabolising CYP Isozymes

Each drug metabolising CYP isozyme has its own unique characteristics, which are important to note during the drug design process. These characteristics include the expression level in different organs, substrate specificity, and its known inducers and inhibitors (Johnson et al., 2021).

CYP1A2 metabolises 15% of clinically used drugs, and it is expressed in the endoplasmic reticulum of hepatic tissue. Preferred substrates of CYP1A2 include amides, amines, aromatics, heterocyclics, planars, and polyaromatics. Inducers of CYP1A2 include methylcholanthrene, naphthoflavone, omeprazole, and tobacco. Lastly, CYP1A2's prominent inhibitors include cimetidine, fluvoxamine, and furafylline (Fekete et al., 2022; Wang & Zhou, 2009).

CYP2A6 metabolises 5% of clinically used drugs, and it is expressed both in extrahepatic tissue and hepatic tissue; CYP2A6 is predominantly expressed in the liver. Substrate preferences of CYP2A6 include ketones, nitrosamines, and nonplanars. CYP2A6's activity is induced by artemisinin, carbamazepine, estrogen, and phenobarbital. Inhibitors of CYP2A6 include 8-methoxypsoralen, selegiline, and trancylpromine (Kramlinger et al., 2012; McDonagh et al., 2012; Mo et al., 2009).

CYP2B6 metabolises 12% of clinically used drugs. It is expressed within gastrointestinal tissue and hepatic tissue, with the majority of it being expressed in the liver. Anesthetics, herbicides, insecticides, neutral bases, weak bases, and lipophilic nonplanar molecules are preferred substrates of CYP2B6. Known inducers of CYP2B6's activity include artemisinin, nevirapine, and phenobarbital. Recognised inhibitors of CYP2B6's activity include clopidogrel and ticlopidine (Langmia et al., 2021; Wang & Tompkins, 2008).

CYP2C8 metabolises 8% of clinically used drugs, and it is primarily expressed in hepatic tissue. Expression in extrahepatic, lung, and gastrointestinal tissue is evident as well. Preferred substrates of CYP2C8 include antidiabetic, antimalarial, and large and weak acidic molecules. Rifampicin is a known inducer of CYP2C8's activity, and inhibitors of CYP2C8's activity include gemfibrozil, montelukast, quercetin, and trimethoprim (Aquilante et al., 2013; Daily & Aquilante, 2009; Lai et al., 2010).

CYP2E1 metabolises 5% of clinically used drugs. It is expressed in extrahepatic, lung, and gastrointestinal tissue, while the majority of its expression is localised in hepatic tissue. Alcohol, aliphatic, halogenated alkanes, and neutral hydrophilic planar molecules are known substrates of CYP2E1. A recognised inducer of CYP2E1's activity is ethanol, while recognised inhibitors of CYP2E1's activity includes 4-methylpyrazole, clomethiazole and disulfiram (Guengerich, 2020; Hakkola et al., 2020).

CYP2J2 metabolises 5% of clinical drugs. Unlike the previously mentioned CYP isozymes, CYP2J2's predominant expression is found in cardiovascular tissue. CYP2J2 is also expressed in hepatic tissue and gastrointestinal tissue. Fatty acids, linear chain-containing molecules, and antihistamines are preferred substrates of CYP2J2. Based on past and current studies, there are no known inducers for CYP2J2's activity. Recognised inhibitors of CYP2J2 include apixaban, arachidonic acid, danazol, ketoconazole, and terfenadine (Aliwarga et al., 2018; Lee et al., 2010; Tian et al., 2021).

CYP3A5 metabolises 50% of clinically used drugs alongside CYP3A4. The majority of CYP3A5's expression is located in hepatic tissue. As CYP3A5 shares 85% amino acid sequence homology with CYP3A4, they have high substrate similarity; preferred substrate types are categorised as large and lipophilic molecules. Inducers of CYP3A5's activity include carbamazepine, efavirenzes, and rifampicin. Azamulin, fluconazole, and ketoconazole are recognised inhibitors of CYP3A5's activity (Khan et al., 2020; Smith et al., 2018).

1.3.3 Inhibition of CYP Isozymes

Foremost concern regarding CYP-based drug metabolism is the possibility and extent of drug-drug interactions, herb-drug interactions, and as a focus of this research project, nanoparticle-drug interactions (NDI) (Pan et al., 2019). A major type of NDIs observed in terms of CYP-based drug metabolism is the inhibition of CYP isozymes (Zhang et al., 2021). Inhibition of CYP isozymes can be categorised as reversible and/or irreversible (Fowler & Zhang, 2008). Reversible inhibition's subtypes include competitive, non-competitive, uncompetitive, and mixed mode inhibition (Tu et al., 2021). The subtypes of reversible inhibition

can be graphically illustrated using Lineweaver-Burk plots (Figure 1.3), which is a double reciprocal plot; the reciprocal of the substrate's concentration is presented on the x-axis, and the reciprocal of the reaction velocity is presented on the y-axis (Johnson, 2013).

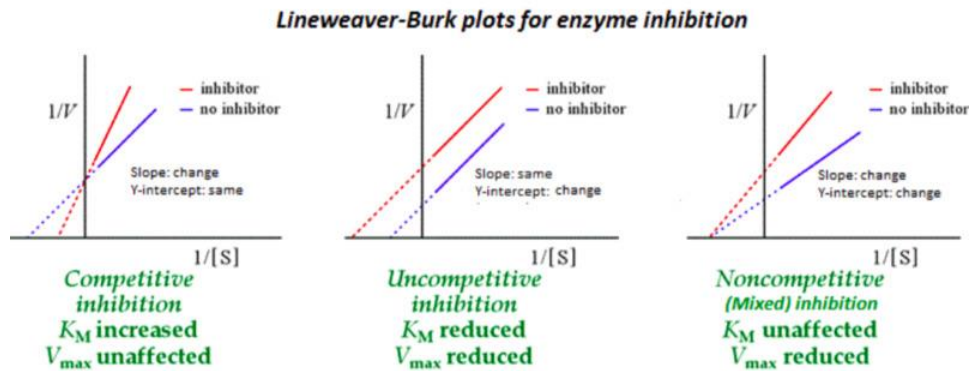


Figure 1.3. Lineweaver-Burk plots of different types of reversible inhibition: competitive, uncompetitive, and noncompetitive. K_m Michaelis constant, V_{max} maximum rate of reaction (Delaune & Alsayouri, 2022)

1.3.3.1 Reversible Inhibition

A reversible inhibitor inactivates an enzyme's activity via non-covalent binding with the enzyme. Alteration in an enzymes' maximum velocity (V_{max}) and the Michaelis constant (K_m) are indicators of the type of reversible inhibition observed (Strelow et al., 2012). V_{max} is defined as the enzyme's reaction rate at which the substrate's concentration completely saturates the active site of the targeted enzyme (Attaallah & Amine, 2021). K_m is the required substrate concentration to attain the half reaction rate of V_{max} and is defined as the inverse measurement of the affinity between the substrate and the enzyme (Robin et al., 2018).

Competitive inhibition occurs when the inhibitor and the substrate aim to attach to the enzyme at the same active site, as they are structural analogs. The affinity and concentration of the inhibitor influences the strength of competitive inhibition observed. During competitive inhibition, an inhibitor with stronger affinity to the enzyme has the ability to displace a substrate with weaker affinity to the enzyme (Attaallah & Amine, 2021). This interaction results in the decrease of affinity and the extent of breakdown of the substrate, leading to its accumulation within the system (Zolghadri et al., 2019). If an ingested drug serves as the substrate with the weaker infinity, it will result in the decreased clearance and increased bio-availability of the drug. The increased plasma concentration of a clinically prescribed medication may result in adverse side effects. Alternatively, if the ingested drug is a pro-drug, the formation of metabolites would decrease, and it would lead to decreased therapeutic efficacy (Cho & Yoon, 2018). Competitive inhibition is evident immediately upon introduction

of the inhibitor, and it is not affected by the incubation if the concentration of the substrate is kept equal. However, manipulating the substrate's concentration can mitigate the impact of competitive inhibition. In a Lineweaver-Burk plot depicting competitive inhibition, the data set exhibits an unchanged V_{\max} and an increased K_m (Delaune & Alsayouri, 2022).

During non-competitive inhibition, the inhibitor aims to bind to an allosteric site of the enzyme, while the substrate aims to bind to the active site of the enzyme; the inhibitor and the substrate are not structural analogs (Delaune & Alsayouri, 2022). The binding of the inhibitor onto the allosteric site is independent of the substrate's ability to bind onto the active site. Once the non-competitive inhibitor is able to bind onto the allosteric site of the enzyme, it results in a conformational change of the enzyme, which reduces the enzyme's catalytic activity; the reduction in enzymatic activity is not dependent on the substrate's concentration (Deodhar et al., 2020). Therefore, the enzyme's catalytic reaction's maximal rate decreases while the substrate's affinity to the enzyme stays the same during non-competitive inhibition; the data set on a Lineweaver-Burk plot's exhibits a decreased V_{\max} and an unchanged K_m (Robinson, 2015).

In an un-competitive inhibition scenario, the inhibitor binds onto the enzyme-substrate complex directly resulting in a cessation of the complex's activity. As the enzymatic activity is reduced, an increase of the substrate's concentration is expected (Ramsay & Tipton, 2017). An important characteristic of un-competitive inhibition is that as the inhibitor only binds onto the enzyme-substrate complex, and the affinity of the substrate for the enzyme remains unchanged; the Lineweaver-Burk plot illustrating un-competitive inhibition exhibits a decreased V_{\max} and K_m (Strelow et al., 2012).

Mixed-mode inhibition occurs through different scenarios: competitive-uncompetitive or competitive-non-competitive inhibition. In the first scenario, the mixed-mode inhibitor is able to bind to both the enzyme, and the enzyme substrate complex which decreases enzyme's affinity towards the substrate and increases the enzyme's affinity towards the inhibitor. In the second scenario, the mixed-mode inhibitor binds onto the allosteric site of the enzyme, which results in a conformation change (Cortes et al., 2001). Mixed-mode inhibitors are potent compared to other types of reversible inhibitors (Deodhar et al., 2020). The Lineweaver-Burk plot illustrating mixed-mode inhibition exhibits a decreased V_{\max} and an increased K_m (Ring et al., 2014).

1.3.3.2 Irreversible Inhibition

Irreversible inhibition is also known as mechanism-based inhibition. An irreversible inhibitor forms a covalent bond with the targeted enzyme, which results in permanent inactivation of the enzyme; the covalent bond forms between the functional group of the inhibitor and a nucleophilic amino acid residue of the enzyme. The sole solution to overcome the irreversible inhibition of an enzyme is to generate new enzymes. Mechanism-based inhibition is dependent on three factors: time, concentration of inhibitor, and the presence of NADPH (Deodhar et al., 2020; Mohutsky & Hall, 2014).

1.3.4 Investigation of Inhibitory Effects of NPs on CYP Isozymes

Several *in vivo* and *in vitro* studies have been conducted to investigate the outcome of the interaction between CYP isozymes and various types of NPs (Pan et al., 2019).

A study conducted in 2008 investigated the relationship between spherical shaped AuNPs (9 nm) and AgNPs (15 nm) with CYP1A2, CYP2C9, CYP2C19, and CYP3A4. CYP isozymes were isolated from male WISTAR albino rat slices. Of the two metal NPs, AgNPs demonstrated stronger inhibitory potential towards the tested CYP isozymes compared to AuNPs (Sereemasapun et al., 2008). In Lamb's 2010 study, human liver microsomes were incubated with AgNPs at a concentration range of 0 μM to 70 μM . Based on the results, AgNPs were able to inhibit the metabolic activity of the following drug metabolizing isozymes: CYP1A2, CYP2A6, CYP2B6, CYP2C9, CYP2C19, CYP2D6, CYP2E1, and CYP3A4. Of the isozymes inhibited, CYP2C9, CYP2C19, and CYP3A4 were strongly inhibited as the interaction yielded half maximal inhibitory concentration (IC_{50}) values of less than 10 $\mu\text{g/mL}$ (Lamb et al., 2010). In a 2011 study, similar results were achieved by Warisnoicharoen. Spherical shaped AgNPs (~12.42 nm) were introduced to CYP isozymes sourced from baculovirus-infected cells at a concentration range of 10 μM to 80 μM . These AgNPs were able to inhibit CYP1A2, CYP2C9, CYP2C19, and CYP3A4's activity with IC_{50} values of 43.51 μM , 26.46 μM , 14.31 μM , and 13.52 μM respectively; AgNPs were categorized as moderate inhibitors of these isozymes (Warisnoicharoen et al., 2011).

TiO_2 NPs were used in an *in vitro* study conducted by Yang in 2017. These NPs had surface areas ranging from 35-65 m^2/mg and an average size of 21 nm. CYP isozymes (CYP2B10, CYP2C37, CYP2C39, CYP3A11, CYP7A1, CYP8B1, and CYP2C37) were sourced from male C57/BLG mice. A concentration range of 5 mg/kg/day to 150 mg/kg/day was introduced orally for 14 days. Expression of the hepatic CYP2B10 and CYP2C37 genes

were upregulated by 4-folds and 20-folds respectively. However no significant changes were observed in the gene expression of CYP3A11 and CYP2C39 (Yang et al., 2017).

Silica nanoparticles (SNPs) was used in an *in vitro* study to investigate the effect of the NPs on CYP3A4's activity using human liver microsomes and HepG2 cells. 20 nm, 70 nm, 300 nm, and 1000 nm sized SNPs were used, and the mean particle size ranged from 36.8 nm to 1253.3 nm in water, and 84.9 nm and 1083.8 nm in medium. Based on the IC₅₀ values yielded in the human liver microsome test, the smaller sized SNPs exhibited stronger inhibitory potential on CYP3A4 when compared to the larger sized SNPs. Similar results were yielded from the HepG2 assay. Surface modifications of SNPs played a crucial role in the variation of their inhibitory potential towards CYP3A4's activity (Imai et al., 2014).

1.4 Problem Statement and Research Gap

The existing literature suggests that NPs can impact various biological factors. In regard to the toxicity exhibited towards *C. elegans*, several types of NPs were able to alter the reproductive capacity, pharyngeal pumping rate, and lifespan of the nematode. Furthermore, notable variations were noted in the expression of several genes in the nematode. Additionally, various NPs were able to inhibit the activity of the drug metabolising CYP isozymes, which causes the potential increased propensity of adverse side effects and potential toxicity. Despite the prevalent use of ZnONPs in various industries and the established detrimental relationship between NPs, and *C. elegans* and CYP isozymes, there is a lack of research on the size-dependent toxicity potential and inhibitory potential of ZnONPs on *C. elegans* and CYP isozymes respectively. As the nematode shares a large portion of its genome with humans, and CYP isozymes play a vital role in human drug metabolism, both sets of data are vital to further investigate the potential adverse effects of ZnONPs on human health.

1.5 Scope of Research Project

Whilst the disadvantageous relationship between other types of NPs, and *C. elegans* and CYP isozymes has been well documented, the size-dependent toxicity of ZnO particles on *C. elegans* and inhibitory potential on CYP isozymes is poorly understood. The aim of this research project was to report on the size-dependent effect of ZnO particle exposure on *C. elegans* and CYP isozymes.

The scope of this study involved the use of zinc oxide nanoparticles <50 nm (ZnONP50), zinc oxide nanoparticles <100 nm (ZnONP100), and zinc oxide bulk particles (ZnOBP), to understand the size-dependent effect of ZnO particles on the reproductive capacity, pharyngeal pumping rate, and lifespan of N2, on the expression of the nematodes' *cep-1*, *pmk-*

l, and *tba-1* genes, and lastly on the metabolic activity of CYP1A2, CYP2A6, CYP2B6, CYP2C8, CYP2E1, CYP2J2, and CYP3A5.

1.6 Objectives of Research Project

The objectives for this research project were as follows:

- 1) Assess the size range, and purity of each type of ZnO particle (ZnONP50, ZnONP100, and ZnOBP) tested
- 2) Investigate the size-dependent toxicological effect of ZnO particles on the reproductive capacity, pharyngeal pumping rate, and lifespan of N2
- 3) Evaluate the size-dependent gene expression variance of the *cep-1* and *pmk-1* genes under ZnO particles exposure
- 4) Determine the size-dependent inhibitory effect of ZnO particles on CYP1A2, CYP2A6, CYP2B6, CYP2C8, CYP2E1, CYP2J2, and CYP3A5
- 5) Identify the mode of inhibition of each type of ZnO particles on the relevant CYP isozymes

1.7 Hypothesis of Research Project

Based on the literature review conducted, it was hypothesized that size-dependent toxicological and inhibitory potential will be observed towards *C. elegans* and CYP isozymes respectively.

Chapter 2: Characterisation of ZnO Particles

2.1 Background

The physicochemical properties, including size, shape, and elemental composition, of ZnONP50, ZnONP100, and ZnOBP used in this research project need to be determined prior to subsequent down-stream usage. Insights into the physical and chemical properties of ZnO particles can be gained by characterising them, which is essential for designing experiments and predicting their behaviour in different systems. Additionally, the purity of the ZnO particles needs to be evaluated to ensure reliability and reproducibility of experimental results, which may be significantly impacted by unwanted contaminants. Field emission electron microscopy (FESEM) and energy dispersive X-ray elemental analysis (EDX) have several benefits when compared to other methods of characterisation, such as UV-visible spectroscopy, dynamic light scattering, and dark field microscopy, including high-resolution imaging, non-destructive analysis, real-time analysis, and quantitative analysis. Thus, FESEM and EDX were chosen to characterise the ZnO particles used in this research project.

FESEM is able to provide accurate representation of physical features and elemental evidence in three-dimension at a range of 10X to 300,000X magnification, with extensive depth. In comparison with conventional scanning electron microscopy, images with clear distinction and less contortion with resolutions of 1.5 nm are possible using FESEM. Additionally, FESEM allows users to obtain high-quality images with minimal voltage, as minimal electrical charging of samples is required (Panessa-Warren et al., 2007). FESEM does not require insulating materials to be coated with conducting materials (Zheng et al., 2017). The working principle is as follows. The field emission gun frees low-energy and high-energy electrons in an electric field gradient within the high vacuum column; the electronic lenses within focuses and deflects the primary electrons which produces a narrow scan beam, allowing the sample to be blasted by electrons. The sample emits secondary electrons, whose angle and velocity are dependent on the sample's surface structure. A detector within the instrument is able to capture the secondary electrons and to subsequently produce electrical signals. The electrical signals are amplified and translated into a video scan, which is projected onto the monitor as an image (Mayeen et al., 2018).

The elemental analysis technique, EDX, is linked to electron microscopy. It is based on the establishment of characteristic X-rays which discloses the presence of various elements within the tested sample. It allows researchers to identify the elemental composition of the sample, and the information provided can be categorised as both qualitative and quantitative

(Goriuc et al., 2021). Users are able to gain information regarding the type of elements present within the sample, and the percentage of each element's presence within the sample. Additionally, it provides a spatial distribution of elements via mapping. Similar to FESEM, EDX requires minimal to no preparation of samples, and it is non-destructive, which prevents damage to limited sample availability (Wyroba et al., 2015). The working principle is as follows: The sample is projected onto by an electron beam, which emits several X-rays. The energy associated with these X-rays are unique to specific elements. The built-in silicon drift detector collects the emitted X-rays and interprets it via the software. The data is presented in several ways including elemental mapping (Scimeca et al., 2018).

This chapter of the research project presents the characterization of the ZnO particles (ZnONP50, ZnONP100, and ZnOBP) utilised in this study using FESEM and EDX.

2.2 Methodology

2.2.1 Materials and Reagents

ZnONP50, ZnONP100, and ZnOBP were acquired from Sigma Aldrich (St Louis, Missouri, USA). Analytical grade dimethyl sulfoxide (DMSO) was procured from Nacalai Tesque (Kyoto, Japan).

2.2.2 ZnO Particles' Characterization

ZnO particles were imaged using FESEM (Fei Quanta 400F). ZnO particles were prepared by being adhered to carbon-based double-sided tape and were affixed onto an electron microscope stub. High resolution secondary electron images were acquired at ranges between 50,000X to 240,000X with the in-lens detector's speed set at 20.00 kV. The imaging conditions were as follows: working distance was set between 10.0-10.3 mm, and the aperture size was set between 2 μm - 500 nm. Additionally, EDX (Oxford-Instruments INCA 400 with X-Max Detector) was used to derive the elemental maps of all three sizes of ZnO particles. Elemental composition in terms of carbon, oxygen, zinc, and aluminum were measured. The X-ray detectors' tilt, elevation, and azimuth degree for all ZnO particles were set at 0.0°, 35.0°, and 0.0° respectively. The accelerating voltage of the beam was kept consistent at 20.00 kV.

2.3 Results and Discussion

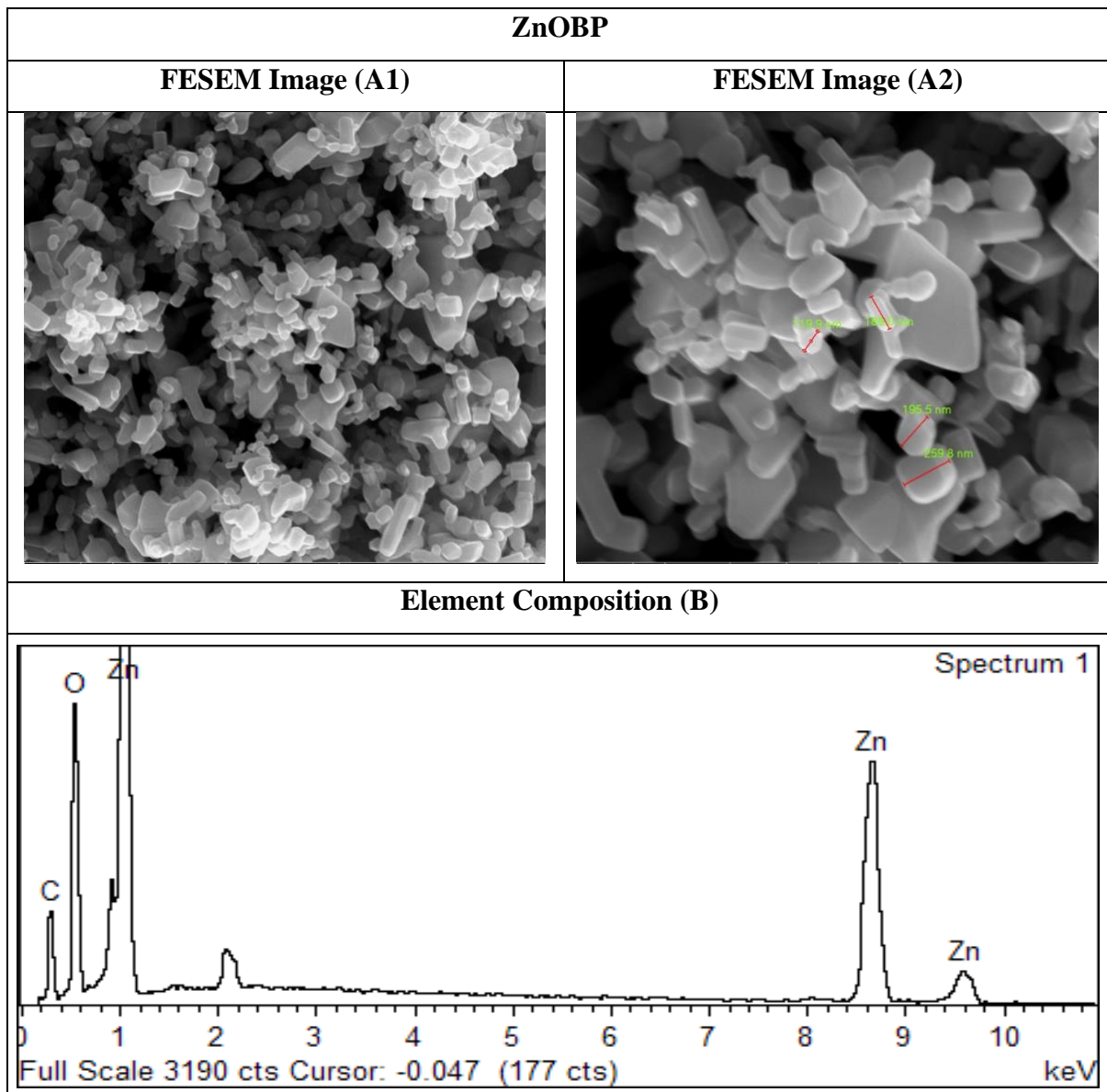


Figure 2.1. ZnOBPs' **A1)** shape, **A2)** size characterisation under FESEM (magnification: 50X-120X) and **B)** EDX analysis of elemental composition. Red lines indicate the dimensions measured under FESEM, and the measurements are denoted in green. *ZnOBP* Zinc oxide bulk particles, *FESEM* Field emission scanning electron microscopy, *EDX* energy dispersive X-ray spectroscopy, *cts* counts, *keV* kilo-electron volts.

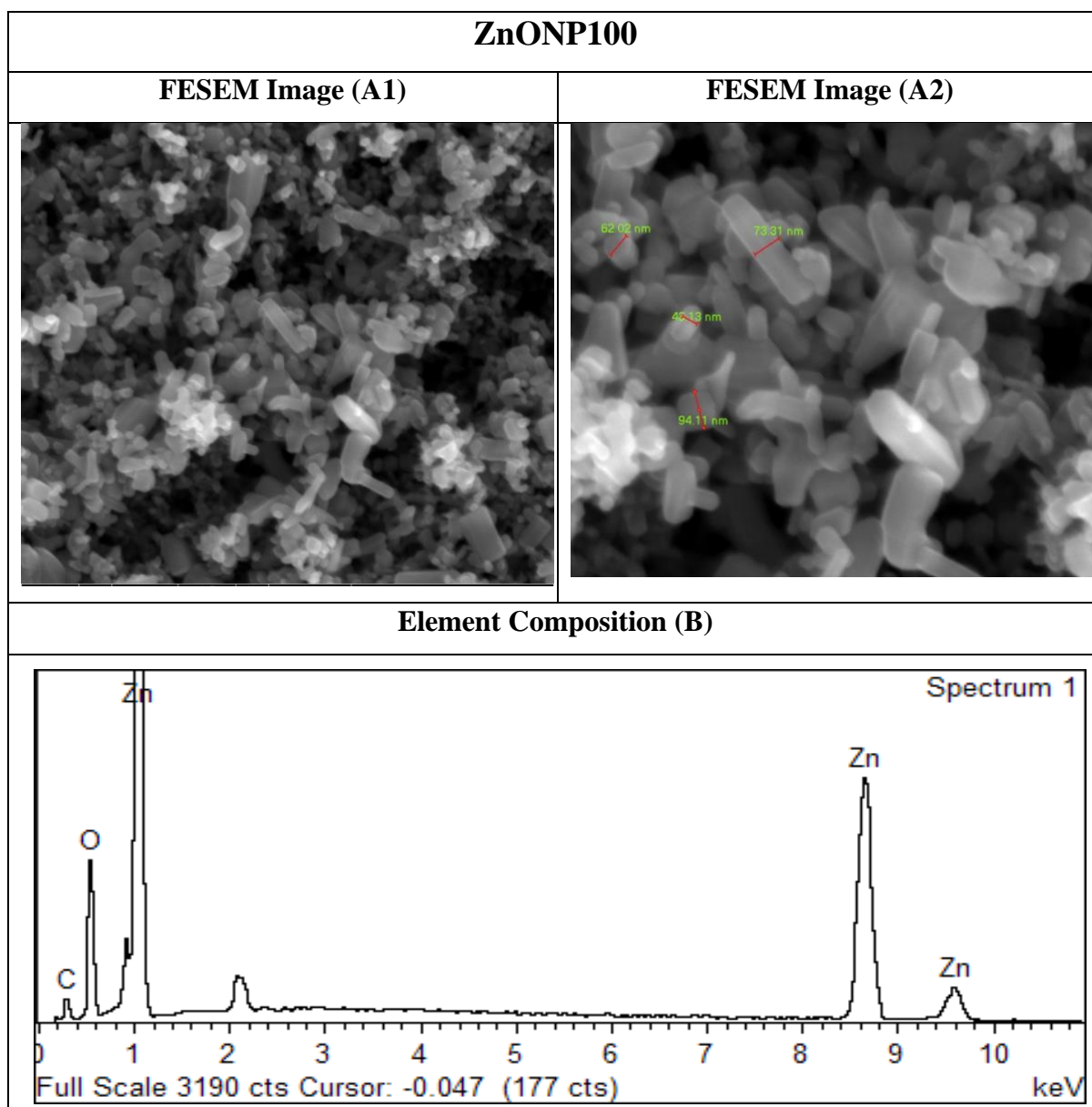


Figure 2.2. ZnONP100' **A1)** shape, **A2)** size characterisation under FESEM (magnification: 120X-240X) and **B)** EDX analysis of elemental composition. Red lines indicate the dimensions measured under FESEM, and the measurements are denoted in green. *ZnONP100* Zinc oxide nanoparticles <100 nm, *FESEM* Field emission scanning electron microscopy, *EDX* Energy dispersive X-ray spectroscopy, *cts* counts, *keV* kilo-electron volts.

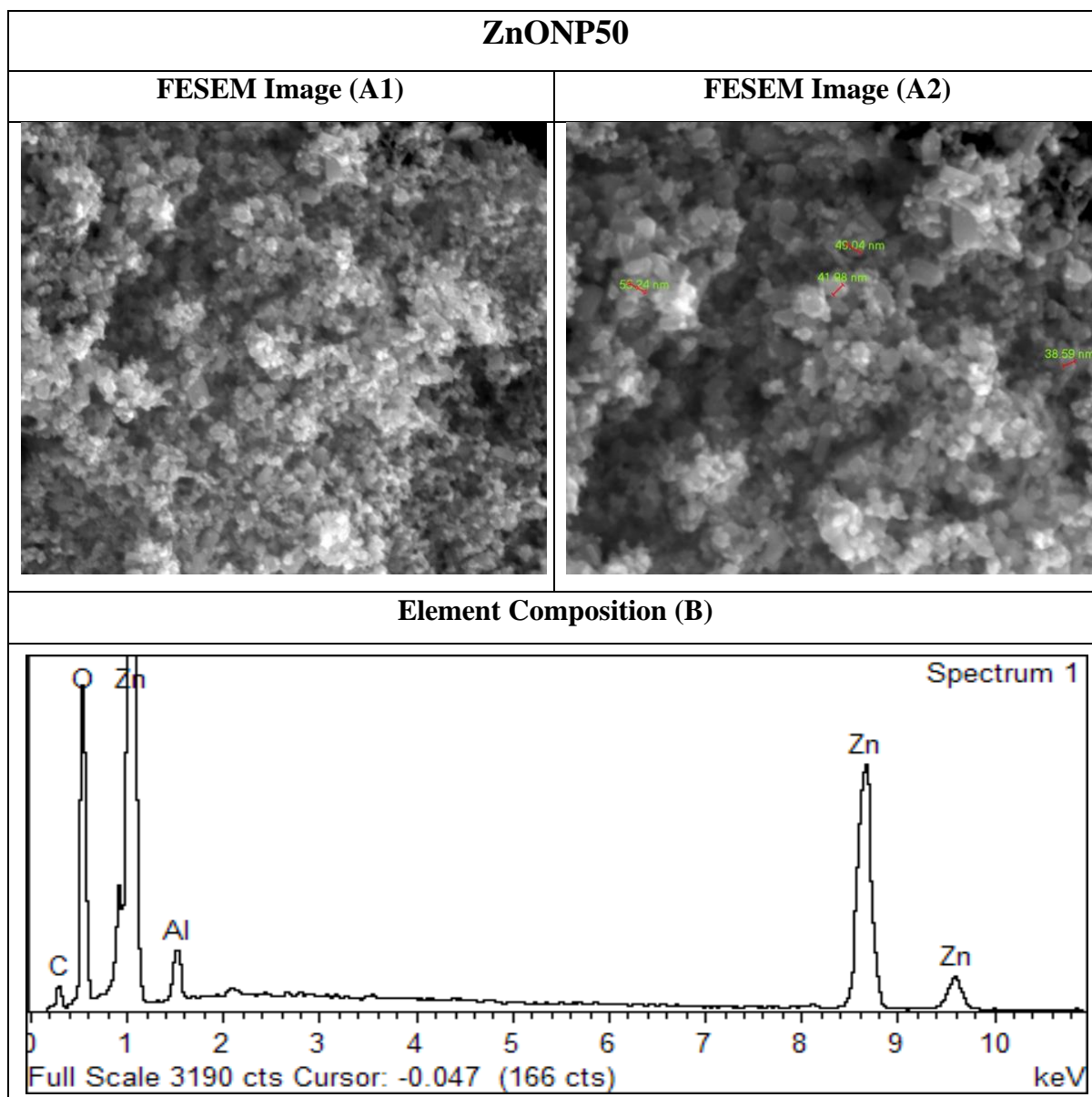


Figure 2.3. ZnONP50' **A1)** shape, **A2)** size characterisation under FESEM (magnification: 120X-200X) and **B)** EDX analysis of elemental composition. Red lines indicate the dimensions measured under FESEM, and the measurements are denoted in green. *ZnONP50* Zinc oxide nanoparticles <50 nm, *FESEM* Field emission scanning electron microscopy, *EDX* Energy dispersive X-ray spectroscopy *cts* counts, *keV* kilo-electron volts.

Based on Figure 2.1 A1 and A2, ZnOBP did not have a uniform shape, and the particles' size ranged between 119.9 nm to 259.8 nm. The elemental analysis conducted showed a presence of 20.72% of carbon, 23.52% of oxygen, and 55.76% of zinc. The analysis was confirmed by elemental mapping, as shown in Figure 2.1B, where signal peaks are visible for carbon, oxygen, and zinc at 0.3, 0.5, and 1.0, 8.6, 9.8 keV respectively. In reference to Figure 2.2 A1 and A2, ZnONP100 mostly had a cylindrical shape, and the NPs' size ranged between 43.13 nm to 94.11 nm. The elemental analysis conducted showed a presence of 8.53% of carbon, 16.06% of oxygen, and 75.41% of zinc. The analysis was confirmed by elemental mapping, as shown in Figure 2.2B, where signal peaks are visible for carbon, oxygen, and zinc at 0.3, 0.5, and 1.0, 8.6, 9.6 keV respectively. The multiple peaks are known absorptions of ZnONPs (S et al., 2017). Appertaining to Figure 2.3 A1 and A2, ZnONP50' shape was not fully defined due to the aggregation under the microscope, however, the NP's size ranged between 38.59 nm and 50.24 nm. The elemental analysis conducted showed a presence of 2.50% of aluminium, 7.17% of carbon, 25.19% of oxygen, and 65.14% of zinc. The analysis was confirmed by elemental mapping, as shown in Figure 2.3B, where signal peaks are visible for carbon, oxygen, aluminium, and zinc at 0.3, 0.5, 1.5, and 1.0, 8.6, 9.8 keV respectively. Multiple signal speaks across all sizes of ZnO particles are known absorptions of ZnO particles, including the presence of aluminium (Akhtar et al., 2015; S et al., 2017).

The absence of unwanted peaks allowed the confirmation of ZnON50, ZnONP100, and ZnOBP's purity.

The properties of NPs differ from their bulk particles (BPs) counterparts owing to their size, and their surface area to volume ratio. The physicochemical properties of NPs play influential roles in their behaviour, bio-distribution, and toxicological effects (Zhang et al., 2016). Size and chemical composition are vital factors which contribute to NPs' toxicity (Wang et al., 2016). As a point of comparison, to investigate the size-dependent toxicity and inhibitory potential of ZnONPs, ZnOBP were utilised in this study.

The ZnOBP tested in this study had an average particle size of $191.05 \text{ nm} \pm 57.19 \text{ nm}$ (n=4), which by definition categorises these particles as bulk-sized rather than nano-sized. ZnONP100's average particle size was $68.14 \text{ nm} \pm 21.23 \text{ nm}$ (n=4) and ZnONP50's average particle size was $44.96 \text{ nm} \pm 5.94 \text{ nm}$ (n=4), which are in agreement with the definition of a NP's size description (Jeevanandam et al., 2018). Additionally, the absence of any unwanted elements within all three sized ZnO particles allowed the confirmation of the particles' compositional purity (Kumar et al., 2013).

As this research project focused on the size-dependent toxicological and inhibitory potential of ZnO particles, a primary limitation needs to be addressed in future studies to improve the reproducibility of the results reported and to improve the understanding of the toxicological and inhibitory properties of ZnO particles. While this study employed ZnONPs of sizes less than 50 nm and 100 nm, it is recommended that future studies should incorporate both specific and various sizes of ZnONPs to obtain more comprehensive knowledge.

2.4 Conclusion

Through the use of FESEM and EDX, purity and size of all three sizes of ZnO particles were confirmed. Thus, this research project was able to proceed with investigating the size-dependent toxicological and inhibitory potential of three different sized ZnO particles.

Chapter 3: Toxicological Effects of Various Sized Zinc Oxide Particles on *Caenorhabditis elegans*

3.1 Background

C. elegans were introduced to the research community in the 1960s by Sydney Brenner, and N2 has since been defined as the canonical wild type (Nigon & Felix, 2017). These specific nematodes are ecologically significant as they are abundant in soils and in sediments rich with decomposing plant materials. Thus, N2 are widely used as *in vivo* models for eco-toxicological assays (Berg et al., 2016). The use of N2 over deletion mutants and transgenic strains of *C. elegans* and other invertebrate models offers researchers vital advantages (Ha et al., 2022). As N2 are hermaphrodites and have a short reproductive cycle, fast and efficient generation of large, isogenic, and age-synchronised progeny populations is possible (Johnson, 2003). The anatomy, genetic makeup, and the neuronal connectivity of N2 is fully mapped; 80% of N2 genes are orthologs to human genes, which provides significant translational potential of findings (Zhang et al., 2020). N2 is able to produce an average progeny of 220 or more offspring within the strain's entire lifespan, which is beneficial to investigate its reproduction capacity post-exposure to xenobiotics (Meneely et al., 2019). However, the large progeny constitutes as a hurdle while investigating the toxicological effect of xenobiotics on the nematode's pharyngeal pumping rate and the average lifespan within a singular generation.

To overcome this issue, the DNA synthesis inhibitor, 5-fluorodeoxyuridine (FUDR), is used to prevent the production of progeny while investigating the effect of xenobiotics exposure within a singular generation of N2 (McIntyre et al., 2021). As all cells in an adult N2 are post-mitotic, researchers assumed that the compound did not elicit any unwanted physiological effects on the adult nematode (Raices et al., 2005). Studies requiring sterile N2 have applied FUDR at concentrations ranging from 50 to 200 µg/mL. However, studies have established that the introduction of FUDR at premature stages and at high concentrations yielded unwanted side-effects: increase in the average lifespan and unexpected progeny production (Saul et al., 2021). Recent studies have demonstrated and concluded that supplementation of FUDR at lower concentrations (10 to 50 µM) on L4 nematodes produced negligible effect on the lifespan and behaviour of the treated worms, while the targeted sterility was achieved (Wang et al., 2019).

This chapter of the research project presents the evaluation of the size-dependent toxicological effects of ZnONP50, ZnONP100, and ZnOBP on *C. elegans*' sublethal endpoints: reproduction capacity, pharyngeal pumping rate, and lifespan. Additionally, analysis of

alterations in the expression of the *cep-1* and *pmk-1* genes is presented to elicit a plausible mechanism of toxicity.

3.2 Methodology

3.2.1 Materials and Reagents

DMSO and sodium hydroxide (NaOH) were procured from Nacalai Tesque (Kyoto, Japan). Ampicillin sodium salt and streptomycin sulfate salt were obtained from Sigma-Aldrich (St. Louis, Missouri, USA). Carbenicillin sodium salt was acquired from Fisher Bioreagents (Loughborough, Leicestershire, UK). FUDR was purchased from Thermo Scientific (Heysham, Lancashire, UK). Isopropyl β -d-1-thiogalactopyranoside (IPTG) was procured from Thermo Scientific (Italy). Bacteriological agar, bacteriological peptone, calcium chloride (CaCl₂), dipotassium hydrogen phosphate (K₂HPO₄) and potassium dihydrogen phosphate (KH₂PO₄) were acquired from Friendmann Schmidt Chemical (Parkwood, Western Australia, Australia). Lysogeny broth (LB) agar and LB broth were acquired from Merck (Darmstadt, Germany). Cholesterol was purchased from Solarbio (Beijing, China). Magnesium sulfate (MgSO₄) was procured from Sime Scientific (Petaling Jaya, Selangor, Malaysia). Sodium chloride (NaCl) was obtained from Vivantis (Shah Alam, Selangor, Malaysia). 30 mm, 60 mm, and 90 mm sterile petri dishes were purchased from NEST Scientific (Woodbridge, New Jersey, USA). N2 were provided by the *Caenorhabditis* Genetics Center (CGC), under the University of Minnesota.

3.2.2 Preparation of ZnO Particles

The following concentration range of ZnONP50, ZnONP100, and ZnOBP was chosen as the testing concentrations for the reproductive capacity, pharyngeal pumping rate, and lifespan assays: 0, 1, 10, 100, and 1000 μ g/mL. Respective stock solutions were prepared using DMSO as the solvent and were sonicated for use as per Table 3.1. An increased sonication period was required for higher testing concentrations to ensure proper dispersion.

Table 3.1. Concentration and sonication specifications for ZnO particle. *ZnO* zinc oxide.

ZnO Particle	Testing Concentration ($\mu\text{g/mL}$)	Stock Solution Concentration (mg/mL)	Sonication (Time & Temperature)
ZnONP50	Negative Control	-	-
	Vehicle Control	0	-
	1	0.1	30 minutes, 30°C
	10	1	30 minutes, 30°C
	100	10	60 minutes, 30°C
	1000	100	60 minutes, 30°C
ZnONP100	Negative Control	-	-
	Vehicle Control	0	-
	1	0.1	30 minutes, 30°C
	10	1	30 minutes, 30°C
	100	10	60 minutes, 30°C
	1000	100	60 minutes, 30°C
ZnOBP	Negative Control	-	-
	Vehicle Control	0	-
	1	0.1	30 minutes, 30°C
	10	1	30 minutes, 30°C
	100	10	60 minutes, 30°C
	1000	100	60 minutes, 30°C

3.2.3 Solution Preparation

All solution used for maintenance and assays purposes were prepared according to Table A.3.1 in the Appendix. CaCl_2 , MgSO_4 , and KPO_4 were autoclaved prior to use. Streptomycin, carbenicillin, ampicillin, cholesterol, and IPTG solutions were filtered using polytetrafluoroethylene (PTFE) membrane (0.22 μm pore size) to ensure sterility. All prepared solutions were stored at 4°C for future use.

3.2.4 Selection of Optimal FUDR Concentration

FUDR and ampicillin were chosen as the method to eliminate progeny production from synchronous populations when required. A concentration range of FUDR was tested to determine the optimal concentration: 5, 10, 15, 20, and 25 μM . 15 N2 adults were transferred onto a nematode growth medium (NGM) agar plate, without FUDR and ampicillin, and were incubated until a sufficient number of eggs were laid. The adult N2 nematodes were removed, and the eggs were allowed to hatch and develop until L4. Five of these L4 nematodes were transferred onto NGM plates containing ampicillin (100 mg/mL) and FUDR at different concentrations. The following parameters were observed and tabulated for 30 days: number of eggs laid, number of viable progenies, and the average lifespan. NGM plates were incubated at 16°C throughout the entire duration. Triplicates were performed.

3.2.5 Agar Preparation

3.2.5.1 Nematode Growth Medium (NGM) Agar

NGM agar was prepared for the maintenance of N2 and for all toxicological behavioral assays; 9 mm and 6 mm petri dishes were used for culturing and maintenance purposes, and 3 mm plates were used for the assays.

The concentration of the NGM agar's components per 100 mL of water have been summarised under Table A.3.2 in the Appendix. Majority of the constituents remained constant for all purposes, while certain constituents were altered according to specific needs.

3.2.5.2 Lysogeny Broth (LB) Agar

LB agar was prepared on 9 mm petri dishes to culture *E. coli* OP50, which served as the bacterial food source for N2. The concentration of the LB agar's components per 100mL of water have been summarised in Table A.3.3 in the Appendix.

3.2.6 Bacterial Food Source Preparation

As NGM agar medium contains a negligible amount of uracil, *E. coli* OP50 was chosen as the bacterial food source for all maintenance and assay purposes; due to its uracil auxotroph characteristic, *E. coli* OP50 is not able to cultivate into a thick layer and obscure the observation of the nematodes (Macneil & Walhout, 2013).

2.0 g of LB broth powder per 100 mL of water was autoclaved, and 100 μL of 100 mg/mL of streptomycin and *E. coli* OP50 cryostock were added post-autoclave in proportion. The solution was incubated overnight (180 rpm, 37°C), and then centrifuged (30 minutes, 4000 rpm, 4°C). The *E. coli* OP50 pellet was resuspended using fresh LB broth. *E. coli* OP50 was seeded directly onto 60 mm maintenance plates (300 μL /plate), but was heat-killed (30 minutes,

80°C) and combined with ZnO particles as per Table 3.1 prior to being seeded onto 30 mm assay plates (50 µL/plate).

3.2.7 Age Synchronisation Procedure

To achieve age synchronised N2, a process termed ‘egg preparation’ was conducted from NGM agar plates filled with eggs and gravid L4 nematodes. The plates were washed with water to retrieve the eggs and nematodes, and they were both combined with lysis buffer. The lysis buffer was prepared as per Table A.3.4 in the Appendix. The combined solution was vortexed until homogenised, and then centrifuged (1 minute, 2000 rpm, 16°C). The supernatant was poured out, fresh water was added to the egg pellet, and the solution was centrifuged again. The cycle was repeated until the supernatant was clear. The egg pellet was then seeded around the *E. coli* OP50 lawn on NGM plates, and was left to incubate at 16°C.

3.2.8 Cryopreservation

3.2.8.1 *E. coli* OP50

Overnight cultured *E. coli* OP50 solution was prepared as described in Section 3.2.6. The overnight culture and freezing solution were combined at a ratio of 7:3 and was stored at -80°C for future use. The freezing solution was prepared as per Table A.3.5 in the Appendix. LB agar plates were streaked with cryopreserved *E. coli* OP50 regularly to ensure the stocks’ viability.

3.2.8.2 N2

After the age synchronization procedure (Section 3.2.7), the progeny was cryopreserved, if necessary, at L1. The nematodes were washed off the plate using water, and the solution was combined with the freezing solution at a ratio of 7:3. The freezing solution was prepared as per Table A.3.5 in the Appendix. The final solution was stored at 4°C for 2-3 hours, before being stored at -80°C for future use. To assess the viability of cryopreserved N2, the cryostocks were thawed at room temperature and dispensed onto NGM plates to observe the nematodes’ motility.

3.2.9 Reproductive Capacity Assay

Reproductive capacity assay plates were prepared according to Table A.3.2 in the Appendix, *E. coli* OP50 lawn was prepared as per Section 3.2.6, and ZnO particles were introduced according to Table 3.1. Three biological replicates were conducted per ZnO particle type at 16°C; three assay plates were prepared per ZnO particle concentration, totaling to eighteen plates per biological replicate conducted.

Age synchronisation procedure was conducted to yield a synchronised-aged population. Five L4 N2 were transferred onto the first assay plates of each concentration. At the 48-hours' time point, the L4 nematodes were transferred from the first set of assay plates to the respective second plates. At the 72-hours' time point, the L4 N2 were transferred from the second set of assay plates onto the respective third and final set.

All plates were incubated at 16°C and the plates containing laid/hatched eggs were left to incubate for 48 hours until respective counting days. This marked the end of one biological replicate.

3.2.10 Pharyngeal Pumping Rate Assay

Pharyngeal pumping rate assay plates were prepared according to Table A.3.2 in the Appendix, *E. coli* OP50 lawn was prepared as per Section 3.2.6, and ZnO particles were introduced according to Table 3.1. Three biological replicates, inclusive of three technical replicates, were performed per ZnO particle type at 16°C. For each biological replicate, three assay plates were prepared per ZnO particle concentration, totaling to eighteen plates per biological replicate conducted.

Fifteen fertile L4 N2 were transferred onto NGM plates, without FUDR and ampicillin, and were incubated until a sufficient number of eggs were laid. The L4 nematodes were removed, and the eggs were left to hatch and develop until L4 larva stage. Five L4 nematodes were transferred onto NGM assay plates containing FUDR and ampicillin for 24 hours, prior to the adult nematodes being transferred to NGM plates containing FUDR, ampicillin, and ZnO particle.

The pharyngeal pumping rate of each adult nematode was recorded for five seconds post-exposure to the ZnO particle at 4, 24, 48, 72, and 96 hours. This marked the end of one biological replicate.

3.2.11 Lifespan Assay

Lifespan assay plates were prepared according to Table A.3.2 in the Appendix, *E. coli* OP50 lawn was prepared as per Section 3.2.6, and ZnO particles were introduced according to Table 3.1. Three biological replicates, inclusive of three technical replicates, were performed per ZnO particle type at 16°C. For each biological replicate, three assay plates were prepared per ZnO particle concentration, totaling to eighteen plates per biological replicate conducted.

Fifteen fertile L4 N2 were transferred onto NGM plates, without FUDR and ampicillin, and were incubated until a sufficient number of eggs were laid. The L4 nematodes were removed, and the eggs were left to hatch and develop until L4. Thirty L4-larvae were

transferred onto NGM assay plates containing FUDR and ampicillin for 24 hours, prior to the adult nematodes being transferred to NGM plates containing FUDR, ampicillin, and ZnO particle.

Number of alive and dead N2 were scored daily until all nematodes on each plate perished. This marked the end of one biological replicate.

3.2.12 Sample Preparation for Gene Expression Study

To achieve age synchronised N2, egg preparation was conducted as per Section 3.2.7. The NGM plates were incubated until the progeny reached L4. The nematodes were then washed off with water and seeded onto ZnO particle treated NGM plates (100 µg/mL). N2 were exposed to ZnO particles (ZnONP50, ZnONP100, ZnOBP) using a chronic-exposure method for 72 hours. Post-chronic exposure, the nematodes were washed off the treated plates using M9 buffer, which was prepared according to Table A.3.6 in the Appendix. The nematode-M9 buffer solution was centrifuged (1 minute, 2000 rpm, 16°C). The supernatant was removed, and fresh M9 buffer was added to the nematode pellet. This procedure was repeated until the discarded supernatant was clear. 1000 µL of TRIzol™ reagent was added per nematode pellet prepared.

3.2.13 Ribonucleic Acid (RNA) Extraction

Ribonucleic acid (RNA) extraction from the treated N2 pellets was conducted using TRIzol™ reagent. The samples were vortexed thoroughly and resuspended. 100 µL of chloroform was added per 500 µL of nematode sample to conduct chloroform extraction. The solution was inverted and placed at room temperature for 3 minutes to allow phase separation to occur before centrifugation (15 minutes, 12000 rpm, 4°C). The RNA, isolated within the aqueous phase, was transferred to a new tube and mixed with 500 µL of isopropanol to precipitate the RNA. The solution was inverted and placed at room temperature for 10 minutes prior to centrifugation (10 minutes, 12000 rpm, 4°C). The supernatant was removed, and 500 µL of 75% ethanol was added to the RNA pellet to remove the remaining traces of TRIzol™ reagent and other contaminants. The solution was centrifuged (5 minutes, 7500 rpm, 4°C), and the supernatant was removed. The RNA pellet was placed on ice for 5 minutes and then suspended in 20 µL of RNase-free water afterwards. The RNA sample was incubated at 55°C for 15 minutes to allow the RNA pellet to dissolve completely within the RNase-free water. NanoDrop™ One Microvolume UV-Vis Spectrophotometer was used to check the purity and concentration of the extracted RNA. RNase-free water served as the blank. Required concentration of the extracted RNA was benchmarked at 1000 ng/µL or above for all samples.

The A260/A280 and A260/A230 ratios were required to be within the 2.0 to 2.5 range to confirm the purity and quality of RNA. Extracted RNA was stored at -80°C for future downstream use. Triplicates were performed.

3.2.14 Complementary Deoxyribonucleic Acid (cDNA) Synthesis

ProtoScript® II First Strand cDNA Synthesis Kit from BioLabs® Inc was used to convert the extracted RNA into complementary deoxyribonucleic acid (cDNA) using the manufacturer's suggested protocol (BioLabs, 2023). 20 µL reactions were prepared according to Table A.3.7 in the Appendix, and the Bio-Rad T100 Thermal Cycler was used to generate the cDNA. The temperature and time settings for the thermal cycler were set according to Table A.3.8 in the Appendix. The synthesised cDNA product was stored at -20°C for future downstream use. Triplicates were performed.

3.2.15 Primer Design and Polymerase Chain Reaction

NetPrimer by PREMIER Biosoft and Primer-BLAST by National Center for Biotechnology Information were used to design and evaluate the forward and reverse primer sequences for each gene studied in this research project.

The following were set as requirements for the selection of primer pairs:

- 1) Polymerase chain reaction (PCR) product size should be between 100 to 300 base pairs (bp).
- 2) Primer length should be between 18 to 22 nucleotides.
- 3) GC% content of each primer should be between 50 to 60%.
- 4) Melting temperature of the primers should be between 59°C to 65°C, and within 2°C of each other.
- 5) Self-complementarity and self 3'-complementarity scores between the forward and reverse primers should be low.
- 6) The primer pair must be specific to the target gene.

Based on these conditions, the primers were designed and procured from Integrated DNA Technologies. Primers were diluted to 10 µM using nuclease-free water. PCR reactions for ZnO particles and the respective gene pairings were performed using the BIOTAQ™ DNA Polymerase from BIOLINE. PCR reactions of 20 µL were prepared according to Table A.3.9 in the Appendix, as per the manufacturer's suggested protocol (BioScience, n.d.). Bio-Rad T100 Thermal Cycler's parameters were set up according to Table A.3.10 in the Appendix, for 35 cycles for the *cep-1*, *pmk-1*, and *tba-1* genes. Once the PCR reactions were complete, the PCR products were stored at -20°C for future downstream use.

3.2.16 Gel Electrophoresis, and Gel Imaging

50 mL of 1X Tris-acetate-EDTA (TAE) buffer was mixed with 1 g of molecular biology-grade agarose to yield a 2% agarose mixture. The mixture was heated to ensure complete homogenisation and 1.5 μ L of SYBR Safe DNA Gel Stain was added prior to casting the gel. Once the gel solidified, it was submerged in 1X TAE buffer in the electrophoresis tank. 3 μ L of 100 bp DNA ladder, and 5 μ L of PCR products mixed with 1 μ L of 6X DNA loading dye were loaded into their respective wells. The power supply's parameters were set accordingly: 100 V, 400 mA, and 35 minutes. Once the run was complete, the Biorad Gel Doc XR+ Imaging System was used to visualise the gel. Intense bands were visualised at an exposure time of 0.50 seconds. Triplicates were performed.

3.2.17 Data Analysis

3.2.17.1 Reproductive Capacity Assay and Pharyngeal Pumping Rate Assay

Once all three biological replicates were completed, a bar chart was derived for each ZnO particle as the average number of progeny against time (hours), and pharyngeal pumping rate (contractions/5 seconds) against time (hours) for the reproductive assay and pharyngeal pumping rate assay respectively.

GraphPad Prism Version 9.4.1 for Mac (GraphPad Software, La Jolla California, USA) was used to run 'two-way analysis of variance' (two-way ANOVA) for the statistical analysis of the reproductive capacity assay and pharyngeal pumping rate assay. Two-way ANOVA and Holm-Šídák's multiple comparison tests were first used to determine whether statistically significant difference ($p < 0.05$) was present between the vehicle control and negative control data sets. Subsequently, the statistical tests were used to determine whether statistically significant difference ($p < 0.05$) was present between the negative control and the tested ZnO particle' concentration data sets. Concentration-dependent and size-dependent comparison was conducted to conclude (Sofela et al., 2021).

3.2.17.2 Lifespan Assay

Once all biological replicates were completed, the survival rate percentage for the nematodes were averaged, and the standard deviation was derived for each concentration.

GraphPad Prism Version 9.4.1 for Mac (GraphPad Software, La Jolla California, USA) was used to run the statistical analysis for the lifespan assay. Kaplan-Meier curves, for all concentrations of each ZnO particle, were derived and plotted as probability of survival (%) against time (day). Log-rank (Mantel-Cox) and Grehan-Breslow-Wilcoxon tests were conducted as well to statistically compare the survival curve of each ZnO particles'

concentration-treatment group to the survival curve of the control-treatment group (Park et al., 2017).

3.2.17.3 Gene Expression Study

ImageJ (National Institute of Health, Bethesda, Maryland, USA) has been widely used to quantify the density of gene expression in agarose gels (Alonso Villela et al., 2020; Ciniselli et al., 2015; Ziraldo et al., 2019). In this research project, it was employed to quantify the intensity of the DNA fragment bands produced through gel electrophoresis to yield the quantified density of each band produced under the different ZnO particle treatments and the 500 bp standard of the molecular-weight size marker. The 500 bp standard was utilised as an internal standard to normalize the variation between individual gels. Subsequently, the *cep-1* and *pmk-1* bands' density were normalised by dividing the reference gene, *tba-1*, bands' density under the same respective conditions. Lastly, the fold changes in *cep-1* and *pmk-1*'s expression under each ZnO particles' treatment was quantified by dividing the untreated-group (control). A relative fold change of more than 1 indicated upregulation of the examined gene, and a relative fold change of less than 1 indicated downregulation of the examined gene. The mean and standard deviation of the three replicates were derived and were plotted as the relative fold change in the density of DNA fragments against the target genes (*cep-1* and *pmk-1*).

3.3 Results and Discussion

3.3.1 Selection of Optimal FUDR Concentration

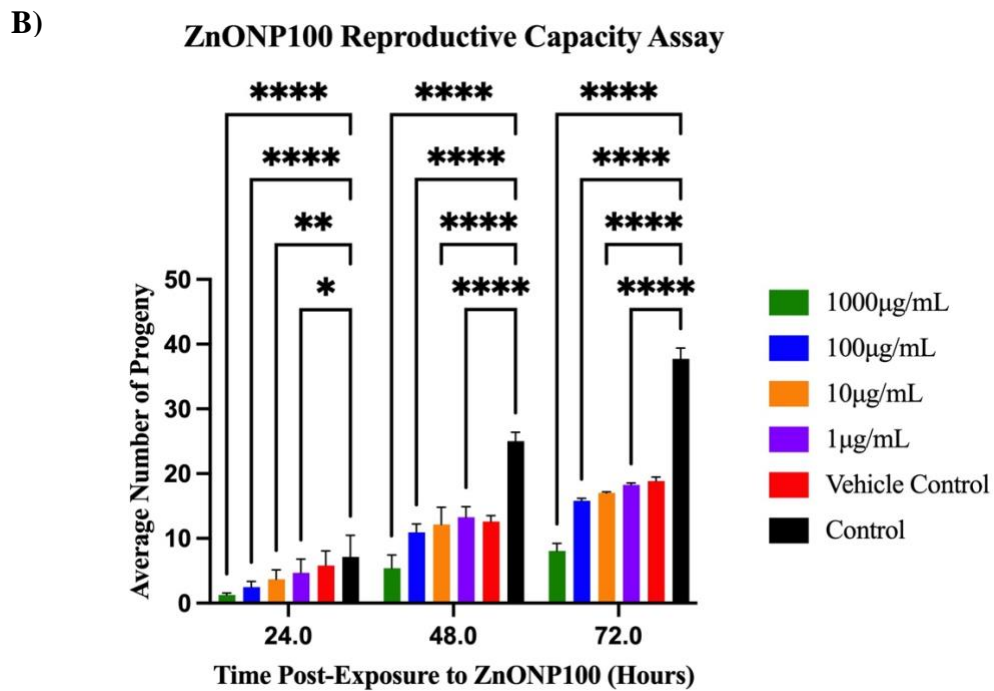
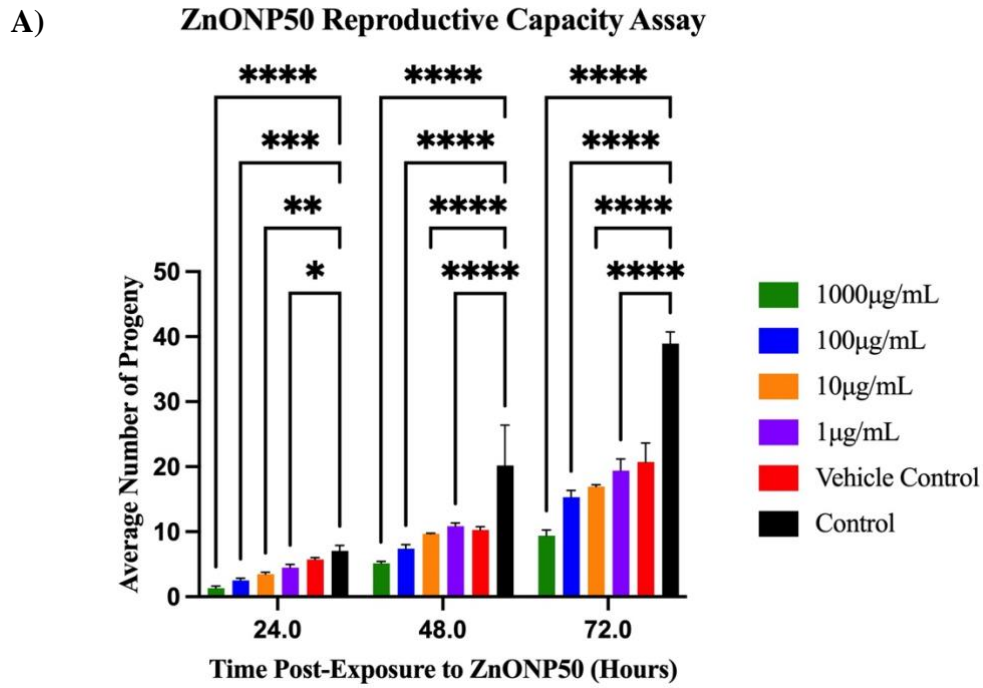
The optimal concentration of FUDR to be used for the pharyngeal pumping rate and lifespan assays was determined by assessing three parameters: number of eggs laid, number of viable progeny, and alterations in the lifespan compared to the control-treatment group (0 μM). Five L4 N2 were exposed to a range of FUDR concentrations (5 to 25 μM) for 30 days, and the results have been tabulated in Table 3.2.

As a large number of eggs were laid and a substantial number of viable progeny were generated by the N2 under the 5 μM , 10 μM , and the 15 μM treatment groups, these FUDR concentrations were considered unsuitable for the intended assays, as the progeny would interfere with the data collection of a single generation. The 25 μM treatment group yielded the smallest number of viable progeny, however, the average lifespan increased considerably compared to the control group. Based on the statistical test conducted, the survival curve for the 25 μM treatment group yielded a p-value of <0.0001 , compared to the control treatment group. Since the increased lifespan could bias the results during the lifespan assays, 25 μM was ill-suited for the project. Thus, taking all the parameters into consideration, 20 μM of FUDR was chosen as the optimal concentration for the subsequent pharyngeal pumping rate and lifespan assays.

Table 3.2. Summary of FUDR Concentrations 30-Day Trial (n=3). *FUDR* 5-fluorodeoxyuridine.

Concentration of FUDR	Number of Eggs Laid	Number of Viable Progeny	Average Life Span (Days)	p-value
Control (0 μM)	228	201	22.0 \pm 0.71	-
5 μM	204	59	20.6 \pm 0.89	0.1298
10 μM	198	41	22.2 \pm 0.84	0.4350
15 μM	184	30	21.4 \pm 1.52	0.2878
20 μM	97	4	23.2 \pm 0.84	0.0449
25 μM	84	3	28 \pm 1.58	<0.0001

3.3.2 Reproduction Capacity of *C. elegans* Treated with Zinc Oxide Particles



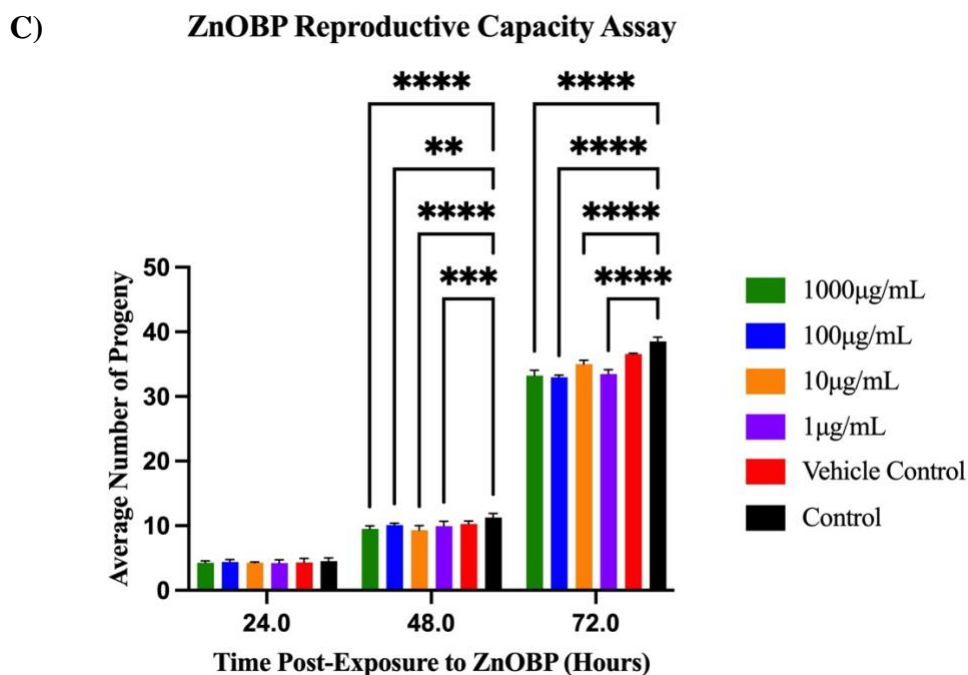


Figure 3.1. Reproductive capacity of L4 N2 post-exposure to a concentration range of A) ZnONP50, B) ZnONP100, and C) ZnOBP (1, 10, 100, 1000 µg/mL) in combination with *E. coli* OP50 for 24-hours, 48-hours, and 72-hours. DMSO, in combination with *E. coli* OP50, served as the vehicle control. *E. coli* OP50 served as the negative control. Three biological replicates were performed for each type of ZnO particle. Data is presented as the average number of progenies laid per parental nematode against time after exposure to the respective ZnO particle (hours). Each data point represents the mean \pm SD (n=3). Asterisk (*) indicates statistically significant difference (p<0.05) with the control treatment group. L4 fourth-larval stage, N2 Bristol strain N2, ZnONP50 Zinc oxide nanoparticles <50 nm, ZnONP100 Zinc oxide nanoparticles <100 nm, ZnOBP Zinc oxide bulk particles, *E. coli* OP50 Escherichia coli, DMSO dimethyl sulfoxide, ZnO zinc oxide.

The average number of progeny laid by five L4 N2 under exposure to a concentration range of various sized ZnO particles have been presented graphically in Figure 3.1A (ZnONP50), Figure 3.1B (ZnONP100), and Figure 3.1C (ZnOBP). The tabulated data from each figure has been presented in the Appendix: Table A.3.11 (ZnONP50), Table A.3.12 (ZnONP100), and Table A.3.13 (ZnOBP). Statistical tests were conducted to confirm that the solvent, 1% DMSO, did not play a statistically significant role in altering the number of progeny during the assay's complete duration: 24-hours (p=0.8371), 48-hours (p=0.6184), and 72-hours (p=0.4749).

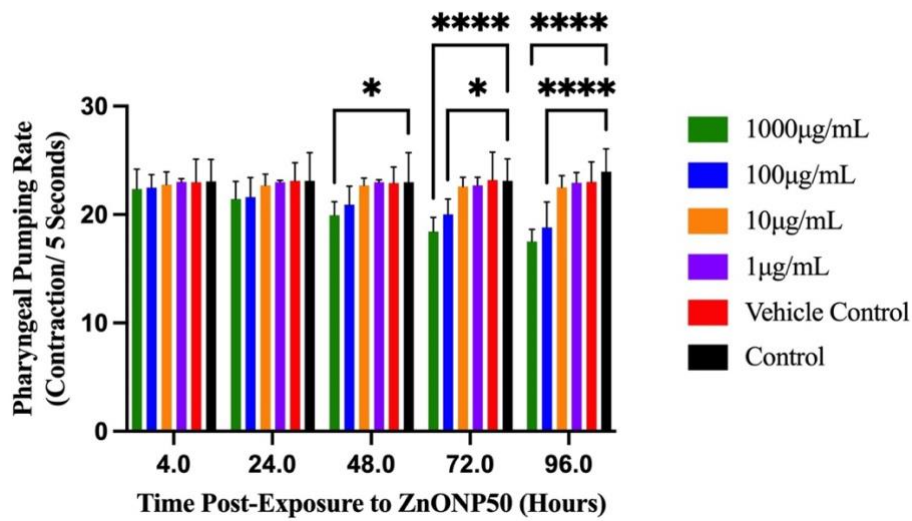
In comparison to their respective control-treatment groups, the total progeny production by N2 over 72 hours reduced by 76.04%, 78.9%, and 13.49% by the ZnONP50, ZnONP100, and ZnOBP-treatment groups respectively. Based on this information, ZnONP100 elicited the strongest toxicological impact on the reproduction capacity of N2, when compared to ZnONP50 and ZnOBP.

Based on the statistical analysis conducted, concentration and duration of exposure of all three sizes of ZnO particles affected the reproduction capacity of N2 significantly ($p < 0.0001$). The duration of exposure accounted for 52.53%, 48.02%, and 99.03% of the variance in results for ZnONP50, ZnONP100, and ZnOBP respectively in Figure 3.1.

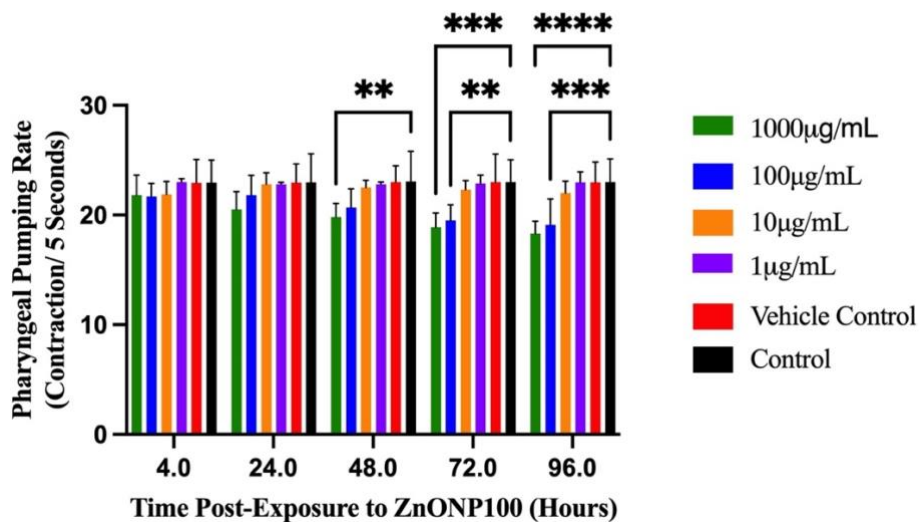
In comparison to the control-treatment group, the number of progeny laid by the ZnONP50-treatment groups (Figure 3.1A) was significantly statistically different ($p < 0.0001$) at the 24-hours (1000 $\mu\text{g/mL}$), 48-hours (1000 $\mu\text{g/mL}$, 100 $\mu\text{g/mL}$, 10 $\mu\text{g/mL}$, and 1 $\mu\text{g/mL}$), and 72-hours (1000 $\mu\text{g/mL}$, 100 $\mu\text{g/mL}$, 10 $\mu\text{g/mL}$, and 1 $\mu\text{g/mL}$)' time points. In terms of the difference in the number progeny laid by the ZnONP100-treatment groups and the control-treatment group (Figure 3.1B), significant statistical difference ($p < 0.0001$) was evident at the 24-hours (1000 $\mu\text{g/mL}$, and 100 $\mu\text{g/mL}$), 48-hours (1000 $\mu\text{g/mL}$, 100 $\mu\text{g/mL}$, 10 $\mu\text{g/mL}$, and 1 $\mu\text{g/mL}$), and 72-hours (1000 $\mu\text{g/mL}$, 100 $\mu\text{g/mL}$, 10 $\mu\text{g/mL}$, and 1 $\mu\text{g/mL}$)' time points. In regards to the ZnOBP-treatment groups (Figure 3.1C), significant statistical difference ($p < 0.0001$) with the control-treatment group was evident at the 48-hours (1000 $\mu\text{g/mL}$, and 10 $\mu\text{g/mL}$), and 72-hours (1000 $\mu\text{g/mL}$, 100 $\mu\text{g/mL}$, 10 $\mu\text{g/mL}$, and 1 $\mu\text{g/mL}$)' time points.

3.3.3 Pharyngeal Pumping Rate of *C. elegans* Treated with Zinc Oxide Particles

A) ZnONP50 Pharyngeal Pumping Rate Assay



B) ZnONP100 Pharyngeal Pumping Rate Assay



C) ZnOBP Pharyngeal Pumping Rate Assay

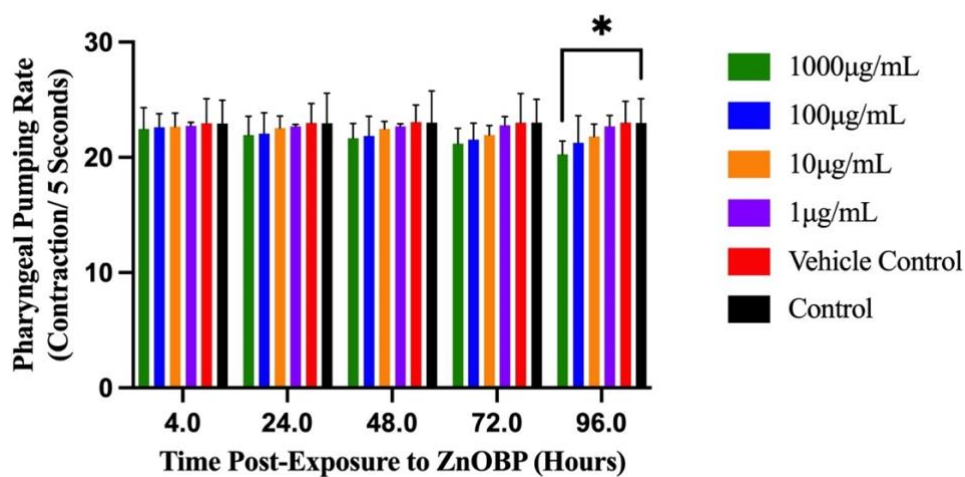


Figure 3.2. Pharyngeal pumping rate of L4 N2 post-exposure to a concentration range of **A)** ZnONP50, **B)** ZnONP100, and **C)** ZnOBP (1, 10, 100, 1000 $\mu\text{g}/\text{mL}$) in combination with *E. coli* OP50 for 4-hours, 24-hours, 48-hours, 72-hours, and 96-hours. DMSO, in combination with *E. coli* OP50, served as the vehicle control. *E. coli* OP50 served as the negative control. Three biological replicates, inclusive of three technical replicates, were performed for each size of ZnO particle. Data is presented as the average pharyngeal pumping rate (contraction per 5 seconds) against time after exposure (hours). Each data point represents the mean \pm SD (n=3). Asterisk (*) indicates statistically significant difference ($p < 0.05$) with the control treatment group. *L4* fourth-larval stage, *N2* Bristol strain N2, *ZnONP50* Zinc oxide nanoparticles <50 nm, *ZnONP100* Zinc oxide nanoparticles <100 nm, *ZnOBP* Zinc oxide bulk particles, *E. coli* OP50 Escherichia coli, *DMSO* dimethyl sulfoxide, *ZnO* zinc oxide.

The average pharyngeal pumping rate of L4 N2 under exposure to a concentration range of various sized ZnO particles have been presented graphically in Figure 3.2A (ZnONP50), Figure 3.2B (ZnONP100), and Figure 3.2C (ZnOBP). The tabulated data from each figure has been presented in the Appendix: Table A.3.14 (ZnONP50), Table A.3.15 (ZnONP100), and Table A.3.16 (ZnOBP). Statistical tests were conducted to confirm that the solvent, 1% DMSO, did not play a statistically significant role in altering the pharyngeal pumping rate during the assay's complete duration: 4-hours ($p=0.3284$), 24-hours ($p=0.1100$), 48-hours ($p=0.5900$), 72-hours ($p=0.7493$), and 96-hours ($p=0.6173$).

In comparison to their respective control-treatment groups, the average pharyngeal pumping rate per L4 N2 deferred the most at the 96-hours' time point and at the exposure concentration of 1000 $\mu\text{g}/\text{mL}$ by 26.96%, 20.50%, and 11.83% for the ZnONP50, ZnONP100, and ZnOBP-treatment groups respectively. Based on this information, ZnONP50 elicited the strongest toxicological impact on the pharyngeal pumping rate of N2 in a size-dependent manner.

Pertaining to the statistical analysis, concentration of all three sizes of ZnO particles affected the pharyngeal pumping rate of N2 significantly ($p < 0.0001$). However, the duration of exposure was not a statistically significant factor as it accounted for 5.33%, 3.58%, and 2.4% of the variance in results for ZnONP50 ($p=0.12$), ZnONP100 ($p=0.0815$), and ZnOBP ($p=0.475$) respectively in Figure 3.2.

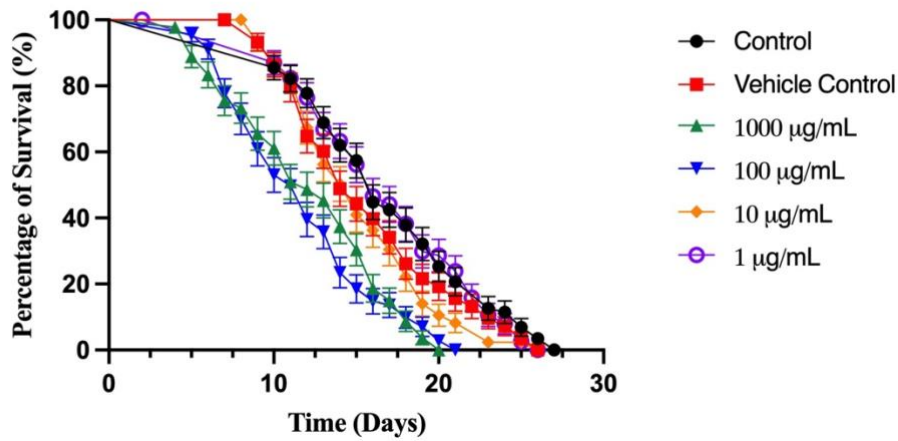
In comparison to the control-treatment group, the average pharyngeal pumping rate of the ZnONP50-treatment groups (Figure 3.2A) was significantly statistically different ($p < 0.0001$) at the 72-hours (1000 $\mu\text{g}/\text{mL}$), and 96-hours (1000 $\mu\text{g}/\text{mL}$, and 100 $\mu\text{g}/\text{mL}$)' time points. In terms of the average pharyngeal pumping rate of the ZnONP100-treatment groups and the control-treatment group (Figure 3.2B), significant statistical difference ($p < 0.0001$) was evident at the 96-hours (1000 $\mu\text{g}/\text{mL}$) time point. In contrast, no significant statistical

difference ($p < 0.0001$) was evident between the different ZnOBP-treatment groups and the control treatment group (Figure 3.2C) at any time point.

3.3.4 Lifespan of *C. elegans* Treated with Zinc Oxide Particles

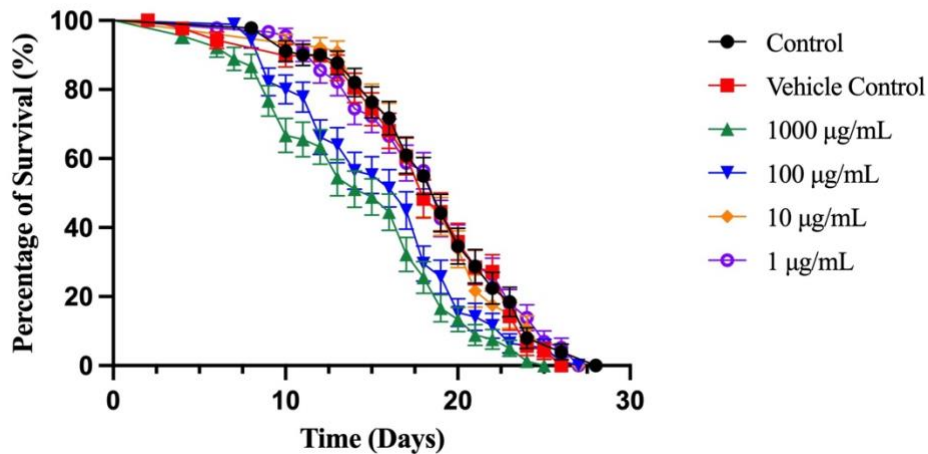
Survival Curves of *Caenorhabditis elegans* Post ZnONP50 Treatment

A)



Survival Curves of *Caenorhabditis elegans* Post ZnONP100 Treatment

B)



Survival Curves of *Caenorhabditis elegans* Post ZnOBP Treatment

C)

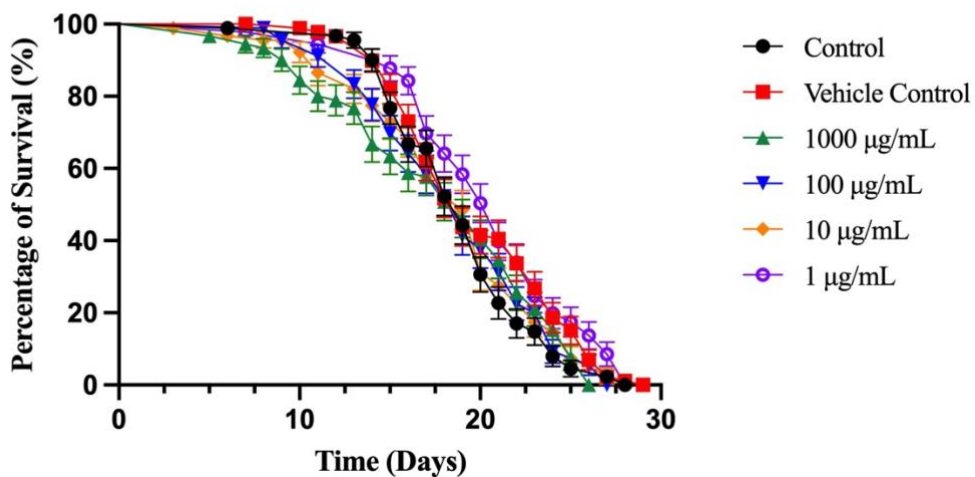


Figure 3.3. Lifespan of L4 N2 post-exposure to a concentration range of **A) ZnONP50, B) ZnONP100, and C) ZnOBP** (1, 10, 100, 1000 µg/mL) in combination with *E. coli* OP50. Survival was recorded from Day 1 of L4 till death. DMSO, in combination with *E. coli* OP50, served as the vehicle control. *E. coli* OP50 served as the negative control. Three biological replicates, inclusive of three technical replicates, were performed for each type of ZnO particle. Data is presented as the percentage of survival (%) against time after exposure (days). Each data point represents the mean ± SD (n=3). *L4* fourth-larval stage, *N2* Bristol strain N2, *ZnONP50* Zinc oxide nanoparticles <50 nm, *ZnONP100* Zinc oxide nanoparticles <100 nm, *ZnOBP* Zinc oxide bulk particles, *E. coli* OP50 Escherichia coli, *DMSO* dimethyl sulfoxide, *ZnO* zinc oxide.

The lifespan of 30 L4 N2 under exposure to a concentration range of various sized ZnO particles have been presented graphically in Figure 3.3A (ZnONP50), Figure 3.3B (ZnONP100), and Figure 3.3C (ZnOBP). The tabulated data from each figure has been presented in the Appendix: Table A.3.17 (ZnONP50), Table A.3.18 (ZnONP100), and Table A.3.19 (ZnOBP). Statistical tests were conducted to confirm that the solvent, 1% DMSO, did not play a statistically significant role in altering the lifespan of N2 under all three sizes of ZnO particle treatment: $p=0.0733$ (ZnONP50), $p=0.5852$ (ZnONP100), and $p=0.0939$ (ZnOBP).

Based on the survival curves of ZnONP50-treatment groups (Figure 3.3A), the 1000 µg/mL, 100 µg/mL, 10 µg/mL, and 1 µg/mL treatment groups demonstrated a left-shifted curve compared to the control-treatment group; the mean survival rate decreased by 28.55% ($p<0.0001$), 31.25% ($p<0.0001$), 10.44% ($p=0.0058$), and 4.98% respectively. In terms of the survival curves of ZnONP100-treatment groups (Figure 3.3B), the 1000 µg/mL, 100 µg/mL, 10 µg/mL, and 1 µg/mL treatment groups demonstrated a left-shifted curve compared to the control-treatment group; the mean survival rate decreased by 21.46% ($p<0.0001$), 16.38% ($p=0.0011$), 2.24%, and 0.27% respectively. In reference to the survival curves of ZnOBP-treatment groups (Figure 3.3C), the 1000 µg/mL, 100 µg/mL, and 10 µg/mL treatment groups demonstrated a left-shifted curve compared to the control-treatment group; the mean survival rate decreased by 7.81%, 1.77%, and 4.84% respectively. In contrast, the 1 µg/mL ZnOBP-treatment group demonstrated a right-shifted survival curve compared to the control-treatment group, with the mean-survival rate increasing by 6.7% ($p=0.0057$). Based on this information, ZnONP50 elicited the strongest toxicological impact on the lifespan of N2 in a size-dependent manner.

3.3.5 Primer Design

Table 3.3. Product size, NCBI reference sequence, primer sequence, annealing temperature, guanine-cytosine percentage, self-complementary score, and self-3' complementary score of the chosen primer pairs for the target genes' (*cep-1* and *pmk-1*) and the reference gene's (*tba-1*) amplification by PCR. PCR polymerase chain reaction.

Gene Symbol	NCBI Reference Sequence	Sequence (5'-3')	Annealing Temperature (°C)	Guanine-Cytosine Content (%)	SC Score	S3'C Score
<i>cep-1</i> (177bp)	NM_001026307.8	F: ATTCGCAGGACATCGGCGTA	62.01	55	3	2
		R: CGCCATTGCCAGTATTCCG	61.79	60	4	2
<i>pmk-1</i> (258bp)	NM_068964.7	F: TGCTGAATGTACTCGCTCGG	60.18	55	4	1
		R: TGGTCATCGTTGAGTCGCTG	60.39	55	6	1
<i>tba-1</i> (244bp)	NM_001392888.1	F: TATGCTCTCCAACACCACCG	59.75	55	2	2
		R: GCAGGCGGCACGAGTTTA	60.74	61.11	3	2

bp – Base Pairs

F – Forward Primer

R – Reverse Primer

SC – Self-complementary

S3'C – Self-3' complementary

The genes included in this toxicological study were *cep-1*, *pmk-1*, and *tba-1*. The selected primer pair sequences for each gene and the respective characteristics have been tabulated above in Table 3.3.

3.3.6 Extracted Ribonucleic Acid (RNA)'s Concentration and Purity

RNA extraction's results were validated using NanoDrop™ One Microvolume UV-Vis Spectrophotometer. The results of the extracted RNA from ZnONP50-treated N2, ZnONP100-treated N2, ZnOBP-treated N2, and non-treated (control) N2, have been presented below in Table 3.4.

Table 3.4. Concentration and purity results of extracted RNA from N2. RNA ribonucleic acid, N2 Bristol strain N2.

Treatment	Concentration	A260/A280	A260/A230
ZnONP50	1002.8 ng/μL	2.11	2.22
ZnONP100	1047.7 ng/μL	2.10	2.39
ZnOBP	1486.7 ng/μL	2.16	2.11
Control	1634.2 ng/μL	2.14	2.17

As the concentration of the ZnONP50-treatment's extracted RNA was the closest to the 1000 ng/ μ L benchmark set, the other samples' concentrations were adjusted to 1002 ng/ μ L during cDNA synthesis to ensure that the DNA concentration was standardised. As the A260/A280 and the A260/A230 ratios of all treatment groups' extracted RNA fell within the acceptable ranges, all four sets of RNA were deemed suitable to use for all future downstream purposes.

3.3.7 Agarose Gel Analysis of N2 Genes

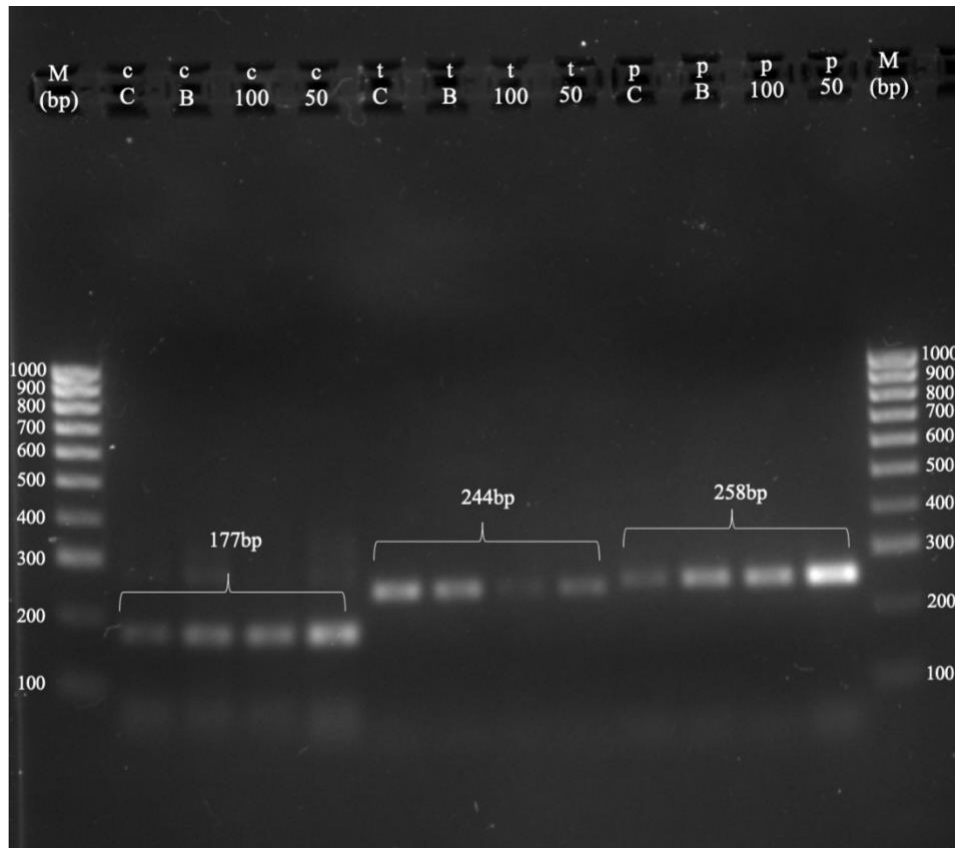


Figure 3.4. Agarose gel electrophoresis (2% agarose) of PCR amplified DNA samples (*cep-1*, *tba-1*, *pmk-1*) of L4 N2 post-exposure to ZnO particles (100 μ g/mL) for 72 hours. Both lanes labelled as 'M' contain molecular weight markers ranging from 100 bp to 1000 bp. Lanes c-C, c-B, c-100, and c-50 contain *cep-1* PCR products from the four different treatment groups: control, ZnOBP, ZnONP100, and ZnONP50. Lanes t-C, t-B, t-100, and t-50 *tba-1* PCR products from the four different treatment groups: control, ZnOBP, ZnONP100, and ZnONP50. p-C, p-B, p-100, and p-50 contain *pmk-1* PCR products from the four different treatment groups: control, ZnOBP, ZnONP100, and ZnONP50. Electrophoresis was performed using 1X TAE buffer at 100 V and 400 mA for 35 minutes. Gel was stained with SYBR Safe DNA Gel Stain and visualized using Bio-Rad Gel Doc XR+ Imaging System. Expected band sizes for *cep-1*, *tba-1*, and *pmk-1* were 177 bp, 244 bp, and 258 bp respectively. PCR polymerase chain reaction, DNA deoxyribonucleic acid, L4 fourth larval stage, N2 Bristol strain N2, ZnO zinc oxide, bp base pairs, ZnOBP Zinc oxide bulk particles, ZnONP100 Zinc oxide nanoparticles <100 nm, ZnONP50 Zinc oxide nanoparticles <50 nm, TAE Tris-acetate-EDTA, bp base pairs.

Agarose gel electrophoresis was utilised to separate, identify, and analyse DNA fragments of ZnO particle-treatment groups and the non-treated control treatment group. Evident differences in the intensity of the DNA bands of each treatment group indicates a variance in the expression of the respective gene post-chronic exposure to various sized ZnO particles for 72 hours in Figure 3.4, which is a representative gel of the triplicates performed for each gene. In terms of the expression of the *cep-1* and *pmk-1* genes, the ZnONP50-treatment group N2 yielded the band with the highest intensity, indicating an increased expression of the genes in comparison to the control-treatment group which generated the faintest band for the target genes. The visualised interpretation of gene expression variance under each ZnO particle treatment group was validated through densitometric analysis, during which the 500bp standard of the DNA ladder was utilised as the internal standard to normalize the gel-to-gel variance. The data is presented in the Appendix for *cep-1*, *pmk-1*, and *tba-1* gene under Table A.3.20, A.3.21, and A.3.22 respectively.

To evaluate the variance in expression of the *cep-1* and *pmk-1* genes under different ZnO particle treatments and to determine whether the gene expression variance is size dependent, the relative fold change of each DNA band was determined as per Section 3.2.17.3. The expression of the *cep-1* gene under ZnONP50, ZnONP100, and ZnOBP treatment was upregulated by 8.33, 6.66, and 3.51-folds respectively. The expression of the *pmk-1* gene under ZnONP50, ZnONP100, and ZnOBP treatment was upregulated by 13.55, 11.61, and 5.26-folds respectively. The variance of the *cep-1* and *pmk-1* genes' expression is illustrated in Figure 3.5.

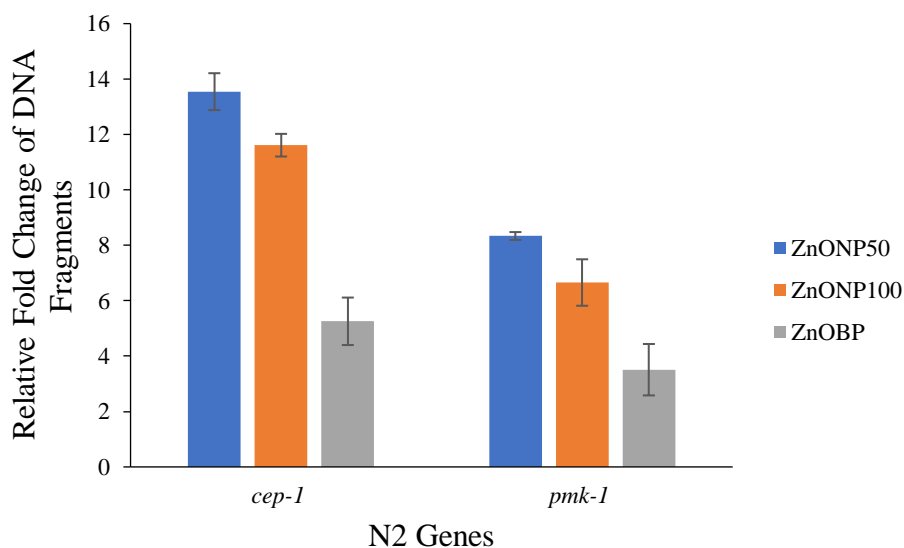


Figure 3.5. Relative fold change of ZnO particle-treated *cep-1* and *pmk-1* DNA bands of L4 N2 in comparison to their respective untreated-control DNA bands. ZnO zinc oxide, L4 fourth larval stage, N2 Bristol strain N2, ZnONP50 Zinc oxide nanoparticles <50 nm, ZnONP100 Zinc oxide nanoparticles <100 nm, ZnOBP Zinc oxide bulk particles.

With the increased use of ZnONPs and its production, the risk of the NPs entering the ecosystem increases significantly. ZnONPs can be introduced into the terrestrial environment through various pathways including waste incineration residues, landfill leachate, and wastewater treatment (Baun et al., 2017). ZnONPs can also be introduced into the soil directly through the use of herbicides and pesticide (Cochran et al., 2023). Through a modelled estimate conducted in 2009, ZnONPs environmental concentration ranges between 0.25 to 0.66 $\mu\text{g}/\text{kg}$; this concentration is expected to have increased significantly over the past decade (Gottschalk et al., 2009). Upon entering the environment, the physicochemical properties and behaviour are influenced by various factors, including the soil. The soil serves as a drainage system for environmental pollutants, and also as a source of nutrients for surrounding plants and terrestrial organisms (García-Gómez et al., 2018). Terrestrial animals, such as *C. elegans*, are vulnerable to the toxicological effects of ZnONPs as they have direct contact with the contaminated soil, which serves as their food source (Zečić et al., 2019).

As the movement of ZnO particles in the soil are influenced by the physicochemical properties, specifically the size, it was hypothesised that a size-dependent trend would be evident while investigating the toxicological property of ZnO particles on the reproduction capacity, pharyngeal pumping rate, and lifespan of N2; the smallest sized ZnO particle investigated is expected to yield the greatest toxicity owing to its enhanced mobility and uptake across biological membranes (Gupta et al., 2015; Umar et al., 2023).

Reproduction capacity of L4 N2 was investigated post-exposure to a concentration range of ZnONP50, ZnONP100, and ZnOBP, and it was defined as the total number of viable offspring laid at the 24-hours, 48-hours, and 72-hours' time points. The strongest toxicological effect of the ZnO particles was exhibited at the highest concentration of 1000 $\mu\text{g}/\text{mL}$ by ZnONP100, ZnONP50, and ZnOBP in a descending manner as per Table A.3.12, A.3.11, and A.3.13 respectively in the Appendix. The significant reduction in the reproduction capacity of N2 in the present study was corroborated by previous studies which yielded similar results; ZnONPs yielded the stronger toxicological effect towards the reproduction capacity compared to ZnOBP (Gupta et al., 2015; Khare et al., 2015; Ma et al., 2009; Wang et al., 2009). However, in the size-dependent ZnONPs toxicological study conducted by Gupta and Khare, the smallest size ZnONPs, 21 nm and 50 nm respectively, yielded a larger reduction in progeny compared to the larger sized ZnONPs investigated (Gupta et al., 2015; Khare et al., 2015).

The pharyngeal pumping rate of L4 N2 was examined post-exposure to a concentration range of ZnONP50, ZnONP100, and ZnOBP, and it was defined as the rhythmic contractions

of the pharynx for 5 seconds at the 4-hours, 24-hours, 48-hours, 72-hours, and 96-hours' time points. The strongest toxicological effect of the ZnO particles was exhibited at the highest concentration of 1000 µg/mL by ZnONP50, ZnONP100, and ZnOBP in a descending manner as per Table A.3.14, A.3.15, and A.3.16 in the Appendix respectively. The significant reduction in the pharyngeal pumping rate of N2 was validated by previous studies using various types of metal-oxide NPs which yielded similar results, with NPs eliciting a stronger toxicological effect compared to their respective BPs (Hu et al., 2018; Mashock et al., 2016; Yang et al., 2014). However, there is lack of studies investigating the size-dependent effect of various sized ZnONPs.

The lifespan of L4 N2 was observed post-exposure to a concentration range of ZnONP50, ZnONP100, and ZnOBP. Based on the survival curves generated, ZnONP50 exhibited the strongest statistically significant toxicological effects towards the lifespan of N2, followed by ZnONP100, and ZnOBP in a descending manner as per Table A.3.17, A.3.18, and A.3.19 in the Appendix respectively. The significant reduction in the average lifespan of N2 in the present study was validated by similar patterns observed in previous projects utilizing different types of metal-oxide NPs; the smallest sized NPs elicited a stronger toxicological effect in comparison to the larger sized NPs and their respective BPs (Gonzalez-Moragas et al., 2017; Walczynska et al., 2018). However, in a nanotoxicology study conducted by Piechulek and Mikecz using a similar concentration range of ZnONPs, they concluded that nano-sized ZnO did not have a significant effect on the longevity of N2 (Piechulek & von Mikecz, 2018).

Several plausible underlying mechanisms of ZnONPs-induced toxicity have been suggested, however, ROS production and the subsequent oxidative stress is the best understood mechanism accountable for ZnONPs-induced toxicity in animal models (Chong et al., 2021; Rahman et al., 2022). The general process of oxidative stress generation is as follows: generation of ROS on ZnONPs' surface, dissolution, and release of Zn²⁺ ions from ZnONPs, and physical interaction between the biological molecules within the organism and ZnONPs (Saliani et al., 2016). Oxygen containing radicals, ROS, are produced by the mitochondria as a metabolic byproduct. They serve as signaling molecules in many essential cellular activities (Liu et al., 2018). Conversely, increased levels of ROS are considered the main promoter of inducing oxidative stress within cells, tissues, and organs (Schieber & Chandel, 2014). ZnONPs exposure resulting in the unwarranted production of ROS may result in oxidative damage of the DNA. HO• radicals are extremely reactive with the deoxyribose backbone and the bases of DNA, which triggers the fracturing of the DNA strands, oxidation of nucleotides,

and the formation of DNA adduct, which leads to carcinogenicity and mutagenicity (Martins et al., 2021). DNA damage may induce apoptosis by activating the p53 pathway, which plausibly leads to tissue damage (Abass et al., 2017; Ma & Yang, 2016). ZnONPs are also able to damage organs by commencing oxidative stress mediated inflammation. ZnONPs induced oxidative stress and inflammation work conjointly to emphasize the progressive damage in the tissues and/or the organs (Pizzino et al., 2017; Sharifi-Rad et al., 2020). ZnONPs are able to induce inflammation in multiple organs of animal models through the MAPK signal transduction pathway; inflammatory cells are recruited, and mediators and pro-inflammatory cytokines are triggered (Qiao et al., 2018; Saptarshi et al., 2015). The *cep-1* and *pmk-1* genes, which are vital components of the p53 and MAPK pathways, were chosen as the biomarkers to investigate the potential role of oxidative stress in ZnONP's exhibited toxicity.

The gene expression study conducted revealed a variance in the expression of the *cep-1* and *pmk-1* genes upon exposure to ZnONP50, ZnONP100, and ZnOBP as seen in Figure 3.5. Compared to the control-treatment group, *cep-1* and *pmk-1*'s expression was upregulated, with the ZnONP50-treatment group exhibiting the largest increment by 13.55 and 8.33 folds respectively as per Figure 3.5. Based on this information, it can be concluded that the variation in the expression of the *cep-1* and *pmk-1* genes upon ZnO particle exposure is size-dependent.

In a study conducted by O'Donnell and her team, N2 were exposed to various concentrations of ZnONPs. The strain was used to investigate the expression of genes involved in the apoptosis pathway, including the *cep-1* gene. The *cep-1* gene, which is a p53 ortholog, was upregulated in the gene expression assay. Additionally, the *cep-1* loss of function mutant was exposed to ZnONPs. However, no significant increase in apoptosis was observed, unlike N2 (O'Donnell et al., 2017). Thus, it can be concluded that the reduced progeny production observed by ZnONP50 and ZnONP100-treatment groups in this research project is plausibly *cep-1/p53* dependent. Janus-faced *cep-1/p53* defines the duality of the transcription factor's role in the cell. It is able to act as a tumor suppressor to prevent the development of cancer cells through the induction of the cell cycle arrest and apoptosis. Alternatively, it is able to promote cellular senescence. This duality of *cep-1/p53* is dependent on its ability to sense and react to different levels of oxidative stress signals within the cell. In a mild oxidative stress affected environment with repairable damage, *cep-1/p53* is able to elicit its protective response to repair and/or prevent further damage towards the cell and the organism, which results in cell survival, growth, and increased longevity of the organism. Alternatively, in a severe oxidative stress affected environment with irreversible damage, *cep-1/p53* is able to elicit its suppressive

response to eliminate the irreparable cells, which results in apoptosis, cell cycle arrest, and decreased longevity of the organism. Based on this characteristic, *cep-1/p53* sensed severe oxidative stress within the ZnO particle treated N2, which induced its suppressive response and resulted in cell cycle arrest, apoptosis of germ cells, and decreased the life span of the nematodes (Hao et al., 2020; Rotblat et al., 2012; Toma-Jonik et al., 2019; Ventura et al., 2009).

MAPKs are known to serve as transducers of extracellular stimuli such as stress response. The *C. elegans* ortholog of p38 MAPK, PMK-1, has a vital role in the organism's response against oxidative stress and its innate immunity. In a study conducted by Lim and his team, an increased expression of the *pmk-1* gene and PMK-1 protein was evident post-exposure to AgNPs, which alludes to the nematode's defense mechanism towards NPs exposure. During bacterial infections, *C. elegans* are able to generate ROS as a host-defense mechanism, which triggers the stress-response mechanism (Chávez et al., 2007, 2009). As ROS expression increased in AgNPs-exposed nematodes, it was suggested that N2 produced ROS as an immune-response-like reactions to the NPs exposure (Lim et al., 2012). As innate immunity is elicited through PMK-1/p38 MAPK, it is plausible that *pmk-1* is involved in ROS production in N2 post-exposure to ZnO particles in this study.

The primary quantitative method to study variance in gene expression is real-time quantitative PCR. However, due to budgetary and time constraints, conventional PCR was performed. Nevertheless, to validate and normalize the results retrieved from the conventional PCR, a reference gene was employed as an internal control (Huggett et al., 2005; Radonić et al., 2004; Zhao et al., 2014). Zhang and their team evaluated several housekeeping genes in terms of their stability upon exposure to the metal oxide NP, CuONPs. The housekeeping genes, including *tba-1*, were appraised in terms of their stability of expression using four algorithms: geNorm, NormFinder, BestKeeper, and the Comparative Δ Ct method (Andersen et al., 2004; Pfaffl et al., 2004; Silver et al., 2006; Vandesompele et al., 2002). Based on the results retrieved, *tba-1* was identified as a reliable reference gene to be used in NPs-based toxicological studies (Zhang et al., 2012). However, as per the gene expression study conducted in this research project, its expression fluctuated slightly upon exposure to ZnO particles when compared to the control-treatment group. Thus, further evaluations are needed regarding the use of *tba-1* as a reference gene in ZnONPs based studies.

This study has a primary limitation, and it should be addressed in future studies to improve the reproducibility of the results and to improve the understanding of the ecotoxicological properties of ZnO particles on *C. elegans*. As ingestion of NPs is the most common route of exposure for *C. elegans*, optical imaging is a suitable technique to confirm

the ingestion of the desired concentration of NPs is conducted prior to data sets being collected (Li et al., 2021). As *C. elegans* have a transparent body, it allows easy visualization of the NPs tagged with fluorescent proteins using a confocal microscope. Additionally, this would provide supplementary information regarding the biodistribution of the various sizes of ZnO particles in the nematode and structural changes of vital organs associated with the investigated parameters (Wang et al., 2021).

It is worth noting that *C. elegans* are used as an ecotoxicity model, and as a non-mammalian *in vivo* model to investigate human NP-toxicity screening. As the nematode and humans share conserved molecular pathways and genes which are involved in oxidative stress response, apoptosis, and DNA damage repair, it is possible to extrapolate *C. elegans*' toxicity study results to humans (Kim et al., 2018; Lai et al., 2000). However, to identify the precise mechanism of size-dependent ZnO particles toxicity in humans, comparative toxicity studies using various biological models may be required. As the above-mentioned pathways have several key players, further gene expression studies of orthologous genes will present a clearer picture of ZnO particles' induced toxicity and its mechanism. Additionally, as ROS quantification is an essential tool to decipher the role of oxidative stress in the pathological and physiological processes, it is vital for future studies to do so. The use of fluorogenic dyes, such as MitoSOX Green and MitoSOX Red, may be employed to quantify the superoxide production from mitochondria in live cells (Kauffman et al., 2016).

3.4 Conclusion

This chapter reported that ZnONP50 was able to exert greater toxicological effect towards the lifespan of N2 nematodes and significantly increase the expression of the nematode's *cep-1* and *pmk-1* genes compared to the larger ZnO particles. ZnONP100 demonstrated the highest toxicity towards the nematode's reproductive capacity and pharyngeal pumping rate, while ZnOBP displayed the lowest toxicity. Further studies using different models is required to validate and understand the mechanism of ZnO particles' size-dependent toxicological effects.

Chapter 4: Inhibitory Effects of Various Sized Zinc Oxide Particles on Human CYP isozymes

4.1 Background

Several metal oxide NPs, including ZnONPs, have demonstrated significant inhibitory effects towards the drug metabolising CYP isozymes through various modes of inhibition as reported under Section 1.3.4. Inhibition of these isozymes have detrimental clinical consequences due to decreased clearance and increased bioavailability of the co-administered drug (Ahmmed et al., 2015; Bahadur et al., 2016; Lim et al., 2022; Yim et al., 2020).

To evaluate the inhibition potential, the kit utilises Vivid® Substrates and CYP450 BALCUSOMES® Plus Reagents, which are microsomes composed of insect cells expressing a single CYP isozyme, human CYP reductase, and human cytochrome b₅. As the CYP450 BALCUSOMES® Plus Reagents express a singular CYP isozyme, it prevents the metabolism of Vivid® Substrates by irrelevant CYP isozymes (Ozgenic, n.d.). Vivid® Substrates have one or two probable metabolic sites, illustrated in Figure 4.1, and are metabolised into highly fluorometric products in an aqueous solution. The metabolites of the fluorogenic Vivid® Substrates utilised in this study are listed in Table 4.1.

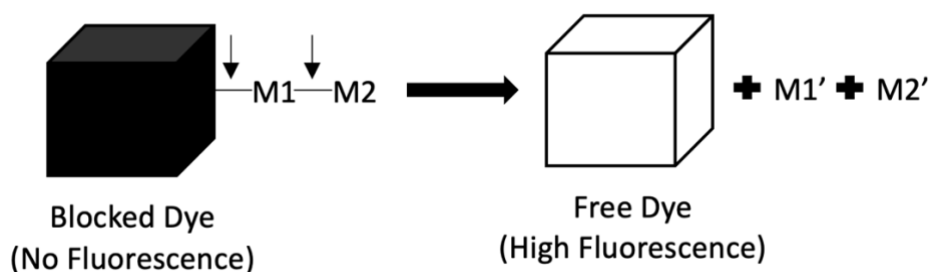


Figure 4.1. Schematic representation of the metabolism of Vivid® Substrates into fluorescent metabolites by CYP450 BALCUSOMES® Plus Reagents. M1 and M2 denote metabolic sites. M1' and M2' denote fluorometric metabolites (Ozgenic, n.d.).

Table 4.1. Vivid® Substrates and their corresponding metabolites (Ozgenç, n.d.; Wu et al., 2021).

Vivid® Substrates*	Metabolite
EOMCC	3-cyano-hydroxycoumarin
BOMCC	3-cyano-hydroxycoumarin
CC	3-hydroxycoumarin
DBOMF	Fluorescein
MOBFC	7-hydroxy-4-(trifluoromethyl)coumarin

*EOMCC: 7-ethoxy-methoxy-3-cyano-coumarin

BOMCC: 7-benzyloxymethoxy-3-cyano-coumarin

CC: 3-cyano-coumarin

DBOMF: di-(benzyl-O-methyl)-fluorescein

MOBFC: 7-P-methoxy-benzyloxy-4-trifluorocoumarin

This chapter of the research project presents the evaluation of the size-dependent inhibitory effects of ZnONP50, ZnONP100, and ZnOBP on primary drug-metabolizing CYP isozymes (CYP1A2, CYP2A6, CYP2B6, CYP2C8, CYP2E1, CYP2J2, and CYP3A5) using Vivid® CYP450 Screening Kits.

4.2 Methodology

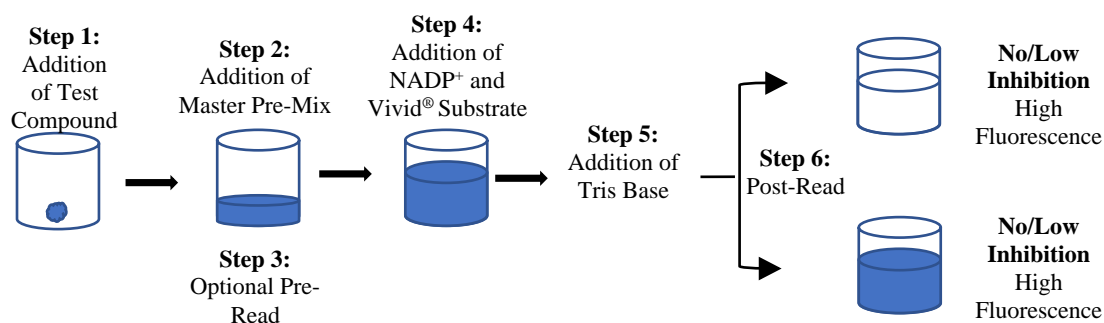


Figure 4.2. Schematic representation of the six steps of a Vivid® CYP450 assay conducted in the endpoint mode (Ozgen, n.d.).

The size-dependent inhibitory potential of ZnONP50, ZnONP100, and ZnOBP on the enzymatic activity of CYP1A2, CYP2A6, CYP2B6, CYP2C8, CYP2E1, CYP2J2, and CYP3A5 was investigated using Vivid® CYP450 Screening Kits in the endpoint mode comprising of six steps as presented in Figure 4.2. Incubation with a total volume of 100 μ L per well was carried out in Black Costar® 96-well plates at a constant temperature of 27°C, as the kit performs optimally between 25°C to 37°C (Ozgen, n.d.). Master Pre-Mix was a mixture of CYP450 BALCUSOMES® Plus Reagent, Vivid® Regeneration System, and Vivid® CYP450 Reaction Buffer. Vivid® Regeneration System contains 30 U/mL of glucose-6-phosphate dehydrogenase and 333mM of glucose-6-phosphate in 100 mM potassium phosphate (pH 8.0). The combination allowed Vivid® Regeneration System to convert the nicotinamide adenine dinucleotide phosphate (NADP⁺) into NADPH, subsequently allowing the reaction to commence. Measurement of the background fluorescence was taken 30-minutes post addition of ZnO particle to the Master Pre-Mix as the ‘pre-read.’ The addition of NADP⁺ and the respective Vivid® Substrate initiated the enzymatic reaction. Once initiated, the reaction plate was incubated for a pre-determined time period to obtain optimal fluorometric readings. Lastly 50 μ L of 0.5 M Tris-base was added to terminate the enzymatic reaction, and the final fluorescent readings were taken. Fluorometric readings were obtained using the Thermo Scientific Varioskan Flash Plate Reader using the settings stated in Table 4.2. ZnO particle’s inhibition potential was determined by their ability to inhibit the formation of Vivid® Substrate’s metabolite, indicated by the reduction of fluorometric metabolite formation (Ozgen, n.d.). The final concentration of all reagents required for respective CYP450 isozyme assays are summarised in Table 4.3.

Table 4.2. Varioskan Flash Plate Reader's settings based on each CYP isozymes and their respective Vivid® Fluorescent Standards (Ozgen, n.d.). CYP cytochrome P450.

	Vivid® Fluorescent Standards		
	Blue	Green	Cyan
CYP Isozyme	1A2, 2A6, 2B6, 2E1, 3A5	2C8	2J2
Excitation Wavelength (nm)	415	490	415
Emission Wavelength (nm)	460	520	520
Bandwidth	20	12	20

Table 4.3. Final concentration of reagents for each CYP isozyme reaction. CYP cytochrome P450.

CYP Isozyme	CYP Isozyme (nM)	Vivid® CYP450 Reaction Buffer (nM)	Vivid® Substrate (µM)*	Vivid® NADP⁺ (µM)
1A2	3	Buffer I – 100	EOMCC - 5	30
2A6	10	0.5X Buffer II - 25	CC - 10	30
2B6	3	Buffer I - 100	BOMCC - 5	30
2C8	1	Buffer II - 50	DBOMF - 5	100
2E1	10	Buffer III - 200	EOMCC - 20	30
2J2	3	Buffer II - 50	MOBFC - 5	30
3A5	10	Buffer I – 100	BOMCC - 5	30

*EOMCC: 7-ethoxy-methoxy-3-cyano-coumarin

BOMCC: 7-benzyloxymethoxy-3-cyano-coumarin

CC: 3-cyano-coumarin

DBOMF: di-(benzyl-O-methyl)-fluorescein

MOBFC: 7-P-methoxy-benzyloxy-4-trifluoro-coumarin

4.2.1 Materials and Reagents

Vivid® CYP1A2, CYP2A6, CYP2B6, CYP2C8, CYP2E1, CYP2J2 and CYP3A5 screening kits were acquired from Life Technologies™ (Carlsbad, CA, USA). Respective positive inhibitor of each isozyme and Black Costar® 96-well plates were purchased from Thermo Fisher Scientific® (Pittsburgh, PA, USA). Analytical grade acetonitrile was purchased from Fisher Scientific (Loughborough, Leicestershire, UK). Tris-base powder was obtained from Amresco® LLC (Solon, Ohio, USA).

4.2.2 Establishment of Standard Curves

Fluorometric metabolites' formation in subsequent assays were quantified using equations from established standard curves using respective metabolite standards (Brooks et al., 2012). The manufacturer's protocol was followed, with the exception of alterations to the concentration level of Vivid® Fluorescent Standards (Ozgen, n.d.). Vivid® Fluorescent Standards underwent two-time serial dilution with the respective Vivid® CYP450 Reaction Buffer to attain a concentration range: 500, 250, 125, 62.5, 31.25, 15.6, 7.81, 3.91, and 0 nM. The fluorometric reading of the metabolites produced by Vivid® Blue Standard (3-cyano-7-hydroxycoumarin), Vivid® Green Standard (fluorescein) and Vivid® Cyan Standard (7-hydroxy-4-tri-fluoromethylcoumarin) were taken without an incubation period. The bandwidth, excitation wavelength, and emission wavelength of each reading were set as per Table 4.2. The assays were performed as triplicates, and the required equations were derived once the respective R² value was above 0.99. The results were plotted on a graph as fluorescent reading (FRU) against the range of the Vivid® Standard's concentration.

4.2.3 Establishment of Time Curves

To ascertain the time period required to obtain the optimal fluorometric reading for each CYP isozyme, time curves were established. Each reaction-well contained 90 µL of Master Pre-Mix based on Table 4.3. The final well, the 'background' well, contained 90 µL of Vivid® CYP450 Reaction Buffer solely. To attain 'pre-read' values, the reaction was incubated for 30 minutes. Afterwards, the addition of 10 µL mixture of Vivid® Substrate, Vivid® CYP450 Reaction Buffer and Vivid® NADP⁺, based on Table 4.3, initiated the enzymatic reaction. The reaction plate was incubated and fluorometric readings were recorded at 5, 10, 20, 30, 60, 90, 120, 180, and 240 minutes time-points. The assays were performed as triplicates. The results were plotted on a graph as FRU against the range of incubation time-points (minutes). Optimal incubation period for each CYP isozyme was determined post-linear phase, as it indicated substrate depletion (Pant, 2022).

4.2.4 Inhibition of CYP Isozymes by Positive Inhibitors

The inhibition of CYP isozymes by their positive inhibitors were evaluated as per Table 4.4; initial 100 mM stocks of each positive inhibitor was prepared using DMSO and further dilution to required concentrations was conducted using water. DMSO's concentration was kept to a minimum to avoid unwanted inhibition of the isozymes. 50 μ L of Master Pre-Mix was prepared based on Table 4.3, and was combined with 40 μ L of Vivid[®] CYP450 Reaction Buffer and the respective positive inhibitor. This mixture was dispensed into the first reaction-well. The subsequent wells contained the same mixture, however, the test compound solution was replaced with the positive inhibitor's solvent. The final well, which served as the 'background' well, contained a solution of the positive inhibitor's solvent and Vivid[®] CYP450 Reaction Buffer. To attain 'pre-read' values, the reaction plate was incubated for 30 minutes. Subsequently, 10 μ L of substrate mix containing Vivid[®] Substrate, Vivid[®] NADP⁺, and Vivid[®] CYP450 Reaction Buffer was added to all reaction wells. The reaction plate was incubated for the pre-determined time period, prior to the addition of 50 μ L of 0.5 M Tris-base per reaction well. The assays were performed in triplicates.

Table 4.4. Concentration range of each CYP isozyme's positive inhibitor. *CYP* cytochrome P450.

CYP Isozyme	Positive Inhibitor	Tested Concentration Range (nM)
CYP1A2	α -naphthoflavone	50, 25, 12.5, 6.25, 3.13, 1.56, 0
CYP2A6	Tranlycypromine	100, 50, 25, 12.5, 6.25, 3.13, 1.56, 0
CYP2B6	Miconazole	200, 100, 50, 25, 12.5, 6.25, 3.13, 1.56, 0
CYP2C8	Montelukast	10, 5, 2.5, 1.25, 0.63, 0.31, 0
CYP2E1	Tranlycypromine	10, 5, 2.5, 1.25, 0.63, 0.31, 0
CYP2J2	Terfenadine	100, 50, 25, 12.5, 6.25, 3.13, 1.56, 0
CYP3A5	Ketoconazole	200, 100, 50, 25, 12.5, 6.25, 3.13, 0

4.2.5 Preparation of ZnO Particles

ZnONP50, ZnONP100, and ZnOBP were prepared freshly on a per-assay basis to avoid contamination and aggregation of the bulk or nano powder. 5 mg of the respective ZnO particle was added to 500 μ L of pure DMSO to attain a starting concentration of 10 mg/mL. The solution was then sonicated for 30 minutes at 30°C to ensure highest dispersion stability.

4.2.6 Determination of Half Maximal Inhibitory Concentration (IC₅₀)

To evaluate a test compound's inhibitory potential towards a biological and/or biochemical function, IC₅₀ is derived. It is a quantitative measurement (Brooks et al., 2012).

Thus, to determine the inhibitory potential of ZnONP50, ZnONP100, and ZnOBP on the pre-chosen CYP isozymes, IC₅₀ assays were performed. Protocol of IC₅₀ assays was similar to that of positive inhibitor assays, with the exception of the positive inhibitor being replaced with ZnO particles. Two-time serial dilution of ZnO particles were carried out to attain final concentrations of 100, 50, 25, 12.5, 6.25, and 3.13 µg/mL. The assays were performed as triplicates.

4.2.7 Time-Dependent Inhibition (TDI) Assay

To determine whether a test compound possesses the potential of mechanical-based inhibitory effects and if it can be categorised as an irreversible inhibitor, time-dependent inhibition (TDI) assays are conducted (Riley et al., 2007). The assay is comprised of two experimental conditions: 30-minutes with NADPH and 30-minutes without NADPH. For the first experimental condition, Vivid® NADP⁺ was added to the previously described Master Pre-Mix and the 10µL of substrate mix consisted of Vivid® Substrate and Vivid® CYP450 Reaction Buffer only. For the second experimental condition, the Master Pre-Mix and substrate mix remained the same as the IC₅₀ assays as described in Section 4.2.6. IC₅₀ shift was calculated as a ratio of the 30-minutes without NADPH condition to 30-minutes with NADPH condition. The assays were performed as triplicates.

4.2.8 Determination of K_i and Mode of Inhibition

The inhibition constant (K_i) value indicates the affinity of an inhibitor to an enzyme (Burlingham & Widlansk, 2003). Thus, K_i values and the mode of inhibition were further determined for those pairings in which the ZnO particles demonstrated significant inhibition towards the respective CYP isozymes (IC₅₀ < 100 µg/mL). The K_i assays were conducted under various concentrations of the ZnO particles and Vivid® Substrates, as stated in Table 4.5, to examine the differences in enzymatic activities. The assay conditions and reagent concentrations remained the same as the previously conducted IC₅₀ assays, with the exception of the ZnO particle's and Vivid® Substrate's concentrations; ZnO particle concentrations were determined based on the retrieved IC₅₀ values, and were incubated with four concentrations of Vivid® Substrate. Assays were performed as triplicates.

Table 4.5. Concentration range of each CYP isozyme's ZnO particle and Vivid® Substrate's concentration for their respective K_i assays. *CYP* cytochrome P450, *ZnO* zinc oxide, K_i inhibition constant.

CYP Isozyme	ZnO Particle*	ZnO Particle Concentration ($\mu\text{g/mL}$)	Vivid® Substrate Concentration (μM)*
CYP2B6	ZnONP50	50, 25, 12.5, 6.25, 0	BOMCC – 2.5, 5, 10, 20
	ZnONP100	50, 25, 12.5, 6.25, 0	
CYP2C8	ZnONP50	50, 25, 12.5, 6.25, 0	DBOMF - 2.5, 5, 10, 20
CYP2E1	ZnONP50	50, 25, 12.5, 6.25, 0	EOMCC – 10, 20, 40, 80
	ZnONP100	100, 50, 25, 12.5, 0	
	ZnOBP	50, 25, 12.5, 6.25, 0	
CYP2J2	ZnONP50	50, 25, 12.5, 6.25, 0	MOBFC – 2.5, 5, 10, 20
	ZnONP100	100, 50, 25, 12.5, 0	
CYP3A5	ZnONP50	100, 50, 25, 12.5, 0	BOMCC – 2.5, 5, 10, 20
	ZnONP100	50, 25, 12.5, 6.25, 0	

*ZnONPs: zinc oxide nanoparticles

ZnOBP: zinc oxide bulk particles

**EOMCC: 7-ethoxy-methoxy-3-cyano-coumarin

BOMCC: 7-benzyloxymethoxy-3-cyano-coumarin

DBOMF: di-(benzyl-O-methyl)-fluorescein

MOBFC: 7-P-methoxy-benzyloxy-4-trifluoro-coumarin

4.2.9 Data Analysis

4.2.9.1 Determination of Half Maximal Inhibitory Concentration (IC₅₀)

The percentage of control activity (%) at each concentration (µg/mL) of ZnO particle was calculated as *Percentage Control Activity (%) = $\frac{\text{Fluorescence Reading in the Presence of Test Compound}}{\text{Fluorescence Reading in the Absence of Test Compound}} \times 100$* . The concentration values of ZnO particles were converted into logarithmic values. The values were plotted on a graph of percentage of control activity (%) against a log scale concentration of ZnO particle (µg/mL) on GraphPad Prism Version 9.4.1 for Mac (GraphPad Software, La Jolla California, USA) to retrieve the IC₅₀ values for each data set using non-linear regression.

4.2.9.2 Determination of IC₅₀ Shift

The IC₅₀ values for the two experimental conditions were obtained, and the IC₅₀ shift for each CYP isozyme and ZnO particle pairing was calculated accordingly:

$IC_{50} \text{ Shift} = \frac{IC_{50} \text{ without NADPH}}{IC_{50} \text{ with NADPH}}$. A ratio of more than 2.0 suggested time-dependent/mechanism-based inhibition, thus the respective ZnO particle was categorised as an irreversible inhibitor (Riley et al., 2007).

4.2.9.3 Determination of K_i and Mode of Inhibition

The equations generated from the standard curves were used to determine the metabolite formation from which the reaction velocity was calculated. Lineweaver-Burk plots were plotted on Microsoft Excel, as the reciprocal of the reaction velocity against the reciprocal of the substrate concentration. The mode of inhibition was determined graphically for each CYP isozyme and ZnO particle pairing. A ‘secondary plot’ was plotted as the varying concentrations of the ZnO particle (µg/mL) against the slopes of the Lineweaver-Burk plot. K_i values were obtained from the slope of the ‘secondary plot’ represented by the X-intercept.

4.3 Results and Discussion

4.3.1 Establishment of Standard Curves

The standard curves for Vivid[®] CYP450 Reaction Buffer I, Vivid[®] CYP450 Reaction 0.5X Buffer II, Vivid[®] CYP450 Reaction Buffer II, and Vivid[®] CYP450 Reaction Buffer III are presented as Figure A.4.1, A.4.2, A.4.3, and A.4.4 in the Appendix respectively. The equations derived from each standard curve have been summarised under Table A.4.1 in the Appendix. These equations were used to determine the value of the reaction rate (velocity), and subsequently the K_i values for applicable CYP isozymes if deemed necessary.

4.3.2 Establishment of Time Curves

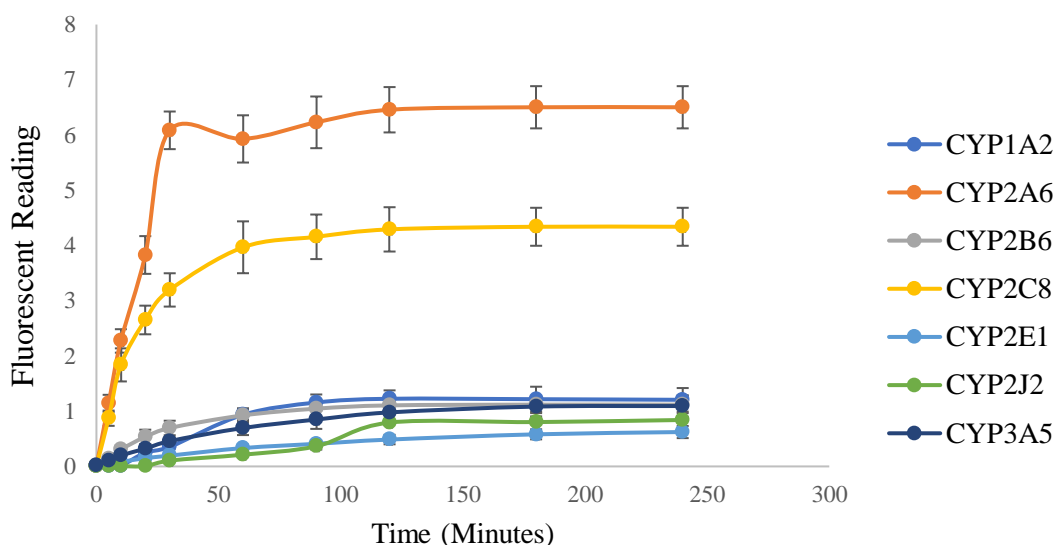


Figure 4.3. Time curves of CYP isozymes: CYP1A2, CYP2A6, CYP2B6, CYP2C8, CYP2E1, CYP2J2 and CYP3A5. The data sets were generated by plotting the fluorescent readings of metabolites formed from the oxidation of their respective Vivid[®] Substrates, against a range of incubation period; 5, 10, 20, 30, 60, 90, 120, 180, and 240 minutes. Each data point represents the mean \pm SD (n=3).

Time curves for the CYP isozymes were generated by plotting the fluorescent reading of the metabolites formed by the oxidation of respective Vivid[®] Substrate, BOMCC (CYP2B6 and CYP3A5), EOMCC (CYP1A2 and CYP2E1), CC (CYP2A6), MOBFC (CYP2J2), and DBOMF (CYP2C8) against a range of incubation periods (Figure 4.3). The time curves were generated to determine the optimum incubation period for each CYP isozyme to reach peak enzymatic activity and to obtain adequate fluorescent readings to determine the inhibitory potential of various ZnO particles. An incubation period of 120 minutes was chosen for all CYP isozyme reactions involved in subsequent assays.

4.3.3 Inhibition of CYP Isozymes by Positive Inhibitors

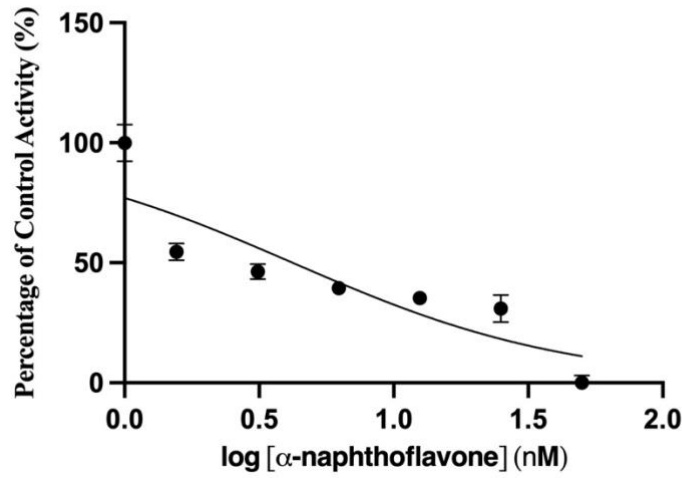
Based on the optimal incubation period determined, CYP isozyme assays using their respective positive inhibitors were carried out to validate subsequent assay' conditions. Positive inhibitors are also known as inhibitor probes; at a given concentration, the chosen molecule is able to selectively inhibit the bio-target (Gestwicki & Shao, 2019). The positive inhibitors chosen in this study were suggested by the Vivid CYP450 screening kits' manufacturer including α -naphthoflavone (CYP1A2), tranylcypromine (CYP2A6 and CYP2E1), miconazole (CYP2B6), montelukast (CYP2C8), terfenadine (CYP2J2), and ketoconazole (CYP3A5) (Ozgenic, n.d.).

IC₅₀ values were retrieved using non-linear aggression analysis (GraphPad Prism Version 9.5.0). The remaining enzymatic of each isozyme post-exposure to the highest concentration of their respective positive inhibitors and the derived IC₅₀ values have been summarised below in Table 4.6.

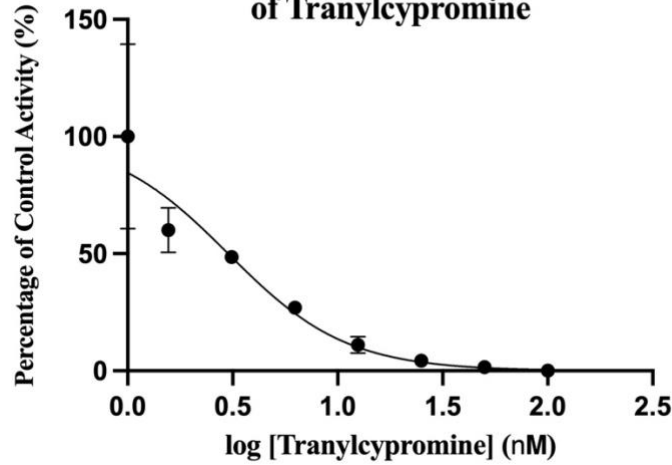
Table 4.6. Summary of derived IC₅₀ values and the remaining enzymatic activity of CYP isozymes post-exposure to the highest concentration of their respective positive inhibitors. IC₅₀ half maximal inhibitory concentration, CYP cytochrome P450.

CYP Isozyme	Positive Inhibitor Concentration (nM)	Remaining Enzymatic Activity	IC ₅₀ value (nM)
CYP1A2 (Figure 4.4A)	α -naphthoflavone: 50	5.7%	4.21
CYP2A6 (Figure 4.4B)	Tranylcypromine: 100	3.82%	2.99
CYP2B6 (Figure 4.4C)	Miconazole: 200	4.71%	5.5
CYP2C8 (Figure 4.4D)	Montelukast: 10	42.46%	2.70
CYP2E1 (Figure 4.4E)	Tranylcypromine: 10	14.94%	1.24
CYP2J2 (Figure 4.4F)	Terfenadine: 100	25.29%	1.49
CYP3A5 (Figure 4.4G)	Ketoconazole: 200	27.59%	7.89

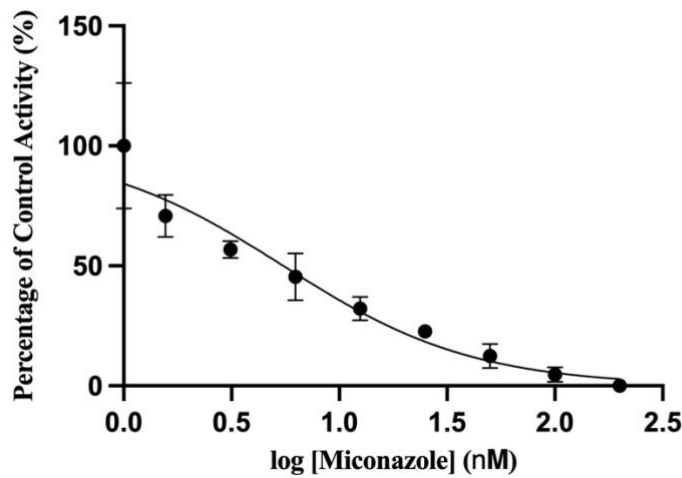
A) **CYP1A2 Activity in Presence of Varying Concentrations of α -naphthoflavone**



B) **CYP2A6 Activity in Presence of Varying Concentrations of Tranlycypromine**

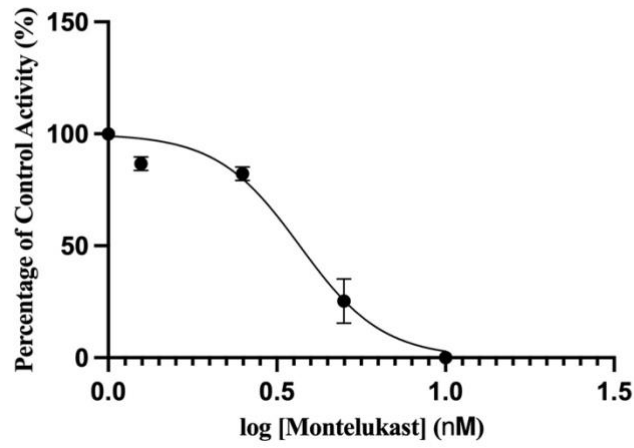


C) **CYP2B6 Activity in Presence of Varying Concentrations of Miconazole**



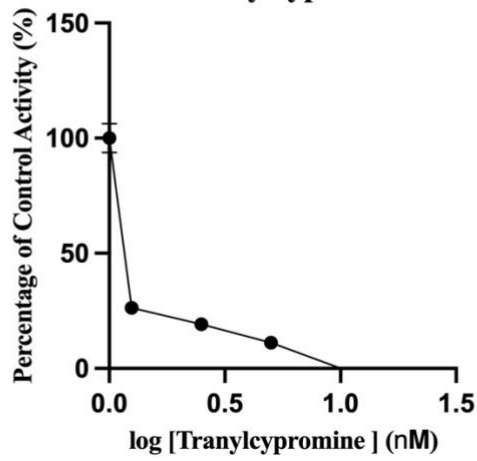
D)

CYP2C8 Activity in Presence of Varying Concentrations of Montelukast



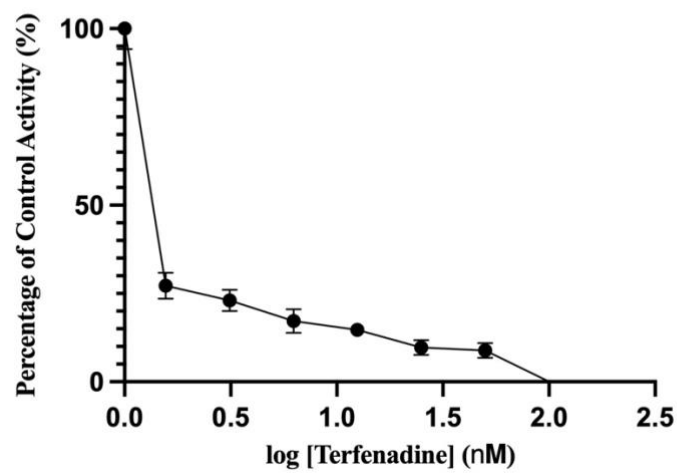
E)

CYP2E1 Activity in Presence of Varying Concentrations of Tranlycypromine



F)

CYP2J2 Activity in Presence of Varying Concentrations of Terfenadine



G)

CYP3A5 Activity in Presence of Varying Concentrations of Ketoconazole

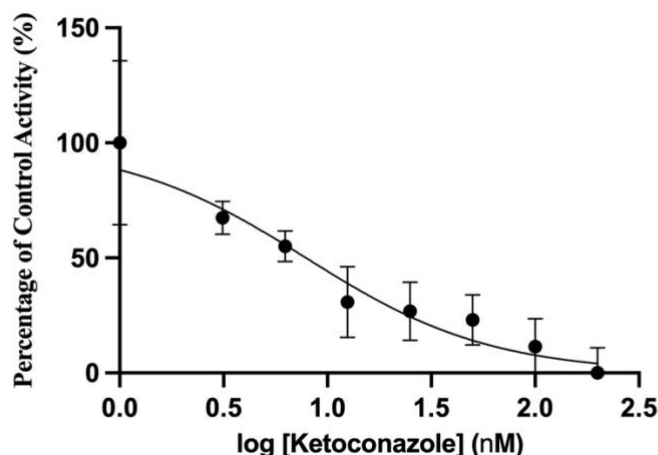


Figure 4.4. Inhibition of (A) CYP1A2, (B) CYP2A6, (C) CYP2B6, (D) CYP2C8, (E) CYP2E1, (F) CYP2J2, and (G) CYP3A5 by their respective positive inhibitors: α -naphthoflavone (0, 1.56, 3.13, 6.25, 12.5, 25, and 50 nM), tranilcypromine (0, 1.56, 3.16, 6.25, 12.5, 25, 50, and 100 nM), miconazole (0, 1.56, 3.16, 6.25, 12.5, 25, 50, 100, and 200 nM), montelukast (0, 0.31, 0.63, 1.25, 2.5, 5, and 10 nM), tranilcypromine (0, 0.31, 0.63, 1.25, 2.5, 5, and 10 nM), terfenadine (0, 1.56, 3.13, 6.25, 12.5, 25, 50, and 100 nM), and ketoconazole (0, 3.13, 6.25, 12.5, 25, 50, 100, and 200 nM). The data sets were generated by plotting the respective percentage of control activity (%) against the range of respective positive inhibitor's concentration ($\mu\text{g/mL}$) presented as logarithmic values. Percentage of control activity (%) denotes the remaining enzymatic activity based on the activity of the control reaction set at 100%. Each data point represents the mean \pm SD ($n=3$). CYP cytochrome P450.

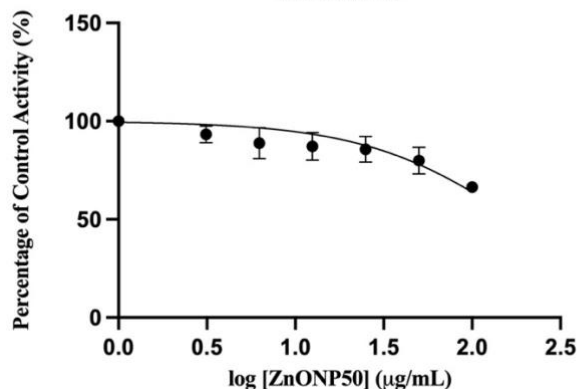
Based on these results, it was concluded that all CYP isozyme's enzymatic activity were inhibited by the probe inhibitors within the micromolar range (Krippendorff et al., 2007). The retrieved IC_{50} values fell within the range of previously reported IC_{50} values under the presence of respective positive inhibitors at a similar concentration (Table 4.7). Thus, it was confirmed that the established assays were valid and well developed to be employed in all subsequent inhibition screenings.

Table 4.7. Retrieved and reported IC_{50} values of CYP isozymes under the presence of their respective positive inhibitors. IC_{50} half maximal inhibitory concentration, CYP cytochrome P450.

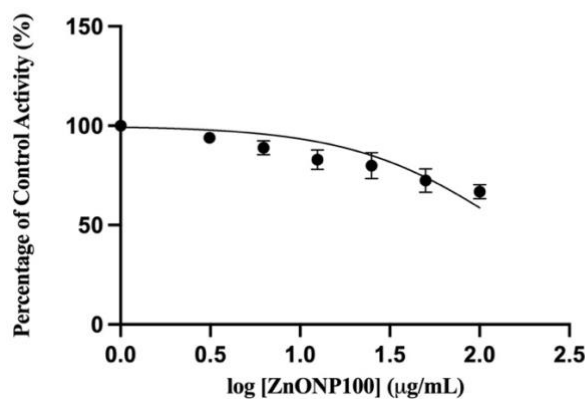
CYP Isozymes	Positive Inhibitor	Retrieved IC_{50} Values (nM)	Reported IC_{50} Values (nM)	Reference
CYP1A2 (Figure 4.4A)	α -naphthoflavone	4.21	3.0 – 20.0	(Dutour & Poirier, 2017; Juvonen et al., 2020; Marinas et al., 2010)
CYP2A6 (Figure 4.4B)	Tranlycypromine	2.99	0.40 - 3.0	(Dinger et al., 2016; Taavitsainen et al., 2001; Zhang et al., 2001)
CYP2B6 (Figure 4.4C)	Miconazole	5.5	0.02 - 6.76	(Moody et al., 2015; Shibata et al., 2021; Thomford et al., 2016)
CYP2C8 (Figure 4.4D)	Montelukast	2.70	0.5 - 3	(Jaakkola et al., 2006; Nagar et al., 2014; Walsky et al., 2005)
CYP2E1 (Figure 4.4E)	Tranlycypromine	1.24	2.85 – 3.2	(Dinger et al., 2016; Taavitsainen et al., 2001)
CYP2J2 (Figure 4.4F)	Terfenadine	1.49	0.07 -13.6	(Khan et al., 2023; Lafite et al., 2007; Liu, 2011)
CYP3A5 (Figure 4.4G)	Ketoconazole	7.89	0.11 – 50.3	(Novotná et al., 2014; Vermeer et al., 2016; Weiss et al., 2022)

4.3.4 Determination of Half Maximal Inhibitory Concentration (IC₅₀)

A) CYP1A2 Activity in Presence of Varying Concentrations of ZnONP50



B) CYP1A2 Activity in Presence of Varying Concentrations of ZnONP100



C) CYP1A2 Activity in Presence of Varying Concentrations of ZnOBP

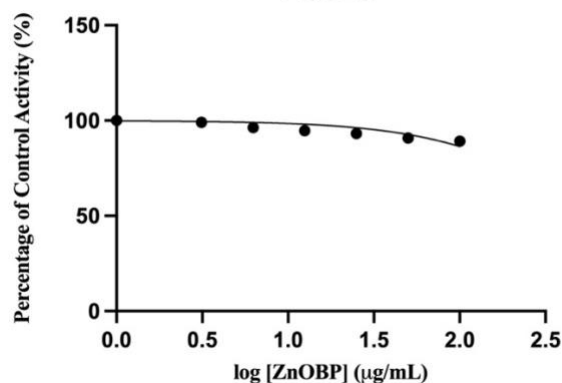
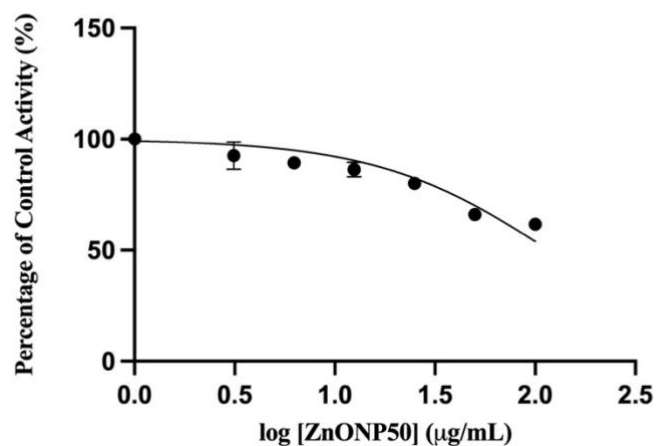
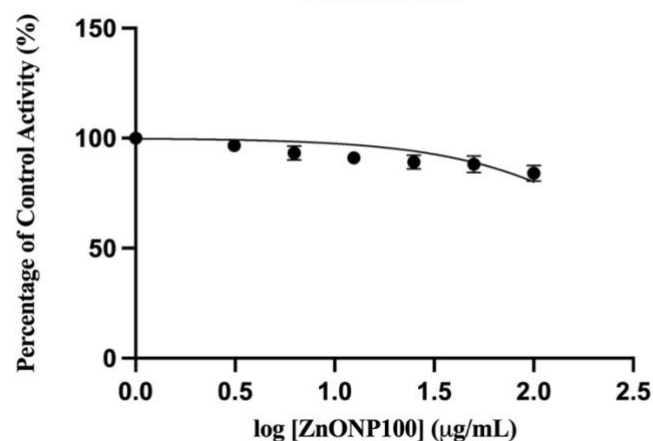


Figure 4.5. Inhibitory effects of (A) ZnONP50, (B) ZnONP100, and (C) ZnOBP on CYP1A2. The data sets were generated by plotting the percentage of control activity (%) against the range of the respective ZnO particle's concentration (µg/mL) presented as log concentration. Percentage of control activity (%) denotes the remaining enzymatic activity based on the activity of the control reaction set at 100%. Each data point represents the mean ± SD (n=3). *ZnONP50* Zinc oxide nanoparticles <50 nm, *ZnONP100* Zinc oxide nanoparticles <100 nm, *ZnOBP* Zinc oxide bulk particles, *CYP* cytochrome P450, *ZnO* Zinc oxide.

A) **CYP2A6 Activity in Presence of Varying Concentrations of ZnONP50**



B) **CYP2A6 Activity in Presence of Varying Concentrations of ZnONP100**



C) **CYP2A6 Activity in Presence of Varying Concentrations of ZnOBP**

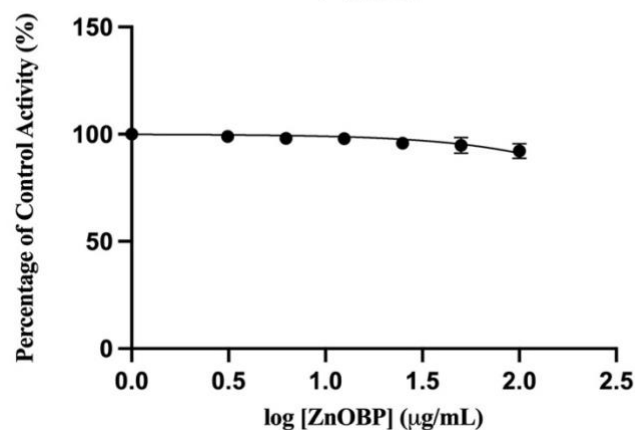
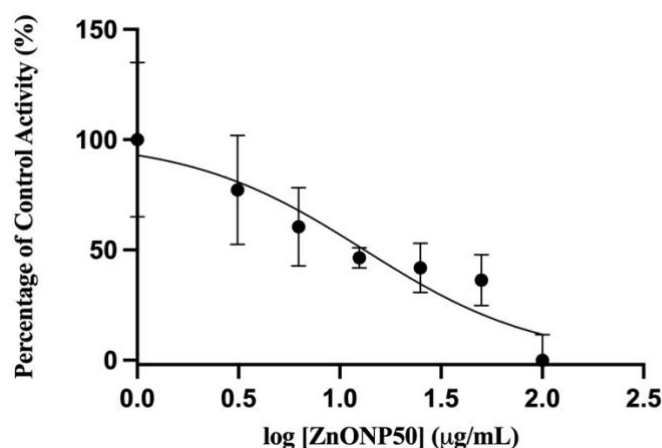
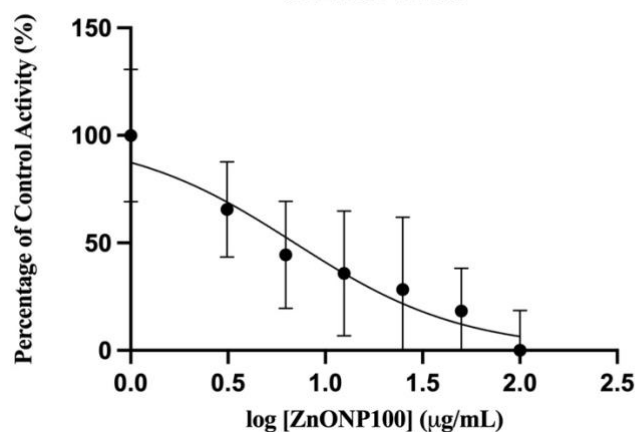


Figure 4.6. Inhibitory effects of (A) ZnONP50, (B) ZnONP100, and (C) ZnOBP on CYP2A6. The data sets were generated by plotting the percentage of control activity (%) against the range of the respective ZnO particle's concentration (µg/mL) presented as log concentration. Percentage of control activity (%) denotes the remaining enzymatic activity based on the activity of the control reaction set at 100%. Each data point represents the mean \pm SD (n=3). *ZnONP50* Zinc oxide nanoparticles <50 nm, *ZnONP100* Zinc oxide nanoparticles <100 nm, *ZnOBP* Zinc oxide bulk particles, *CYP* cytochrome P450, *ZnO* Zinc oxide.

A) **CYP2B6 Activity in Presence of Varying Concentrations of ZnONP50**



B) **CYP2B6 Activity in Presence of Varying Concentrations of ZnONP100**



C) **CYP2B6 Activity in Presence of Varying Concentrations of ZnOBP**

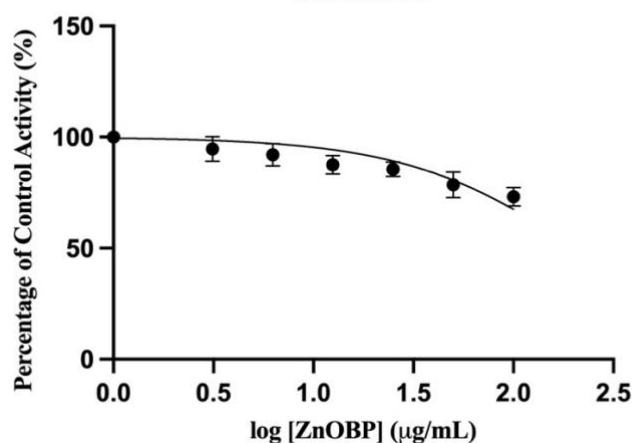
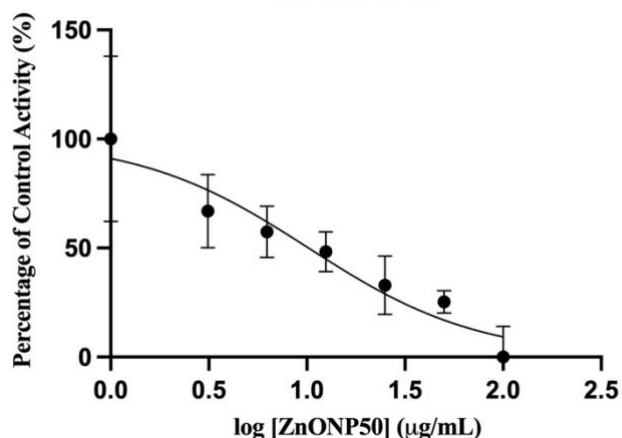
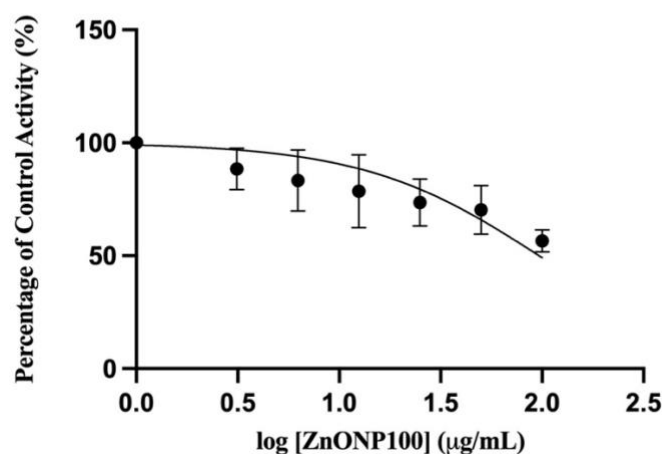


Figure 4.7. Inhibitory effects of (A) ZnONP50, (B) ZnONP100, and (C) ZnOBP on CYP2B6. The data sets were generated by plotting the percentage of control activity (%) against the range of the respective ZnO particle's concentration (µg/mL) presented as log concentration. Percentage of control activity (%) denotes the remaining enzymatic activity based on the activity of the control reaction set at 100%. Each data point represents the mean \pm SD (n=3). *ZnONP50* Zinc oxide nanoparticles <50 nm, *ZnONP100* Zinc oxide nanoparticles <100 nm, *ZnOBP* Zinc oxide bulk particles, *CYP* cytochrome P450, *ZnO* Zinc oxide.

A) **CYP2C8 Activity in Presence of Varying Concentrations of ZnONP50**



B) **CYP2C8 Activity in Presence of Varying Concentrations of ZnONP100**



C) **CYP2C8 Activity in Presence of Varying Concentrations of ZnOBP**

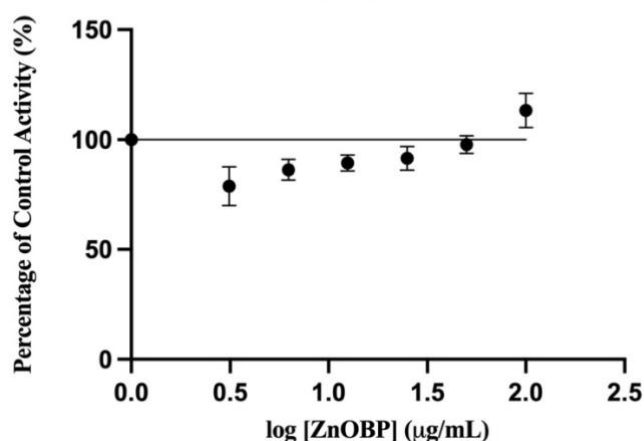
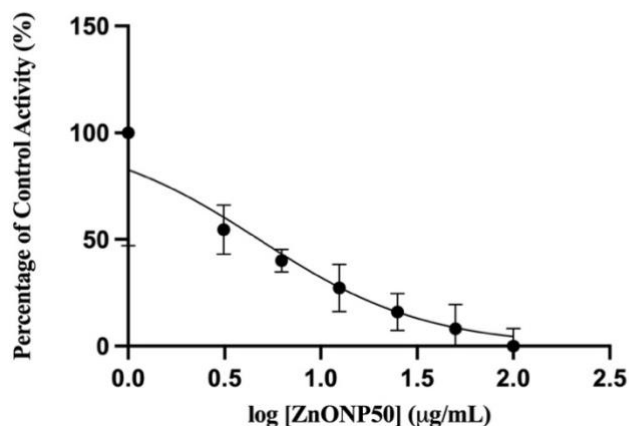


Figure 4.8. Inhibitory effects of (A) ZnONP50, (B) ZnONP100, and (C) ZnOBP on CYP2C8. The data sets were generated by plotting the percentage of control activity (%) against the range of the respective ZnO particle's concentration (µg/mL) presented as log concentration. Percentage of control activity (%) denotes the remaining enzymatic activity based on the activity of the control reaction set at 100%. Each data point represents the mean \pm SD (n=3). *ZnONP50* Zinc oxide nanoparticles <50 nm, *ZnONP100* Zinc oxide nanoparticles <100 nm, *ZnOBP* Zinc oxide bulk particles, *CYP* cytochrome P450, *ZnO* Zinc oxide.

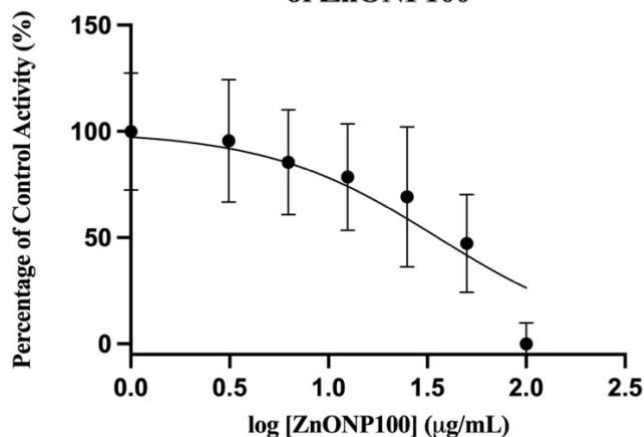
A)

CYP2E1 Activity in Presence of Varying Concentrations of ZnONP50



B)

CYP2E1 Activity in Presence of Varying Concentrations of ZnONP100



C)

CYP2E1 Activity in Presence of Varying Concentrations of ZnOBP

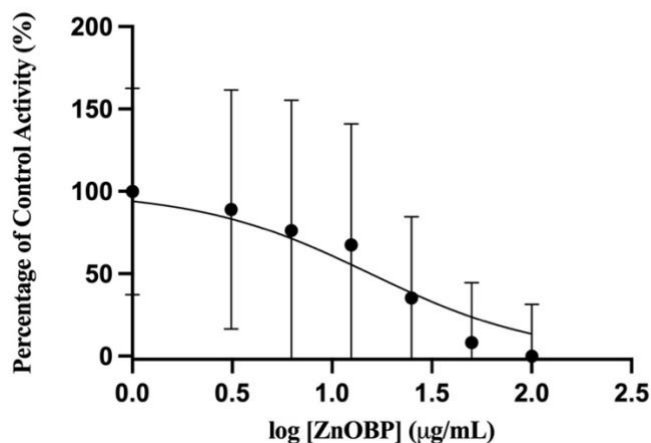
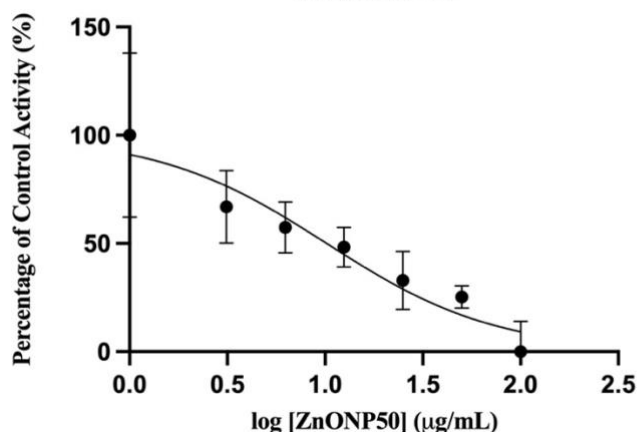
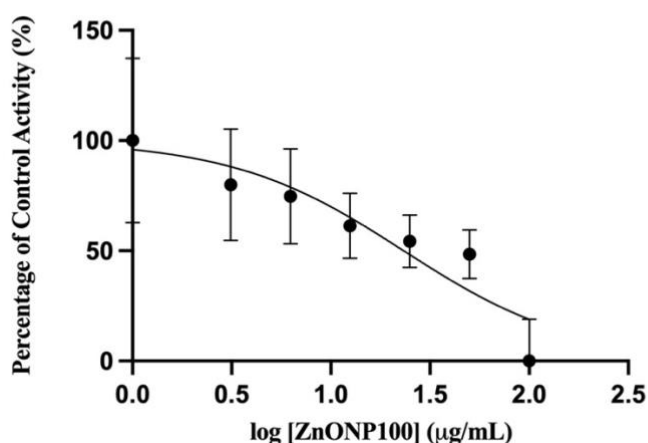


Figure 4.9. Inhibitory effects of (A) ZnONP50, (B) ZnONP100, and (C) ZnOBP on CYP2E1. The data sets were generated by plotting the percentage of control activity (%) against the range of the respective ZnO particle's concentration (µg/mL) presented as log concentration. Percentage of control activity (%) denotes the remaining enzymatic activity based on the activity of the control reaction set at 100%. Each data point represents the mean \pm SD (n=3). *ZnONP50* Zinc oxide nanoparticles <50 nm, *ZnONP100* Zinc oxide nanoparticles <100 nm, *ZnOBP* Zinc oxide bulk particles, *CYP* cytochrome P450, *ZnO* Zinc oxide.

A) **CYP2J2 Activity in Presence of Varying Concentrations of ZnONP50**



B) **CYP2J2 Activity in Presence of Varying Concentrations of ZnONP100**



C) **CYP2J2 Activity in Presence of Varying Concentrations of ZnOBP**

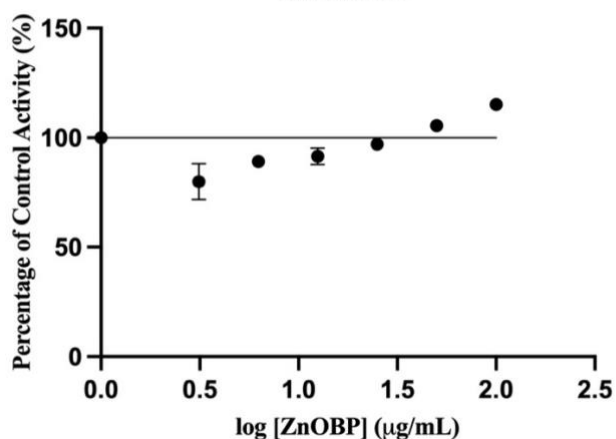
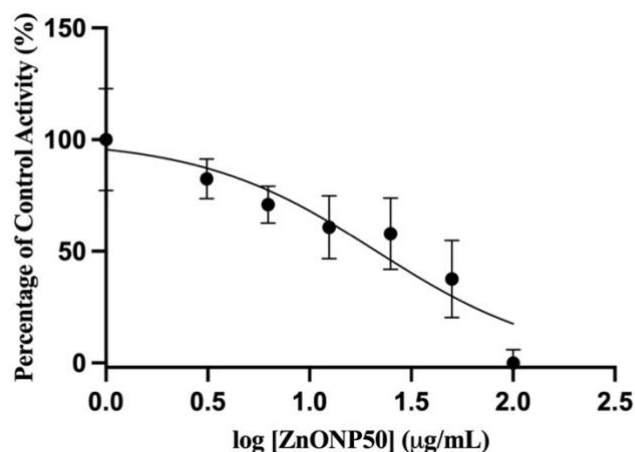
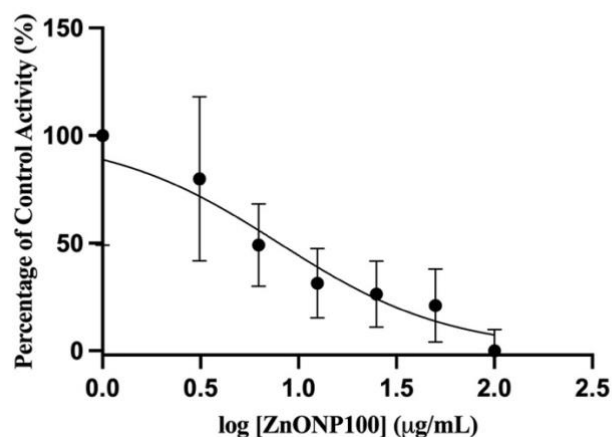


Figure 4.10. Inhibitory effects of (A) ZnONP50, (B) ZnONP100, and (C) ZnOBP on CYP2J2. The data sets were generated by plotting the percentage of control activity (%) against the range of the respective ZnO particle's concentration ($\mu\text{g/mL}$) presented as log concentration. Percentage of control activity (%) denotes the remaining enzymatic activity based on the activity of the control reaction set at 100%. Each data point represents the mean \pm SD ($n=3$). *ZnONP50* Zinc oxide nanoparticles <50 nm, *ZnONP100* Zinc oxide nanoparticles <100 nm, *ZnOBP* Zinc oxide bulk particles, *CYP* cytochrome P450, *ZnO* Zinc oxide.

A) **CYP3A5 Activity in Presence of Varying Concentrations of ZnONP50**



B) **CYP3A5 Activity in Presence of Varying Concentrations of ZnONP100**



C) **CYP3A5 Activity in Presence of Varying Concentrations of ZnOBP**

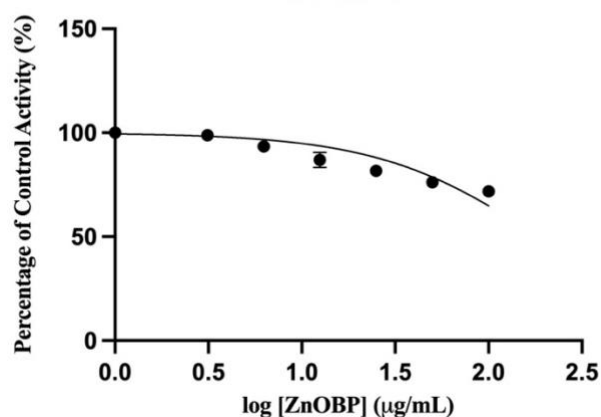


Figure 4.11. Inhibitory effects of (A) ZnONP50, (B) ZnONP100, and (C) ZnOBP on CYP3A5. The data sets were generated by plotting the percentage of control activity (%) against the range of the respective ZnO particle's concentration (µg/mL) presented as log concentration. Percentage of control activity (%) denotes the remaining enzymatic activity based on the activity of the control reaction set at 100%. Each data point represents the mean \pm SD (n=3). *ZnONP50* Zinc oxide nanoparticles <50 nm, *ZnONP100* Zinc oxide nanoparticles <100 nm, *ZnOBP* Zinc oxide bulk particles, *CYP* cytochrome P450, *ZnO* Zinc oxide.

IC₅₀ values indicate the strength of an inhibitor: strong (IC₅₀ < 1 μM), moderate (1 μM < IC₅₀ < 10 μM), and weak (IC₅₀ > 10 μM) (Krippendorff et al., 2007).

In reference to CYP1A2 (Figure 4.5A, B, and C) and CYP2A6 (Figure 4.6A, B, and C), concentration-dependent decrease of activity was noted by ZnONP50, ZnONP100, and ZnOBP, however, the inhibition was negligible with IC₅₀ values more than 100 μg/mL as enzymatic activity remained over 50%. Upon exposure to highest concentration of ZnONP50, ZnONP100, and ZnOBP, the enzymatic activity of CYP1A2 remained at 66.47%, 64.86%, and 88.14% respectively, and the enzymatic activity of CYP2A6 remained at 61.14%, 84.10%, and 92.19% respectively.

Inhibition of CYP2B6 and CYP3A5 by ZnONP50, ZnONP100, and ZnOBP followed similar patterns. While all ZnO particles were able to elicit a concentration-dependent decrease of activity, the inhibition by ZnOBP of both CYP isozymes was negligible with IC₅₀ values more than 100 μg/mL; enzymatic activity remained at 73.14% for CYP2B6 (Figure 4.7C) and 71.83% for CYP3A5 (Figure 4.11C) upon exposure to the highest concentration. The significant inhibition of CYP2B6 and CYP3A5 by ZnONP50 yielded respective IC₅₀ values of 8.07 μg/mL and 21.34 μg/mL as their respective enzymatic activity remained at 45.37% (Figure 4.7A) and 15.36% (Figure 4.11A) upon exposure to the highest concentration. ZnONP50 was categorised as a moderate and weak inhibitor of CYP2B6 and CYP3A5 respectively. The significant inhibition of CYP2B6 and CYP3A5 by ZnONP100 yielded respective IC₅₀ values of 8.43 μg/mL and 7.93 μg/mL as their enzymatic activity remained at 43.06% (Figure 4.7B) and 18.88% (Figure 4.11B) upon exposure to the highest concentration. ZnONP100 was categorised as a moderate inhibitor of CYP2B6 and CYP3A5.

In regard to CYP2C8, concentration-dependent decrease of activity by ZnONP50 and ZnONP100 (Figure 4.8A and B) was observed; the enzymatic activity remained at 45% and 56.51% upon exposure to the highest concentration of ZnONP50 and ZnONP100 respectively. The inhibition by ZnONP100 was negligible with IC₅₀ values more than 100 μg/mL. IC₅₀ value of 10.2 μg/mL was derived for ZnONP50, and it was categorised as moderate inhibitor of CYP2C8. Based on Figure 4.8C, concentration-dependent increase in activity was exhibited, with CYP2C8's enzymatic activity increasing to 113.25% upon exposure to highest concentration of ZnOBP.

Concentration-dependent decrease of activity of CYP2J2 by ZnONP50 and ZnONP100 was observed. Significant inhibition by ZnONP50 and ZnONP100 yielded respective IC₅₀ values of 2.23 μg/mL and 23.25 μg/mL, as enzymatic activities remained at 46.91% (Figure 4.10A) and 32.38% (Figure 4.10B) upon exposure to the highest concentrations of respective

ZnONPs. ZnONP50 and ZnONP100 were categorised as moderate and weak inhibitors of CYP2J2 respectively. Based on Figure 4.10C, concentration-dependent increase in activity was exhibited, with CYP2J2's enzymatic activity increasing to 115.21% upon exposure to highest concentration of ZnOBP.

All three categories of ZnO particles were able to inhibit CYP2E1 significantly (Figure 4.9A, B, and C). Enzymatic activities remained at 27.56%, 44.01%, and 48.36% upon exposure to the highest concentration of ZnONP50, ZnONP100, and ZnOBP respectively; the ZnO particles yielded IC₅₀ values of 4.85 µg/mL, 36.10 µg/mL, and 16.32 µg/mL. ZnONP50 was categorised as a moderate inhibitor of CYP2E1, while ZnONP100 and ZnOBP were categorised weak inhibitors.

Applicable IC₅₀ values for each CYP isozyme's activity upon exposure to each type of ZnO particle (ZnONP50, ZnONP100, and ZnOBP) have been summarised below in Table 4.8.

Table 4.8. Summary of IC_{50} assay' results for each CYP isozyme. IC_{50} half maximal inhibitory

CYP Isozyme	ZnO Particles	IC_{50} ($\mu\text{g/mL}$)
CYP1A2	ZnONP50	177.0
	ZnONP100	142.3
	ZnOBP	634.2
CYP2A6	ZnONP50	229.4
	ZnONP100	404.2
	ZnOBP	1029
CYP2B6	ZnONP50	8.07
	ZnONP100	8.43
	ZnOBP	207.9
CYP2C8	ZnONP50	10.2
	ZnONP100	101.65
	ZnOBP	Unstable
CYP2E1	ZnONP50	4.85
	ZnONP100	36.10
	ZnOBP	16.32
CYP2J2	ZnONP50	2.12
	ZnONP100	23.25
	ZnOBP	Unstable
CYP3A5	ZnONP50	21.34
	ZnONP100	7.93
	ZnOBP	184.6

Evaluation of ZnO Particle's Size-Dependent Inhibition

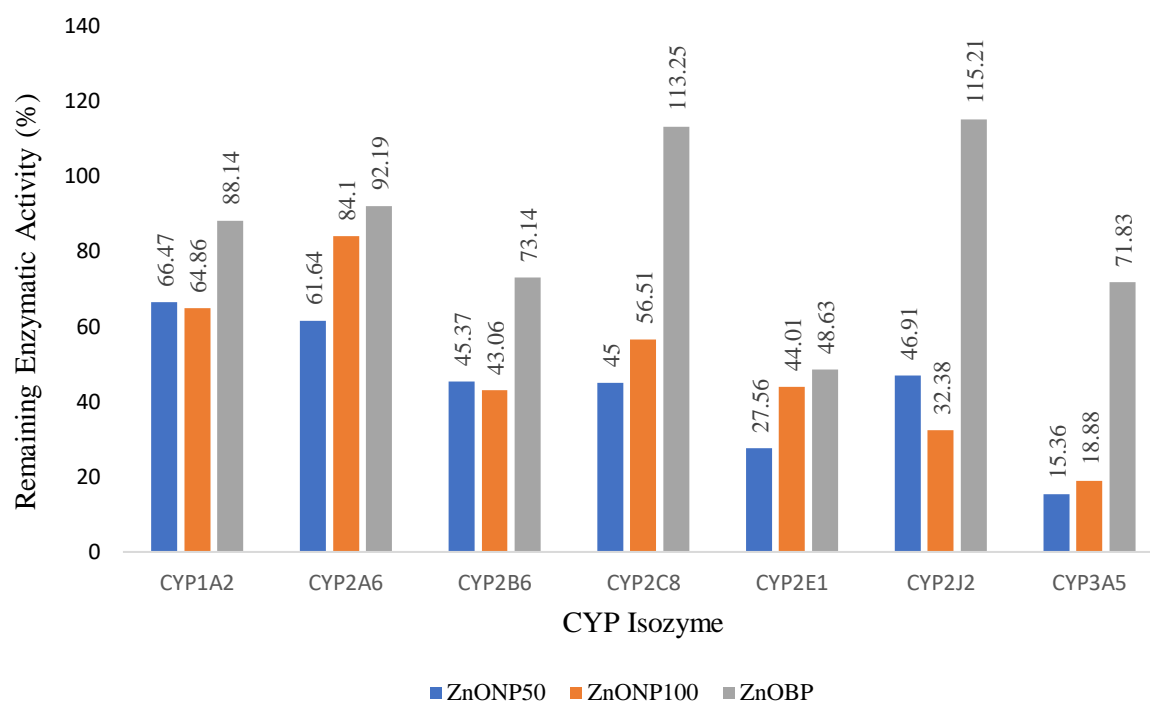


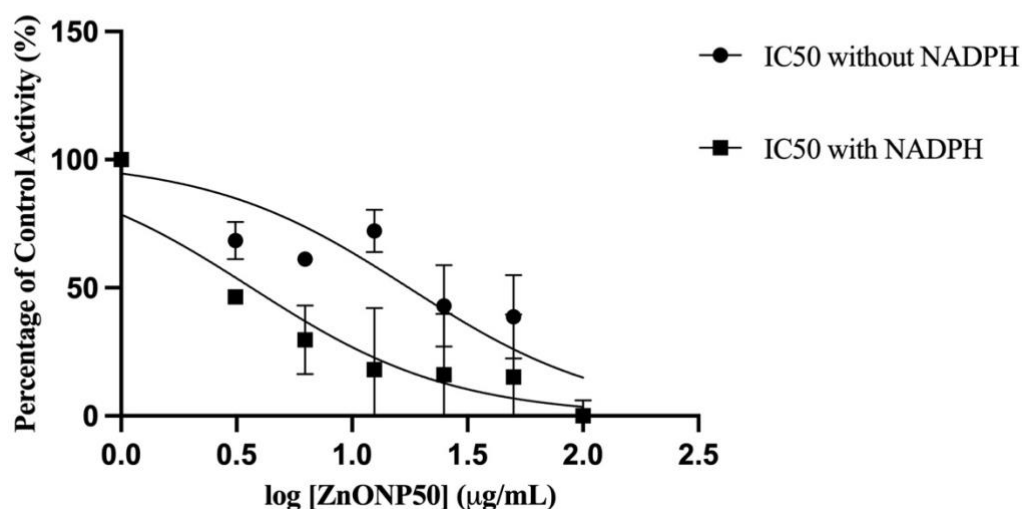
Figure 4.12. Evaluation of the size-dependent inhibition of CYP isozymes by ZnONP50, ZnONP100, and ZnOBP. *ZnONP50* Zinc oxide nanoparticles <50 nm, *ZnONP100* Zinc oxide nanoparticles <100 nm, *ZnOBP* Zinc oxide bulk particles, *CYP* cytochrome P450.

As reported previously, all CYP isozymes displayed concentration-dependent decrease in enzymatic activity by all sizes of ZnO particles with the exception of CYP2C8 and CYP2J2 under the exposure of ZnOBP. Additionally, a comparison of the remaining enzymatic activity upon exposure to the highest concentration of various sized ZnO particles was conducted to determine where the inhibition occurred in a size-dependent manner (Figure 4.12). As seen above, CYP1A2, CYP2B6, and CYP2J2 were inhibited the most by ZnONP100. Whereas ZnONP50 was able to inhibit CYP2A6, CYP2C8, CYP2E1, and CYP3A5 at a larger capacity. Thus, it can be concluded that CYP2C8, CYP2E1, and CYP3A5 were inhibited in a size-dependent manner.

4.3.5 Determination of IC₅₀ Shift and Time-Dependent Inhibition

Subsequent assays were conducted for all CYP isozymes with their respective ZnO particle whose enzymatic activity was reduced by 50% or more upon exposure to the highest concentration (100 µg/mL). To determine the potential of mechanism-based (time-dependent) inhibitory effects of ZnONP50, ZnONP100, and ZnOBP, IC₅₀-shift for each pairing (CYP isozyme and ZnO particle) was calculated as the ratio of IC₅₀ with pre-incubation to IC₅₀ without pre-incubation; IC₅₀ with pre-incubation is denoted as 'IC₅₀ without NADPH' and IC₅₀ without pre-incubation is denoted as 'IC₅₀ with NADPH' in Figure 4.13, 4.14, 4.15, 4.16, and 4.17. All IC₅₀-shift values have been summarised below in Table 4.9.

A) **Time Dependent Inhibition of CYP2B6 in Presence of Varying Concentrations of ZnONP50**



B) **Time Dependent Inhibition of CYP2B6 in Presence of Varying Concentrations of ZnONP100**

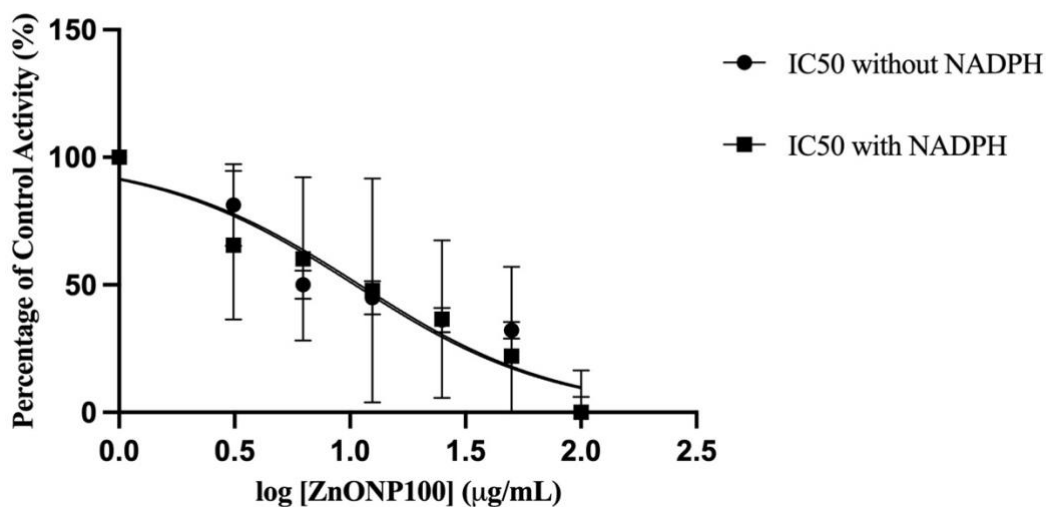


Figure 4.13. Time dependent inhibition of CYP2B6 by (A) ZnONP50 and (B) ZnONP100. The data sets were generated by plotting the percentage of control activity (%) against a range of ZnONPs' concentrations ($\mu\text{g/mL}$) presented as log concentration. IC_{50} with pre-incubation is denoted as 'IC₅₀ without NADPH' and IC_{50} without pre-incubation is denoted as 'IC₅₀ with NADPH'. Percentage of control of activity (%) denotes the remaining enzymatic activity based on the activity of the control reaction set at 100%. Each data point represents the mean \pm SD (n=3). CYP cytochrome P450, ZnONP50 Zinc oxide nanoparticles <50 nm, ZnONP100 Zinc oxide nanoparticles <100 nm, IC₅₀ half-maximal inhibitory concentration, NADPH nicotinamide adenine dinucleotide phosphate.

Time Dependent Inhibition of CYP2C8 in Presence of Varying Concentrations of ZnONP50

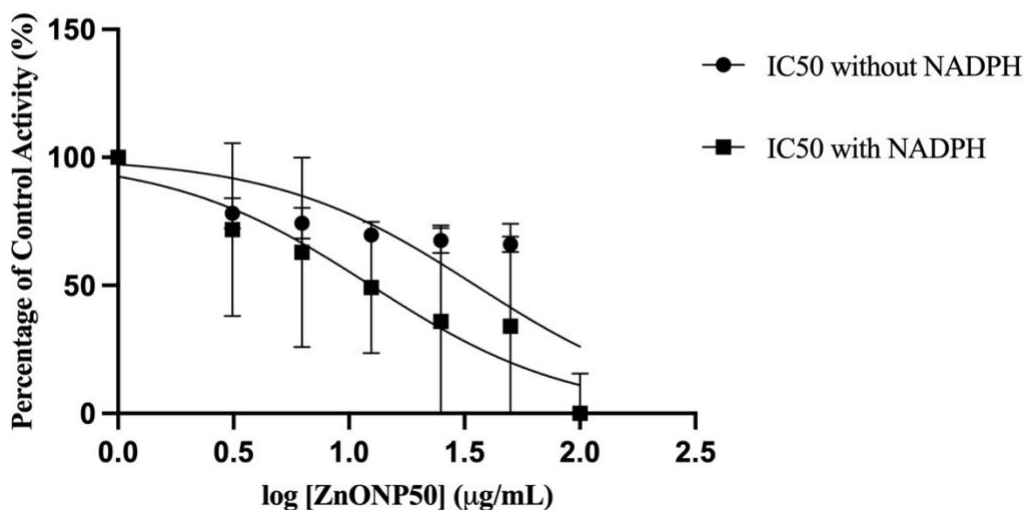
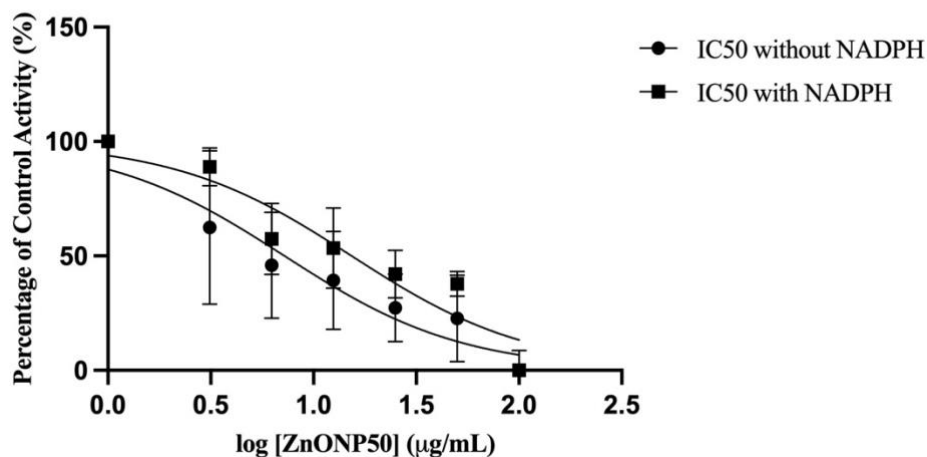
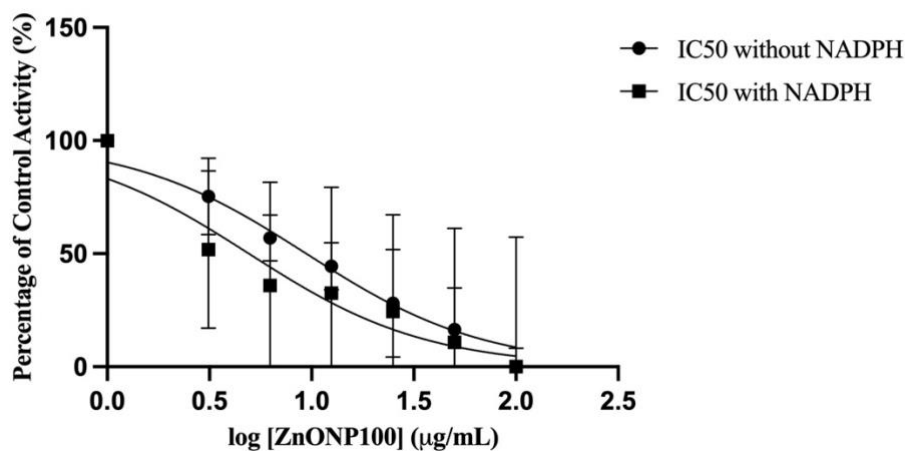


Figure 4.14. Time dependent inhibition of CYP2C8 by ZnONP50. The data set was generated by plotting the percentage of control activity (%) against a range of ZnONPs' concentrations ($\mu\text{g/mL}$) presented as log concentration. IC_{50} with pre-incubation is denoted as ' IC_{50} without NADPH' and IC_{50} without pre-incubation is denoted as ' IC_{50} with NADPH'. Percentage of control activity (%) denotes the remaining enzymatic activity based on the activity of the control reaction set at 100%. Each data point represents the mean \pm SD ($n=3$). CYP cytochrome P450, ZnONP50 Zinc oxide nanoparticles <50 nm, IC_{50} half-maximal inhibitory concentration, NADPH nicotinamide adenine dinucleotide phosphate.

A) Time Dependent Inhibition of CYP2E1 in Presence of Varying Concentrations of ZnONP50



B) Time Dependent Inhibition of CYP2E1 in Presence of Varying Concentrations of ZnONP100



C) Time Dependent Inhibition of CYP2E1 in Presence of Varying Concentrations of ZnOBP

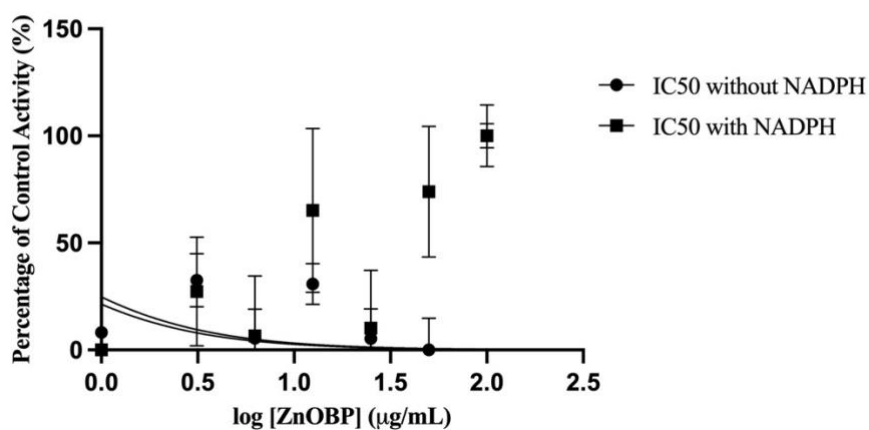
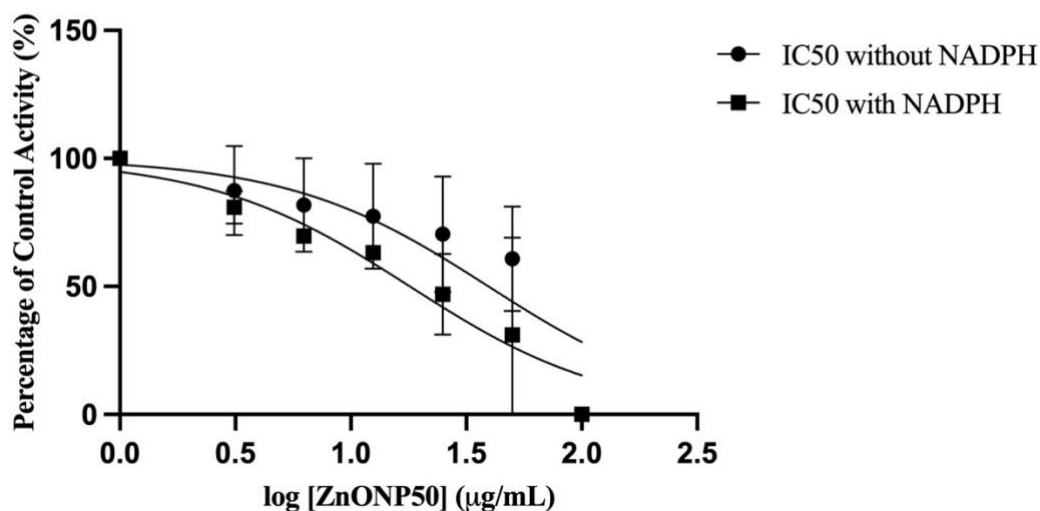


Figure 4.15. Time dependent inhibition of CYP2E1 by (A) ZnONP50, (B) ZnONP100, and (C) ZnOBP. The data sets were generated by plotting the percentage of control activity (%) against a range of ZnO particles' concentrations ($\mu\text{g/mL}$) presented as log concentration. IC_{50} with pre-incubation is denoted as 'IC₅₀ without NADPH' and IC_{50} without pre-incubation is denoted as 'IC₅₀ with NADPH'. Percentage of control activity (%) denotes the remaining enzymatic activity based on the activity of the control reaction set at 100%. Each data point represents the mean \pm SD ($n=3$). CYP cytochrome P450, ZnONP50 Zinc oxide nanoparticles <50 nm, ZnONP100 Zinc oxide nanoparticles <100 nm, ZnOBP Zinc oxide bulk particles, IC_{50} half-maximal inhibitory concentration, NADPH nicotinamide adenine dinucleotide phosphate.

A) **Time Dependent Inhibition of CYP2J2 in Presence of Varying Concentrations of ZnONP50**



B) **Time Dependent Inhibition of CYP2J2 in Presence of Varying Concentrations of ZnONP100**

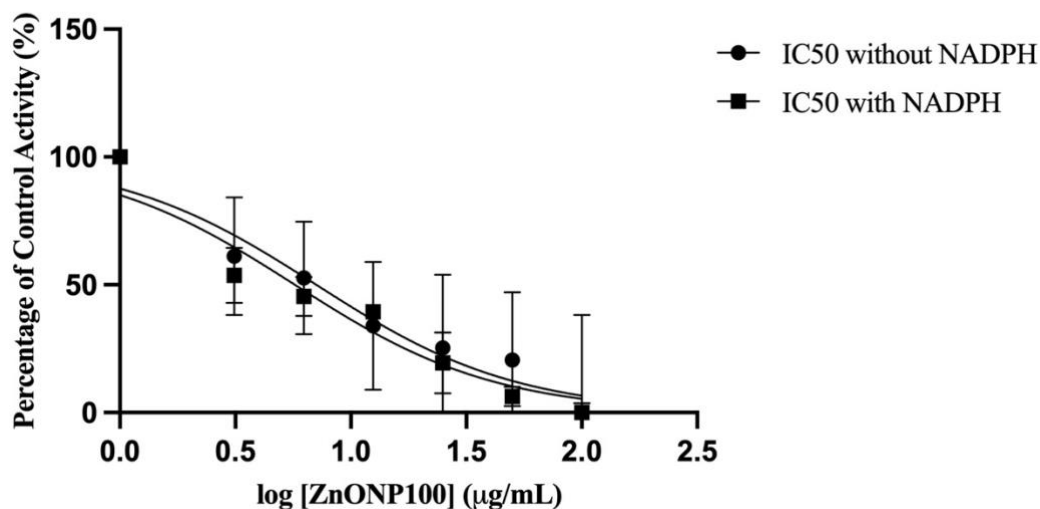
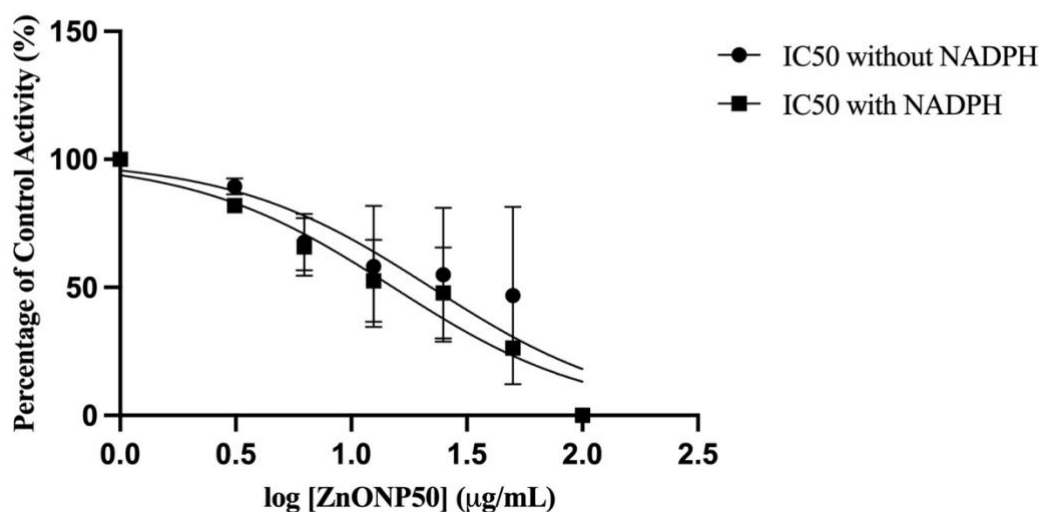


Figure 4.16. Time dependent inhibition of CYP2J2 by (A) ZnONP50 and (B) ZnONP100. The data sets were generated by plotting the percentage of control activity (%) against a range of ZnONPs' concentrations ($\mu\text{g/mL}$) presented as log concentration. IC_{50} with pre-incubation is denoted as 'IC₅₀ without NADPH' and IC_{50} without pre-incubation is denoted as 'IC₅₀ with NADPH'. Percentage of control of activity (%) denotes the remaining enzymatic activity based on the activity of the control reaction set at 100%. Each data point represents the mean \pm SD (n=3). CYP cytochrome P450, ZnONP50 Zinc oxide nanoparticles <50 nm, ZnONP100 Zinc oxide nanoparticles <100 nm, IC₅₀ half-maximal inhibitory concentration, NADPH nicotinamide adenine dinucleotide phosphate.

A) **Time Dependent Inhibition of CYP3A5 in Presence of Varying Concentrations of ZnONP50**



B) **Time Dependent Inhibition of CYP3A5 in Presence of Varying Concentrations of ZnONP100**

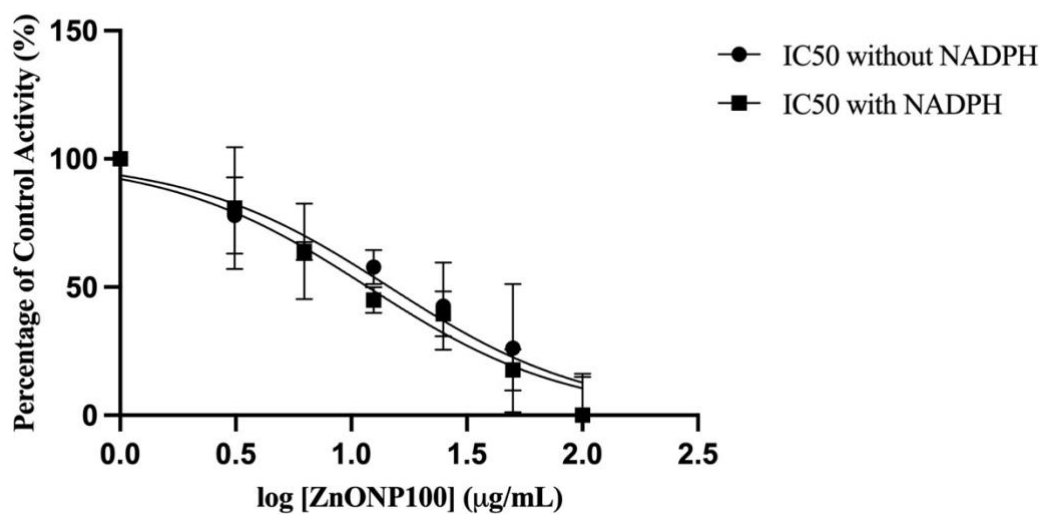


Figure 4.17. Time dependent inhibition of CYP3A5 by (A) ZnONP50 and (B) ZnONP100. The data sets were generated by plotting the percentage of control activity (%) against a range of ZnONPs' concentrations ($\mu\text{g/mL}$) presented as log concentration. IC_{50} with pre-incubation is denoted as ' IC_{50} without NADPH' and IC_{50} without pre-incubation is denoted as ' IC_{50} with NADPH'. Percentage of control of activity (%) denotes the remaining enzymatic activity based on the activity of the control reaction set at 100%. Each data point represents the mean \pm SD ($n=3$). CYP cytochrome P450, ZnONP50 Zinc oxide nanoparticles <50 nm, ZnONP100 Zinc oxide nanoparticles <100 nm, IC_{50} half-maximal inhibitory concentration, NADPH nicotinamide adenine dinucleotide phosphate.

Table 4.9. Summary of IC_{50} -shift ratios for all CYP isozymes tested for mechanism-based inhibition by their respective ZnO particle. IC_{50} half maximal inhibitory concentration, CYP cytochrome P450, ZnO zinc oxide.

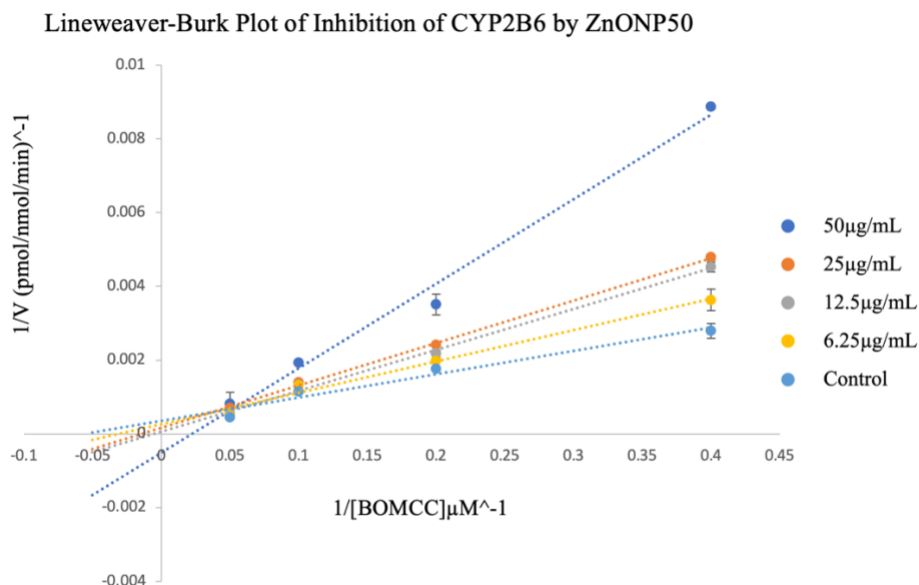
CYP Isozyme	ZnO Particle	Figure	IC_{50} -shift
CYP2B6	ZnONP50	4.13A	4.79
	ZnONP100	4.13B	1.05
CYP2C8	ZnONP50	4.14	2.84
CYP2E1	ZnONP50	4.15A	0.47
	ZnONP100	4.15B	1.91
	ZnOBP	4.15C	1.21
CYP2J2	ZnONP50	4.16A	2.19
	ZnONP100	4.16B	1.24
CYP3A5	ZnONP50	4.17A	1.46
	ZnONP100	4.17B	1.24

Based on Table 4.9, the pairings of ZnONP50 and CYP2B6, CYP2C8, and CYP2J2 were able to yield a fold-shift greater than 2. Thus, ZnONP50 were categorised as time-dependent inhibitor of these CYP isozymes.

4.3.6 Determination of K_i and Mode of Inhibition

IC_{50} values were determined to collect quantitative information and to assess whether the three types of ZnO particles were able to inhibit the examined CYP isozymes in a size-dependent manner (Cer et al., 2009). As IC_{50} value determination allows efficient screening owing to its requirement of minimal consumables and time, the previous assays were used to screen potential inhibition pairings. However, IC_{50} -value based ranking of potential inhibitors' potency, may be misleading as they depend on several factors such as the concentration of the substrate chosen. Additionally, IC_{50} values retrieved is dependent on the type of inhibition by reversible inhibitors (Georgakis et al., 2020). Thus, to compare the potency of inhibition of the different ZnO particles, K_i is preferred. K_i assays are more time consuming and require more consumables compared to IC_{50} assays, therefore they were only conducted with pairings which exhibited significant inhibitory potential (Table 4.8). Additionally, the IC_{50} assay results were used as a guide to decide the appropriate substrate and ZnO particle concentration for each CYP isozyme and ZnO particle pairing (Jeong et al., 2009).

A)



B)

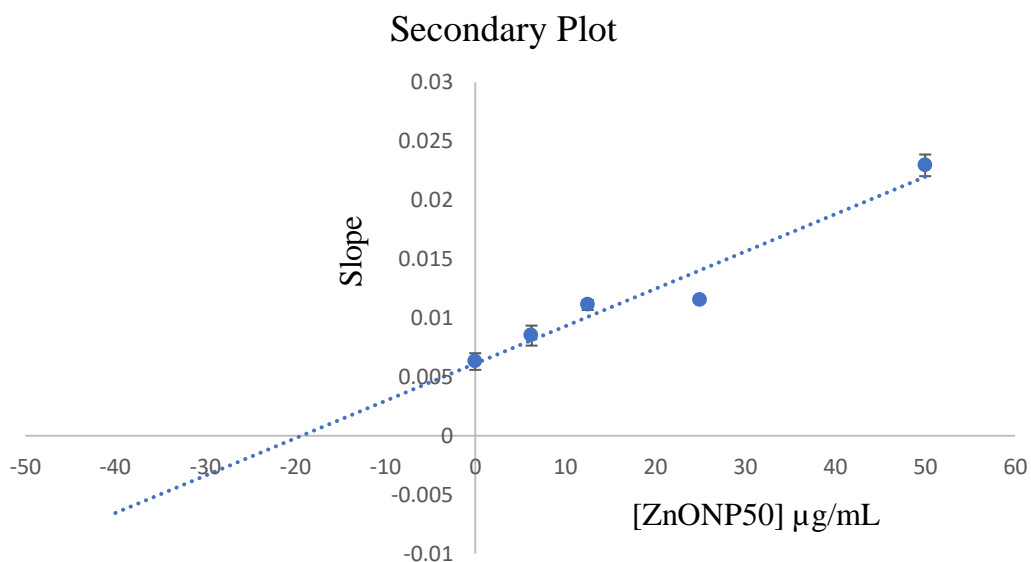
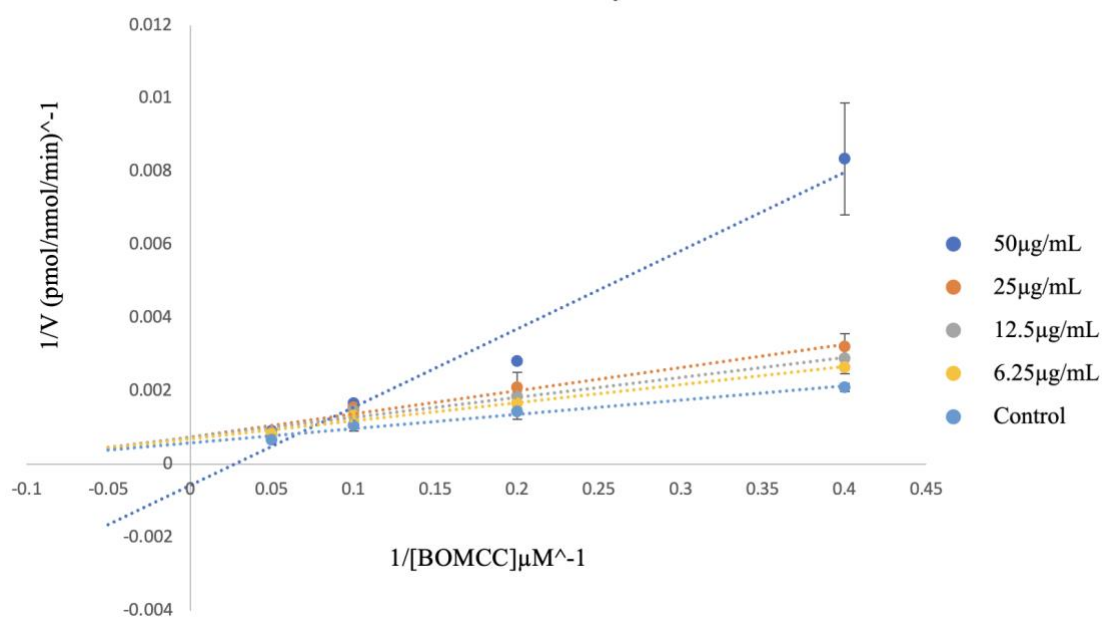


Figure 4.18. **A)** Lineweaver-Burk plot of inhibition of CYP2B6 by ZnONP50 at the indicated concentrations of ZnONP50 (0, 6.25, 12.5, 25, and 50 μg/mL) and Vivid® Substrate (BOMCC) (2.5, 5, 10, and 20 μM). **B)** Secondary plot derived from the slopes of the Lineweaver-Burk plot against the ZnONP50 concentration (0, 6.25, 12.5, 25, and 50 μg/mL) was used to derive the inhibition constant, K_i . Each data point represents the mean \pm SD (n=3). *CYP* cytochrome P450, *ZnONP50* Zinc oxide nanoparticles <50 nm, *BOMCC* 7-benzyloxymethyloxy-3-cyanocoumarin.

A) Lineweaver-Burk Plot of Inhibition of CYP2B6 by ZnONP100



B) Secondary Plot

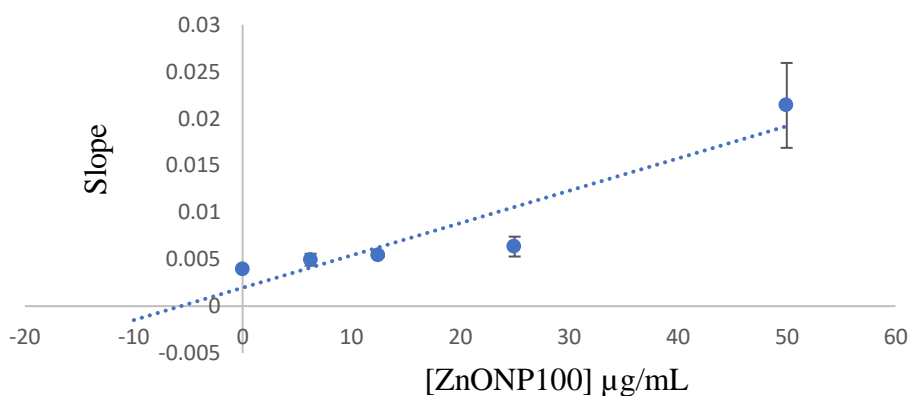
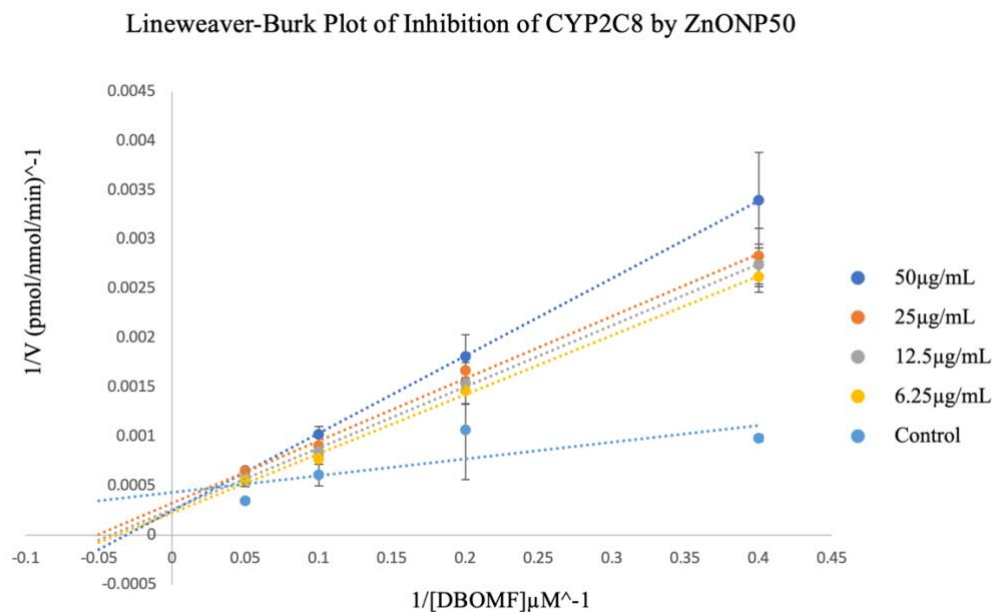


Figure 4.19. **A)** Lineweaver-Burk plot of inhibition of CYP2B6 by ZnONP100 at the indicated concentrations of ZnONP100 (0, 6.25, 12.5, 25, and 50 μg/mL) and Vivid® Substrate (BOMCC) (2.5, 5, 10, and 20 μM). **B)** Secondary plot derived from the slopes of the Lineweaver-Burk plot against the ZnONP100 concentration (0, 6.25, 12.5, 25, and 50 μg/mL) was used to derive the inhibition constant, K_i . Each data point represents the mean \pm SD (n=3). CYP cytochrome P450, ZnONP100 Zinc oxide nanoparticles <100 nm, BOMCC 7-benzyloxymethoxy-3-cyanocoumarin.

A)



B)

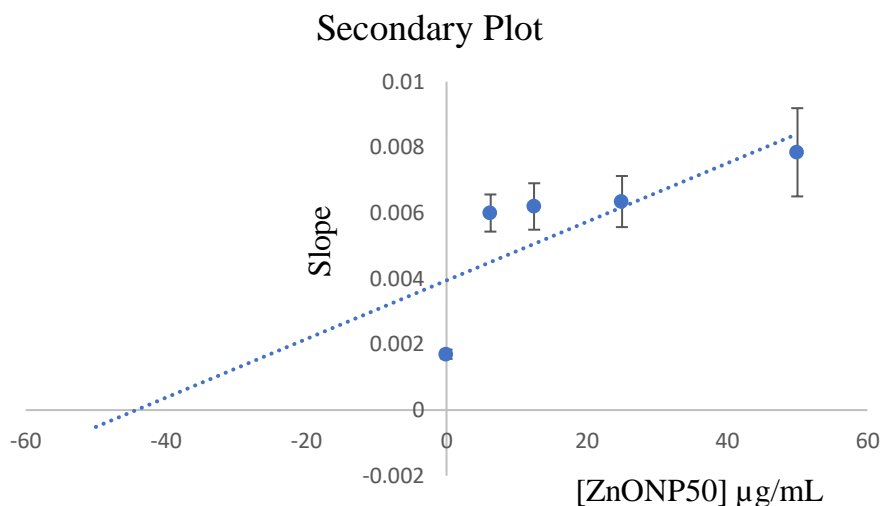


Figure 4.20. A) Lineweaver-Burk plot of inhibition of CYP2C8 by ZnONP50 at the indicated concentrations of ZnONP50 (0, 6.25, 12.5, 25, and 50 $\mu\text{g/mL}$) and Vivid[®] Substrate (DBOMF) (2.5, 5, 10, and 20 μM). B) Secondary plot derived from the slopes of the Lineweaver-Burk plot against the ZnONP50 concentration (0, 6.25, 12.5, 25, and 50 $\mu\text{g/mL}$) was used to derive the inhibition constant, K_i . Each data point represents the mean \pm SD (n=3). CYP cytochrome P450, ZnONP50 Zinc oxide nanoparticles <50 nm, DBOMF di-(benzyl-O-methyl)-fluorescein.

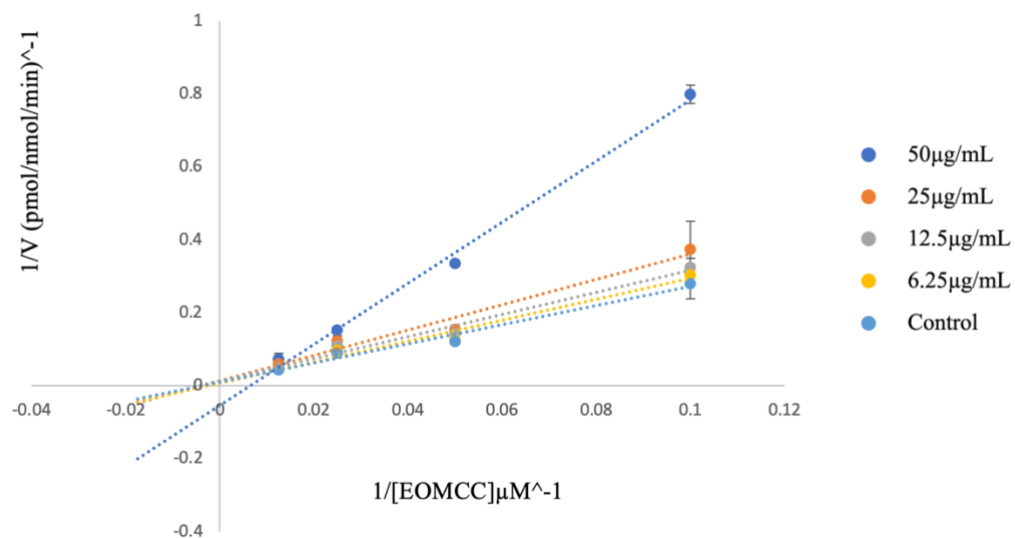
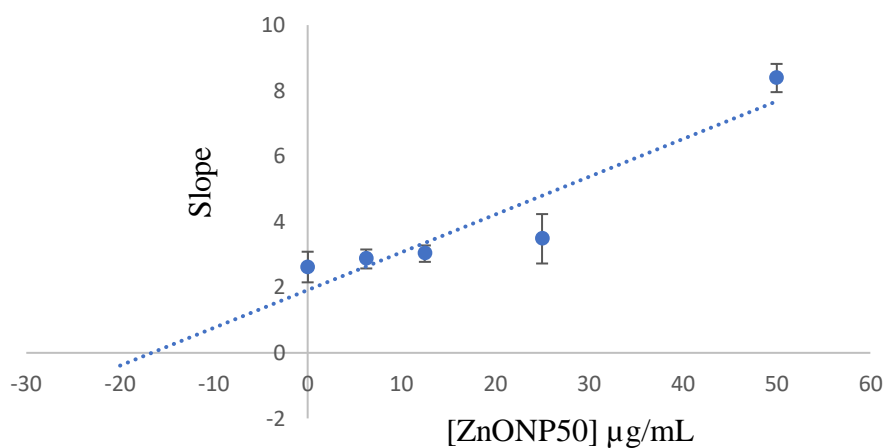
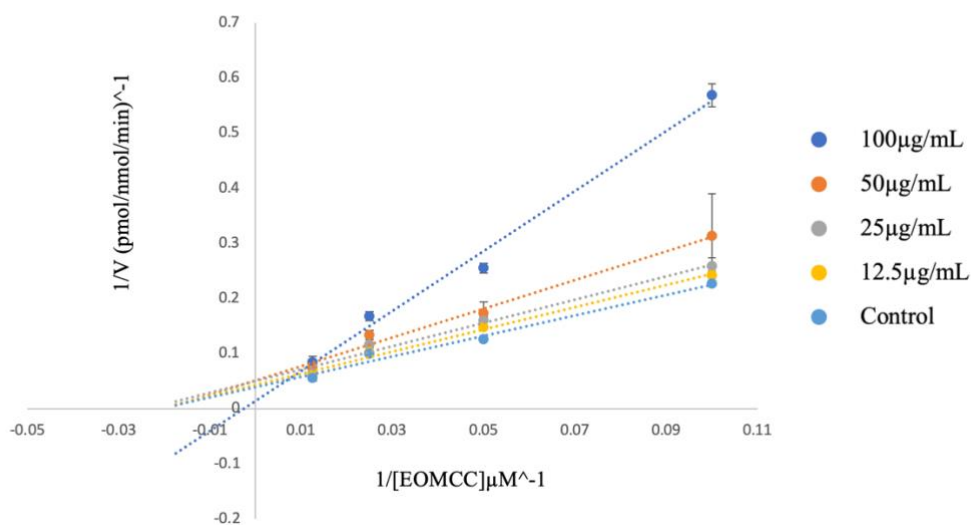
A**Lineweaver-Burk Plot of Inhibition of CYP2E1 by ZnONP50****B****Secondary Plot**

Figure 4.21. A) Lineweaver-Burk plot of inhibition of CYP2E1 by ZnONP50 at the indicated concentrations of ZnONP50 (0, 6.25, 12.5, 25, and 50 μg/mL) and Vivid® Substrate (EOMCC) (10, 20, 40, and 80 μM). **B)** Secondary plot derived from the slopes of the Lineweaver-Burk plot against the ZnONP50 concentration (0, 6.25, 12.5, 25, and 50 μg/mL) was used to derive the inhibition constant, K_i . Each data point represents the mean \pm SD (n=3). CYP cytochrome P450, ZnONP50 Zinc oxide nanoparticles <50 nm, EOMCC 7-ethoxy-methoxy-3-cyano-coumarin.

A) Lineweaver-Burk Plot of Inhibition of CYP2E1 by ZnONP100



B) Secondary Plot

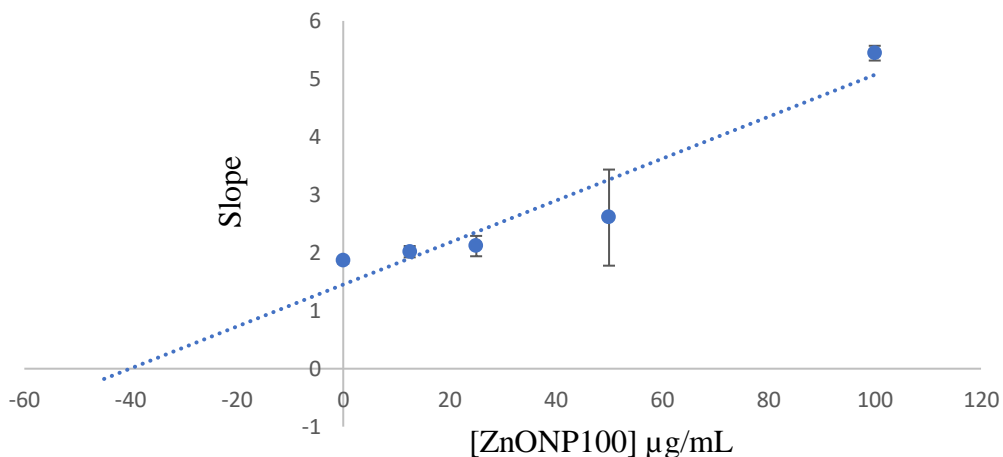
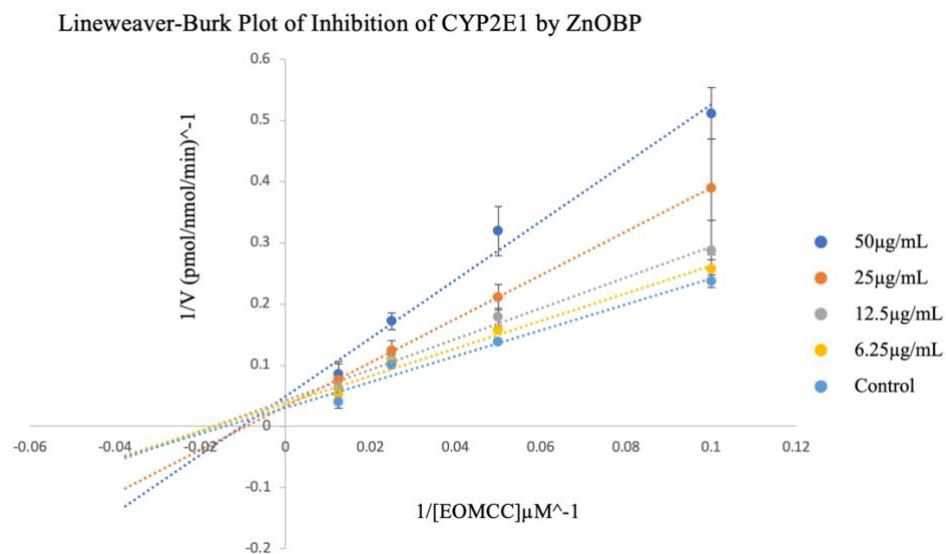


Figure 4.22. **A)** Lineweaver-Burk plot of inhibition of CYP2E1 by ZnONP100 at the indicated concentrations of ZnONP100 (0, 12.5, 25, 50, and 100 µg/mL) and Vivid® Substrate (EOMCC) (10, 20, 40, and 80 µM). **B)** Secondary plot derived from the slopes of the Lineweaver-Burk plot against the ZnONP100 concentration (0, 12.5, 25, 50, and 100 µg/mL) was used to derive the inhibition constant, K_i . Each data point represents the mean \pm SD ($n=3$). *CYP* cytochrome P450, *ZnONP100* Zinc oxide nanoparticles <100 nm, *EOMCC* 7-ethoxy-methoxy-3-cyano-coumarin.

A)



B)

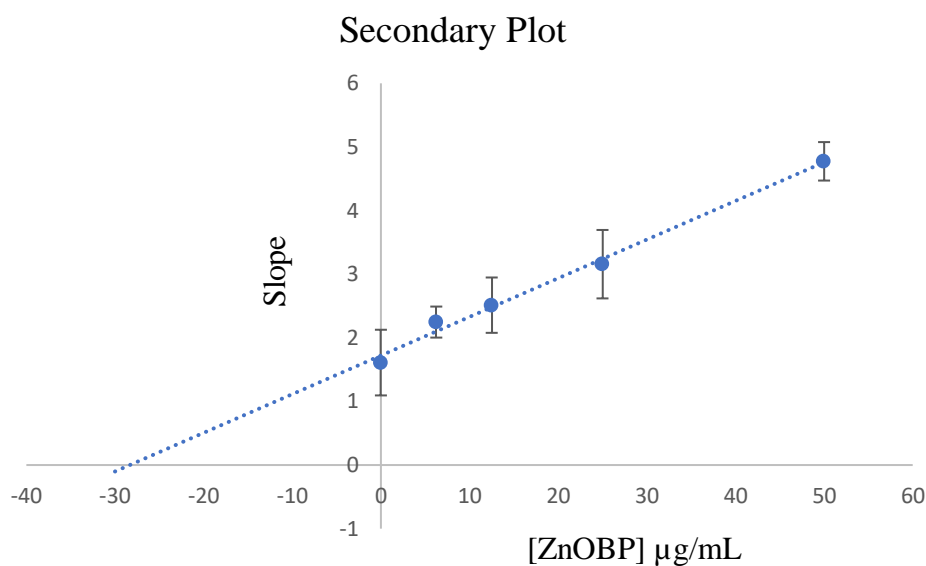


Figure 4.23. **A)** Lineweaver-Burk plot of inhibition of CYP2E1 by ZnOBP at the indicated concentrations of ZnOBP (0, 6.25, 12.5, 25, and 50 µg/mL) and Vivid[®] Substrate (EOMCC) (10, 20, 40, and 80 µM). **B)** Secondary plot derived from the slopes of the Lineweaver-Burk plot against the ZnOBP concentration (0, 6.25, 12.5, 25, and 50 µg/mL) was used to derive the inhibition constant, K_i . Each data point represents the mean \pm SD (n=3). *CYP* cytochrome P450, *ZnOBP* Zinc oxide bulk particles, *EOMCC* 7-ethoxy-methoxy-3-cyano-coumarin.

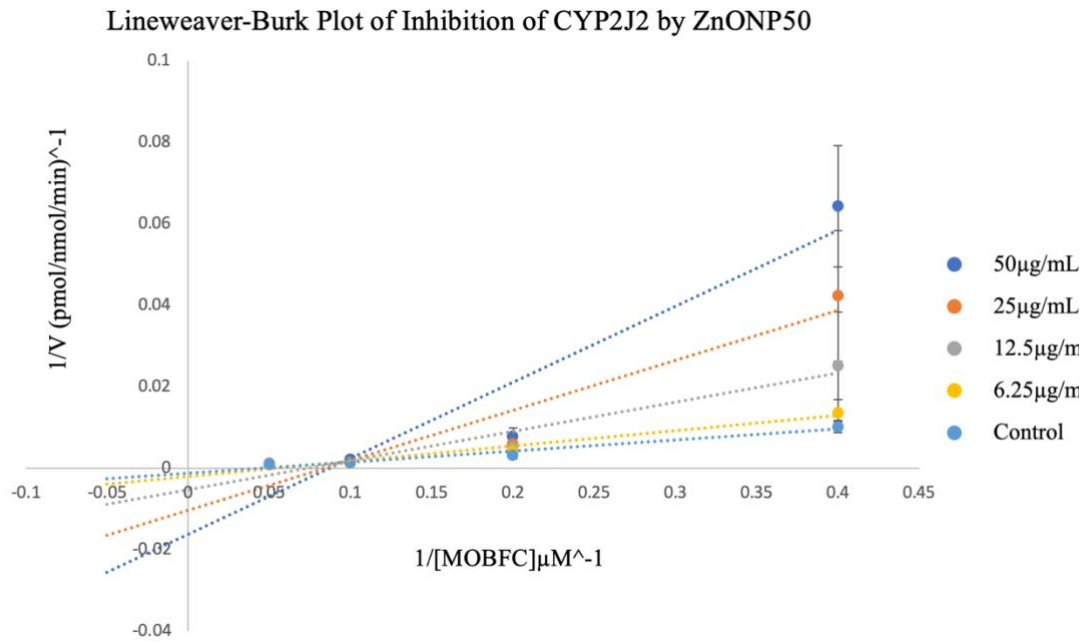
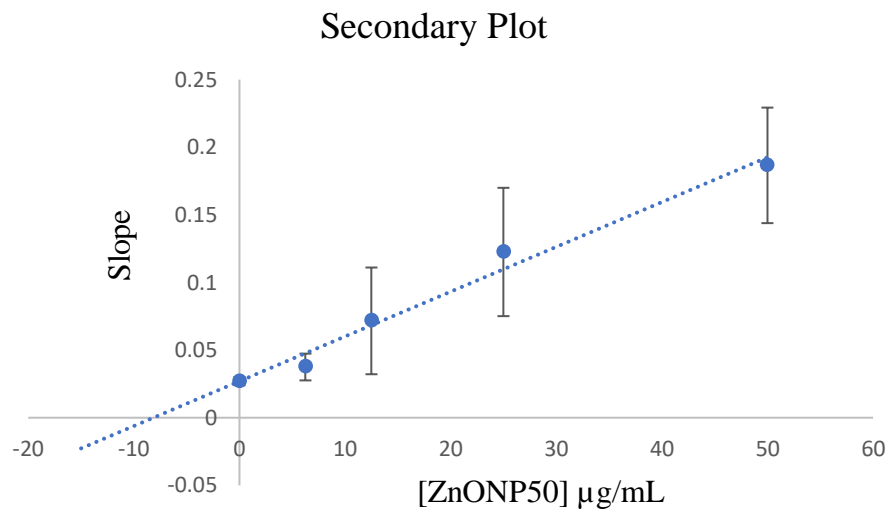
A**B**

Figure 4.24. **A)** Lineweaver-Burk plot of inhibition of CYP2J2 by ZnONP50 at the indicated concentrations of ZnONP50 (0, 6.25, 12.5, 25, and 50 μg/mL) and Vivid® Substrate (MOBFC) (2.5, 5, 10, and 20 μM). **B)** Secondary plot derived from the slopes of the Lineweaver-Burk plot against the ZnONP50 concentration (0, 6.25, 12.5, 25, and 50 μg/mL) was used to derive the inhibition constant, K_i . Each data point represents the mean \pm SD (n=3). *CYP* cytochrome P450, *ZnONP50* Zinc oxide nanoparticles <50 nm, *MOBFC* 7-P-methoxy-benzyloxy-4-trifluoro-coumarin.

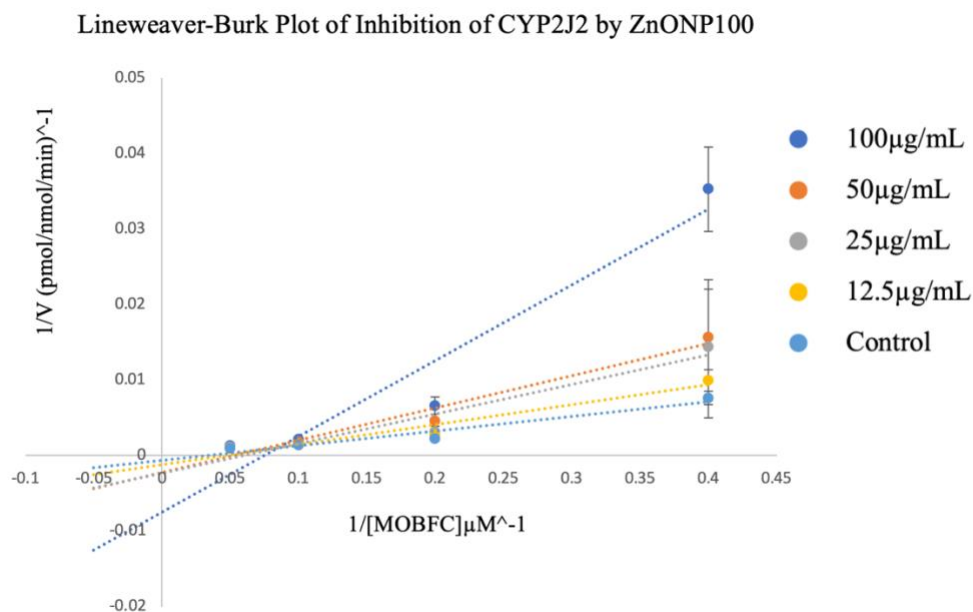
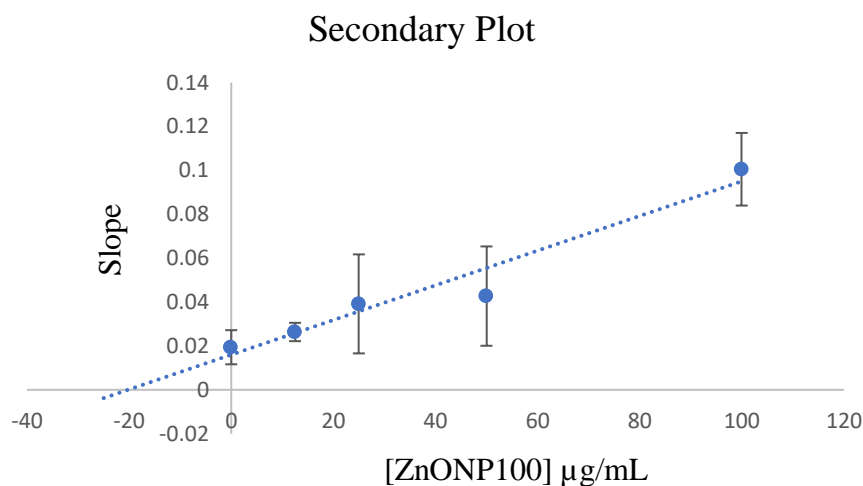
A)**B)**

Figure 4.25. **A)** Lineweaver-Burk plot of inhibition of CYP2J2 by ZnONP100 at the indicated concentrations of ZnONP100 (0, 12.5, 25, 50, and 100 μg/mL) and Vivid[®] Substrate (MOBFC) (2.5, 5, 10, and 20 μM). **B)** Secondary plot derived from the slopes of the Lineweaver-Burk plot against the ZnONP100 concentration (0, 12.5, 25, 50, and 100 μg/mL) was used to derive the inhibition constant, K_i . Each data point represents the mean ± SD (n=3). CYP cytochrome P450, ZnONP100 Zinc oxide nanoparticles <100 nm, MOBFC 7-P-methoxy-benzyloxy-4-trifluoro-coumarin.

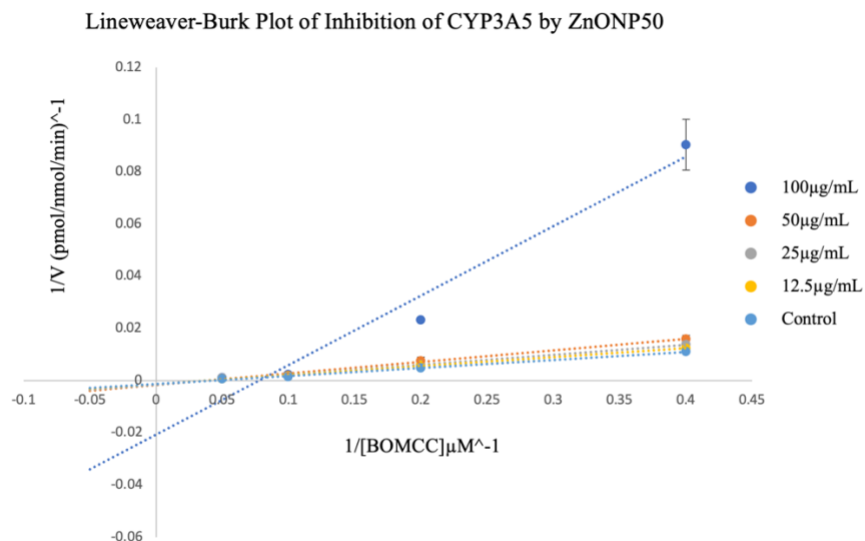
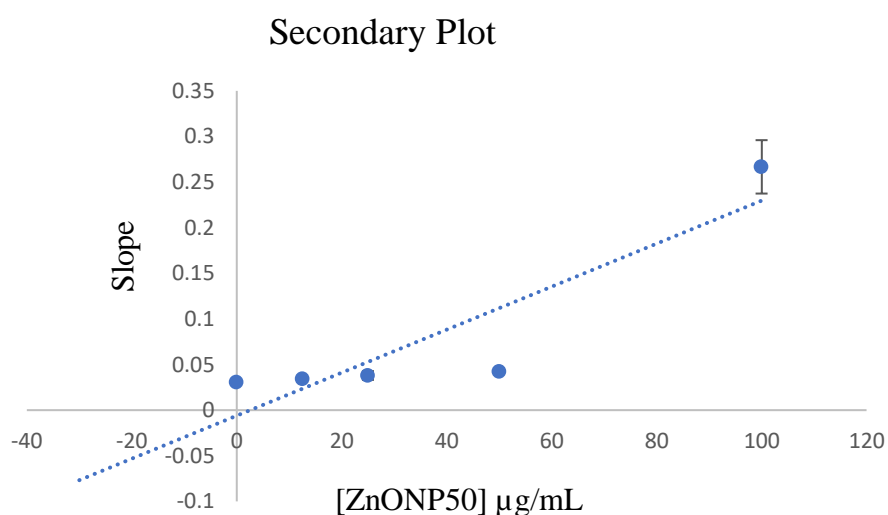
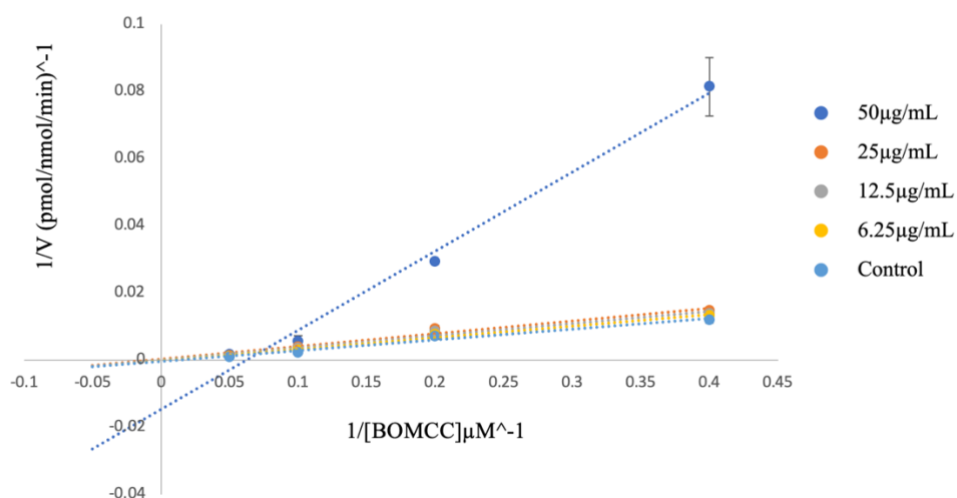
A)**B)**

Figure 4.26. **A)** Lineweaver-Burk plot of inhibition of CYP3A5 by ZnONP50 at the indicated concentrations of ZnONP50 (0, 12.5, 25, 50, and 100 $\mu g/mL$) and Vivid[®] Substrate (BOMCC) (2.5, 5, 10, and 20 μM). **B)** Secondary plot derived from the slopes of the Lineweaver-Burk plot against the ZnONP50 concentration (0, 12.5, 25, 50, and 100 $\mu g/mL$) was used to derive the inhibition constant, K_i . Each data point represents the mean \pm SD ($n=3$). *CYP* cytochrome P450, *ZnONP50* Zinc oxide nanoparticles <50 nm, *BOMCC* 7-benzyloxymethoxy-3-cyanocoumarin.

A)

Lineweaver-Burk Plot of Inhibition of CYP3A5 by ZnONP100

**B)**

Secondary Plot

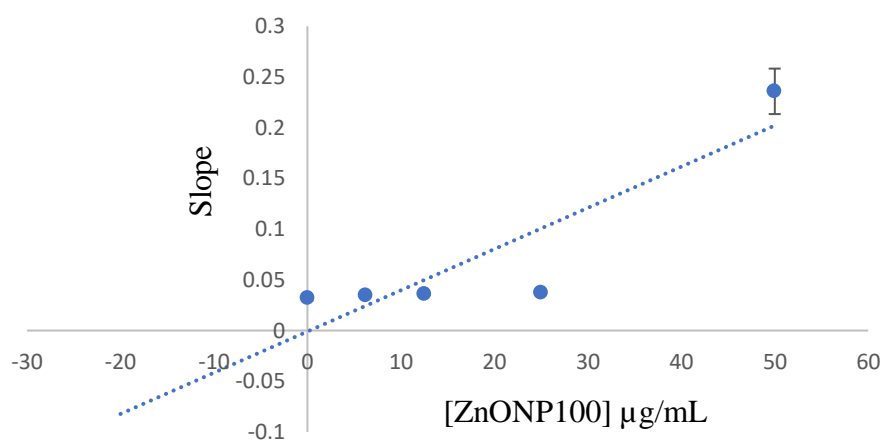


Figure 4.27. **A)** Lineweaver-Burk plot of inhibition of CYP3A5 by ZnONP100 at the indicated concentrations of ZnONP100 (0, 6.25, 12.5, 25, 50, and 100 $\mu\text{g/mL}$) and Vivid[®] Substrate (BOMCC) (2.5, 5, 10, and 20 μM). **B)** Secondary plot derived from the slopes of the Lineweaver-Burk plot against the ZnONP100 concentration (0, 6.25, 12.5, 25, 50, and 100 $\mu\text{g/mL}$) was used to derive the inhibition constant, K_i . Each data point represents the mean \pm SD ($n=3$). CYP cytochrome P450, BOMCC 7-benzyloxymethoxy-3-cyanocoumarin.

The inhibition constant, K_i , and inhibition mode of ZnO particles on CYP isozymes were determined for CYP2B6 (ZnONP50 and ZnONP100), CYP2C8 (ZnONP50), CYP2E1 (ZnONP50, ZnONP100, and ZnOBP), CYP2J2 (ZnONP50 and ZnONP100) and CYP3A5 (ZnONP50 and ZnONP100).

The standard curve equations derived from Figure A.4.1 to A.4.5 in the Appendix were used to calculate the formation of metabolites of the CYP isozymes under the presence of respective ZnO particles. The inhibition pattern of the ZnO particles were estimated from the Lineweaver-Burk plots, which were plotted as the linear regression reciprocal of the respective substrate concentrations against the reciprocal of the enzymatic velocities. For all CYP isozyme and ZnO particle pairings, the enzymatic activity diminished following a concentration-dependent pattern. The equations and estimated mode of inhibition for each CYP isozyme and ZnO particle pairing have been summarised in the Appendix under Table A.4.2 and Table 4.10 respectively. Secondary plots were generated by plotting the slopes from the primary Lineweaver-Burk plot against the concentration range of the respective ZnO particle. The equation obtained from the secondary plot was used to derive the K_i value. The K_i values yielded for each CYP isozyme and ZnO particle have been summarised under Table 4.10.

Based on Table 4.10, ZnONP50 inhibited CYP2B6, CYP2E1, and CYP2J2 in a more potent manner when compared to the larger sized ZnONP100. Thus, it can be concluded, that these CYP isozymes were inhibited in a size-dependent manner.

Table 4.10. Summary of the modes of inhibition and K_i for all CYP isozymes under the presence of the respective ZnO particle. K_i inhibition constant, CYP cytochrome P450, ZnO zinc oxide.

CYP Isozyme	ZnO Particle	Figure	Mode of Inhibition	Inhibition Constant (K_i) ($\mu\text{g/mL}$)
CYP2B6	ZnONP50	4.18A, 4.18B	Mixed	20.33
	ZnONP100	4.19, 4.19B	Mixed	6.67
CYP2C8	ZnONP50	4.20A, 4.20B	Competitive	43.33
CYP2E1	ZnONP50	4.21A, 4.21B	Mixed	16.63
	ZnONP100	4.22A, 4.22B	Mixed	40.1
	ZnOBP	4.23A, 4.23B	Competitive	28.3
CYP2J2	ZnONP50	4.24A, 4.24B	Non-competitive	8.18
	ZnONP100	4.25A, 4.25B	Mixed or Non-competitive	20.0
CYP3A5	ZnONP50	4.26A, 4.26B	Non-competitive	2.54
	ZnONP100	4.27A, 4.27B	Non-competitive	0.5

Infiltrating a biological system allows foreign particles, such as NPs and BPs, to interact with various biomolecules (Ahsan et al., 2018). A leading cause of NP-based toxicity is due to NP-protein interaction. NP-protein interaction may lead to conformational changes within the protein (Mukhopadhyay et al., 2018). These changes may influence a loss in the protein's activity, leading to probable unfavorable outcomes (Prabantu et al., 2021).

ZnONPs are an inorganic compound commonly used in several industrial fields (Siddiqi et al., 2018). Despite its beneficial roles, exposure to biological systems via different routes have demonstrated that ZnONPs are able to elicit detrimental effects (Vimercati et al., 2020). Amongst commonly used engineered-metal oxide particles, ZnONPs have been categorised as one of the most toxic due to its low medial dose value (Chen et al., 2012). Bioavailable ZnONPs are able to permeate into the blood stream by the gastrointestinal tract; this property allows several organs, including the liver, to be influenced by its effects (Mittag et al., 2022).

The liver metabolises pharmaceutical drugs through the CYP system (Gilani & Cassagnol, 2021). The pharmacokinetics of drugs can be modified through the inhibition of CYP isozymes, which subsequently changes the intended metabolic process of the ingested medication. The alteration in the metabolic process may result in decreased clinical efficacy and/or adverse drug reactions (Deodhar et al., 2020). Additionally, decreased metabolism increases the bioavailability of the drug, as the clearance rate declines. This may lead to the manifestation of drug toxicity (Zhao et al., 2021).

It is important to note that NPs have a higher number of atoms on their surface when compared to their respective BPs, which make them more reactive and responsive. Additionally, as a particle's size decreases, its dispersion and transparency properties increase (Gupta & Xie, 2018). These properties call into question whether the biological activity of ZnONPs may differ significantly from that of ZnOBP. This study evaluated the size-dependent inhibitory potential and the mode of inhibition of ZnONP50, ZnONP100, and ZnOBP at concentrations ranging from 3.13 µg/mL - 100 µg/mL on seven major drug metabolizing CYP isozymes: CYP1A2, CYP2A6, CYP2B6, CYP2C8, CYP2E1, CYP2J2, and CYP3A5.

There are several screening methods available to investigate the enzymatic activity of CYP isozymes, and they each have advantages and disadvantages associated with them. Some of these screening methods include: the usage of precision-cut liver slices (PCLS), high performance liquid chromatography (HPLC), luminescence-based assays, and fluorescence-based assays (N. et al., 2023; Ung et al., 2018).

PCLS retain all hepatic tissue and cells in their native environment including all intracellular and extracellular matrices (Dewyse et al., 2021). Due to the model's retention of available metabolising enzymes, it allows researchers to use it to investigate hepatic metabolism. Despite its advantageous features allowing it to be used as an *ex vivo* model, PCLS have three major disadvantages. Firstly, as human donor tissue is scarce, there is high competition between researchers (De Graaf et al., 2010). Secondly, as the liver tissue's quality differs from one individual to the next, the reproducibility of results is affected; the basal CYP isozyme expression can vary up to 500-fold (Dewyse et al., 2021). Lastly, PCLS undergo rapid damage and necrosis within 4-6 days of harvesting (De Graaf et al., 2010).

In terms of HPLC, the assay mixture containing the required components (buffer, probe substrate, cofactors, and CYP isozymes) is incubated before the quantification of formed metabolites is conducted by the HPLC system. The results attained by HPLC are of high precision and sensitivity (Blum, 2014). However, the extraction procedure encompassing the removal of protein and other biomolecules from the sample is laborious. Additionally, a large assay volume and high concentration of the enzyme is necessary to reach the threshold required for optimal detection. Furthermore, HPLC assays require a substantial amount of time per sample (Petrova & Sauer, 2017).

Luminescent-based assays utilise multi-well plates to quantify the enzymatic activity of CYP isozymes. These assays utilise luciferin derivatives as CYP isozyme's probe substrates as they are luminogenic, which are metabolised into luciferin by the enzyme. Luciferin interacts with the surrounding luciferase and is able to produce a luminescent light (Kudryasheva & Kovel, 2019). While these assays are highly sensitive, effective, and cheap as they require minimal reagents, the activity readings are lower compared to the actual activity. The low readings occur due to low concentrations of the luminescent substrate used to obtain the optimal luminescent signal-to-noise ratio reading (Zaver et al., 2021).

Fluorometric-based assays are carried out in multi-well plates to screen the inhibitory potential of various compounds on CYP isozymes. The assays require fluorogenic substrate probes which solubilise and form metabolites efficiently and possess minimal background fluorescence to quantify the enzyme's activity. The required time to run multiple samples and to attain results is considerably short. As the requirement of reagents are minimal, fluorometric-based assays are affordable (Wannigama et al., 2019). However, the assay requires the potential inhibitor to not exhibit fluorometric properties as to not interfere with the acquired results. Additionally, fluorometric readings may be skewed under the presence of excess NADPH, requiring additional experimental steps to remove the excess compound (Donato et al., 2004).

Considering the various advantages and disadvantages of each screening method, fluorometric-based assays were chosen as the optimal option. The disadvantages regarding fluorometric-based assays have been addressed by the Vivid® CYP450 Screening Kits.

Vivid® CYP450 screening kits were utilised in this study for its distinct advantages. Firstly, BACULOSOMES® Plus Reagent's express a singular isoform, which allow researchers to evaluate the individual enzymatic activity under the presence of test compounds, without the involvement and interference of other isozymes (Ozgenic, n.d.). Secondly, Vivid® Substrates were developed with blocked fluorophores, which eliminates substantial amounts of produced background fluorescence. Another advantage associated with Vivid® Substrates are their excitation and emission wavelengths as they do not interfere or intersect with those of NADPH. Thus, it does not interfere with metabolite level detection. In terms of metabolic reactions, Vivid® Substrates are composed of two sites for metabolic cleavage, which allows oxidation to occur at either site and to subsequently release the desired high fluorescent product. This characteristic contributes to the high rate of metabolic reaction. Additionally, Vivid® Substrates are highly soluble in aqueous solvents, which permits a reduced amount of solvent to be used; inhibitory effect of the solvent on the isozymes' enzymatic activity is decreased as well (Ozgenic, n.d.). Lastly, as the kit employs fluorogenic high throughput screening methods to measure inhibition, loss of reagents and time required to obtain data is minimised (Marks et al., 2002; Ung et al., 2018).

Reversible inhibition' plausibility was investigated for each ZnO particle and CYP isozyme pairing using IC_{50} and K_i . IC_{50} provides quantitative information regarding the quantity of an inhibitor required to reduce the biomolecule's metabolic activity by 50% (Aykul & Martinez-Hackert, 2016). K_i is an indicator of the inhibitor's potency. Additionally, it allows researchers to graphically categorise the type of reversible inhibition exhibited by the inhibitor (Bachmann & Lewis, 2005).

ZnONP50 reversibly inhibited CYP2B6 and CYP2E1 via mixed mode of inhibition. Reversible inhibition of CYP2C8 by ZnONP50 was evident via competitive mode of inhibition. Lastly, ZnONP50 reversibly inhibited CYP2J2 and CYP3A5 via non-competitive mode of inhibition. ZnONP100 reversibly inhibited CYP2B6 and CYP2E1 via mixed mode of inhibition. Reversible inhibition of CYP2J2 by ZnONP100 was evident via mixed or non-competitive mode of inhibition. Lastly, ZnONP100 reversibly inhibited CYP3A5 via non-competitive mode of inhibition. ZnOBP reversibly inhibited CYP2E1 via competitive mode of inhibition.

During competitive inhibition, the ZnO particle and the substrate compete for the mutual active site of the CYP isozyme. Once the ZnO particle is able to occupy the active site, it forms a CYP-ZnO particle complex, which inhibits the enzyme's metabolic capabilities until the ZnO particle dissociates. Competitive inhibitors are usually structural analogs to the substrate but are unreactive. Competitive inhibition can be surmounted at any concentration by increasing the substrate's concentration (Attaallah & Amine, 2021). During noncompetitive inhibition, the ZnO particle binds to the allosteric site instead of the active site of the CYP isozyme. This results in a conformational change of the active site of the CYP isozyme, which affects the substrate's binding ability. Due to the structural change, noncompetitive inhibition cannot be surmounted by increasing the substrate's concentration (Delaune & Alsayouri, 2022). During uncompetitive inhibition, the ZnO particle binds directly onto the enzyme-substrate complex, as the inhibitor does not have strong affinity towards free isozymes (Ramsay & Tipton, 2017). The underlying principle of mixed-type reversible inhibition suggests that the inhibitor, ZnO particle, is able to affect the binding of the substrate by blocking it and is able to reduce the velocity of the CYP isozyme's catalytic reaction (Delaune & Alsayouri, 2022). All sub-types of reversible inhibition results in decreased metabolism and clearance of bioavailable drugs, which is a pharmacokinetic parameter (Deodhar et al., 2020). Clearance is defined as the amount of plasma, from which a substance is removed per unit of time. If the clearance rate of a prescribed medication is known, doctors and pharmacists are able to determine the correct dosage (concentration and time) required to maintain certain plasma levels to attain optimal therapeutic efficacy; clearance is important to determine the maintenance dose (Benet et al., 2021). An unexpected decrease in the drug's clearance results in an increase of its half-life, which increases the drug's bioavailability. Increased bioavailability may lead to unwanted side effects: inefficacy, adverse drug reactions, and toxicity (Price & Patel, 2022).

As concluded based on Figure 4.12, CYP2B6, CYP2C8, CYP2E1, and CYP3A5 were inhibited in a size-dependent manner as the smallest sized ZnO particle elicited the strongest reversible inhibition towards these isozymes. Comparing the IC_{50} assay results with the K_i assay results, ZnONP50 exhibited the highest affinity towards CYP2B6, CYP2C8, CYP2E1, and CYP2J2. The outlier in this relationship is the CYP3A5 isozyme; ZnONP100 demonstrated stronger affinity towards the isozyme compared the smaller sized ZnONP50. Studies employing other variations of NPs yielded similar results; smaller sized NPs generated stronger reversible inhibition towards majority of the investigated CYP isozymes (Fröhlich et al., 2010;

Imai et al., 2014; Lamb et al., 2010; Sereemasapun et al., 2008; Warisnoicharoen et al., 2011; Yang et al., 2017).

Inhibition of CYP isozymes may also occur in an irreversible manner (Tu et al., 2021). Irreversible inhibition is also termed mechanism-based inhibition which is observed as TDI. As presented in Table 4.9, only ZnONP50 was able to generate a fold shift greater than 2 for CYP2B6, CYP2C8, and CYP2J2. Thus, it was categorised as an irreversible inhibitor. Greater concern is associated with mechanism-based inhibition, as the clinical outcome and inhibition may be more profound and long-lasting, when compared to reversible inhibition (Rock & Wienkers, 2022). TDIs manifest via irreversible covalent or non-covalent tight binding, which results in the loss of the enzyme's function. In a TDI, the degree of inhibition of the enzyme increases when it is incubated with the inhibitor prior to the addition of the substrate. It is important to note that irreversible inhibition persists despite the removal of the inhibitor (Tuley & Fast, 2018). Thus, TDIs involving CYP isozymes will display an amplified systematic exposure of co-administered drugs. An important example to note is mibefradil. Mibefradil is a mechanism-based inhibitor of CYP3A5. A low dosage of 50 mg prescribed once daily for three days is able to increase the plasma exposure of triazolam by nine-fold. Increased bioavailability of triazolam manifests as adverse symptoms including slurred speech, difficulty in breathing, seizures, and comas (Foti et al., 2011).

In terms of understanding the mechanism of interaction between ZnO particles and CYP isozymes, there are three plausible explanations.

The first mechanism focuses on the presence of oxygen groups in ZnO particles. The presence of oxygen molecules provides the particles with a negative surface charge, which allows them to create weak hydrogen bonds. Moreover, the oxygen molecular allow interactions sites to form between biomolecules via covalent and non-covalent bonding (Jiang et al., 2010; Limo et al., 2018). As confirmed through the EDX results, all three categories contained a substantial percentage of oxygen; ZnONP50 has the largest percentage of oxygen when compared to ZnONP100 and ZnOBP. This hypothesis supports the results retrieved in this study, as ZnONP50 were able to inhibit CYP2B6, CYP2C8, CYP2E1, and CYP3A5 in a size-dependent manner.

CYP isozymes are monooxygenases, as they require an external electron donor to function (Gilani & Cassagnol, 2022). In terms of the microsomal CYP isozymes used in this study, the reductase was required to generate and transport electrons for the enzymatic reaction to proceed. NADPH serves as the electron source. The transfer of the electron results in the activation of the oxygen molecule, while exposing an atom on the substrate, which transpires

simultaneously with the reduction of the second atom (Sangar et al., 2013). ZnONPs ability to permeate the cellular membrane and to disrupt enzymatic activity may obstruct the electron transport chain required for the CYP isozyme to function, which can alter the cycles leading to potential inhibition (Nakamura & Watano, 2018; Zhang et al., 2021).

ZnONPs' high surface area allows the majority of ZnO molecules to be distributed across the surface of the particle. In an active state, the oxygen atoms are able to form bonds with hydrogen atoms, leading to the dissolution of zinc ions. The reaction equation is as follows: $\text{ZnO} + 2\text{H}^+ \rightarrow \text{Zn}^{2+} + \text{H}_2\text{O}$ (Yang & Xie, 2006). As the dissolution and release rate of Zn^{2+} and the size of ZnO particles share a negative correlation, it is expected that the release rate is faster for smaller size ZnO particles when compared to their larger counterparts (Seray et al., 2021). As the dissolution of Zn^{2+} from ZnO particles is a key mechanism of its toxicity, it is hypothesised that it plays a role in its inhibition activity as well. Additionally, the increased rate of Zn^{2+} release from smaller sized ZnO particles, may explain the stronger inhibitory potential exhibited by ZnONP50 in this study.

This study has established that ZnO particles of various sizes, notably the smallest sized ZnONP50, were able to notably inhibit the metabolic function of various CYP isozymes, leading to an increased plausibility of adverse drug reactions of co-administered drugs. Thus, it is important to take note of a few commonly used clinical medications that are susceptible to CYP isozymes' inhibition consequences.

Efavirenz, a commonly prescribed human immunodeficiency virus (HIV) treatment, is a non-nucleoside reverse transcriptase inhibitor. As efavirenz has a narrow therapeutic window, the difference between the therapeutic plasma concentration and the toxic plasma concentration is slim (Tadesse et al., 2022). It undergoes hepatic metabolism by CYP2B6 into 8-hydroxy-efavirenz and 7-hydroxy-efavirenz. If inhibited, the plasma concentration of efavirenz is significantly higher than intended (Naidoo et al., 2014). Elevated plasma levels of the parent drug elicit adverse side effects: neurotoxicity and hepatic injury. Additionally, drug resistance may present as well (Hedrich et al., 2016).

Paclitaxel is a chemotherapeutic agent used to treat various types of solid cancers including breast, ovarian, and lung cancer (Wang & Du, 2022). Paclitaxel's metabolism occurs via oxidative metabolism within the liver by the CYP2C8 isozyme. CYP2C8 is primarily responsible for metabolizing paclitaxel into its primary metabolite, 6- α -hydroxypaclitaxel (Nakajima et al., 2005). As the therapeutic efficacy of paclitaxel depends on the metabolism of the parent compound into its metabolite, inhibition of CYP2C8's metabolic activity would significantly reduce the intended therapeutic efficacy. Additionally, the increased serum

concentration of the parent compound incites side effects including nausea, inflammation, and muscle pain (Wang & Du, 2022).

Halothane is an inhalation anesthetic used for inducing and maintaining general anesthesia. It is able to reduce the patient's blood pressure, pulse rate, and respiration rate (Gyorfi & Kim, 2022). Halothane is hepatically metabolised primarily by CYP2E1. CYP2E1's inhibition post-halothane administration commonly results in hepatotoxicity. Adverse consequences of increased bioavailable halothane include hepatitis, liver failure, and cardiac instability (Huang et al., 2017).

Tacrolimus is an immunosuppressive medication, which is prescribed to patients undergoing organ transplantation, mainly renal transplants. It acts as a calcineurin inhibitor and is able to prevent T-cell activation via inhibiting phosphate calcineurin. It is able to reduce the risk of graft rejections (Venkataramanan et al., 1995). As it has a narrow therapeutic window, the optimum dosage and plasma concentration is required for the drug to function properly. Tacrolimus is hepatically metabolised primarily by CYP3A5. Inhibition of CYP3A5 results in decreased metabolism, which subsequently leads to an increased plasma concentration resulting in neurotoxicity and/or nephrotoxicity. Additionally, elevated plasma levels of tacrolimus have resulted in patients experiencing graft dysfunction and rejection (Khan et al., 2020).

Despite the notable results yielded from this study, it is important to address two major limitations of the project. Firstly, as seen in the FESEM results, despite sonicating the ZnO particles to ensure complete dispersion prior to imaging, it is evident that all three sizes of ZnO particles displayed agglomeration and/or accumulation. Agglomeration of nanoparticles is known to occur due to the attraction of the particles to each other by weak forces. This leads to the formation of micron-sized entities. Nanoparticle aggregation may arise as a result of covalent and/or metabolic bonds forming between particles (Gosens et al., 2010). As a key component of this study focused on investigating the size-dependent inhibitory potential of ZnO particles, the formation of ZnO particle clusters may have amplified and/or compressed the actual inhibitory potential of the various sizes. To overcome this issue, it is suggested that the sonication process needs to be further optimized. Time, power, and temperature are the key components of the sonication process. It is important to overcome the aggregation issue, while ensuring no damage is done upon the particle's surface affecting its surface properties (Kaur et al., 2017). Secondly, as ZnO particles were directly introduced to the CYP isozymes *in vitro*, the assays conducted were not able to accurately imitate the actual oral, dermal, and/or inhalation of ZnOBP and ZnONPs that occur in the day-to-day life. ZnO

exposure via the three routes involves the mouth, stomach, blood stream, and the small intestines primarily (Mittag et al., 2022; Mittag et al., 2022). Thus, it is vital to investigate the size-dependent inhibitory effect of ZnO particles using a model which is able to imitate intestinal absorption to yield translatable clinical results. A proposed solution to overcome this limitation is the use of parallel artificial membrane permeability assays (PAMPA). PAMPA assays allow researchers to predict the transcellular passive absorption via artificial lipophilic membranes, which imitate the membrane barriers within the small intestines (Sun et al., 2017).

For a better understanding of the inhibitory relationship between ZnO particles and CYP isozymes, *in silico* studies are recommended, as molecular docking will allow researchers to model the interaction between the ZnO particle and the CYP isozyme at the atomic level. This will allow researchers to characterise the behavior of the ZnO particle near the active site of the target protein, and to further understand the underlying biochemical mechanism of the interaction (Meng et al., 2011). For clinically translatable results, *in vivo* studies using suitable models are required.

4.4 Conclusion

This chapter reported that ZnONP50 was able to strongly inhibit CYP2B6, CYP2C8, CYP2E1 and CYP2J2 in a size-dependent manner, while ZnONP100 demonstrated stronger inhibitory effects towards CYP3A5. Moreover, ZnONP50 was able to exert an irreversible inhibitory effect towards CYP2B6, CYP2C8, and CYP2J2. The findings of this chapter encourage additional *in silico* and *in vivo* studies to be carried out to better understand ZnONPs' inhibitory mechanism towards CYP isozymes.

References

- Abass, M. A., Selim, S. A., Selim, A. O., El-Shal, A. S., & Gouda, Z. A. (2017). Effect of orally administered zinc oxide nanoparticles on albino rat thymus and spleen. *IUBMB Life*, *69*(7), 528–539. <https://doi.org/10.1002/iub.1638>
- Ahmed, S. K. M., Mukherjee, P. K., Bahadur, S., Kar, A., Mukherjee, K., Karmakar, S., & Bandyopadhyay, A. (2015). Interaction potential of *Trigonella foenum-graceum* through cytochrome P450 mediated inhibition. *Indian Journal of Pharmacology*, *47*(5), 530. <https://doi.org/10.4103/0253-7613.165179>
- Ahsan, S. M., Rao, C. M., & Ahmad, M. F. (2018). Nanoparticle-protein interaction: The significance and role of protein corona. *Advances in Experimental Medicine and Biology*, *1048*, 175–198. https://doi.org/10.1007/978-3-319-72041-8_11/COVER
- Aijie, C., Huimin, L., Jia, L., Lingling, O., Limin, W., Junrong, W., Xuan, L., Xue, H., & Longquan, S. (2017). Central neurotoxicity induced by the instillation of ZnO and TiO₂ nanoparticles through the taste nerve pathway. *https://doi.org/10.2217/Nnm-2017-0171*, *12*(20), 2453–2470. <https://doi.org/10.2217/NNM-2017-0171>
- Akhtar, M. J., Alhadlaq, H. A., Alshamsan, A., Majeed Khan, M. A., & Ahamed, M. (2015). Aluminum doping tunes band gap energy level as well as oxidative stress-mediated cytotoxicity of ZnO nanoparticles in MCF-7 cells. *Scientific Reports*, *5*(September). <https://doi.org/10.1038/srep13876>
- Akiyama, R., Sato, Y., Kajiwarra, S., & Shishido, K. (2002). Cloning and Expression of Cytochrome P450 Genes, Belonging to a New P450 Family, of the Basidiomycete *Lentinul*. *Bioscience, Biotechnology and Biochemistry*, *66*(10), 2183–2188. <https://doi.org/10.1271/bbb.66.2183>
- Alberts, B., Johnson, A., Lewis, J., Raff, M., Roberts, K., & Walter, P. (2002). *Caenorhabditis Elegans: Development from the Perspective of the Individual Cell. Molecular Biology of the Cell, 4th Edition.* <https://www.ncbi.nlm.nih.gov/books/NBK26861/>
- Albertson, D. G., & Thomson, J. N. (1976). The pharynx of *Caenorhabditis elegans*. *Philosophical Transactions of the Royal Society of London. B, Biological Sciences*, *275*(938), 299–325. <https://doi.org/10.1098/RSTB.1976.0085>
- Aliwarga, T., Evangelista, E. A., Sotoodehnia, N., Lemaitre, R. N., & Totah, R. A. (2018). Regulation of CYP2J2 and EET Levels in Cardiac Disease and Diabetes. *International Journal of Molecular Sciences 2018, Vol. 19, Page 1916, 19*(7), 1916. <https://doi.org/10.3390/IJMS19071916>
- Alonso Villela, S. M., Kraïem, H., Bouhaouala-Zahar, B., Bideaux, C., Aceves Lara, C. A., & Fillaudeau, L. (2020). A protocol for recombinant protein quantification by densitometry. *MicrobiologyOpen*, *9*(6), 1175–1182. <https://doi.org/10.1002/MBO3.1027>
- Altammar, K. A. (2023). A review on nanoparticles: characteristics, synthesis, applications, and challenges. *Frontiers in Microbiology*, *14*(April), 1–20. <https://doi.org/10.3389/fmicb.2023.1155622>
- Andersen, C. L., Jensen, J. L., & Ørntoft, T. F. (2004). Normalization of real-time quantitative reverse transcription-PCR data: a model-based variance estimation approach to identify genes suited for normalization, applied to bladder and colon cancer data sets. *Cancer Research*, *64*(15), 5245–5250. <https://doi.org/10.1158/0008-5472.CAN-04-0496>

- Anjum, S., Hashim, M., Malik, S. A., Khan, M., Lorenzo, J. M., Abbasi, B. H., & Hano, C. (2021). Recent advances in zinc oxide nanoparticles (Zno nps) for cancer diagnosis, target drug delivery, and treatment. *Cancers*, *13*(18). <https://doi.org/10.3390/cancers13184570>
- Antoniou, C., Kosmadaki, M. G., Stratigos, A. J., & Katsambas, A. D. (2008). Sunscreens - What's important to know. *Journal of the European Academy of Dermatology and Venereology*, *22*(9), 1110–1119. <https://doi.org/10.1111/J.1468-3083.2007.02580.X>
- Aquilante, C. L., Niemi, M., Gong, L., Altman, R. B., & Klein, T. E. (2013). PharmGKB summary: very important pharmacogene information for cytochrome P450, family 2, subfamily C, polypeptide 8. *Pharmacogenetics and Genomics*, *23*(12), 721. <https://doi.org/10.1097/FPC.0B013E3283653B27>
- Aslantas, Y., & Surmeli, N. B. (2019). Effects of N-terminal and C-terminal polyhistidine tag on the stability and function of the thermophilic P450 CYP119. *Bioinorganic Chemistry and Applications*, *2019*. <https://doi.org/10.1155/2019/8080697>
- Athar, F., & Templeman, N. M. (2022). C. elegans as a model organism to study female reproductive health. *Comparative Biochemistry and Physiology Part A: Molecular & Integrative Physiology*, *266*, 111152. <https://doi.org/10.1016/J.CBPA.2022.111152>
- Attaallah, R., & Amine, A. (2021). The kinetic and analytical aspects of enzyme competitive inhibition: Sensing of tyrosinase inhibitors. *Biosensors*, *11*(9). <https://doi.org/10.3390/BIOS11090322>
- Attia, H., Nounou, H., & Shalaby, M. (2018). Zinc Oxide Nanoparticles Induced Oxidative DNA Damage, Inflammation and Apoptosis in Rat's Brain after Oral Exposure. *Toxics 2018, Vol. 6, Page 29*, *6*(2), 29. <https://doi.org/10.3390/TOXICS6020029>
- Avery, L., & Horvitz, H. R. (1987). A cell that dies during wild-type C. elegans development can function as a neuron in a ced-3 mutant. *Cell*, *51*(6), 1071–1078. [https://doi.org/10.1016/0092-8674\(87\)90593-9](https://doi.org/10.1016/0092-8674(87)90593-9)
- Avery, L., & Shtonda, B. B. (2003). Food transport in the C. elegans pharynx. *Journal of Experimental Biology*, *206*(14), 2441–2457. <https://doi.org/10.1242/JEB.00433>
- Aykul, S., & Martinez-Hackert, E. (2016). Determination of half-maximal inhibitory concentration using biosensor-based protein interaction analysis. *Analytical Biochemistry*, *508*, 97–103. <https://doi.org/10.1016/J.AB.2016.06.025>
- Bachmann, K. A., & Lewis, J. D. (2005). Predicting inhibitory drug-drug interactions and evaluating drug interaction reports using inhibition constants. *Annals of Pharmacotherapy*, *39*(6), 1064–1072. <https://doi.org/10.1345/aph.1E508>
- Bahadur, S., Mukherjee, P., Milan Ahmmed, S., Kar, A., Harwansh, R., & Pandit, S. (2016). Metabolism-mediated interaction potential of standardized extract of *Tinospora cordifolia* through rat and human liver microsomes. *Indian Journal of Pharmacology*, *48*(5), 576–581. <https://doi.org/10.4103/0253-7613.190758>
- Bai Aswathanarayan, J., Rai Vittal, R., & Muddegowda, U. (2018). Anticancer activity of metal nanoparticles and their peptide conjugates against human colon adenorectal carcinoma cells. *Artificial Cells, Nanomedicine, and Biotechnology*, *46*(7), 1444–1451. <https://doi.org/10.1080/21691401.2017.1373655>
- Bai, D. P., Zhang, X. F., Zhang, G. L., Huang, Y. F., & Gurunathan, S. (2017). Zinc oxide nanoparticles induce apoptosis and autophagy in human ovarian cancer cells. *International Journal of Nanomedicine*, *12*, 6521–6535. <https://doi.org/10.2147/IJN.S140071>

- Barr, J. T., Wang, Z., Min, X., Wienkers, H. J., Rock, B. M., Rock, D. A., & Wienkers, L. C. (2020). Mechanistic Studies of Cytochrome P450 3A4 Time-Dependent Inhibition Using Two Cysteine-Targeting Electrophiles. *Drug Metabolism and Disposition*, *48*(6), 508–514. <https://doi.org/10.1124/dmd.119.089813>
- Baun, A., Sayre, P., Steinhäuser, K. G., & Rose, J. (2017). Regulatory relevant and reliable methods and data for determining the environmental fate of manufactured nanomaterials. *NanoImpact*, *8*, 1–10. <https://doi.org/10.1016/J.IMPACT.2017.06.004>
- Benet, L. Z., Sodhi, J. K., Makrygiorgos, G., & Mesbah, A. (2021). There is Only One Valid Definition of Clearance: Critical Examination of Clearance Concepts Reveals the Potential for Errors in Clinical Drug Dosing Decisions. *AAPS Journal*, *23*(3), 1–8. <https://doi.org/10.1208/s12248-021-00591-z>
- Berg, M., Stenuit, B., Ho, J., Wang, A., Parke, C., Knight, M., Alvarez-Cohen, L., & Shapira, M. (2016). Assembly of the *Caenorhabditis elegans* gut microbiota from diverse soil microbial environments. *ISME Journal*, *10*(8), 1998–2009. <https://doi.org/10.1038/ismej.2015.253>
- BioLabs, N. E. (2023). ProtoScript™ First Strand cDNA Synthesis Kit. In *Spring* (Vol. 5227, Issue 3, pp. 1–5).
- BioScience, M. (n.d.). *BIOTAQ™ DNA Polymerase* (Vol. 49, Issue 0, p. 60222).
- Bisht, G., Rayamajhi, S., Kc, B., Paudel, S. N., Karna, D., & Shrestha, B. G. (2016). Synthesis, Characterization, and Study of In Vitro Cytotoxicity of ZnO-Fe₃O₄ Magnetic Composite Nanoparticles in Human Breast Cancer Cell Line (MDA-MB-231) and Mouse Fibroblast (NIH 3T3). *Nanoscale Research Letters*, *11*(1). <https://doi.org/10.1186/S11671-016-1734-9>
- Blum, F. (2014). High Performance Liquid Chromatography (HPLC) with Fluorescence Detection for Quantification of Steroids in Clinical, Pharmaceutical, and Environmental Samples: A Review. *British Journal of Hospital Medicine*, *75*(SUPPL. 2). <https://doi.org/10.12968/hmed.2014.75.Sup2.C18>
- Brooks, H. B., Geeganage, S., Kahl, S. D., Montrose, C., Sittampalam, S., Smith, M. C., & Weidner, J. R. (2012). Basics of Enzymatic Assays for HTS. *Assay Guidance Manual*. <https://www.ncbi.nlm.nih.gov/books/NBK92007/>
- Burlingham, B. T., & Widlansk, T. S. (2003). An Intuitive Look at the Relationship of Ki and IC₅₀: A More General Use for the Dixon Plot. *Journal of Chemical Education*, *80*.
- Byerly, L., Cassada, R. C., & Russell, R. L. (1976). The life cycle of the nematode *Caenorhabditis elegans*. *Developmental Biology*, *51*(1), 23–33. [https://doi.org/10.1016/0012-1606\(76\)90119-6](https://doi.org/10.1016/0012-1606(76)90119-6)
- Cabreiro, F., & Gems, D. (2013). Worms need microbes too: microbiota, health and aging in *Caenorhabditis elegans*. *EMBO Molecular Medicine*, *5*(9), 1300. <https://doi.org/10.1002/EMMM.201100972>
- Cer, R. Z., Mudunuri, U., Stephens, R., & Lebeda, F. J. (2009). IC₅₀-to-Ki: A web-based tool for converting IC₅₀ to Ki values for inhibitors of enzyme activity and ligand binding. *Nucleic Acids Research*, *37*(SUPPL. 2), 441–445. <https://doi.org/10.1093/nar/gkp253>
- Chávez, V., Mohri-Shiomi, A., & Garsin, D. A. (2009). Ce-Duox1/BLI-3 Generates Reactive Oxygen Species as a Protective Innate Immune Mechanism in *Caenorhabditis elegans*. *Infection and Immunity*, *77*(11), 4983. <https://doi.org/10.1128/IAI.00627-09>
- Chávez, V., Mohri-Shiomi, A., Maadani, A., Vega, L. A., & Garsin, D. A. (2007). Oxidative stress enzymes are required for DAF-16-mediated immunity due to

- generation of reactive oxygen species by *Caenorhabditis elegans*. *Genetics*, *176*(3), 1567–1577. <https://doi.org/10.1534/GENETICS.107.072587>
- Chen, B., Hong, W., Yang, P., Tang, Y., Zhao, Y., Aguilar, Z. P., & Xu, H. (2020). Nano Zinc Oxide Induced Fetal Mice Growth Restriction, Based on Oxide Stress and Endoplasmic Reticulum Stress. *Nanomaterials*, *10*(2). <https://doi.org/10.3390/NANO10020259>
- Chen, Y., Li, K., Chen, Y., Zhang, W., Pu, Z., & Jiang, L. (2012). Surface interactions affect the toxicity of engineered metal oxide nanoparticles toward *Paramecium*. *Chemical Research in Toxicology*, *25*(8), 1675–1681. <https://doi.org/10.1021/TX300151Y>
- Chen, Y. Y., Lee, Y. H., Wang, B. J., Chen, R. J., & Wang, Y. J. (2022). Skin damage induced by zinc oxide nanoparticles combined with UVB is mediated by activating cell pyroptosis via the NLRP3 inflammasome–autophagy–exosomal pathway. *Particle and Fibre Toxicology*, *19*(1), 1–22. <https://doi.org/10.1186/S12989-021-00443-W/FIGURES/9>
- Cho, S., & Yoon, Y. R. (2018). Understanding the pharmacokinetics of prodrug and metabolite. *Translational and Clinical Pharmacology*, *26*(1), 1. <https://doi.org/10.12793/TCP.2018.26.1.1>
- Cho, W. S., Duffin, R., Howie, S. E. M., Scotton, C. J., Wallace, W. A. H., MacNee, W., Bradley, M., Megson, I. L., & Donaldson, K. (2011). Progressive severe lung injury by zinc oxide nanoparticles; the role of Zn²⁺ dissolution inside lysosomes. *Particle and Fibre Toxicology*, *8*. <https://doi.org/10.1186/1743-8977-8-27>
- Choi, J. S., Kim, R. O., Yoon, S., & Kim, W. K. (2016). Developmental Toxicity of Zinc Oxide Nanoparticles to Zebrafish (*Danio rerio*): A Transcriptomic Analysis. *PLOS ONE*, *11*(8), e0160763. <https://doi.org/10.1371/JOURNAL.PONE.0160763>
- Chong, C. L., Fang, C. M., Pung, S. Y., Ong, C. E., Pung, Y. F., Kong, C., & Pan, Y. (2021). Current Updates On the In vivo Assessment of Zinc Oxide Nanoparticles Toxicity Using Animal Models. *BioNanoScience*, *11*(2), 590–620. <https://doi.org/10.1007/s12668-021-00845-2>
- Ciniselli, C. M., Pizzamiglio, S., Malentacchi, F., Gelmini, S., Pazzagli, M., Hartmann, C. C., Ibrahim-Gawel, H., & Verderio, P. (2015). Combining qualitative and quantitative imaging evaluation for the assessment of genomic DNA integrity: The SPIDIA experience. *Analytical Biochemistry*, *479*, 60–62. <https://doi.org/10.1016/J.AB.2015.03.023>
- Cochran, J. C., Unrine, J. M., Coyne, M., & Tsyusko, O. V. (2023). Multiple stressor effects on a model soil nematode, *Caenorhabditis elegans*: Combined effects of the pathogen *Klebsiella pneumoniae* and zinc oxide nanoparticles. *Science of the Total Environment*, *865*(September 2022), 161307. <https://doi.org/10.1016/j.scitotenv.2022.161307>
- Cong, Y., Jin, F., Wang, J., & Mu, J. (2017). The embryotoxicity of ZnO nanoparticles to marine medaka, *Oryzias melastigma*. *Aquatic Toxicology*, *185*, 11–18. <https://doi.org/10.1016/J.AQUATOX.2017.01.006>
- Cordier, S. (2008). Evidence for a role of paternal exposures in developmental toxicity. *Basic and Clinical Pharmacology and Toxicology*, *102*(2), 176–181. <https://doi.org/10.1111/j.1742-7843.2007.00162.x>
- Corsi, A. K. (2006). A Biochemist's Guide to *C. elegans*. *Analytical Biochemistry*, *359*(1), 1. <https://doi.org/10.1016/J.AB.2006.07.033>
- Cortes, A., Cascante, M., Cardenas, M. L., & Cornish-Bowden, A. (2001). Relationships between inhibition constants, inhibitor concentrations for 50% inhibition and types

- of inhibition: new ways of analysing data. *Biochemical Journal*, 357(1), 263–268. <https://doi.org/10.1042/bj3570263>
- Culetto, E., & Sattelle, D. B. (2000). A role for *Caenorhabditis elegans* in understanding the function and interactions of human disease genes. *Human Molecular Genetics*, 9(6), 869–877. <https://doi.org/10.1093/HMG/9.6.869>
- Cutter, A. D., Dey, A., & Murray, R. L. (2009). Evolution of the *Caenorhabditis elegans* genome. *Molecular Biology and Evolution*, 26(6), 1199–1234. <https://doi.org/10.1093/molbev/msp048>
- da Silva Faria, T., de Bittencourt Brasil, F., Sampaio, F. J. B., & da Fonte Ramos, C. (2010). Effects of maternal undernutrition during lactation on estrogen and androgen receptor expressions in rat ovary at puberty. *Nutrition*, 26(10), 993–999. <https://doi.org/10.1016/J.NUT.2009.09.027>
- Daily, E. B., & Aquilante, C. L. (2009). Cytochrome P450 2C8 pharmacogenetics: a review of clinical studies. *Pharmacogenomics*, 10(9), 1489. <https://doi.org/10.2217/PGS.09.82>
- De Angelis, I., Barone, F., Zijno, A., Bizzarri, L., Russo, M. T., Pozzi, R., Franchini, F., Giudetti, G., Uboldi, C., Ponti, J., Rossi, F., & De Berardis, B. (2013). Comparative study of ZnO and TiO₂ nanoparticles: physicochemical characterisation and toxicological effects on human colon carcinoma cells. *Nanotoxicology*, 7(8), 1361–1372. <https://doi.org/10.3109/17435390.2012.741724>
- De Graaf, I. A. M., Olinga, P., De Jager, M. H., Merema, M. T., De Kanter, R., Van De Kerkhof, E. G., & Groothuis, G. M. M. (2010). Preparation and incubation of precision-cut liver and intestinal slices for application in drug metabolism and toxicity studies. *Nature Protocols* 2010 5:9, 5(9), 1540–1551. <https://doi.org/10.1038/nprot.2010.111>
- de Jong, L. M., Jiskoot, W., Swen, J. J., & Manson, M. L. (2020). Distinct Effects of Inflammation on Cytochrome P450 Regulation and Drug Metabolism: Lessons from Experimental Models and a Potential Role for Pharmacogenetics. *Genes*, 11(12), 1–24. <https://doi.org/10.3390/GENES11121509>
- de Souza, J. M., Mendes, B. de O., Guimarães, A. T. B., Rodrigues, A. S. de L., Chagas, T. Q., Rocha, T. L., & Malafaia, G. (2018). Zinc oxide nanoparticles in predicted environmentally relevant concentrations leading to behavioral impairments in male swiss mice. *Science of The Total Environment*, 613–614, 653–662. <https://doi.org/10.1016/J.SCITOTENV.2017.09.051>
- Delaune, K. P., & Alsayouri, K. (2022). Physiology, Noncompetitive Inhibitor. *StatPearls*. <https://www.ncbi.nlm.nih.gov/books/NBK545242/>
- Deodhar, M., Al Rihani, S. B., Arwood, M. J., Darakjian, L., Dow, P., Turgeon, J., & Michaud, V. (2020). Mechanisms of CYP450 Inhibition: Understanding Drug-Drug Interactions Due to Mechanism-Based Inhibition in Clinical Practice. *Pharmaceutics*, 12(9), 1–18. <https://doi.org/10.3390/PHARMACEUTICS12090846>
- Dewyse, L., Reynaert, H., & van Grunsven, L. A. (2021). Best practices and progress in precision-cut liver slice cultures. *International Journal of Molecular Sciences*, 22(13), 1–18. <https://doi.org/10.3390/ijms22137137>
- Dhivya, R., Ranjani, J., Rajendhran, J., Mayandi, J., & Annaraj, J. (2018). Enhancing the anti-gastric cancer activity of curcumin with biocompatible and pH sensitive PMMA-AA/ZnO nanoparticles. *Materials Science & Engineering. C, Materials for Biological Applications*, 82, 182–189. <https://doi.org/10.1016/J.MSEC.2017.08.058>
- Dinger, J., Woods, C., Brandt, S. D., Meyer, M. R., & Maurer, H. H. (2016). Cytochrome P450 inhibition potential of new psychoactive substances of the

- tryptamine class. In *Toxicology Letters* (Vol. 241). Elsevier Ireland Ltd.
<https://doi.org/10.1016/j.toxlet.2015.11.013>
- Donato, M. T., Jiménez, N., Castell, J. V., & Gómez-Lechón, M. J. (2004). Fluorescence-based assays for screening nine cytochrome P450 (P450) activities in intact cells expressing individual human P450 enzymes. *Drug Metabolism and Disposition: The Biological Fate of Chemicals*, *32*(7), 699–706.
<https://doi.org/10.1124/DMD.32.7.699>
- Drummond, A. E., & Findlay, J. K. (1999). The role of estrogen in folliculogenesis. *Molecular and Cellular Endocrinology*, *151*(1–2), 57–64.
[https://doi.org/10.1016/S0303-7207\(99\)00038-6](https://doi.org/10.1016/S0303-7207(99)00038-6)
- Dutour, R., & Poirier, D. (2017). Inhibitors of cytochrome P450 (CYP) 1B1. *European Journal of Medicinal Chemistry*, *135*, 296–306.
<https://doi.org/10.1016/J.EJMECH.2017.04.042>
- Fang-Yen, C., Avery, L., & Samuel, A. D. T. (2009). Two size-selective mechanisms specifically trap bacteria-sized food particles in *Caenorhabditis elegans*. *Proceedings of the National Academy of Sciences of the United States of America*, *106*(47), 20093–20096.
https://doi.org/10.1073/PNAS.0904036106/SUPPL_FILE/SM7.MOV
- Fekete, F., Mangó, K., Minus, A., Tóth, K., & Monostory, K. (2022). CYP1A2 mRNA Expression Rather Than Genetic Variants Indicate Hepatic CYP1A2 Activity. *Pharmaceutics*, *14*(3). <https://doi.org/10.3390/pharmaceutics14030532>
- Fogal, B., & Hewett, S. J. (2008). Interleukin-1 β : a bridge between inflammation and excitotoxicity? *Journal of Neurochemistry*, *106*(1), 1–23.
<https://doi.org/10.1111/J.1471-4159.2008.05315.X>
- Forslund, K., Schreiber, F., Thanintorn, N., & Sonnhammer, E. L. L. (2011). OrthoDisease: tracking disease gene orthologs across 100 species. *Briefings in Bioinformatics*, *12*(5), 463–473. <https://doi.org/10.1093/BIB/BBR024>
- Foti, R. S., Rock, D. A., Pearson, J. T., Wahlstrom, J. L., & Wienkers, L. C. (2011). Mechanism-Based Inactivation of Cytochrome P450 3A4 by Mibefradil through Heme Destruction. *Drug Metabolism and Disposition*, *39*(7), 1188–1195.
<https://doi.org/10.1124/DMD.111.038505>
- Fowler, S., & Zhang, H. (2008). In vitro evaluation of reversible and irreversible cytochrome P450 inhibition: Current status on methodologies and their utility for predicting drug-drug interactions. *AAPS Journal*, *10*(2), 410–424.
<https://doi.org/10.1208/s12248-008-9042-7>
- Fröhlich, E., Kueznik, T., Samberger, C., Roblegg, E., Wrighton, C., & Pieber, T. R. (2010). Size-dependent effects of nanoparticles on the activity of cytochrome P450 isoenzymes. *Toxicology and Applied Pharmacology*, *242*(3), 326–332.
<https://doi.org/10.1016/J.TAAP.2009.11.002>
- Frontiers, S., Toxicology, D., Committee, R. A., Toxicology, D., Studies, E., Isbn, C., Pdf, T., Press, N. A., Press, N. A., Academy, N., Academy, N., & Press, N. A. (2000). Scientific Frontiers in Developmental Toxicology and Risk Assessment. In *Scientific Frontiers in Developmental Toxicology and Risk Assessment*.
<https://doi.org/10.17226/9871>
- Gallo, V., & Deneen, B. (2014). Glial Development: The Crossroads of Regeneration and Repair in the CNS. *Neuron*, *83*(2), 283–308.
<https://doi.org/10.1016/J.NEURON.2014.06.010>
- García-Gómez, C., Fernández, M. D., García, S., Obrador, A. F., Letón, M., & Babín, M. (2018). Soil pH effects on the toxicity of zinc oxide nanoparticles to soil

- microbial community. *Environmental Science and Pollution Research*, 25(28), 28140–28152. <https://doi.org/10.1007/S11356-018-2833-1/METRICS>
- Georgakis, N., Ioannou, E., Varotsou, C., & Premetis, G. (2020). Determination of Half-Maximal Inhibitory Concentration of an Enzyme Inhibitor. *Methods in Molecular Biology*.
- Gerth, K., Kodidela, S., Kumar, S., Mahon, M., Haque, S., & Verma, N. (2019). Circulating extracellular vesicles containing xenobiotic metabolizing CYP enzymes and their potential roles in extrahepatic cells via cell–cell interactions. *International Journal of Molecular Sciences*, 20(24). <https://doi.org/10.3390/ijms20246178>
- Gestwicki, J. E., & Shao, H. (2019). Inhibitors and chemical probes for molecular chaperone networks. *Journal of Biological Chemistry*, 294(6), 2151–2161. <https://doi.org/10.1074/jbc.TM118.002813>
- Gilani, B., & Cassagnol, M. (2021). Biochemistry, Cytochrome P450. *StatPearls*. <https://www.ncbi.nlm.nih.gov/books/NBK557698/>
- Gilani, B., & Cassagnol, M. (2022). Biochemistry, Cytochrome P450. *StatPearls*. <https://www.ncbi.nlm.nih.gov/books/NBK557698/>
- Gilbert, S. F. (2000). Early Development of the Nematode *Caenorhabditis elegans*. *Developmental Biology*. <https://www.ncbi.nlm.nih.gov/books/NBK10011/>
- Ginzburg, A. L., Blackburn, R. S., Santillan, C., Truong, L., Tanguay, R. L., & Hutchison, J. E. (2021). Zinc oxide-induced changes to sunscreen ingredient efficacy and toxicity under UV irradiation. *Photochemical and Photobiological Sciences*, 20(10), 1273–1285. <https://doi.org/10.1007/s43630-021-00101-2>
- Giovannoni, G. (2014). Cerebrospinal fluid analysis. *Handbook of Clinical Neurology*, 122, 681–702. <https://doi.org/10.1016/B978-0-444-52001-2.00029-7>
- Goessling, W., & Stainier, D. Y. (2016). Endoderm specification and liver development. *Methods in Cell Biology*, 134, 463–483. <https://doi.org/10.1016/BS.MCB.2016.03.042>
- Gómez-Orte, E., Cornes, E., Zheleva, A., Sáenz-Narciso, B., de Toro, M., Iñiguez, M., López, R., San-Juan, J. F., Ezcurra, B., Sacristán, B., Sánchez-Blanco, A., Cerón, J., & Cabello, J. (2018). Effect of the diet type and temperature on the *C. elegans* transcriptome. *Oncotarget*, 9(11), 9556–9571. <https://doi.org/10.18632/oncotarget.23563>
- Gonzalez-Moragas, L., Berto, P., Vilches, C., Quidant, R., Kolovou, A., Santarella-Mellig, R., Schwab, Y., Stürzenbaum, S., Roig, A., & Laromaine, A. (2017). In vivo testing of gold nanoparticles using the *Caenorhabditis elegans* model organism. *Acta Biomaterialia*, 53, 598–609. <https://doi.org/10.1016/J.ACTBIO.2017.01.080>
- Goriuc, A., Jitoreanu, A., Mârțu, I., Dascălu, C., Kappenberg-Nițescu, D., Solomon, S.-M., Mârțu, A., Foia, L., Țapu, I., Istrate, B., Tatarciuc, M., & Luchian, I. (2021). Experimental EDX analysis of different periodontal splinting systems. *Experimental and Therapeutic Medicine*, 22(6), 1–7. <https://doi.org/10.3892/etm.2021.10820>
- Gosens, I., Post, J. A., de la Fonteyne, L. J. J., Jansen, E. H. J. M., Geus, J. W., Cassee, F. R., & de Jong, W. H. (2010). Impact of agglomeration state of nano- and submicron sized gold particles on pulmonary inflammation. *Particle and Fibre Toxicology*, 7(1), 37. <https://doi.org/10.1186/1743-8977-7-37>
- Gottschalk, F., Sonderer, T., Scholz, R. W., & Nowack, B. (2009). Modeled environmental concentrations of engineered nanomaterials (TiO₂, ZnO, Ag, CNT, fullerenes) for different regions. *Environmental Science and Technology*, 43(24),

- 9216–9222.
https://doi.org/10.1021/ES9015553/SUPPL_FILE/ES9015553_SI_001.PDF
- Grasso, A., Ferrante, M., Moreda-Piñeiro, A., Arena, G., Magarini, R., Oliveri Conti, G., Cristaldi, A., & Copat, C. (2022). Dietary exposure of zinc oxide nanoparticles (ZnO-NPs) from canned seafood by single particle ICP-MS: Balancing of risks and benefits for human health. *Ecotoxicology and Environmental Safety*, *231*, 113217. <https://doi.org/10.1016/J.ECOENV.2022.113217>
- Greenberg, M. I., & Vearrier, D. (2015). Metal fume fever and polymer fume fever. *Clinical Toxicology (Philadelphia, Pa.)*, *53*(4), 195–203. <https://doi.org/10.3109/15563650.2015.1013548>
- Gudkov, S. V., Burmistrov, D. E., Serov, D. A., Rebezov, M. B., Semenova, A. A., & Lisitsyn, A. B. (2021). A Mini Review of Antibacterial Properties of ZnO Nanoparticles. *Frontiers in Physics*, *9*, 49. <https://doi.org/10.3389/FPHY.2021.641481/BIBTEX>
- Guengerich, F. P. (2020). Cytochrome P450 2E1 and Its Roles in Disease. *Chemico-Biological Interactions*, *322*, 109056. <https://doi.org/10.1016/J.CBI.2020.109056>
- Gupta, R., & Xie, H. (2018). Nanoparticles in Daily Life: Applications, Toxicity and Regulations. *Journal of Environmental Pathology, Toxicology and Oncology : Official Organ of the International Society for Environmental Toxicology and Cancer*, *37*(3), 209. <https://doi.org/10.1615/JENVIRONPATHOLTOXICOLONCOL.2018026009>
- Gupta, S., Kushwah, T., Vishwakarma, A., & Yadav, S. (2015). Optimization of ZnO-NPs to Investigate Their Safe Application by Assessing Their Effect on Soil Nematode *Caenorhabditis elegans*. *Nanoscale Research Letters*, *10*(1). <https://doi.org/10.1186/s11671-015-1010-4>
- Gyorfi, M. J., & Kim, P. Y. (2022). Halothane Toxicity. *StatPearls*. <https://www.ncbi.nlm.nih.gov/books/NBK545281/>
- Ha, N. M., Tran, S. H., Shim, Y. H., & Kang, K. (2022). *Caenorhabditis elegans* as a powerful tool in natural product bioactivity research. *Applied Biological Chemistry*, *65*(1). <https://doi.org/10.1186/s13765-022-00685-y>
- Haghani, A., Dalton, H. M., Safi, N., Shirmohammadi, F., Sioutas, C., Morgan, T. E., Finch, C. E., & Curran, S. P. (2019). Air Pollution Alters *Caenorhabditis elegans* Development and Lifespan: Responses to Traffic-Related Nanoparticulate Matter. *The Journals of Gerontology Series A: Biological Sciences and Medical Sciences*, *74*(8), 1189. <https://doi.org/10.1093/GERONA/GLZ063>
- Hakkola, J., Hukkanen, J., Turpeinen, M., & Pelkonen, O. (2020). Inhibition and induction of CYP enzymes in humans: an update. *Archives of Toxicology*, *94*(11), 3671. <https://doi.org/10.1007/S00204-020-02936-7>
- Hall, D. H., & Herndon, L. A. (2017). Introduction to *C.elegans* Embryo Anatomy. *WormAtlas*.
- Han, Z., Yan, Q., Ge, W., Liu, Z. G., Gurunathan, S., De Felici, M., Shen, W., & Zhang, X. F. (2016). Cytotoxic effects of ZnO nanoparticles on mouse testicular cells. *International Journal of Nanomedicine*, *11*, 5187–5203. <https://doi.org/10.2147/IJN.S111447>
- Hao, Q., Chen, Y., & Zhou, X. (2020). The Janus Face of p53-Targeting Ubiquitin Ligases. *Cells*, *9*(7). <https://doi.org/10.3390/CELLS9071656>
- Hedrich, W. D., Hassan, H. E., & Wang, H. (2016). Insights into CYP2B6-mediated drug-drug interactions. *Acta Pharmaceutica Sinica B*, *6*(5), 413–425. <https://doi.org/10.1016/j.apsb.2016.07.016>

- Hegazy, A. A., Ahmed, M. M., Shehata, M. A., & Abdelfattah, M. M. (2018). Changes in Rats' Liver Structure Induced by Zinc Oxide Nanoparticles and the Possible Protective Role of Vitamin E. *International Journal of Human Anatomy*, 1(3), 1–16. <https://doi.org/10.14302/ISSN.2577-2279.IJHA-18-2384>
- Hoffman, S., Martin, D., Meléndez, A., & Bargonetti, J. (2014). C. elegans CEP-1/p53 and BEC-1 Are Involved in DNA Repair. *PLoS ONE*, 9(2), 88828. <https://doi.org/10.1371/JOURNAL.PONE.0088828>
- Hosseini, S. M., Moshrefi, A. H., Amani, R., Razavimehr, S. V., Aghajanihah, M. H., Sokouti, Z., & Holari, B. B. (2019). Subchronic effects of different doses of Zinc oxide nanoparticle on reproductive organs of female rats: An experimental study. *International Journal of Reproductive BioMedicine*, 17(2), 107–118. <https://doi.org/10.18502/IJRM.V17I2.3988>
- Hotamisligil, G. S., & Davis, R. J. (2016). Cell signaling and stress responses. *Cold Spring Harbor Perspectives in Biology*, 8(10). <https://doi.org/10.1101/cshperspect.a006072>
- Hu, C. C., Wu, G. H., Lai, S. F., Muthaiyan Shanmugam, M., Hwu, Y., Wagner, O. I., & Yen, T. J. (2018). Toxic Effects of Size-tunable Gold Nanoparticles on Caenorhabditis elegans Development and Gene Regulation. *Scientific Reports*, 8(1), 1–10. <https://doi.org/10.1038/s41598-018-33585-7>
- Hu, Q., D'Amora, D. R., MacNeil, L. T., Walhout, A. J. M., & Kubiseski, T. J. (2018). The Caenorhabditis elegans Oxidative Stress Response Requires the NHR-49 Transcription Factor. *G3: Genes/Genomes/Genetics*, 8(12), 3857. <https://doi.org/10.1534/G3.118.200727>
- Huang, C. W., Li, S. W., & Liao, V. H. C. (2019). Long-term sediment exposure to ZnO nanoparticles induces oxidative stress in Caenorhabditis elegans. *Environmental Science: Nano*, 6(8), 2602–2614. <https://doi.org/10.1039/C9EN00039A>
- Huang, L., Sang, C. N., & Desai, M. S. (2017). Beyond Ether and Chloroform-A Major Breakthrough With Halothane. *Journal of Anesthesia History*, 3(3), 87–102. <https://doi.org/10.1016/J.JANH.2017.05.003>
- Hubbard, E. J. A., & Greenstein, D. (2005). Introduction to the germ line. *WormBook: The Online Review of C. Elegans Biology*, 1–4. <https://doi.org/10.1895/WORMBOOK.1.18.1>
- Huggett, J., Dheda, K., Bustin, S., & Zumla, A. (2005). Real-time RT-PCR normalisation; strategies and considerations. *Genes and Immunity*, 6(4), 279–284. <https://doi.org/10.1038/SJ.GENE.6364190>
- Hurd, D. D. (2018). Tubulins in C. elegans. *Wormbook*, 1–34. <https://doi.org/10.1895/wormbook.1.182.1.1>
- Iannarelli, L., Giovannozzi, A. M., Morelli, F., Viscotti, F., Bigini, P., Maurino, V., Spoto, G., Martra, G., Ortel, E., Hodoroaba, V. D., Rossi, A. M., & Diomede, L. (2016). Shape engineered TiO2 nanoparticles in Caenorhabditis elegans: a Raman imaging based approach to assist tissue-specific toxicological studies. *RSC Advances*, 6(74), 70501–70509. <https://doi.org/10.1039/C6RA09686G>
- Imai, S., Yoshioka, Y., Morishita, Y., Yoshida, T., Uji, M., Nagano, K., Mukai, Y., Kamada, H., Tsunoda, S. ichi, Higashisaka, K., & Tsutsumi, Y. (2014). Size and surface modification of amorphous silica particles determine their effects on the activity of human CYP3A4 in vitro. *Nanoscale Research Letters*, 9(1), 651. <https://doi.org/10.1186/1556-276X-9-651>
- Inoue, H., Hisamoto, N., Jae, H. A., Oliveira, R. P., Nishida, E., Blackwell, T. K., & Matsumoto, K. (2005). The C. elegans p38 MAPK pathway regulates nuclear

- localization of the transcription factor SKN-1 in oxidative stress response. *Genes & Development*, 19(19), 2278. <https://doi.org/10.1101/GAD.1324805>
- Jaakkola, T., Laitila, J., Neuvonen, P. J., & Backman, J. T. (2006). Pioglitazone is metabolised by CYP2C8 and CYP3A4 in vitro: Potential for interactions with CYP2C8 inhibitors. *Basic and Clinical Pharmacology and Toxicology*, 99(1), 44–51. https://doi.org/10.1111/j.1742-7843.2006.pto_437.x
- Jeevanandam, J., Barhoum, A., Chan, Y. S., Dufresne, A., & Danquah, M. K. (2018). Review on nanoparticles and nanostructured materials: history, sources, toxicity and regulations. *Beilstein J. Nanotechnol*, 9, 1050–1074. <https://doi.org/10.3762/bjnano.9.98>
- Jeong, S., Nguyen, P. D., & Desta, Z. (2009). Comprehensive in vitro analysis of voriconazole inhibition of eight cytochrome P450 (CYP) enzymes: Major effect on CYPs 2B6, 2C9, 2C19, and 3A. *Antimicrobial Agents and Chemotherapy*, 53(2), 541–551. <https://doi.org/10.1128/AAC.01123-08>
- Jiang, W., Yang, K., Vachet, R. W., & Xing, B. (2010). Interaction between oxide nanoparticles and biomolecules of the bacterial cell envelope as examined by infrared spectroscopy. *Langmuir : The ACS Journal of Surfaces and Colloids*, 26(23), 18071–18077. <https://doi.org/10.1021/LA103738E>
- Jo, E., Seo, G., Kwon, J. T., Lee, M., Lee, B. cheun, Eom, I., Kim, P., & Choi, K. (2013). Exposure to zinc oxide nanoparticles affects reproductive development and biodistribution in offspring rats. *The Journal of Toxicological Sciences*, 38(4), 525–530. <https://doi.org/10.2131/JTS.38.525>
- Joe, A., Park, S. H., Shim, K. D., Kim, D. J., Jhee, K. H., Lee, H. W., Heo, C. H., Kim, H. M., & Jang, E. S. (2017). Antibacterial mechanism of ZnO nanoparticles under dark conditions. *Journal of Industrial and Engineering Chemistry*, 45, 430–439. <https://doi.org/10.1016/J.JIEC.2016.10.013>
- Johnson, K. A. (2013). A Century of Enzyme Kinetic Analysis, 1913 to 2013. *FEBS Letters*, 587(17), 2753. <https://doi.org/10.1016/J.FEBSLET.2013.07.012>
- Johnson, K. M., Su, D., & Zhang, D. (2021). Characteristics of Major Drug Metabolizing Cytochrome P450 Enzymes. In *Cytochrome P450 In Vitro Methods and Protocols* (pp. 37–64).
- Johnson, T. E. (2003). Advantages and disadvantages of *Caenorhabditis elegans* for aging research. *Experimental Gerontology*, 38(11–12), 1329–1332. <https://doi.org/10.1016/J.EXGER.2003.10.020>
- Juvonen, R. O., Jokinen, E. M., Javaid, A., Lehtonen, M., Raunio, H., & Pentikäinen, O. T. (2020). Inhibition of human CYP1 enzymes by a classical inhibitor α -naphthoflavone and a novel inhibitor N-(3, 5-dichlorophenyl)cyclopropanecarboxamide: An in vitro and in silico study. *Chemical Biology & Drug Design*, 95(5), 520–533. <https://doi.org/10.1111/CBDD.13669>
- Kapila, V., & Chaudhry, K. (2022). Physiology, Placenta. *StatPearls*. <https://www.ncbi.nlm.nih.gov/books/NBK538332/>
- Kauffman, M., Kauffman, M., Traore, K., Zhu, H., Trush, M., Jia, Z., & Li, Y. (2016). MitoSOX-Based Flow Cytometry for Detecting Mitochondrial ROS. *Reactive Oxygen Species (Apex, N.C.)*, 2(5). <https://doi.org/10.20455/ROS.2016.865>
- Kaur, I., Ellis, L. J., Romer, I., Tantra, R., Carriere, M., Allard, S., Mayne-L'hermite, M., Minelli, C., Unger, W., Potthoff, A., Rades, S., & Valsami-Jones, E. (2017). Dispersion of Nanomaterials in Aqueous Media: Towards Protocol Optimization. *Journal of Visualized Experiments : JoVE*, 2017(130), 56074. <https://doi.org/10.3791/56074>

- Kerr, R. A. (2006). Imaging the activity of neurons and muscles. *WormBook: The Online Review of C. Elegans Biology*, 1–13. <https://doi.org/10.1895/WORMBOOK.1.113.1>
- Khan, A. R., Raza, A., Firasat, S., & Abid, A. (2020). CYP3A5 gene polymorphisms and their impact on dosage and trough concentration of tacrolimus among kidney transplant patients: a systematic review and meta-analysis. *Pharmacogenomics Journal*, 20(4), 553–562. <https://doi.org/10.1038/s41397-019-0144-7>
- Khan, N., Ahmed, S., Sheraz, M. A., Anwar, Z., & Ahmad, I. (2023). Pharmaceutical based cosmetic serums. *Profiles of Drug Substances, Excipients and Related Methodology*. <https://doi.org/10.1016/bs.podrm.2022.11.006>
- Khare, P., Sonane, M., Nagar, Y., Moin, N., Ali, S., Gupta, K. C., & Satish, A. (2015). Size dependent toxicity of zinc oxide nano-particles in soil nematode *Caenorhabditis elegans*. *Nanotoxicology*, 9(4), 423–432. <https://doi.org/10.3109/17435390.2014.940403>
- Kim, Y., Park, Y., Hwang, J., & Kwack, K. (2018). Comparative genomic analysis of the human and nematode *Caenorhabditis elegans* uncovers potential reproductive genes and disease associations in humans. *Physiological Genomics*, 50(11), 1002–1014. <https://doi.org/10.1152/physiolgenomics.00063.2018>
- Klass, M. R. (1977). Aging in the nematode *Caenorhabditis elegans*: major biological and environmental factors influencing life span. *Mechanisms of Ageing and Development*, 6(6), 413–429. [https://doi.org/10.1016/0047-6374\(77\)90043-4](https://doi.org/10.1016/0047-6374(77)90043-4)
- Kolodziejczak-Radzimska, A., & Jesionowski, T. (2014). Zinc Oxide—From Synthesis to Application: A Review. *Materials 2014, Vol. 7, Pages 2833-2881*, 7(4), 2833–2881. <https://doi.org/10.3390/MA7042833>
- Kondo, M., Senoo-Matsuda, N., Yanase, S., Ishii, T., Hartman, P. S., & Ishii, N. (2005). Effect of oxidative stress on translocation of DAF-16 in oxygen-sensitive mutants, *mev-1* and *gas-1* of *Caenorhabditis elegans*. *Mechanisms of Ageing and Development*, 126(6–7), 637–641. <https://doi.org/10.1016/J.MAD.2004.11.011>
- Kong, T., Zhang, S. H., Zhang, C., Zhang, J. L., Yang, F., Wang, G. Y., Yang, Z. J., Bai, D. Y., Shi, Y. Y., Liu, T. Q., & Li, H. L. (2020). The Effects of 50 nm Unmodified Nano-ZnO on Lipid Metabolism and Semen Quality in Male Mice. *Biological Trace Element Research*, 194(2), 432–442. <https://doi.org/10.1007/S12011-019-01792-6/METRICS>
- Kramlinger, V. M., Von Weymarn, L. B., & Murphy, S. E. (2012). Inhibition and inactivation of cytochrome P450 2A6 and cytochrome P450 2A13 by menthofuran, β -nicotyrine and menthol. *Chemico-Biological Interactions*, 197(2–3), 87. <https://doi.org/10.1016/J.CBI.2012.03.009>
- Krippendorff, B. F., Lienau, P., Reichel, A., & Huisinga, W. (2007). Optimizing classification of drug-drug interaction potential for CYP450 isoenzyme inhibition assays in early drug discovery. *Journal of Biomolecular Screening*, 12(1), 92–99. <https://doi.org/10.1177/1087057106295897>
- Kudryasheva, N. S., & Kovel, E. S. (2019). Monitoring of Low-Intensity Exposures via Luminescent Bioassays of Different Complexity: Cells, Enzyme Reactions, and Fluorescent Proteins. *International Journal of Molecular Sciences*, 20(18). <https://doi.org/10.3390/IJMS20184451>
- Kumar, L., Kumar, P., Narayan, A., & Kar, M. (2013). Rietveld analysis of XRD patterns of different sizes of nanocrystalline cobalt ferrite. *International Nano Letters*, 3(1). <https://doi.org/10.1186/2228-5326-3-8>

- Kumar, T. R., Wang, Y., Lu, N., & Matzuk, M. M. (1997). Follicle stimulating hormone is required for ovarian follicle maturation but not male fertility. *Nature Genetics* 1997 15:2, 15(2), 201–204. <https://doi.org/10.1038/ng0297-201>
- Lafite, P., Dijols, S., Zeldin, D. C., Dansette, P. M., & Mansuy, D. (2007). Selective, competitive and mechanism-based inhibitors of human cytochrome P450 2J2. *Archives of Biochemistry and Biophysics*, 464(2), 155–168. <https://doi.org/10.1016/j.abb.2007.03.028>
- Lai, C. H., Chou, C. Y., Ch'ang, L. Y., Liu, C. S., & Lin, W. C. (2000). Identification of novel human genes evolutionarily conserved in *Caenorhabditis elegans* by comparative proteomics. *Genome Research*, 10(5), 703–713. <https://doi.org/10.1101/gr.10.5.703>
- Lai, X.-S., Yang, L.-P., Li, X.-T., Liu, J.-P., Zhou, Z.-W., & Zhou, S.-F. (2010). Human CYP2C8: Structure, Substrate Specificity, Inhibitor Selectivity, Inducers and Polymorphisms. *Current Drug Metabolism*, 10(9), 1009–1047. <https://doi.org/10.2174/138920009790711832>
- Lamb, J. G., Hathaway, L. B., Munger, M. A., Raucy, J. L., & Franklin, M. R. (2010). Nanosilver Particle Effects on Drug Metabolism In Vitro. *Drug Metabolism and Disposition*, 38(12), 2246–2251. <https://doi.org/10.1124/DMD.110.035238>
- Langmia, I. M., Just, K. S., Yamoune, S., Brockmüller, J., Masimirembwa, C., & Stingl, J. C. (2021). CYP2B6 Functional Variability in Drug Metabolism and Exposure Across Populations—Implication for Drug Safety, Dosing, and Individualized Therapy. *Frontiers in Genetics*, 12, 692234. <https://doi.org/10.3389/FGENE.2021.692234>
- Larsen, S. T., Jackson, P., Poulsen, S. S., Levin, M., Jensen, K. A., Wallin, H., Nielsen, G. D., & Koponen, I. K. (2016). Airway irritation, inflammation, and toxicity in mice following inhalation of metal oxide nanoparticles. *Nanotoxicology*, 10(9), 1254–1262. <https://doi.org/10.1080/17435390.2016.1202350>
- Lee, C. A., Neul, D., Clouser-Roche, A., Dalvie, D., Wester, M. R., Jiang, Y., Jones, J. P., Freiwald, S., Zientek, M., & Totah, R. A. (2010). Identification of Novel Substrates for Human Cytochrome P450 2J2. *Drug Metabolism and Disposition*, 38(2), 347–356. <https://doi.org/10.1124/DMD.109.030270>
- Lezzerini, M., Van De Ven, K., Veerman, M., Brul, S., & Budovskaya, Y. V. (2015). Specific RNA Interference in *Caenorhabditis elegans* by Ingested dsRNA Expressed in *Bacillus subtilis*. *PLoS ONE*, 10(4). <https://doi.org/10.1371/JOURNAL.PONE.0124508>
- L'Hernault, S. W. (2006). Spermatogenesis. *WormBook: The Online Review of C. Elegans Biology*, 1–14. <https://doi.org/10.1895/wormbook.1.85.1>
- Li, Y., Zhong, L., Zhang, L., Shen, X., Kong, L., & Wu, T. (2021). Research Advances on the Adverse Effects of Nanomaterials in a Model Organism, *Caenorhabditis elegans*. *Environmental Toxicology and Chemistry*, 40(9), 2406–2424. <https://doi.org/10.1002/ETC.5133>
- Liang, H., Chen, A., Lai, X., Liu, J., Wu, J., Kang, Y., Wang, X., & Shao, L. (2018). Neuroinflammation is induced by tongue-instilled ZnO nanoparticles via the Ca²⁺-dependent NF-κB and MAPK pathways. *Particle and Fibre Toxicology*, 15(1), 1–21. <https://doi.org/10.1186/S12989-018-0274-0/TABLES/3>
- Lim, D., Roh, J. Y., Eom, H. J., Choi, J. Y., Hyun, J., & Choi, J. (2012). Oxidative stress-related PMK-1 P38 MAPK activation as a mechanism for toxicity of silver nanoparticles to reproduction in the nematode *Caenorhabditis elegans*. *Environmental Toxicology and Chemistry*, 31(3), 585–592. <https://doi.org/10.1002/etc.1706>

- Lim, S. Y. M., Loo, J. S. E., Alshagga, M., Alshawsh, M. A., Ong, C. E., & Pan, Y. (2022). In vitro and In silico studies of interactions of cathinone with human recombinant cytochrome P450 CYP(1A2), CYP2A6, CYP2B6, CYP2C8, CYP2C19, CYP2E1, CYP2J2, and CYP3A5. *Toxicology Reports*, 9, 759–768. <https://doi.org/10.1016/J.TOXREP.2022.03.040>
- Limo, M. J., Sola-Rabada, A., Boix, E., Thota, V., Westcott, Z. C., Puddu, V., & Perry, C. C. (2018). Interactions between Metal Oxides and Biomolecules: From Fundamental Understanding to Applications. *Chemical Reviews*, 118(22), 11118–11193. https://doi.org/10.1021/ACS.CHEMREV.7B00660/ASSET/IMAGES/LARGE/CR-2017-006605_0023.JPEG
- Liu, H., Fu, G., Li, W., Liu, B., Ji, X., Zhang, S., & Qiao, K. (2023). Oxidative stress and mitochondrial damage induced by a novel pesticide fluopimomide in *Caenorhabditis elegans*. *Environmental Science and Pollution Research International*. <https://doi.org/10.1007/S11356-023-28893-Z>
- Liu, H., Yang, H., Fang, Y., Li, K., Tian, L., Liu, X., Zhang, W., Tan, Y., Lai, W., Bian, L., Lin, B., & Xi, Z. (2020). Neurotoxicity and biomarkers of zinc oxide nanoparticles in main functional brain regions and dopaminergic neurons. *Science of The Total Environment*, 705, 135809. <https://doi.org/10.1016/J.SCITOTENV.2019.135809>
- Liu, K. (2011). *Screening of Potential Anticancer Compounds from Marketed Drugs : Aripiprazole*, 서 론 인체의 항상성 유지에 시약 및 재료. 21(11), 1558–1564.
- Liu, M., Liu, X., Zhou, P., Jiang, S., Huang, J. G., & Dong, Z. (2022). Environmental factors have a major effect in shaping the gene expression of Siberian larch in the Altai Mountains of China. *The Plant Genome*, 15(3), e20240. <https://doi.org/10.1002/TPG2.20240>
- Liu, Z., Ren, Z., Zhang, J., Chuang, C. C., Kandaswamy, E., Zhou, T., & Zuo, L. (2018). Role of ROS and nutritional antioxidants in human diseases. *Frontiers in Physiology*, 9(MAY), 1–14. <https://doi.org/10.3389/fphys.2018.00477>
- Llorens, F., Villar-Piqué, A., Candelise, N., Zerr, I. F. and I., Llorens, F., Villar-Piqué, A., Candelise, N., & Zerr, I. F. and I. (2018). Tau Protein as a Biological Fluid Biomarker in Neurodegenerative Dementias. *Cognitive Disorders*. <https://doi.org/10.5772/INTECHOPEN.73528>
- Lu, Y. M., & Zheng, C. (2022). The Expression and Function of Tubulin Isoforms in *Caenorhabditis elegans*. *Frontiers in Cell and Developmental Biology*, 10, 860065. <https://doi.org/10.3389/FCELL.2022.860065/BIBTEX>
- Luster, M. I., Simeonova, P. P., Gallucci, R. M., Bruccoleri, A., Blazka, M. E., & Yucosoy, B. (2001). Role of inflammation in chemical-induced hepatotoxicity. *Toxicology Letters*, 120(1–3), 317–321. [https://doi.org/10.1016/S0378-4274\(01\)00284-3](https://doi.org/10.1016/S0378-4274(01)00284-3)
- Ma, D. D., & Yang, W. X. (2016). Engineered nanoparticles induce cell apoptosis: Potential for cancer therapy. *Oncotarget*, 7(26), 40882–40903. <https://doi.org/10.18632/oncotarget.8553>
- Ma, H., Bertsch, P. M., Glenn, T. C., Kabengi, N. J., & Williams, P. L. (2009). Toxicity of manufactured zinc oxide nanoparticles in the nematode *Caenorhabditis elegans*. *Environmental Toxicology and Chemistry*, 28(6), 1324–1330. <https://doi.org/10.1897/08-262.1>
- Macneil, L. T., & Walhout, A. J. (2013). The multifaceted nature of a bacterial diet. *Worm*, December, 1–4.

- Manzo, S., Schiavo, S., Oliviero, M., Toscano, A., Ciaravolo, M., & Cirino, P. (2017). Immune and reproductive system impairment in adult sea urchin exposed to nanosized ZnO via food. *Science of The Total Environment*, 599–600, 9–13. <https://doi.org/10.1016/J.SCITOTENV.2017.04.173>
- Marder, E., & Calabrese, R. L. (1996). Principles of rhythmic motor pattern generation. *Physiological Reviews*, 76(3), 687–717. <https://doi.org/10.1152/PHYSREV.1996.76.3.687>
- Marinas, M., Sa, E., Rojas, M. M., Moalem, M., Urbano, F. J., Guillou, C., & Rallo, L. (2010). A nuclear magnetic resonance (^1H and ^{13}C) and isotope ratio mass spectrometry ($\delta^{13}\text{C}$, $\delta^2\text{H}$ and $\delta^{18}\text{O}$) study of Andalusian olive oils. *Rapid Communications in Mass Spectrometry*, 24, 1457–1466. <https://doi.org/10.1002/rcm>
- Marks, B. D., Smith, R. W., Braun, H. A., Goossens, T. A., Christenson, M., Ozers, M. S., Lebakken, C. S., & Trubetskoy, O. V. (2002). A High Throughput Screening Assay to Screen for CYP2E1 Metabolism and Inhibition Using a Fluorogenic Vivid® P450 Substrate. *Assay and Drug Development Technologies*, 1(1), 73–81. <https://doi.org/10.1089/154065802761001329>
- Martins, S. G., Zilhão, R., Thorsteinsdóttir, S., & Carlos, A. R. (2021). Linking Oxidative Stress and DNA Damage to Changes in the Expression of Extracellular Matrix Components. *Frontiers in Genetics*, 12(July). <https://doi.org/10.3389/fgene.2021.673002>
- Mashock, M. J., Zanon, T., Kappell, A. D., Petrella, L. N., Andersen, E. C., & Hristova, K. R. (2016). Copper Oxide Nanoparticles Impact Several Toxicological Endpoints and Cause Neurodegeneration in *Caenorhabditis elegans*. *PLOS ONE*, 11(12), e0167613. <https://doi.org/10.1371/JOURNAL.PONE.0167613>
- Mayeen, A., Shaji, L. K., Nair, A. K., & Kalarikkal, N. (2018). Morphological Characterization of Nanomaterials. *Characterization of Nanomaterials: Advances and Key Technologies*, 335–364. <https://doi.org/10.1016/B978-0-08-101973-3.00012-2>
- McCarter, J., Bartlett, B., Dang, T., & Schedl, T. (1999). On the Control of Oocyte Meiotic Maturation and Ovulation in *Caenorhabditis elegans*. *Developmental Biology*, 205(1), 111–128. <https://doi.org/10.1006/DBIO.1998.9109>
- McDonagh, E. M., Wassenaar, C., David, S. P., Tyndale, R. F., Altman, R. B., Whirl-Carrillo, M., & Klein, T. E. (2012). PharmGKB Summary - Very Important Pharmacogene Information for Cytochrome P-450, Family 2, Subfamily A, polypeptide 6 (CYP2A6). *Pharmacogenetics and Genomics*, 22(9), 695–708. <https://doi.org/10.1097/fpc.0b013e3283540217>
- McDonnell, A. M., & Dang, C. H. (2013). Basic Review of the Cytochrome P450 System. *Journal of the Advanced Practitioner in Oncology*, 4(4), 263. <https://doi.org/10.6004/JADPRO.2013.4.4.7>
- McIntyre, G., Wright, J., Wong, H. T., Lamendella, R., & Chan, J. (2021). Effects of FUDR on gene expression in the *C. elegans* bacterial diet OP50. *BMC Research Notes*, 14(1), 1–7. <https://doi.org/10.1186/s13104-021-05624-6>
- Meneely, P. M., Dahlberg, C. L., & Rose, J. K. (2019a). Working with Worms: *Caenorhabditis elegans* as a Model Organism. *Current Protocols in Essential Laboratory Techniques*, 19(1). <https://doi.org/10.1002/CPET.35>
- Meneely, P. M., Dahlberg, C. L., & Rose, J. K. (2019b). Working with Worms: *Caenorhabditis elegans* as a Model Organism. *Current Protocols Essential Laboratory Techniques*, 19(1), e35. <https://doi.org/10.1002/CPET.35>

- Meng, X.-Y., Zhang, H.-X., Mezei, M., & Cui, M. (2011). Molecular Docking: A powerful approach for structure-based drug discovery. *Current Computer-Aided Drug Design*, 7(2), 146. <https://doi.org/10.2174/157340911795677602>
- Mittag, A., Owsny, P., Hoera, C., Kämpfe, A., & Gleib, M. (2022). Effects of Zinc Oxide Nanoparticles on Model Systems of the Intestinal Barrier. *Toxics*, 10(2). <https://doi.org/10.3390/TOXICS10020049>
- Mittag, A., Singer, A., Hoera, C., Westermann, M., Kämpfe, A., & Gleib, M. (2022). Impact of in vitro digested zinc oxide nanoparticles on intestinal model systems. *Particle and Fibre Toxicology*, 19(1), 1–15. <https://doi.org/10.1186/s12989-022-00479-6>
- Mo, S.-L., Liu, Y.-H., Duan, W., Wei, M., Kanwar, J., & Zhou, S.-F. (2009). Substrate Specificity, Regulation, and Polymorphism of Human Cytochrome P450 2B6. *Current Drug Metabolism*, 10(7), 730–753. <https://doi.org/10.2174/138920009789895534>
- Mohutsky, M., & Hall, S. D. (2014). Irreversible enzyme inhibition kinetics and drug-drug interactions. *Methods in Molecular Biology*, 1113, 57–91. https://doi.org/10.1007/978-1-62703-758-7_5/COVER
- Montalvo-Katz, S., Huang, H., Appel, M. D., Berg, M., & Shapira, M. (2013). Association with Soil Bacteria Enhances p38-Dependent Infection Resistance in *Caenorhabditis elegans*. *Infection and Immunity*, 81(2), 514. <https://doi.org/10.1128/IAI.00653-12>
- Moody, D. E., Liu, F., & Fang, W. B. (2015). Azole antifungal inhibition of buprenorphine, methadone and oxycodone in vitro metabolism. *Journal of Analytical Toxicology*, 39(5), 374–386. <https://doi.org/10.1093/jat/bkv030>
- Morimoto, Y., Izumi, H., Yoshiura, Y., Tomonaga, T., Oyabu, T., Myojo, T., Kawai, K., Yatera, K., Shimada, M., Kubo, M., Yamamoto, K., Kitajima, S., Kuroda, E., Kawaguchi, K., & Sasaki, T. (2016). Evaluation of Pulmonary Toxicity of Zinc Oxide Nanoparticles Following Inhalation and Intratracheal Instillation. *International Journal of Molecular Sciences*, 17(8), 1241. <https://doi.org/10.3390/IJMS17081241>
- Mozaffari, Z., Parivar, K., Roodbari, N. H., & Irani, S. (2015). Histopathological evaluation of the toxic effects of zinc oxide (ZnO) nanoparticles on testicular tissue of NMRI adult mice. *Advanced Studies in Biology*, 7, 275–291. <https://doi.org/10.12988/ASB.2015.5425>
- Mukhopadhyay, A., Basu, S., Singha, S., & Patra, H. K. (2018). Inner-view of nanomaterial incited protein conformational changes: Insights into designable interaction. *Research*, 2018. <https://doi.org/10.1155/2018/9712832>
- Munro, A. W., McLean, K. J., Grant, J. L., & Makris, T. M. (2018). Structure and function of the cytochrome P450 peroxygenase enzymes. *Biochemical Society Transactions*, 46(1), 183–196. <https://doi.org/10.1042/BST20170218>
- Musana, K. A., Yale, S. H., & Abdulkarim, A. S. (2004). Tests of Liver Injury. *Clinical Medicine and Research*, 2(2), 129. <https://doi.org/10.3121/CMR.2.2.129>
- Muschiol, D., Schroeder, F., & Traunspurger, W. (2009a). Life cycle and population growth rate of *Caenorhabditis elegans* studied by a new method. *BMC Ecology*, 9(1), 1–13. <https://doi.org/10.1186/1472-6785-9-14/TABLES/3>
- Muschiol, D., Schroeder, F., & Traunspurger, W. (2009b). Life cycle and population growth rate of *Caenorhabditis elegans* studied by a new method. *BMC Ecology*, 9, 14. <https://doi.org/10.1186/1472-6785-9-14>

- N., H., C., M., T. R., M., S., S., S., N., K. E., M., S. C., S., Y., N., P. V., D., & R. N., M. (2023). In Vitro Hepatic Models to Assess Herb–Drug Interactions: Approaches and Challenges. *Pharmaceuticals*, *16*(3), 409. <https://doi.org/10.3390/ph16030409>
- Nagar, S., Jones, J. P., & Korzekwa, K. (2014). A numerical method for analysis of in vitro time-dependent inhibition data. Part 1. Theoretical considerations. *Drug Metabolism and Disposition*, *42*(9), 1575–1586. <https://doi.org/10.1124/dmd.114.058289>
- Nagy, S., Wright, C., Tramm, N., Labello, N., Burov, S., & Biron, D. (2013). A longitudinal study of *Caenorhabditis elegans* larvae reveals a novel locomotion switch, regulated by Gas signaling. *ELife*, *2*(2), 782. <https://doi.org/10.7554/ELIFE.00782>
- Naidoo, P., Chetty, V. V., & Chetty, M. (2014). Impact of CYP polymorphisms, ethnicity and sex differences in metabolism on dosing strategies: The case of efavirenz. *European Journal of Clinical Pharmacology*, *70*(4), 379–389. <https://doi.org/10.1007/s00228-013-1634-1>
- Nakajima, M., Fujiki, Y., Kyo, S., Kanaya, T., Nakamura, M., Maida, Y., Tanaka, M., Inoue, M., & Yokoi, T. (2005). Pharmacokinetics of Paclitaxel in Ovarian Cancer Patients and Genetic Polymorphisms of CYP2C8, CYP3A4, and MDR1. *The Journal of Clinical Pharmacology*, *45*(6), 674–682. <https://doi.org/10.1177/0091270005276204>
- Nakamura, H., & Watano, S. (2018). Direct permeation of nanoparticles across cell membrane: A review. *KONA Powder and Particle Journal*, *2018*(35), 49–65. <https://doi.org/10.14356/kona.2018011>
- Nigon, V. M., & Felix, M.-A. (2017). History of research on *C. elegans* and other free-living nematodes as model organisms. *WormBook*, 1–84. <https://doi.org/10.1895/WORMBOOK.1.181.1>
- Nohynek, G. J., Dufour, E. K., & Roberts, M. S. (2008). Nanotechnology, cosmetics and the skin: is there a health risk? *Skin Pharmacology and Physiology*, *21*(3), 136–149. <https://doi.org/10.1159/000131078>
- Novotná, A., Krasulová, K., Bartoňková, I., Korhoňová, M., Bachleda, P., Anzenbacher, P., & Dvořák, Z. (2014). Dual effects of ketoconazole cis-enantiomers on CYP3A4 in human hepatocytes and HepG2 cells. *PLoS ONE*, *9*(10), 1–8. <https://doi.org/10.1371/journal.pone.0111286>
- O'Donnell, B., Huo, L., Polli, J. R., Qiu, L., Collier, D. N., Zhang, B., & Pan, X. (2017). ZnO Nanoparticles Enhanced Germ Cell Apoptosis in *Caenorhabditis elegans*, in Comparison with ZnCl₂. *Toxicological Sciences*, *156*(2), 336–343. <https://doi.org/10.1093/toxsci/kfw258>
- Ortiz, G. G., González-Usigli, H., Pacheco- Moisés, F. P., Mireles-Ramírez, M. A., Sánchez-López, A. L., Torres-Sánchez, E. D., González-Renovato, E. D., Flores-Alvarado, L. J., Macías-Islas, M. Á., Paloma Rivero-Moragrega, González, V. S., Ortiz, G. G., González-Usigli, H., Pacheco- Moisés, F. P., Mireles-Ramírez, M. A., Sánchez-López, A. L., Torres-Sánchez, E. D., González-Renovato, E. D., Flores-Alvarado, L. J., ... González, V. S. (2017). Physiology and Pathology of Neuroimmunology: Role of Inflammation in Parkinson's Disease. *Physiology and Pathology of Immunology*. <https://doi.org/10.5772/INTECHOPEN.70377>
- Osmond-Mcleod, M. J., Oytam, Y., Kirby, J. K., Gomez-Fernandez, L., Baxter, B., & McCall, M. J. (2014). Dermal absorption and short-term biological impact in hairless mice from sunscreens containing zinc oxide nano- or larger particles. *Nanotoxicology*, *8*(Suppl 1), 72. <https://doi.org/10.3109/17435390.2013.855832>

- Ozgenç, A. (n.d.). *Vivid® CYP450 Screening Kits User Guide*. Retrieved December 3, 2019, from www.lifetechnologies.com
- Pan, Y., Ong, C. E., Pung, Y. F., & Chieng, J. Y. (2019). The current understanding of the interactions between nanoparticles and cytochrome P450 enzymes - a literature-based review. *Xenobiotica; the Fate of Foreign Compounds in Biological Systems*, 49(7), 863–876. <https://doi.org/10.1080/00498254.2018.1503360>
- Pandurangan, M., Enkhtaivan, G., & Kim, D. H. (2016). Anticancer studies of synthesized ZnO nanoparticles against human cervical carcinoma cells. *Journal of Photochemistry and Photobiology. B, Biology*, 158, 206–211. <https://doi.org/10.1016/J.JPHOTOBIOL.2016.03.002>
- Panessa-Warren, B. J., Tortora, G. T., & Warren, J. B. (2007). High resolution FESEM and TEM reveal bacterial spore attachment. *Microscopy and Microanalysis*, 13(4), 251–266. <https://doi.org/10.1017/S1431927607070651>
- Pant, V. (2022). Importance of observing the progress curve during enzyme assay in an automated clinical chemistry analyzer: a case study. *Electronic Journal of the International Federation of Clinical Chemistry and Laboratory Medicine*, 33(1), 56–62.
- Parisi, G., Montemiglio, L. C., Giuffrè, A., Macone, A., Scaglione, A., Cerutti, G., Exertier, C., Savino, C., & Vallone, B. (2019). Substrate-induced conformational change in cytochrome P450 OleP. *FASEB Journal*, 33(2), 1787–1800. <https://doi.org/10.1096/fj.201800450RR>
- Park, H. E. H., Jung, Y., & Lee, S. J. V. (2017). Survival assays using *Caenorhabditis elegans*. *Molecules and Cells*, 40(2), 90–99. <https://doi.org/10.14348/molcells.2017.0017>
- Pazdernik, N., & Schedl, T. (2013). Introduction to Germ Cell Development in *C. elegans*. *Advances in Experimental Medicine and Biology*, 757, 1. https://doi.org/10.1007/978-1-4614-4015-4_1
- Peer, D., Karp, J. M., Hong, S., Farokhzad, O. C., Margalit, R., & Langer, R. (2007). Nanocarriers as an emerging platform for cancer therapy. *Nature Nanotechnology*, 2(12), 751–760. <https://doi.org/10.1038/NNANO.2007.387>
- Pei, X., Jiang, H., Xu, G., Li, C., Li, D., & Tang, S. (2022). Lethality of Zinc Oxide Nanoparticles Surpasses Conventional Zinc Oxide via Oxidative Stress, Mitochondrial Damage and Calcium Overload: A Comparative Hepatotoxicity Study. *International Journal of Molecular Sciences*, 23(12). <https://doi.org/10.3390/IJMS23126724>
- Petrova, O. E., & Sauer, K. (2017). High-performance liquid chromatography (HPLC)-based detection and quantitation of cellular c-di-GMP. *Methods in Molecular Biology (Clifton, N.J.)*, 1657, 33. https://doi.org/10.1007/978-1-4939-7240-1_4
- Pfaffl, M. W., Tichopad, A., Prgomet, C., & Neuvians, T. P. (2004). Determination of stable housekeeping genes, differentially regulated target genes and sample integrity: BestKeeper--Excel-based tool using pair-wise correlations. *Biotechnology Letters*, 26(6), 509–515. <https://doi.org/10.1023/B:BILE.0000019559.84305.47>
- Piechulek, A., & von Mikecz, A. (2018). Life span-resolved nanotoxicology enables identification of age-associated neuromuscular vulnerabilities in the nematode *Caenorhabditis elegans*. *Environmental Pollution*, 233, 1095–1103. <https://doi.org/10.1016/j.envpol.2017.10.012>
- Pizzino, G., Irrera, N., Cucinotta, M., Pallio, G., Mannino, F., Arcoraci, V., Squadrito, F., Altavilla, D., & Bitto, A. (2017). Oxidative Stress: Harms and Benefits for Human Health. *Oxidative Medicine and Cellular Longevity*, 2017. <https://doi.org/10.1155/2017/8416763>

- Prabantu, V. M., Naveenkumar, N., & Srinivasan, N. (2021). Influence of Disease-Causing Mutations on Protein Structural Networks. *Frontiers in Molecular Biosciences*, 7(March), 1–11. <https://doi.org/10.3389/fmolb.2020.620554>
- Price, G., & Patel, D. A. (2022). Drug Bioavailability. *XPharm: The Comprehensive Pharmacology Reference*, 1–2. <https://doi.org/10.1016/B978-008055232-3.60035-2>
- Qiao, Y., Liang, X., Yan, Y., Lu, Y., Di Zhang, Yao, W., Wu, W., & Yan, Z. (2018). Identification of exosomal miRNAs in rats with pulmonary neutrophilic inflammation induced by zinc oxide nanoparticles. *Frontiers in Physiology*, 9(MAR), 1–11. <https://doi.org/10.3389/fphys.2018.00217>
- Radonić, A., Thulke, S., Mackay, I. M., Landt, O., Siegert, W., & Nitsche, A. (2004). Guideline to reference gene selection for quantitative real-time PCR. *Biochemical and Biophysical Research Communications*, 313(4), 856–862. <https://doi.org/10.1016/j.bbrc.2003.11.177>
- Rafay Khan, A., Raza, A., Firasat, S., & Abid, A. (2020). CYP3A5 gene polymorphisms and their impact on dosage and trough concentration of tacrolimus among kidney transplant patients: a systematic review and meta-analysis. *The Pharmacogenomics Journal*, 20, 553–562. <https://doi.org/10.1038/s41397-019-0144-7>
- Rahman, H. S., Othman, H. H., Abdullah, R., Edin, H. Y. A. S., & AL-Haj, N. A. (2022). Beneficial and toxicological aspects of zinc oxide nanoparticles in animals. *Veterinary Medicine and Science*, 8(4), 1769–1779. <https://doi.org/10.1002/vms3.814>
- Raices, M., Maruyama, H., Dillin, A., & Kariseder, J. (2005). Uncoupling of longevity and telomere length in *C. elegans*. *PLoS Genetics*, 1(3), 295–301. <https://doi.org/10.1371/journal.pgen.0010030>
- Raizen, D., Song, B. M., Trojanowski, N., & You, Y. J. (2012). Methods for measuring pharyngeal behaviors. *WormBook : The Online Review of C. Elegans Biology*, 1–13. <https://doi.org/10.1895/WORMBOOK.1.154.1>
- Ramsay, R. R., & Tipton, K. F. (2017). Assessment of Enzyme Inhibition: A Review with Examples from the Development of Monoamine Oxidase and Cholinesterase Inhibitory Drugs. *Molecules : A Journal of Synthetic Chemistry and Natural Product Chemistry*, 22(7). <https://doi.org/10.3390/MOLECULES22071192>
- Riddle, D. L., Blumenthal, T., Meyer, B. J., & Priess, J. R. (1997). Life History And Evolution. *C. Elegans II*. <https://www.ncbi.nlm.nih.gov/books/NBK20146/>
- Riley, R. J., Grime, K., & Weaver, R. (2007). Time-dependent CYP inhibition. *Expert Opinion on Drug Metabolism & Toxicology*, 3(1), 51–66. <https://doi.org/10.1517/17425255.3.1.51>
- Riley, T., Sontag, E., Chen, P., & Levine, A. (2008). Transcriptional control of human p53-regulated genes. *Nature Reviews Molecular Cell Biology*, 9(5), 402–412. <https://doi.org/10.1038/nrm2395>
- Ring, B., Wrighton, S. A., & Mohutsky, M. (2014). Reversible mechanisms of enzyme inhibition and resulting clinical significance. *Methods in Molecular Biology*, 1113, 37–56. https://doi.org/10.1007/978-1-62703-758-7_4
- Robin, T., Reuveni, S., & Urbakh, M. (2018). Single-molecule theory of enzymatic inhibition. *Nature Communications* 2018 9:1, 9(1), 1–9. <https://doi.org/10.1038/s41467-018-02995-6>
- Robinson, P. K. (2015). Enzymes: principles and biotechnological applications. *Essays in Biochemistry*, 59, 1–41. <https://doi.org/10.1042/BSE0590001>
- Rock, D. A., & Wienkers, L. C. (2022). Characterization of Cytochrome P450 Mechanism Based Inhibition. *DRUG METABOLISM HANDBOOK: CONCEPTS*

AND APPLICATIONS IN CANCER RESEARCH, 465–526.

<https://doi.org/10.1002/9781119851042.CH15>

- Rodeiro, I., José Gómez-Lechón, M., Perez, G., Hernandez, I., Herrera, J. A., Delgado, R., Castell, J. V., & Teresa Donato, M. (2013). Mangifera indica L. extract and mangiferin modulate cytochrome P450 and UDP-glucuronosyltransferase enzymes in primary cultures of human hepatocytes. *Phytotherapy Research*, 27(5), 745–752. <https://doi.org/10.1002/ptr.4782>
- Rotblat, B., Melino, G., & Knight, R. A. (2012). NRF2 and p53: Januses in cancer? *Oncotarget*, 3(11), 1272. <https://doi.org/10.18632/ONCOTARGET.754>
- Ruszkiewicz, J. A., Pinkas, A., Ferrer, B., Peres, T. V., Tsatsakis, A., & Aschner, M. (2017). Neurotoxic effect of active ingredients in sunscreen products, a contemporary review. *Toxicology Reports*, 4, 245–259. <https://doi.org/10.1016/J.TOXREP.2017.05.006>
- S, G., Belay, A., Reddy AR, C., & Z, B. (2017). Synthesis and Characterizations of Zinc Oxide Nanoparticles for Antibacterial Applications. *Journal of Nanomedicine & Nanotechnology*, s8(April). <https://doi.org/10.4172/2157-7439.S8-004>
- Saliani, M., Jalal, R., & Goharshadi, E. K. (2016). Mechanism of oxidative stress involved in the toxicity of ZnO nanoparticles against eukaryotic cells. *Nanomed. J*, 3(1), 1–14. <https://doi.org/10.7508/nmj.2016.01.001>
- Salim, S. (2017). Oxidative Stress and the Central Nervous System. *Journal of Pharmacology and Experimental Therapeutics*, 360(1), 201–205. <https://doi.org/10.1124/JPET.116.237503>
- Sánchez-Blanco, A., Rodríguez-Matellán, A., González-Paramás, A., González-Manzano, S., Kim, S. K., & Mollinedo, F. (2016). Dietary and microbiome factors determine longevity in *Caenorhabditis elegans*. *Aging*, 8(7), 1513–1539. <https://doi.org/10.18632/AGING.101008>
- Sang, L., Dong, R., Liu, R., Hao, Q., Bai, W., & Sun, J. (2022). *Caenorhabditis elegans* NHR-14/HNF4 α regulates DNA damage-induced apoptosis through cooperating with cep-1/p53. *Cell Communication and Signaling*, 20(1), 1–11. <https://doi.org/10.1186/S12964-022-00920-5/FIGURES/6>
- Sangar, M. C., Bansal, S., & Avadhani, N. (2013). Potential herb–drug interactions for commonly used herbs. *Principles and Practice of Phytotherapy*, 6(10), 970–996. <https://doi.org/10.1016/b978-0-443-06992-5.00073-6>
- Saptarshi, S. R., Feltis, B. N., Wright, P. F. A., & Lopata, A. L. (2015). Investigating the immunomodulatory nature of zinc oxide nanoparticles at sub-cytotoxic levels in vitro and after intranasal instillation in vivo. *Journal of Nanobiotechnology*, 13(1), 1–11. <https://doi.org/10.1186/s12951-015-0067-7>
- Sarwar, S., Chakraborti, S., Bera, S., Sheikh, I. A., Hoque, K. M., & Chakrabarti, P. (2016). The antimicrobial activity of ZnO nanoparticles against *Vibrio cholerae*: Variation in response depends on biotype. *Nanomedicine : Nanotechnology, Biology, and Medicine*, 12(6), 1499–1509. <https://doi.org/10.1016/J.NANO.2016.02.006>
- Sasaki, M., Akahira, A., Oshiman, K. I., Tsuchido, T., & Matsumura, Y. (2005). Purification of cytochrome P450 and ferredoxin, involved in bisphenol A degradation, from *Sphingomonas* sp. strain AO1. *Applied and Environmental Microbiology*, 71(12), 8024–8030. <https://doi.org/10.1128/AEM.71.12.8024-8030.2005>
- Saul, N., Möller, S., Cirulli, F., Berry, A., Luyten, W., & Fuellen, G. (2021). Health and longevity studies in *C. elegans*: the “healthy worm database” reveals strengths,

- weaknesses and gaps of test compound-based studies. *Biogerontology*, 22(2), 215–236. <https://doi.org/10.1007/s10522-021-09913-2>
- Sayre, L. M., Perry, G., & Smith, M. A. (2008). Oxidative stress and neurotoxicity. *Chemical Research in Toxicology*, 21(1), 172–188. https://doi.org/10.1021/TX700210J/ASSET/IMAGES/LARGE/TX-2007-00210J_0001.JPEG
- Scharf, A., Pohl, F., Egan, B. M., Kocsisova, Z., & Kornfeld, K. (2021). Reproductive Aging in *Caenorhabditis elegans*: From Molecules to Ecology. *Frontiers in Cell and Developmental Biology*, 9. <https://doi.org/10.3389/FCELL.2021.718522/FULL>
- Schieber, M., & Chandel, N. S. (2014). ROS function in redox signaling. *Current Biology*, 24(10), 453–462. <https://doi.org/10.1016/j.cub.2014.03.034>
- Schumacher, B., Schertel, C., Wittenburg, N., Tuck, S., Mitani, S., Gartner, A., Conradt, B., & Shaham, S. (2005). *C. elegans* ced-13 can promote apoptosis and is induced in response to DNA damage. *Cell Death and Differentiation*, 12, 153–161. <https://doi.org/10.1038/sj.cdd.4401539>
- Scimeca, M., Bischetti, S., Lamsira, H. K., Bonfiglio, R., & Bonanno, E. (2018). Energy Dispersive X-ray (EDX) microanalysis: A powerful tool in biomedical research and diagnosis. *European Journal of Histochemistry : EJH*, 62(1), 89–99. <https://doi.org/10.4081/EJH.2018.2841>
- Selverston, A. I. (2010). Invertebrate central pattern generator circuits. *Philosophical Transactions of the Royal Society B: Biological Sciences*, 365(1551), 2329–2345. <https://doi.org/10.1098/RSTB.2009.0270>
- Seray, M., Skender, A., & Hadj-Hamou, A. S. (2021). Kinetics and mechanisms of Zn²⁺ release from antimicrobial food packaging based on poly (butylene adipate-co-terephthalate) and zinc oxide nanoparticles. *Polymer Bulletin*, 78(2), 1021–1040. <https://doi.org/10.1007/S00289-020-03145-Z>
- Sereemasapun, A., Hongpiticharoen, P., Rojanathanes, R., Maneewattanapinyo, P., Ekgasit, S., & Warisnoicharoen, W. (2008). Inhibition of human cytochrome P450 enzymes by metallic nanoparticles: A preliminary to nanogenomics. *International Journal of Pharmacology*, 4(6), 492–495. <https://doi.org/10.3923/IJP.2008.492.495>
- Shah, V., & Rajput, P. (2019). Surface decorated mesoporous silica nanoparticles: A promising and emerging tool for cancer targeting. *Indian Journal of Pharmaceutical Education and Research*, 53(3), 382–399. <https://doi.org/10.5530/ijper.53.3.72>
- Shahzad, K., Khan, M. N., Jabeen, F., Kosour, N., Chaudhry, A. S., Sohail, M., & Ahmad, N. (2019). Toxicity of zinc oxide nanoparticles (ZnO-NPs) in tilapia (*Oreochromis mossambicus*): tissue accumulation, oxidative stress, histopathology and genotoxicity. *International Journal of Environmental Science and Technology*, 16(4), 1973–1984. <https://doi.org/10.1007/S13762-018-1807-7>
- Sharifi-Rad, M., Anil Kumar, N. V., Zucca, P., Varoni, E. M., Dini, L., Panzarini, E., Rajkovic, J., Tsouh Fokou, P. V., Azzini, E., Peluso, I., Prakash Mishra, A., Nigam, M., El Rayess, Y., Beyrouthy, M. El, Polito, L., Iriti, M., Martins, N., Martorell, M., Docea, A. O., ... Sharifi-Rad, J. (2020). Lifestyle, Oxidative Stress, and Antioxidants: Back and Forth in the Pathophysiology of Chronic Diseases. *Frontiers in Physiology*, 11(July), 1–21. <https://doi.org/10.3389/fphys.2020.00694>
- Shibata, Y., Tamemoto, Y., Singh, S. P., Yoshitomo, A., Hozuki, S., Sato, H., & Hisaka, A. (2021). Plausible drug interaction between cyclophosphamide and voriconazole via inhibition of CYP2B6. *Drug Metabolism and Pharmacokinetics*, 39, 100396. <https://doi.org/10.1016/j.dmpk.2021.100396>

- Siddiqi, K. S., ur Rahman, A., Tajuddin, & Husen, A. (2018). Properties of Zinc Oxide Nanoparticles and Their Activity Against Microbes. *Nanoscale Research Letters*, 13. <https://doi.org/10.1186/s11671-018-2532-3>
- Silver, N., Best, S., Jiang, J., & Thein, S. L. (2006). Selection of housekeeping genes for gene expression studies in human reticulocytes using real-time PCR. *BMC Molecular Biology*, 7. <https://doi.org/10.1186/1471-2199-7-33>
- Singh, K. P., Miaskowski, C., Dhruva, A. A., Flowers, E., & Kober, K. M. (2018). Mechanisms and Measurement of Changes in Gene Expression. *Biological Research for Nursing*, 20(4), 369. <https://doi.org/10.1177/1099800418772161>
- Singson, A. (2001). Every Sperm Is Sacred: Fertilization in *Caenorhabditis elegans*. *Developmental Biology*, 230(2), 101–109. <https://doi.org/10.1006/DBIO.2000.0118>
- Sirelkhatim, A., Mahmud, S., Seeni, A., Kaus, N. H. M., Ann, L. C., Bakhori, S. K. M., Hasan, H., & Mohamad, D. (2015). Review on Zinc Oxide Nanoparticles: Antibacterial Activity and Toxicity Mechanism. *Nano-Micro Letters*, 7(3), 219. <https://doi.org/10.1007/S40820-015-0040-X>
- Sirim, D., Widmann, M., Wagner, F., & Pleiss, J. (2010). Prediction and analysis of the modular structure of cytochrome P450 monooxygenases. *BMC Structural Biology*, 10. <https://doi.org/10.1186/1472-6807-10-34>
- Smijs, T. G., & Pavel, S. (2011). Titanium dioxide and zinc oxide nanoparticles in sunscreens: Focus on their safety and effectiveness. *Nanotechnology, Science and Applications*, 4(1), 95–112. <https://doi.org/10.2147/nsa.s19419>
- Smith, S. A., Colley, H. E., Sharma, P., Slowik, K. M., Sison-Young, R., Sneddon, A., Webb, S. D., & Murdoch, C. (2018). Expression and enzyme activity of cytochrome P450 enzymes CYP3A4 and CYP3A5 in human skin and tissue-engineered skin equivalents. *Experimental Dermatology*, 27(5), 473–475. <https://doi.org/10.1111/EXD.13483>
- Sofela, S., Sahloul, S., & Song, Y. A. (2021). Biophysical analysis of drug efficacy on *C. elegans* models for neurodegenerative and neuromuscular diseases. *PLoS ONE*, 16(6 June 2021), 1–16. <https://doi.org/10.1371/journal.pone.0246496>
- Soltanmohammadi, N., Wang, S., & Schumacher, B. (2022). Somatic PMK-1/p38 signaling links environmental stress to germ cell apoptosis and heritable euploidy. *Nature Communications* 2022 13:1, 13(1), 1–13. <https://doi.org/10.1038/s41467-022-28225-8>
- Sood, K., Kaur, J., & Khatri, M. (2017). *Comparative Neurotoxicity Evaluation of Zinc Oxide Nanoparticles by Crawling Assay on Drosophila melanogaster*. 4(4), 440–444. www.ijetsr.com
- Spieth, J., Lawson, D., Davis, P., Williams, G., & Howe, K. (2014). Overview of gene structure in *C. elegans*. *WormBook : The Online Review of C. Elegans Biology*, 1–18. <https://doi.org/10.1895/WORMBOOK.1.65.2>
- Stiernagle, T. (2006). Maintenance of *C. elegans*. *WormBook : The Online Review of C. Elegans Biology*, 1–11. <https://doi.org/10.1895/WORMBOOK.1.101.1>
- Strelow, J., Dewe, W., Iversen, P. W., Brooks, H. B., & Jeffrey, A. (2012). Mechanism of Action Assays for Enzymes * Overview of MOA in Drug Discovery Types of Inhibition. *Assay Guidance Manual, Md*, 1–22. <https://www.ncbi.nlm.nih.gov/books/>
- Suganthi, P., Murali, M., Bukhari, S., Mohamed, S., Basu, H., Singhal, R. K., & Sadiq Bukhari, A. (2015). Morphological and liver histological effects of ZnO nanoparticles on Mozambique Tilapia. *JOURNAL OF ADVANCED APPLIED SCIENTIFIC RESEARCH*, 1(1), 68–83. <https://doi.org/10.46947/JOAASR1120158>

- Sun, H., Nguyen, K., Kerns, E., Yan, Z., Yu, K. R., Shah, P., Jadhav, A., Xu, X., Med, B., & Author, C. (2017). Highly Predictive and Interpretable Models for PAMPA Permeability Graphical Abstract HHS Public Access Author manuscript. *Bioorg Med Chem*, 25(3), 1266–1276. <https://doi.org/10.1016/j.bmc.2016.12.049>. Highly
- Susa, S. T., Hussain, A., & Preuss, C. V. (2023). Drug Metabolism. *Introduction to Basics of Pharmacology and Toxicology: Volume 1: General and Molecular Pharmacology: Principles of Drug Action*, 99–116. https://doi.org/10.1007/978-981-32-9779-1_7
- Taavitsainen, P., Juvonen, R., & Pelkonen, O. (2001). In Vitro Inhibition of Cytochrome P450 Enzymes in Human Liver Microsomes by a Potent CYP2A6 inhibitor, trans-2-Phenylcyclopropylamine (Tranlycypromine), and Its Nonamine Analog, Cyclopropylbenzene. *Drug Metabolism and Disposition*, 29(3).
- Tadesse, W. T., Mlugu, E. M., Shibeshi, W., Degu, W. A., Engidawork, E., & Aklillu, E. (2022). CYP3A and CYP2B6 Genotype Predicts Glucose Metabolism Disorder among HIV Patients on Long-Term Efavirenz-Based ART: A Case-Control Study. *Journal of Personalized Medicine*, 12(7). <https://doi.org/10.3390/jpm12071087>
- Taki, F. A., & Zhang, B. (2013). Determination of reliable reference genes for multi-generational gene expression analysis on *C. elegans* exposed to abused drug nicotine. *Psychopharmacology*, 230(1), 77. <https://doi.org/10.1007/S00213-013-3139-0>
- Tang, H. Q., Xu, M., Rong, Q., Jin, R. W., Liu, Q. J., & Li, Y. L. (2016). The effect of ZnO nanoparticles on liver function in rats. *International Journal of Nanomedicine*, 11, 4275–4285. <https://doi.org/10.2147/IJN.S109031>
- Tang, Y., Chen, B., Hong, W., Chen, L., Yao, L., Zhao, Y., Aguilar, Z. P., & Xu, H. (2019). <p>ZnO Nanoparticles Induced Male Reproductive Toxicity Based on the Effects on the Endoplasmic Reticulum Stress Signaling Pathway</p>. *International Journal of Nanomedicine*, 14, 9563–9576. <https://doi.org/10.2147/IJN.S223318>
- Teng, C., Jia, J., Wang, Z., Sharma, V. K., & Yan, B. (2019). Size-dependent maternal-fetal transfer and fetal developmental toxicity of ZnO nanoparticles after oral exposures in pregnant mice. *Ecotoxicology and Environmental Safety*, 182, 109439. <https://doi.org/10.1016/J.ECOENV.2019.109439>
- Thomford, N. E., Awortwe, C., Dzobo, K., Adu, F., Chopera, D., Wonkam, A., Skelton, M., Blackhurst, D., & Dandara, C. (2016). Inhibition of CYP2B6 by medicinal plant extracts: Implication for use of efavirenz and nevirapine based highly active anti-retroviral therapy (HAART) in resource-limited settings. *Molecules*, 21(2), 1–15. <https://doi.org/10.3390/molecules21020211>
- Tian, X., Zhou, M., Ning, J., Deng, X., Feng, L., Huang, H., Yao, D., & Ma, X. (2021). The development of novel cytochrome P450 2J2 (CYP2J2) inhibitor and the underlying interaction between inhibitor and CYP2J2. *Journal of Enzyme Inhibition and Medicinal Chemistry*, 36(1), 737–748. <https://doi.org/10.1080/14756366.2021.1896500>
- Toma-Jonik, A., Vydra, N., Janus, P., & Widłak, W. (2019). Interplay between HSF1 and p53 signaling pathways in cancer initiation and progression: non-oncogene and oncogene addiction. *Cellular Oncology 2019* 42:5, 42(5), 579–589. <https://doi.org/10.1007/S13402-019-00452-0>
- Tripathy, N., Ahmad, R., Ko, H. A., Khang, G., & Hahn, Y. B. (2015). Enhanced anticancer potency using an acid-responsive ZnO-incorporated liposomal drug-delivery system. *Nanoscale*, 7(9), 4088–4096. <https://doi.org/10.1039/C4NR06979J>

- Trojanowski, N. F., Raizen, D. M., & Fang-Yen, C. (2016). Pharyngeal pumping in *Caenorhabditis elegans* depends on tonic and phasic signaling from the nervous system. *Scientific Reports*, 6(1), 1–10. <https://doi.org/10.1038/srep22940>
- Tu, D.-Z., Mao, X., Zhang, F., He, R.-J., Wu, J.-J., Wu, Y., Zhao, X.-H., Zheng, J., & Ge, G.-B. (2021). *Reversible and Irreversible Inhibition of Cytochrome P450 Enzymes by Methylophiopogonanone A S*. <https://doi.org/10.1124/dmd.120.000325>
- Tuley, A., & Fast, W. (2018). The Taxonomy of Covalent Inhibitors. *Biochemistry*, 57(24), 3326–3337. https://doi.org/10.1021/ACS.BIOCHEM.8B00315/ASSET/IMAGES/MEDIUM/BI-2018-00315A_0021.GIF
- Tullet, J. M. A., Green, J. W., Au, C., Benedetto, A., Thompson, M. A., Clark, E., Gilliat, A. F., Young, A., Schmeisser, K., & Gems, D. (2017). The SKN-1/Nrf2 transcription factor can protect against oxidative stress and increase lifespan in *C. elegans* by distinct mechanisms. *Aging Cell*, 16(5), 1191. <https://doi.org/10.1111/ACEL.12627>
- Umar, W., Czinkota, I., Ayub, M. A., & Zulfiqar, M. A. (2023). Effect of Soil Texture , Nanoparticle Size , and Incubation Period on the Dissolution of ZnO Nanoparticles. *Pollutants*, 220–231.
- Ung, Y. T., Ong, C. E., & Pan, Y. (2018). Current high-throughput approaches of screening modulatory effects of xenobiotics on cytochrome P450 (CYP) enzymes. In *High-Throughput* (Vol. 7, Issue 4). MDPI AG. <https://doi.org/10.3390/HT7040029>
- Vandesompele, J., De Preter, K., Pattyn, F., Poppe, B., Van Roy, N., De Paepe, A., & Speleman, F. (2002). Accurate normalization of real-time quantitative RT-PCR data by geometric averaging of multiple internal control genes. *Genome Biology*, 3(7). <https://doi.org/10.1186/GB-2002-3-7-RESEARCH0034>
- Veith, H., Southall, N., Huang, R., James, T., Fayne, D., Artemenko, N., Shen, M., Inglese, J., Austin, C. P., Lloyd, D. G., & Auld, D. S. (2009). Comprehensive characterization of cytochrome P450 isozyme selectivity across chemical libraries. *Nature Biotechnology*, 27(11), 1050–1055. <https://doi.org/10.1038/nbt.1581>
- Venkataramanan, R., Swaminathan, A., Prasad, T., Jain, A., Zuckerman, S., Warty, V., McMichael, J., Lever, J., Burckart, G., & Starzl, T. (1995). Clinical Pharmacokinetics of Tacrolimus. In *Clinical Pharmacokinetics* (Vol. 29, Issue 6, pp. 404–430). <https://doi.org/10.2165/00003088-199529060-00003>
- Ventura, N., Rea, S. L., Schiavi, A., Torgovnick, A., Testi, R., & Johnson, T. E. (2009). p53/CEP-1 Increases or Decreases Lifespan, Depending on Level of Mitochondrial Bioenergetic Stress. *Aging Cell*, 8(4), 380. <https://doi.org/10.1111/J.1474-9726.2009.00482.X>
- Verbic, A., Gorjanc, M., & Simoncic, B. (2019). Zinc Oxide for Functional Textile Coatings: Recent Advances. *Coatings*, 17–23.
- Vermeer, L. M. M., Isringhausen, C. D., Ogilvie, B. W., & Buckley, D. B. (2016). Evaluation of ketoconazole and its alternative clinical CYP3A4/5 inhibitors as inhibitors of drug transporters: The in vitro effects of ketoconazole, ritonavir, clarithromycin, and itraconazole on 13 clinically-relevant drug transporters. *Drug Metabolism and Disposition*, 44(3), 453–459. <https://doi.org/10.1124/dmd.115.067744>
- Vimercati, L., Cavone, D., Caputi, A., De Maria, L., Tria, M., Prato, E., & Ferri, G. M. (2020). Nanoparticles: An Experimental Study of Zinc Nanoparticles Toxicity on Marine Crustaceans. General Overview on the Health Implications in Humans.

- Frontiers in Public Health*, 8(May), 1–19.
<https://doi.org/10.3389/fpubh.2020.00192>
- Walczynska, M., Jakubowski, W., Wasiak, T., Kadziola, K., Bartoszek, N., Kotarba, S., Siatkowska, M., Komorowski, P., & Walkowiak, B. (2018). Toxicity of silver nanoparticles, multiwalled carbon nanotubes, and dendrimers assessed with multicellular organism *Caenorhabditis elegans*. *Toxicology Mechanisms and Methods*, 28(6), 432–439. <https://doi.org/10.1080/15376516.2018.1449277>
- Walsky, R. L., Obach, R. S., Gaman, E. A., Gleeson, J. P. R., & Proctor, W. R. (2005). Selective inhibition of human cytochrome P450C8 by montelukast. *Drug Metabolism and Disposition*, 33(3), 413–418.
<https://doi.org/10.1124/dmd.104.002766>
- Wang, B., & Zhou, S.-F. (2009). Synthetic and natural compounds that interact with human cytochrome P450 1A2 and implications in drug development. *Current Medicinal Chemistry*, 16(31), 4066–4218.
<https://doi.org/10.2174/092986709789378198>
- Wang, C., Lu, J., Zhou, L., Li, J., Xu, J., Li, W., Zhang, L., Zhong, X., & Wang, T. (2016). Effects of long-term exposure to zinc oxide nanoparticles on development, zinc metabolism and biodistribution of minerals (Zn, Fe, Cu, Mn) in mice. *PLoS ONE*, 11(10), 1–14. <https://doi.org/10.1371/journal.pone.0164434>
- Wang, C., Xia, C., Zhu, Y., & Zhang, H. (2021). Innovative fluorescent probes for in vivo visualization of biomolecules in living *Caenorhabditis elegans*. *Cytometry Part A*, 99(6), 560–574. <https://doi.org/10.1002/cyto.a.24325>
- Wang, H., & Tompkins, L. (2008). CYP2B6: New Insights into a Historically Overlooked Cytochrome P450 Isozyme. *Current Drug Metabolism*, 9(7), 598–610.
<https://doi.org/10.2174/138920008785821710>
- Wang, H., Wick, R. L., & Xing, B. (2009). Toxicity of nanoparticulate and bulk ZnO, Al₂O₃ and TiO₂ to the nematode *Caenorhabditis elegans*. *Environmental Pollution*, 157(4), 1171–1177. <https://doi.org/10.1016/j.envpol.2008.11.004>
- Wang, H., Zhao, Y., & Zhang, Z. (2019). Age-dependent effects of floxuridine (FUdR) on senescent pathology and mortality in the nematode *Caenorhabditis elegans*. *Biochemical and Biophysical Research Communications*, 509(3), 694–699.
<https://doi.org/10.1016/J.BBRC.2018.12.161>
- Wang, L., & Du, G. H. (2022). Paclitaxel. *Natural Small Molecule Drugs from Plants*, 537–544. https://doi.org/10.1007/978-981-10-8022-7_89
- Wang, P., Hu, G., Zhao, W., Du, J., You, M., Xv, M., Yang, H., Zhang, M., Yan, F., Huang, M., Wang, X., Zhang, L., & Chen, Y. (2022). Continuous ZnO nanoparticle exposure induces melanoma-like skin lesions in epidermal barrier dysfunction model mice through anti-apoptotic effects mediated by the oxidative stress–activated NF-κB pathway. *Journal of Nanobiotechnology*, 20(1), 111.
<https://doi.org/10.1186/S12951-022-01308-W>
- Wannigama, D. L., Hurst, C., Pearson, L., Saethang, T., Singkham-in, U., Luk-in, S., Storer, R. J., & Chatsuwana, T. (2019). Simple fluorometric-based assay of antibiotic effectiveness for *Acinetobacter baumannii* biofilms. *Scientific Reports* 2019 9:1, 9(1), 1–14. <https://doi.org/10.1038/s41598-019-42353-0>
- Warisnoicharoen, W., Hongpithcharoen, P., & Lawanprasert, S. (2011). Alteration in enzymatic function of human cytochrome P450 by silver nanoparticles. *Research Journal of Environmental Toxicology*, 5(1), 58–64.
<https://doi.org/10.3923/RJET.2011.58.64>

- Waterston, R., & Sulston, J. (1995). The genome of *Caenorhabditis elegans*. *Proceedings of the National Academy of Sciences of the United States of America*, 92(24), 10836. <https://doi.org/10.1073/PNAS.92.24.10836>
- Weiss, J., Foerster, K. I., Weber, M., Burhenne, J., Mikus, G., Lehr, T., & Haefeli, W. E. (2022). Does the circulating ketoconazole metabolite N-deacetyl ketoconazole contribute to the drug-drug interaction potential of the parent compound? *European Journal of Pharmaceutical Sciences*, 169, 106076. <https://doi.org/10.1016/j.ejps.2021.106076>
- Willhite, C. C., & Mirkes, P. E. (2014). Developmental Toxicology. In *Encyclopedia of Toxicology: Third Edition* (Third Edit, Vol. 2). Elsevier. <https://doi.org/10.1016/B978-0-12-386454-3.00014-2>
- Wu, J., Guan, X., Dai, Z., He, R., Ding, X., Yang, L., & Ge, G. (2021). Molecular probes for human cytochrome P450 enzymes: Recent progress and future perspectives. *Coordination Chemistry Reviews*, 427, 213600. <https://doi.org/10.1016/j.ccr.2020.213600>
- Wyroba, E., Suski, S., Miller, K., & Bartosiewicz, R. (2015). Biomedical and agricultural applications of energy dispersive X-ray spectroscopy in electron microscopy. *Cellular and Molecular Biology Letters*, 20(3), 488–509. <https://doi.org/10.1515/cmble-2015-0028>
- Xie, Y., He, Y., Irwin, P. L., Jin, T., & Shi, X. (2011). Antibacterial activity and mechanism of action of zinc oxide nanoparticles against *Campylobacter jejuni*. *Applied and Environmental Microbiology*, 77(7), 2325–2331. <https://doi.org/10.1128/AEM.02149-10/ASSET/288F6553-DA74-4C58-ACD1-2DD913C17E84/ASSETS/GRAPHIC/ZAM9991019360004.JPEG>
- Yang, J., Luo, M., Tan, Z., Dai, M., Xie, M., Lin, J., Hua, H., Ma, Q., Zhao, J., & Liu, A. (2017). Oral administration of nano-titanium dioxide particle disrupts hepatic metabolic functions in a mouse model. *Environmental Toxicology and Pharmacology*, 49, 112–118. <https://doi.org/10.1016/J.ETAP.2016.12.006>
- Yang, X., Jiang, C., Hsu-Kim, H., Badireddy, A. R., Dykstra, M., Wiesner, M., Hinton, D. E., & Meyer, J. N. (2014). Silver nanoparticle behavior, uptake, and toxicity in *Caenorhabditis elegans*: Effects of natural organic matter. *Environmental Science and Technology*, 48(6), 3486–3495. https://doi.org/10.1021/ES404444N/SUPPL_FILE/ES404444N_SI_001.PDF
- Yang, Z., & Xie, C. (2006). Zn²⁺ release from zinc and zinc oxide particles in simulated uterine solution. *Colloids and Surfaces B: Biointerfaces*, 47(2), 140–145. <https://doi.org/10.1016/j.colsurfb.2005.12.007>
- Yaqub, A., Faheem, I., Anjum, K. M., Ditta, S. A., Yousaf, M. Z., Tanvir, F., & Raza, C. (2020). Neurotoxicity of ZnO nanoparticles and associated motor function deficits in mice. *Applied Nanoscience (Switzerland)*, 10(1), 177–185. <https://doi.org/10.1007/S13204-019-01093-3/METRICS>
- Yim, S. K., Kim, K., Chun, S., Oh, T., Jung, W., Jung, K., & Yun, C. H. (2020). Screening of Human CYP1A2 and CYP3A4 Inhibitors from Seaweed In Silico and In Vitro. *Marine Drugs*, 18(12), 1–15. <https://doi.org/10.3390/MD18120603>
- Yousef, M., Al-Hamadani, M., & Kamel, M. A. (2019). Reproductive Toxicity of Aluminum Oxide Nanoparticles and Zinc Oxide Nanoparticles in Male Rats. *Nano Particle*, 1(1), 1–10. <https://doi.org/10.35702/nano.10003>
- Zanger, U. M., & Schwab, M. (2013). Cytochrome P450 enzymes in drug metabolism: Regulation of gene expression, enzyme activities, and impact of genetic variation. *Pharmacology & Therapeutics*, 138(1), 103–141. <https://doi.org/10.1016/J.PHARMTHERA.2012.12.007>

- Zarubin, T., & Han, J. (2005). Activation and signaling of the p38 MAP kinase pathway. *Cell Research* 2005 15:1, 15(1), 11–18. <https://doi.org/10.1038/sj.cr.7290257>
- Zaver, S. A., Pollock, A. J., Boradia, V. M., & Woodward, J. J. (2021). A Luminescence-Based Coupled Enzyme Assay Enables High-Throughput Quantification of the Bacterial Second Messenger 3'3'-Cyclic-Di-AMP. *Chembiochem : A European Journal of Chemical Biology*, 22(6), 1030–1041. <https://doi.org/10.1002/CBIC.202000667>
- Zečić, A., Dhondt, I., & Braeckman, B. P. (2019). The nutritional requirements of *Caenorhabditis elegans*. *Genes and Nutrition*, 14(1), 1–13. <https://doi.org/10.1186/s12263-019-0637-7>
- Zhang, R., Dong, K., Wang, Z., Miao, R., Lu, W., & Wu, X. (2021). Nanoparticulate drug delivery strategies to address intestinal cytochrome p450 cyp3a4 metabolism towards personalized medicine. *Pharmaceutics*, 13(8). <https://doi.org/10.3390/pharmaceutics13081261>
- Zhang, S., Li, F., Zhou, T., Wang, G., & Li, Z. (2020). *Caenorhabditis elegans* as a Useful Model for Studying Aging Mutations. *Frontiers in Endocrinology*, 11, 554994. <https://doi.org/10.3389/FENDO.2020.554994>
- Zhang, W., Kilicarslan, T., Tyndale, R. F., & Sellers, E. M. (2001). Evaluation of Methoxsalen, Tranylcyproamine, and Tryptamine as Specific and Selective CYP2A6 Inhibitors in Vitro. *Drug Metabolism and Disposition*, 29(6).
- Zhang, X. F., Liu, Z. G., Shen, W., & Gurunathan, S. (2016). Silver nanoparticles: Synthesis, characterization, properties, applications, and therapeutic approaches. *International Journal of Molecular Sciences*, 17(9). <https://doi.org/10.3390/ijms17091534>
- Zhang, X., Ma, G., & Wei, W. (2021). Simulation of nanoparticles interacting with a cell membrane: probing the structural basis and potential biomedical application. *NPG Asia Materials*, 13(1). <https://doi.org/10.1038/s41427-021-00320-0>
- Zhang, Y., Chen, D., Smith, M. A., Zhang, B., & Pan, X. (2012). Selection of reliable reference genes in *caenorhabditis elegans* for analysis of nanotoxicity. *PLoS ONE*, 7(3). <https://doi.org/10.1371/journal.pone.0031849>
- Zhang, Y., Nayak, T. R., Hong, H., & Cai, W. (2013). Biomedical applications of zinc oxide nanomaterials. *Current Molecular Medicine*, 13(10), 1633–1645. <https://doi.org/10.2174/1566524013666131111130058>
- Zhao, L. M., Zheng, Z. X., Zhao, X., Shi, J., Bi, J. J., Pei, W., & Feng, Q. (2014). Optimization of reference genes for normalization of the quantitative polymerase chain reaction in tissue samples of gastric cancer. *Asian Pacific Journal of Cancer Prevention*, 15(14), 5815–5818. <https://doi.org/10.7314/APJCP.2014.15.14.5815>
- Zhao, M., Ma, J., Li, M., Zhang, Y., Jiang, B., Zhao, X., Huai, C., Shen, L., Zhang, N., He, L., & Qin, S. (2021). Cytochrome p450 enzymes and drug metabolism in humans. *International Journal of Molecular Sciences*, 22(23), 1–16. <https://doi.org/10.3390/ijms222312808>
- Zhao, X., Wang, S., Wu, Y., You, H., & Lv, L. (2013). Acute ZnO nanoparticles exposure induces developmental toxicity, oxidative stress and DNA damage in embryo-larval zebrafish. *Aquatic Toxicology*, 136–137, 49–59. <https://doi.org/10.1016/J.AQUATOX.2013.03.019>
- Zheng, Y., Cosgrove, D. J., & Ning, G. (2017). High-Resolution Field Emission Scanning Electron Microscopy (FESEM) Imaging of Cellulose Microfibril Organization in Plant Primary Cell Walls. *Microscopy and Microanalysis*, 23(5), 1048–1054. <https://doi.org/10.1017/S143192761701251X>

- Ziraldó, R., Shoura, M. J., Fire, A. Z., & Levene, S. D. (2019). Deconvolution of nucleic-acid length distributions: a gel electrophoresis analysis tool and applications. *Nucleic Acids Research*, *47*(16), e92. <https://doi.org/10.1093/NAR/GKZ534>
- Zolghadri, S., Bahrami, A., Hassan Khan, M. T., Muñoz-Munoz, J., García-Molina, F., García-Canovas, F., & Saboury, A. A. (2019). A comprehensive review on tyrosinase inhibitors. *Journal of Enzyme Inhibition and Medicinal Chemistry*, *34*(1), 279. <https://doi.org/10.1080/14756366.2018.1545767>

Appendix

Table A.3.1. Solutions of chemical used for maintenance and assay of *C. elegans*. *C. elegans* *Caenorhabditis elegans*.

Solute	Solvent	Solution Concentration
CaCl ₂	Autoclaved water	1M
MgSO ₄	Autoclaved water	1M
KPO ₄	Autoclaved water	1M
Streptomycin	Autoclaved water	100 mg/mL
Carbenicillin	Autoclaved water	100 mg/mL
Cholesterol	Absolute ethanol (99.99%)	5 mg/mL
IPTG	Autoclaved water	1 M
Ampicillin	Autoclaved water	100 mg/mL

Table A.3.2. Composition of NGM Agar. *NGM* nematode growth medium.

Constituents	Final Concentration/100 mL of water
Pre-Autoclave	
**Bacteriological Agar	2.0/100 (g/mL)
**Bacteriological Peptone	0.25/100 (g/mL)
**NaCl	0.3/100 (g/mL)
Post-Autoclave	
**KPO ₄	2.5/100 (μL/mL)
**CaCl ₂	100/100 (μL/mL)
**Cholesterol	
**MgSO ₄	
*Streptomycin	
♦Carbenicillin	
♦IPTG	
♦Ampicillin	
♦FUDR	

* a constituent of all maintenance and reproductive capacity assay plates

♦ a constituent of all pharyngeal pumping rate and lifespan assay plates

Table A.3.3. Composition of LB Agar. *LB* Lysogeny broth.

Constituents	Final Concentration/100 mL of water
Pre-Autoclave	
LB Agar Powder	3.5/100 (g/mL)
Post-Autoclave	
Streptomycin	100/100 (µL/mL)

Table A.3.4. Composition of Lysis Buffer.

Constituents	Final Concentration/100 mL of water
Clorox	80/100 (mL/mL)
NaOH	20/100 (mL/ML)

Table A.3.5. Composition of Freezing Solution.

Constituents	Final Concentration/100 mL of water
Pre-Autoclave	
NaCl	0.59/100 (g/mL)
KH ₂ PO ₄	0.68/100 (g/mL)
Glycerol	23.74/100 (mL/mL)
NaOH	0.56/100 (mL/mL)
Post-Autoclave	
MgSO ₄	0.3/100 (mL/mL)

Table A.3.6. Composition of M9 Buffer.

Constituents	Final Concentration/100 mL of water
Pre-Autoclave	
NaCl	0.5/100 (g/mL)
KH ₂ PO ₄	0.3/100 (g/mL)
Na ₂ HPO ₄	0.6/100 (g/mL)
Post-Autoclave	
MgSO ₄	100/100 (µL/mL)

Table A.3.7 Volume of components in 20 μL cDNA synthesis reaction. *cDNA* complementary deoxyribonucleic acid.

Component	Volume (μL)
Nuclease-Free Water	To a total volume of 20 μL
Template RNA	Dependent on RNA concentration
5X ProtoScript II Buffer	4
0.1M DTT	2
Oligo D(T) ₂₃ VN (50 μM)	2
Protoscript II RT (200 U/ μL) *	1
10 mM dNTP Mix*	1
RNase Inhibitor (40 U/ μL)	0.2

*Protoscript II RT (Protoscript II Reverse Transcriptase)
dNTP (deoxynucleotide triphosphates)

Table A.3.8. Settings for thermal cycler (cDNA synthesis). *cDNA* complementary deoxyribonucleic acid.

Temperature	Time
65°C	5 minutes
42°C	60 minutes
65°C	20 minutes
4°C	∞

Table A.3.9. Volume of components in 20 μL PCR reaction. *PCR* polymerase chain reaction.

Component	Volume (μL)
Nuclease-Free Water	12.6
Template DNA	1
10X Standard Taq Reaction Buffer	2
10 mM dNTP Mix	1.6
10 μM Forward Primer	1
10 μM Reverse Primer	1
MgCl ₂	0.4
Taq DNA Polymerase	0.4

Table A.3.10. Settings for the thermal cycler (PCR reaction). *PCR* polymerase chain reaction.

Step	Time	Temperature (°C)
Initial Denaturation	5 minutes	95
Denaturation	30 seconds	95
Annealing	30 seconds	60
Extension	45 seconds	72
Final Extension	5 minutes	72
Hold	∞	4

Table A.3.11. Progeny laid by L4 N2 at 16°C post-exposure to ZnONP50. *L4* fourth larval stage, *N2* Bristol strain N2, *ZnONP50* zinc oxide nanoparticles (<50 nm).

Treatment Group (µg/mL)	Time (Hours)			Total Number of Progeny
	24 Hours	48 Hours	72 Hours	
Control	7.07 ± 0.81	20.20 ± 6.20	38.93 ± 1.79	66.2
Vehicle Control	5.73 ± 0.31 (p=0.2396)	10.27 ± 0.50 (p=0.3491)	20.73 ± 2.91 (p=0.2871)	36.73
1	4.47 ± 0.50 (p=0.0480) *	10.87 ± 0.48 (p<0.0001) *	19.40 ± 1.78 (p<0.0001) *	34.74
10	3.47 ± 0.29 (p=0.0064) *	9.67 ± 0.12 (p<0.0001) *	16.93 ± 0.31 (p<0.0001) *	30.07
100	2.53 ± 0.30 (p=0.006) *	7.40 ± 0.60 (p<0.0001) *	15.33 ± 1.03 (p<0.0001) *	25.26
1000	1.33 ± 0.31 (p<0.0001) *	5.13 ± 0.32 (p<0.0001) *	9.40 ± 0.87 (p<0.0001) *	15.86

*p-value indicate statistically significant difference between the respective treatment groups and the control treatment group (p<0.05)

Table A.3.12. Progeny laid by L4 N2 at 16°C post-exposure to ZnONP100. *L4* fourth larval stage, *N2* Bristol strain N2, *ZnONP100* zinc oxide nanoparticles (<100 nm).

Treatment Group (µg/mL)	Time (Hours)			Total Number of Progeny
	24 Hours	48 Hours	72 Hours	
Control	7.13 ± 3.33	25.00 ± 1.39	37.73 ± 1.67	69.86
Vehicle Control	5.80 ± 2.27 (p=0.1985)	12.60 ± 0.92 (p=0.1972)	18.87 ± 0.61 (p=0.1969)	32.27
1	4.67 ± 2.16 (p=0.0376) *	13.27 ± 1.63 (p<0.0001) *	18.27 ± 0.31 (p<0.0001) *	36.21
10	3.67 ± 1.47 (p=0.0036) *	12.13 ± 2.70 (p<0.0001) *	17.00 ± 0.20 (p<0.0001) *	32.8
100	2.47 ± 0.90 (p<0.0001) *	10.93 ± 1.30 (p<0.0001) *	15.8 ± 0.40 (p<0.0001) *	29.2
1000	1.27 ± 0.31 (p<0.0001) *	5.40 ± 2.03 (p<0.0001) *	8.07 ± 1.14 (p<0.0001) *	14.74

*p-value indicate statistically significant difference between the respective treatment groups and the control treatment group (p<0.05)

Table A.3.13. Progeny laid by L4 N2 at 16°C post-exposure to ZnOBP. L4 fourth larval stage, N2 Bristol strain N2, ZnOBP zinc oxide bulk particles.

Treatment Group (µg/mL)	Time (Hours)			Total Number of Progeny
	24 Hours	48 Hours	72 Hours	
Control	4.53 ± 0.50	11.27 ± 0.61	38.53 ± 0.64	54.33
Vehicle Control	4.32 ± 0.61 (p=0.8848)	20.27 ± 0.46 (p=0.450)	36.57 ± 0.12 (p=0.7848)	61.16
1	4.21 ± 0.53 (p=0.8798)	9.94 ± 0.76 (p=0.0006) *	33.46 ± 0.70 (p<0.0001) *	47.61
10	4.28 ± 0.12 (p=0.8848)	9.32 ± 0.72 (p<0.0001) *	35.00 ± 0.61 (p<0.0001) *	48.6
100	4.41 ± 0.35 (p=0.8848)	10.10 ± 0.31 (p=0.0020) *	32.99 ± 0.31 (p<0.0001) *	47.5
1000	4.25 ± 0.31 (p=0.8848)	9.54 ± 0.42 (p<0.0001) *	33.21 ± 0.87 (p<0.0001) *	47

*p-value indicate statistically significant difference between the respective treatment groups and the control treatment group (p<0.05)

Table A.3.14. Average pharyngeal pumping rate of L4 N2 post-exposure to ZnONP50. L4 fourth larval stage, N2 Bristol strain N2, ZnONP50 zinc oxide nanoparticles (<50 nm).

Treatment Group (µg/mL)	Time				
	4 Hours	24 Hours	48 Hours	72 Hours	96 Hours
Control	23.05 ± 2.03	23.10 ± 2.60	22.98 ± 2.74	23.10 ± 2.04	23.96 ± 2.09
Vehicle Control	22.99 ± 2.13 (p=0.9978)	23.10 ± 1.69 (p>0.9999)	22.91 ± 1.47 (p=0.9981)	23.20 ± 2.55 (p=0.9477)	23.01 ± 1.84 (p=0.523)
1	23.00 ± 0.31 (p=0.9987)	22.98 ± 0.18 (p=0.9913)	22.99 ± 0.22 (p=0.9970)	22.70 ± 0.75 (p=0.9447)	22.93 ± 0.95 (p=0.5324)
10	22.77 ± 1.17 (p=0.9900)	22.68 ± 1.05 (p=0.9679)	22.69 ± 0.66 (p=0.9890)	22.59 ± 0.84 (p=0.9447)	22.5 ± 1.09 (p=0.3993)
100	22.49 ± 1.19 (p=0.9704)	21.60 ± 1.80 (p=0.4664)	20.92 ± 1.69 (p=0.1729)	20.00 ± 1.43 (p=0.0120) *	18.8 ± 2.35 (p<0.0001) *
1000	22.35 ± 1.84 (p=0.9672)	21.44 ± 1.63 (p=0.4333)	19.93 ± 1.27 (p=0.0173) *	18.43 ± 1.30 (p<0.0001) *	17.5 ± 1.13 (p<0.0001) *

*p-value indicate statistically significant difference between the respective treatment groups and the control treatment group (p<0.05)

Table A.3.15. Average pharyngeal pumping rate of L4 N2 post-exposure to ZnONP100. L4 fourth larval stage, N2 Bristol strain N2, ZnONP100 zinc oxide nanoparticles (<100 nm).

Treatment Group (µg/mL)	Time				
	4 Hours	24 Hours	48 Hours	72 Hours	96 Hours
Control	22.97 ± 2.03	22.98 ± 2.60	23.07 ± 2.74	23.00 ± 2.04	23.02 ± 2.09
Vehicle Control	22.93 ± 2.13 (p=0.999)	22.97 ± 1.69 (p=0.9937)	23.02 ± 1.47 (p=0.9611)	23.00 ± 2.55 (p>0.9999)	22.99 ± 1.84 (p=0.9990)
1	23.00 ± 0.31 (p=0.9990)	22.80 ± 0.18 (p=0.9973)	22.80 ± 0.22 (p=0.9569)	22.90 ± 0.75 (p=0.9940)	22.98 ± 0.95 (0.9990)
10	21.90 ± 1.17 (p=0.7059)	22.80 ± 1.05 (p=0.9973)	22.50 ± 0.66 (p=0.9251)	22.30 ± 0.84 (p=0.8714)	22.0 ± 1.08 (p=0.6868)
100	21.70 ± 1.19 (p=0.7059)	21.80 ± 1.80 (p=0.6855)	20.70 ± 1.69 (p=0.0861)	19.50 ± 1.43 (p=0.0034) *	19.1 ± 2.35 (p=0.0008) *
1000	21.80 ± 1.84 (p=0.7057)	20.50 ± 1.63 (p=0.0815)	19.80 ± 1.27 (p=0.0089) *	18.90 ± 1.39 (p=0.0005) *	18.30 ± 1.13 (p<0.0001) *

*p-value indicate statistically significant difference between the respective treatment groups and the control treatment group (p<0.05)

Table A.3.16. Average pharyngeal pumping rate of L4 N2 post-exposure to ZnOBP. L4 fourth larval stage, N2 Bristol strain N2, ZnOBP zinc oxide bulk particles.

Treatment Group (µg/mL)	Time				
	4 Hours	24 Hours	48 Hours	72 Hours	96 Hours
Control	22.93 ± 2.03	22.97 ± 2.60	23.02 ± 2.74	23.00 ± 2.04	22.99 ± 2.10
Vehicle Control	22.97 ± 2.13 (p=0.9959)	22.98 ± 1.69 (p=0.9922)	23.07 ± 1.47 (p=0.9611)	22.98 ± 2.55 (p>0.9999)	23.02 ± 1.84 (p=0.9767)
1	22.73 ± 0.31 (p=0.9959)	22.68 ± 0.18 (p=0.9634)	22.70 ± 0.22 (p=0.9400)	22.78 ± 0.75 (p=0.9712)	22.69 ± 0.95 (p=0.9471)
10	22.67 ± 1.17 (p=0.9959)	22.53 ± 1.05 (p=0.9634)	22.46 ± 0.66 (p=0.9287)	21.93 ± 0.84 (p=0.6538)	21.8 ± 1.09 (p=0.5734)
100	22.60 ± 1.20 (p=0.9960)	22.07 ± 1.80 (p=0.8531)	21.87 ± 1.69 (p=0.7056)	21.53 ± 1.43 (p=0.4865)	21.27 ± 2.35 (p=0.3286)
1000	22.47 ± 1.84 (p=0.9950)	21.93 ± 1.93 (p=0.8454)	21.67 ± 1.27 (p=0.6505)	21.20 ± 1.30 (p=0.3450)	20.27 ± 1.13 (p=0.0435) *

*p-value indicate statistically significant difference between the respective treatment groups and the control treatment group (p<0.05)

Table A.3.17. Effect of ZnONP50 on the lifespan of N2 (mean \pm SD, n=3). *ZnONP50* zinc oxide nanoparticles (<50 nm), N2 Bristol strain N2.

Treatment Group	Mean Lifespan (Days)	% of Control	Maximum Lifespan (Days)
Control	16.67 \pm 5.09	100%	25.67 \pm 1.15
Vehicle Control	15.43 \pm 4.93	92.56% (p=0.0733)	24.67 \pm 1.53
1 μ g/mL	15.84 \pm 5.79	95.02% (p=0.5370)	24 \pm 2.65
10 μ g/mL	14.93 \pm 4.15	89.56% (p=0.0058) *	23 \pm 2
100 μ g/mL	11.41 \pm 4.22	68.45% (p<0.0001) *	19.67 \pm 1.53
1000 μ g/mL	11.91 \pm 4.61	71.45% (p<0.0001) *	19.33 \pm 0.58

*p-value indicates statistically significant difference between the respective treatment groups and the control treatment group (p<0.05)

Table A.3.18. Effect of ZnONP100 on the lifespan of N2 (mean \pm SD, n=3). *ZnONP100* zinc oxide nanoparticles (<100 nm), N2 Bristol strain N2.

Treatment Group	Mean Lifespan (Days)	% of Control	Maximum Lifespan (Days)
Control	18.31 \pm 4.69	100%	26.0 \pm 2
Vehicle Control	17.33 \pm 5.54	94.65% (p=0.5852)	24.67 \pm 0.58
1 μ g/mL	18.26 \pm 4.84	99.73% (p=0.8751)	26 \pm 1.73
10 μ g/mL	17.9 \pm 4.20	97.76% (p=0.4725)	25.33 \pm 0.58
100 μ g/mL	15.31 \pm 5.06	83.62% (p=0.0011) *	23.0 \pm 3
1000 μ g/mL	14.38 \pm 5.41	78.54% (p<0.0001) *	23.33 \pm 0.58

*p-value indicates statistically significant difference between the respective treatment groups and the control treatment group (p<0.05)

Table A.3.19. Effect of ZnOBP on the lifespan of N2 (mean \pm SD, n=3). *ZnOBP* zinc oxide bulk particles, N2 Bristol strain N2.

Treatment Group	Mean Lifespan (Days)	% of Control	Maximum Lifespan (Days)
Control	18.81 \pm 3.94	100.00%	26.33 \pm 2.08
Vehicle Control	19.61 \pm 4.64	104.26% (p=0.0939)	26.67 \pm 0.58
1 μ g/mL	20.07 \pm 4.70	106.70% (p=0.0057) *	26.33 \pm 1.53
10 μ g/mL	17.9 \pm 5.22	95.16% (p=0.6475)	25.0 \pm 2.0
100 μ g/mL	18.1 \pm 4.61	98.23% (p=0.9343)	25.67 \pm 1.53
1000 μ g/mL	17.34 \pm 5.59	92.19% (p=0.8764)	24.67 \pm 1.53

*p-value indicates statistically significant difference between the respective treatment groups and the control treatment group (p<0.05)

Table A.3.20. Densitometric analysis of 2% agarose gels containing *cep-1* DNA bands under different ZnO particle treatments and the 500bp marker. *DNA* deoxyribonucleic acid, *ZnO* zinc oxide, *bp* base pairs.

Replicate	ZnONP50	ZnONP100	ZnOBP	Untreated (Control)	500 bp Marker
1	30625.525	13227.744	11997.673	5765.104	1125681.1
2	26099.434	11861.501	10879.43	4731.276	113515.332
3	26536.383	12455.915	11845.087	4700.619	120247.683

Table A.3.21. Densitometric analysis of 2% agarose gels containing *pmk-1* DNA bands under different ZnO particle treatments and the 500bp marker. *DNA* deoxyribonucleic acid, *ZnO* zinc oxide, *bp* base pairs.

Replicate	ZnONP50	ZnONP100	ZnOBP	Untreated (Control)	500 bp Marker
1	33366.726	15921.714	12596.693	3662.205	138000.663
2	32210.605	16073.785	12703.815	3938.376	138521.763
3	30693.534	14580.371	12085.572	3201.134	130797.177

Table A.3.22. Densitometric analysis of 2% agarose gels containing *tba-1* DNA bands under different ZnO particle treatments and the 500bp marker. *DNA* deoxyribonucleic acid, *ZnO* zinc oxide, *bp* base pairs.

Replicate	ZnONP50	ZnONP100	ZnOBP	Untreated (Control)	500 bp Marker
1	23934.484	12838.744	29034.205	35329.617	105589.023
2	18415.099	11624.179	16875.134	30347.889	118688.914
3	19205.392	10235.673	17928.719	27458.454	114124.357

Vivid® CYP450 Reaction Buffer I

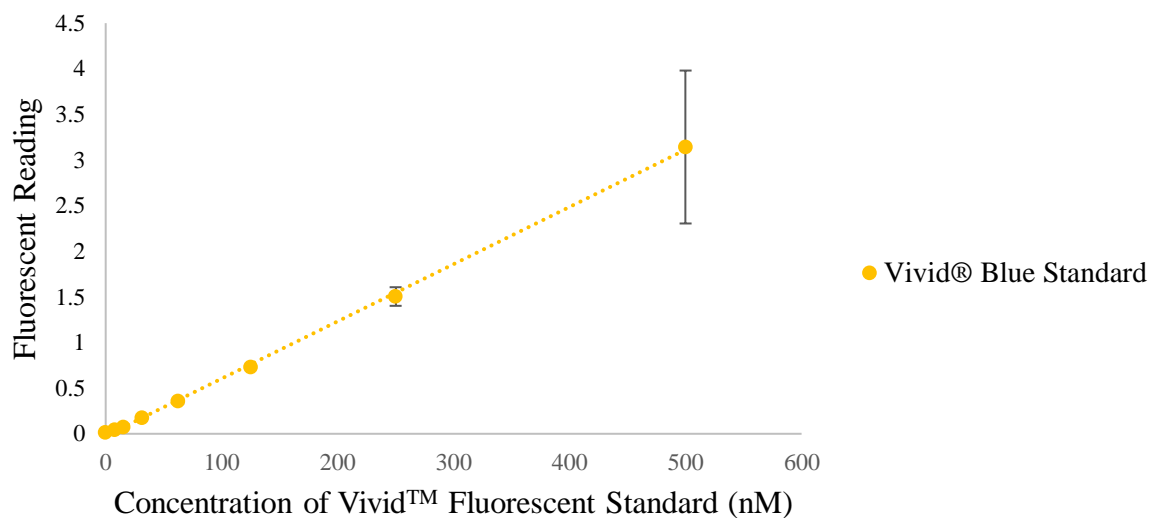


Figure A.4.1. Standard curve for Vivid® CYP450 Reaction Buffer I. Data set was generated by plotting the fluorescent reading of the metabolites formed from the metabolism of Vivid® Fluorescent Blue Standard against a range of its concentrations (500, 250, 125, 62.5, 31.25, 15.63, 7.81, and 0 nM). Each data point represents the mean \pm SD (n=3).

Vivid® CYP450 Reaction 0.5X Buffer II

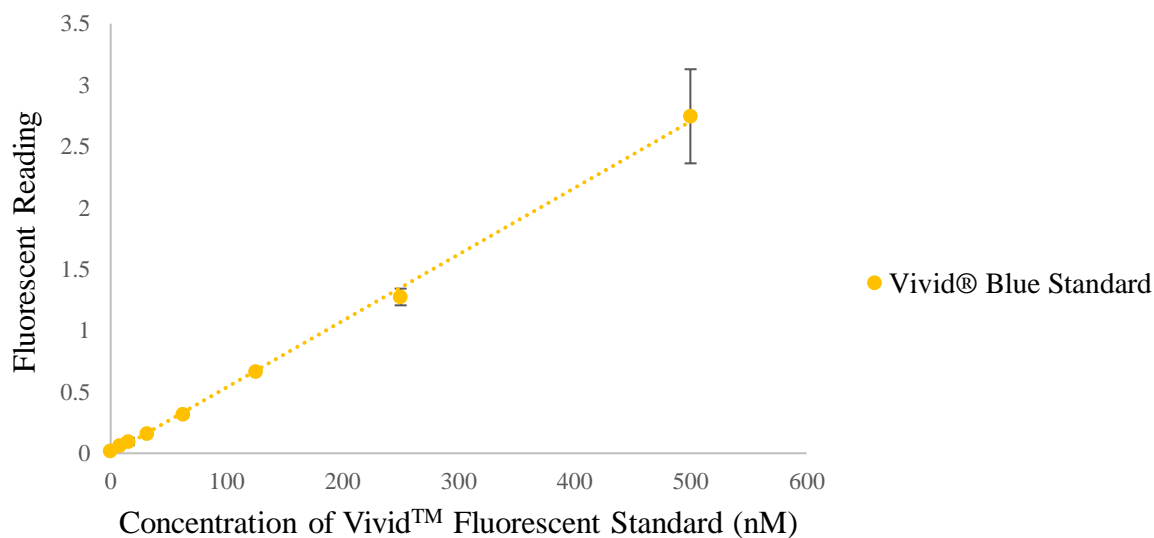


Figure A.4.2. Standard curve for Vivid® CYP450 Reaction 0.5X Buffer II. Data set was generated by plotting the fluorescent reading of the metabolites formed from the metabolism of Vivid® Fluorescent Blue Standard against a range of its concentrations (500, 250, 125, 62.5, 31.25, 15.63, 7.81, and 0 nM). Each data point represents the mean \pm SD (n=3).

Vivid® CYP450 Reaction Buffer II

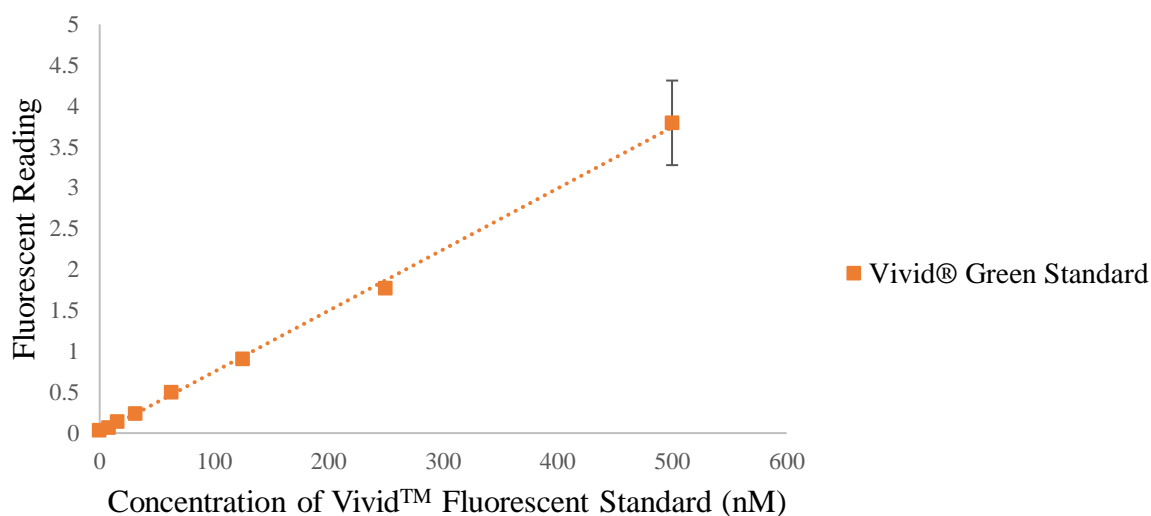


Figure A.4.3. Standard curve for Vivid® CYP450 Reaction Buffer II. Data sets were generated by plotting the fluorescent reading of the metabolites formed from the metabolism of Vivid® Fluorescent Green Standard against a range of its concentrations (500, 250, 125, 62.5, 31.25, 15.63, 7.81, and 0 nM). Each data point represents the mean \pm SD (n=3).

Vivid® CYP450 Reaction Buffer II

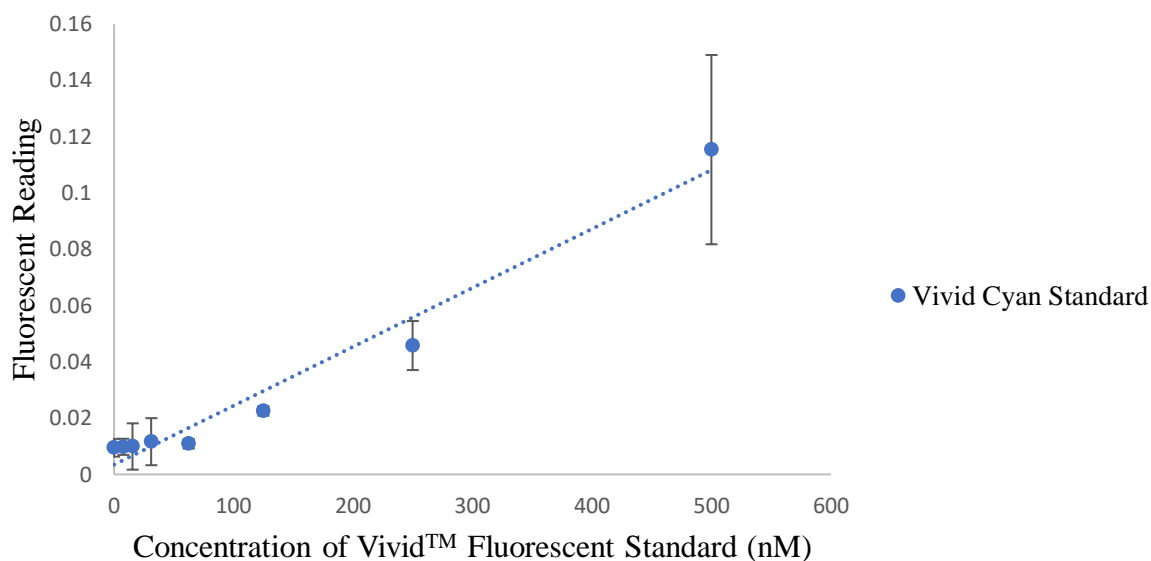


Figure A.4.4. Standard curve for Vivid® CYP450 Reaction Buffer II. Data sets were generated by plotting the fluorescent reading of the metabolites formed from the metabolism of Vivid® Fluorescent Cyan Standard against a range of its concentrations (500, 250, 125, 62.5, 31.25, 15.63, 7.81, and 0 nM). Each data point represents the mean \pm SD (n=3).

Vivid® CYP450 Reaction Buffer III

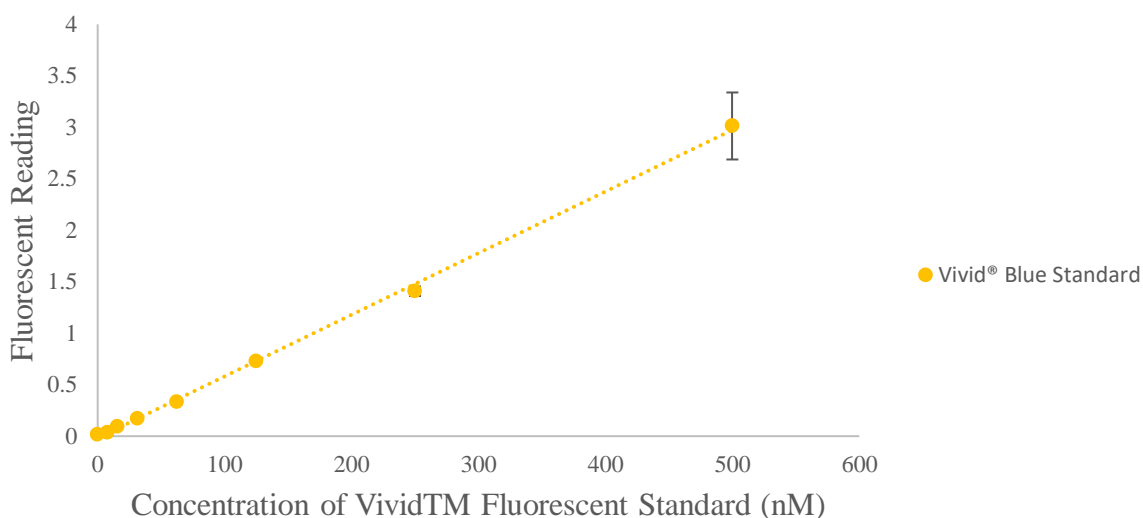


Figure A.4.5. Standard curve for Vivid® CYP450 Reaction Buffer III. Data set is generated by plotting the fluorescent reading of the metabolites formed from the metabolism of Vivid® Fluorescent Blue Standard against a range of its concentrations (500, 250, 125, 62.5, 31.25, 15.63, 7.81, and 0 nM). Each data point represents the mean \pm SD (n=3).

Table A.4.1. Summary of generated equations for each Vivid® CYP450 Reaction Buffer and Vivid® Fluorescent Standard' standard curve and its respective applicable CYP isozyme. CYP cytochrome P450.

Vivid® CYP450 Reaction Buffer	Vivid® Fluorescent Standard	Generated Equation	Applicable CYP Isozyme
Buffer I	Blue	$y = 0.0065x + 0.0329$	CYP1A2, CYP2B6, and CYP3A5
0.5X Buffer II	Blue	$y = 0.0054x - 0.0046$	CYP2A6
Buffer II	Cyan	$y = 0.0002x - 0.0094$	CYP2J2
	Green	$y = 0.0075x + 0.0026$	CYP2C8
Buffer III	Blue	$y = 0.006X - 0.0177$	CYP2E1

Table A.4.2. Equations obtained from Lineweaver-Burk Plots of CYP isozyme and respective ZnO particle pairings. *CYP* cytochrome P450, *ZnO* zinc oxide.

CYP Isozyme	ZnO Particle	Concentration (µg/mL)	Lineweaver-Burk Plot Equation
CYP2B6	ZnONP50	0 (Control)	$y = 0.0063x + 0.0004$
		6.25	$y = 0.0085x + 0.0003$
		12.5	$y = 0.0111x + (6 \times 10^{-5})$
		25	$y = 0.0115x + 0.0002$
		50	$y = 0.023x - 0.005$
	ZnONP100	0 (Control)	$y = 0.0039x + 0.0006$
		6.25	$y = 0.005x + 0.0007$
		12.5	$y = 0.0055x + 0.0007$
		25	$y = 0.0064x + 0.0007$
		50	$y = 0.0214x - 0.006$
CYP2C8	ZnONP50	0 (Control)	$y = 0.0017x + 0.0004$
		6.25	$y = 0.0060x + 0.0002$
		12.5	$y = 0.0062x + 0.0003$
		25	$y = 0.0063x + 0.0003$
		50	$y = 0.0079x + 0.0002$
CYP2E1	ZnONP50	0 (Control)	$y = 2.618x + 0.0105$
		6.25	$y = 2.8648x + 0.0082$
		12.5	$y = 3.027x + 0.0149$
		25	$y = 3.4807x + 0.0142$
		50	$y = 8.3854x - 0.0533$
	ZnONP100	0 (Control)	$y = 1.8594x + 0.00395$
		12.5	$y = 2.0188x + 0.0428$
		25	$y = 2.1155x + 0.05$
		50	$y = 2.6064x + 0.0511$
		100	$y = 5.4436x + 0.0137$
	ZnOBP	0 (Control)	$y = 2.1104x + 0.0301$
		6.25	$y = 2.2471x + 0.0374$
		12.5	$y = 2.513x + 0.0419$
		25	$y = 3.5673x + 0.0329$
50		$y = 4.7741x + 0.0482$	
CYP2J2	ZnONP50	0 (Control)	$y = 0.0217x - 0.0012$
		6.25	$y = 0.0375x - 0.0021$
		12.5	$y = 0.0716x - 0.0053$
		25	$y = 0.1226x - 0.0103$
		50	$y = 0.1866x - 0.0162$
	ZnONP100	0 (Control)	$y = 0.0194x - 0.0006$
		12.5	$y = 0.026x - 0.0012$
		25	$y = 0.0392x - 0.0023$
		50	$y = 0.0427x - 0.0022$
		100	$y = 0.1005x - 0.0075$
CYP3A5	ZnONP50	0 (Control)	$y = 0.0305x - 0.0012$
		12.5	$y = 0.0341x - 0.0013$
		25	$y = 0.038x - 0.0015$
		50	$y = 0.0443x - 0.0017$

		100	$y = 0.2667x - 0.0207$
	ZnONP100	0 (Control)	$y = 0.032x - 0.0005$
		6.25	$y = 0.0346x - 0.0003$
		12.5	$y = 0.036x - (5 \times 10^{-5})$
		25	$y = 0.0376x + 0.0002$
		50	$y = 0.2359x - 0.0148$